Homi Bhabha National Institute

Recommendations of the Viva Voce Board

As members of the Viva Voce Board, we certify that we have read the dissertation prepared by Mr. Chitrasen Jena entitled "Particle Production and Elliptic Flow of Light Nuclei in Relativistic Heavy Ion Collisions at RHIC" and recommend that it may be accepted as fulfilling the dissertation requirement for the Degree of Doctor of Philosophy.

Date: Ajit M Srivastava 21-12-12

Chairman - A. M SRIVASTAVA

Bedangadas Mohanty **Date:** 21/12/2012

Co-Guide / Convener - Prof. Bedanga Das Mohanty

Jane Alam **Date:** 21/12/2012

Member 1 - Prof. Jan-e Alam

Pradip Sahu **Date:** 21/12/2012

Member 2 - Prof. Pradip K. Sahu

Date: 21 12 12

Member 3 -

* Member 4 - (Guide) Prof. D P. Mahapatra

Final approval and acceptance of this dissertation is contingent upon the candidate's submission of the final copies of the dissertation to HBNI.

I hereby certify that I have read this dissertation prepared under my direction and recommend that it may be accepted as fulfilling the dissertation requirement.

* (D P Mahapatra) (Guide)

Date: 21-12-12

Bedangadas Mohanty (Bedangadas Mohanty) (co-guide)

Place: Bhubaneswar

PARTICLE PRODUCTION AND ELLIPTIC FLOW OF LIGHT NUCLEI IN RELATIVISTIC HEAVY ION COLLISIONS AT RHIC

By

CHITRASEN JENA
Institute of Physics
Bhubaneswar, India

A Thesis submitted to the
BOARD OF STUDIES IN PHYSICAL SCIENCES
In partial fulfillment of requirements
FOR THE DEGREE OF
DOCTOR OF PHILOSOPHY
OF
HOMI BHABHA NATIONAL INSTITUTE

DECEMBER, 2012

Statement by Author

This dissertation has been submitted in partial fulfillment of requirements for an advanced degree at Homi Bhabha National Institute (HBNI) and is deposited in the Library to be made available to borrowers under rules of the HBNI.

Brief quotations from this dissertation are allowable without special permission, provided that accurate acknowledgement of source is made. Requests for permission for extended quotation from or reproduction of this manuscript in whole or in part may be granted by the Competent Authority of HBNI when in his or her judgment the proposed use of the material is in the interests of scholarship. In all other instances, however, permission must be obtained from the author.

(Chitrasen Jena)

Declaration

I, Chitrasen Jena, hereby declare that the investigation presented in the thesis has been carried out by me. The work is original and has not been submitted earlier as a whole or in part for a degree / diploma at this or any other Institution / University.

(Chitrasen Jena)

To My Beloved Family

Acknowledgements

First and foremost, I would like to thank God for giving me the power to believe in my passion and pursue my dreams. I could never have done this without the faith I have in you, the Almighty. I thank you for the strength, courage and guidance you have given me.

I would like to express my deep sense of gratitude to my thesis supervisor Prof. D. P. Mahapatra for his invaluable guidance, encouragement and his constant support throughout my research period. His wide knowledge and his logical way of thinking have been of great value for me. I am greatly indebted to him for giving me total freedom both academically and socially during this period.

I would like to express my sincere and heartfelt thanks to my co-supervisor Prof. B. Mohanty for his continuous guidance, invaluable advice, untiring support and encouragement throughout my research period. I have greatly benefited from his deep knowledge and practical experiences of heavy ion physics. His constructive criticisms at every stage during my thesis work guided me to have a better understanding of the subject. I have learnt a lot from him, not only about physics but also about life in general.

It gives me immense pleasure to thank all members of the Relativistic Nuclear Collisions (RNC) group at the Lawrence Berkeley National Laboratory (LBNL). I would like to express my sincere thanks to Dr. N. Xu, the STAR spokesperson and Dr. H. G. Ritter, former RNC group leader, for giving me an opportunity to work in the RNC group at LBNL for two years. This is a wonderful place for research. My special thanks goes to Dr. N. Xu for his continuous support, help and guidance during my research period. I have greatly benefited from many fruitful discussions with him on various aspects of my research. I was equally benefited from many discussions with Dr. A. Poskanzer, Dr. J. Thomas, Dr. (Ms.) G. Odyniec, Dr. P. Jacobs, Dr. E. Sichtermann, Dr. X. Dong, Dr. H. Masui, Dr. Y. Zhang, Dr. (Ms.) V. Tram, Dr. A. Rose, Dr. X. Sun and Dr. A. Schmah. My special thanks goes to Dr. H. Masui for many useful discussions and patiently answering all my queries related to programming and data analysis. I would like to thank all graduate students and postdocs in the RNC group at LBNL. My special thanks goes to Dr. R. Cendejas, Dr. D. Kikola and Mr. C. Powell for their help and inspiring discussions. I would like to thank Ms. L. Bonifacio for helping me during my stay at LBNL.

I would like to thank the RNC group for providing me support to present my analysis work at various conferences and meetings such as Quark Matter 2009, Knoxville, TN, USA; Gordon Research Conference and Gordon-Kenan Research Seminar on Nuclear Physics 2009, Smithfield, RI, USA; Third Joint JPS/DNP Meeting 2009, Big Island, Hawaii, USA. My sincere thanks to Dr. N. Xu and the organizers of 7^{th} International Workshop on Critical Point and Onset of Deconfinement (CPOD 2011) for inviting me and providing financial support to present my analysis work at CPOD 2011, Wuhan, China.

I would like to take this opportunity to thank our STAR colleagues at the Brookhaven National Laboratory (BNL). I would like to express my sincere thanks to Dr. Z. Xu from BNL for giving me an opportunity to work with him on elliptic flow of light nuclei, search for anti-α particle in year 2007 Au+Au data and ZDC calibration in year 2010 Au+Au collisions. He has always been approachable for any discussions and help. I have greatly benefited from many useful discussions with him. I would like to thank Dr. J. Dunlop for many useful discussions and help during my d+Au data analysis. I would like to thank Dr. (Ms.) L. Ruan, Dr. A. Tang and Dr. P. Sorensen for many useful physics discussions and help during my stay at BNL. I would like to thank Dr. J. Laurete, Dr. G. V. Buren, Dr. Y. Fisyak and Dr. V. Fine for many useful STAR software related discussions. I am thankful to Ms. C. Feliciano and Ms. L. Mogavero for their valuable help during my stay at BNL. It was a nice experience to discuss and interact with several graduate students and postdocs at BNL. These include Dr. J. Chen, Dr. Z. Tang, Dr. M. Naglis, Dr. L. Kumar, Dr. J. Bouchet, Dr. (Ms.) Y. Xu, Dr. S. Shi, Dr. (Ms.) N. Li, Dr. X. Zhang, Dr. H. Qiu, Dr. B. Huang, Dr. X. Luo, Dr. J. Fu, Dr. L. Xue, Dr. (Ms.) X. Li, Mr. J. Zhao and Dr. Y. Pandit. I would like to thank all of them for making my stay wonderful and comfortable at BNL.

I would like to thank all the STAR physics working group (PWG) members and their conveners for providing healthy physics discussions and helping me on my analysis work. I wish to thank each and every member of the STAR Collaboration for all their help and support.

I would like to thank the RHIC Operations Group and RACF at BNL, the NERSC Center at LBNL and the Open Science Grid consortium for providing resources and support.

I would like to express my sincere thanks to Dr. Y. P. Viyogi, the PMD project leader and Head of Experimental High Energy Physics and Applications Group (EHEPA) at VECC for his constant support, advice and encouragement. I have greatly benefited from many interesting discussions with him. I would like to thank Prof. S. C. Phatak and Prof. P. K. Sahu for many useful discussions, for their kind support and encouragement during my research period.

My sincere thanks to Dr. T. K. Nayak and Dr. S. Chattopadhayay for their support, advice and encouragement starting from the days when I was working on the hardware and software development for the ALICE experiment at VECC. I would like to thank Prof. B. K. Nandi for his help, advice and encouragement. He helped me a lot to learn ALICE software framework and also to work on the alignment of PMD in ALICE. I would like to thank Prof. R. Verma for his help and many useful discussions during my stay at IIT, Bombay and CERN, Geneva.

During my Ph.D., I have worked closely with many members of the PMD collaboration for whom I have great regards. I would like to extend my sincere thanks to all my collaborators at VECC, Kolkata; Jammu University, Jammu; Panjab University, Chandigarh; Rajasthan University, Jaipur; IIT Bombay, Mumbai. I thank them all for their useful suggestions, help and encouragement. I have spent some very memorable time with them at various conferences, meetings, workshops and during my stay at BNL and CERN.

I would like to thank Mr. Md. Nasim, Dr. L. Kumar, Dr. P. K. Netrakanti and Prof. B. Mohanty for many interesting and stimulating discussions on our paper "Longitudinal scaling of observables in heavy ion collision models". I would also like to thank Mr. Md. R. Haque for many useful discussions on nuclei v_2 analysis. I would like to thank Dr. S. Zhang for many useful discussions on dynamical coalescence model.

I express my sincere thanks to my seniors Dr. D. Mishra, Dr. R. Sahoo, Dr. (Ms.) S. Dash and Dr. A. K. Dash, for all their help and encouragement during my research. I express my hearty thanks to our group members Mr. Rama Chandra Baral, Ms. Sabita Das, Mr. Gautam Mitra and Mr. Nihar Ranjan Panda at IOP. It was a great experience in sharing together many happy moments both in academic and non-academic front. My special thanks to Ms. Sabita Das for her help and support during my thesis writing.

I would like to express my sincere thanks to our director Prof. A. M. Jayannavar and the ex-directors of IOP Dr. R. K. Choudhury, Dr. Y. P. Viyogi and Prof. A. Khare for their help and encouragement in all respect.

I take this opportunity to thank all the faculty members of IOP for their support, teachings and guidance. My Special thanks to Prof. B. R. Sekhar and Prof. G. Tripathy for proofreading my thesis. I would like to thank all my teachers at school, college and university level who taught me and encouraged me to pursue research. This thesis would not have been possible without their blessings.

I would like to express my warm and sincere thanks to all my seniors, my pre-doctoral batchmates and scholar friends at IOP for all their help and good wishes. My special thanks to Ananta bhai, Manas bhai, Amulya bhai, Boby bhai, Mriganka, Sankha, Trilochan, Subrat, Smruti, Ranjita, Ambresh, Ashutosh, Jatis and Partha for spending their valuable time in many occasions with me. It will be impossible for me to forget many moments of fun and togetherness during festivals, picnics and parties at IOP. All of you have made my stay in the beautiful campus of IOP a memorable and pleasing one.

I would also like to thank to all the library, administrative, laboratory, hostel mess, and computer centre staff of IOP for their help and support at every stage.

I would like to take this opportunity to express my humble thanks to all the people who have helped me along the way, whether directly or indirectly, in the completion of this thesis. Here I could list only few names but of course there are many more who have contributed and helped me till now and will continue to do so. Words can never express how much I appreciate your support, advice, encouragement and friendship. I would like to thank all my well wishers here.

Last but most importantly, I would like to express my deepest gratitude to my parents and family members for their continuous love, support, encouragement and blessings. I am indebted to them for giving me the freedom to choose my career and for constantly providing me the much needed moral and emotional support at every stage of my life.

Date: **Chitrasen Jena**

Selected List of Publications/Preprints

*[1] **Yield and elliptic flow of $d(\overline{d})$ and $^{3}He(^{3}\overline{He})$ in Au+Au collisions at $\sqrt{s_{NN}} = 200$ GeV**,
Intended for Phys. Rev. C, is under PWG review.

*[2] **Observation of the antimatter helium-4 nucleus**,
H. Agakishiev *et al.* (STAR Collaboration), Nature **473**, 353, 2011.

*[3] **Elliptic flow of light nuclei in Au+Au collisions at $\sqrt{s_{NN}} = 200$ GeV**,
C. Jena (for the STAR collaboration), Nucl. Phy. A **862-863**, 281 (2011).

[4] **Longitudinal scaling of observables in heavy ion collision models**,
Md. Nasim, C. Jena, L. Kumar, P. K. Netrakanti, B. Mohanty,
Phys. Rev. C **83**, 054902, 2011.

*[5] **Elliptic flow of light nuclei in heavy ion collisions at STAR**,
C. Jena (for the STAR collaboration), To be published in Central European Journal of Physics.

[6] **Inclusive charged hadron elliptic flow in Au+Au collisions at $\sqrt{s_{NN}} =$ 7.7 - 39 GeV**,
L. Adamczyk *et al.* (STAR Collaboration), arXiv:1206.5528 [nucl-ex].

[7] **Di-electron spectrum at mid-rapidity in p+p collisions at $\sqrt{s_{NN}} = 200$ GeV**,
L. Adamczyk *et al.* (STAR Collaboration), arXiv:1204.1890 [nucl-ex].

[8] **Directed flow of identified particles in Au+Au Collisions at $\sqrt{s_{NN}}$ = 200 GeV at RHIC**,
L. Adamczyk *et al.* (STAR Collaboration), Phys. Rev. Lett. **108**, 202301 (2012).

[9] **Identified hadron compositions in $p+p$ and Au+Au collisions at high transverse momenta at $\sqrt{s_{NN}}$ = 200 GeV**,
G. Agakishiev *et al.* (STAR Collaboration), Phys. Rev. Lett. 108, 072302 (2012).

[10] **Directed and elliptic flow of charged particles in Cu+Cu collisions at $\sqrt{s_{NN}}$ = 22.4 GeV**,
G. Agakishiev *et al.* (STAR Collaboration), Phys. Rev. C **85**, 014901 (2012).

[11] **Strangeness Enhancement in Cu+Cu and Au+Au Collisions at $\sqrt{s_{NN}}$ = 200 GeV**,
G. Agakishiev *et al.* (STAR Collaboration), Phys. Rev. Lett. **108**, 072301 (2012).

[12] **Energy and system-size dependence of two- and four-particle v_2 measurements in heavy ion collisions at RHIC and their implications on flow fluctuations and nonflow**,
G. Agakishiev *et al.* (STAR Collaboration), arXiv:1111.5637 [nucl-ex].

[13] **Strange and Multi-strange Particle Production in Au+Au Collisions at $\sqrt{s_{NN}}$ = 62.4 GeV**,
M.M. Aggarwal *et al.* (STAR Collaboration), Phys. Rev. C **83**, 024901 (2011).

[14] **Scaling properties at freeze-out in relativistic heavy ion collisions**,
M.M. Aggarwal *et al.* (STAR Collaboration), Phys. Rev. C **83**, 034910 (2011).

[15] **An Experimental Exploration of the QCD Phase Diagram: The Search for the Critical Point and the Onset of De-confinement**,
M.M. Aggarwal *et al.* (STAR Collaboration), arXiv:1007.2613 [nucl-ex].

[16] K^{*0} **production in Cu+Cu and Au+Au collisions at** $\sqrt{s_{NN}}$**= 62.4 GeV and 200 GeV**,
M.M. Aggarwal *et al.* (STAR Collaboration), Phys. Rev. C **84**, 034909 (2011).

[17] **Charged and strange hadron elliptic flow in Cu+Cu collisions at** $\sqrt{s_{NN}}$ **= 62.4 and 200 GeV**,
B.I. Abelev *et al.* (STAR Collaboration), Phys. Rev. C **81**, 044902 (2010).

[18] **Spectra of identified high-**p_T $\pi^{\pm}$ **and** $p(\bar{p})$ **in Cu+Cu collisions at** $\sqrt{s_{NN}}$ **= 200 GeV**,
B.I. Abelev *et al.* (STAR Collaboration), Phys. Rev. C **81**, 054907 (2010).

[19] **Observation of an Antimatter Hypernucleus**,
B.I. Abelev *et al.* (STAR Collaboration), Science **328**, 58 (2010).

[20] **Identified particle production, azimuthal anisotropy, and interferometry measurements in Au+Au collisions at** $\sqrt{s_{NN}}$ **= 9.2 GeV**,
B.I. Abelev *et al.* (STAR Collaboration), Phys. Rev. C **81**, 024911 (2010).

[21] **Center of mass energy and system-size dependence of photon production at forward rapidity at RHIC**,
B.I. Abelev *et al.* (STAR Collaboration), Nucl. Phys. A **832**, 134 (2010).

*[22] **Particle production and elliptic flow of light nuclei in relativistic heavy ion collisions at RHIC** ,
C. Jena (for the STAR collaboration), Proceedings for DAE Symposium on Nuclear Physics, Vol. **56**, 1180 (2011).

*[23] **Recent results on identified particle spectra from** d**+Au collisions at RHIC**,
C. Jena (for the STAR collaboration), Proceedings for DAE Symposium on Nuclear Physics, Vol. **55**, 572 (2010).

[24] **Simulation framework for Photon Multiplicity Detector in ALICE**,
C. Jena *et al.*, Proceedings for DAE-BRNS Symposium on Nuclear Physics, Vol. **52**, 543 (2007).

[25] **Status of Photon Multiplicity Detector in ALICE**,
S.K. Prasad *et al.*, Proceedings for DAE-BRNS Symposium on Nuclear Physics, Vol. **52**, 650 (2007).

(*) indicates papers on which this thesis is based.

Synopsis

Quantum Chromodynamics (QCD), the theory of strong interactions, predicts the existence of the new state of matter called Quark-Gluon Plasma (QGP) at sufficiently high temperature and/or high energy density [1]. Such a matter is believed to have existed in the early Universe during the first few microseconds after the Big Bang. The primary aim of the heavy ion program at the Relativistic Heavy Ion Collider (RHIC) is to produce and study the dense, thermally equilibrated, strongly interacting matter, the Quark-Gluon Plasma [2-5]. One of the observable used to characterize the produced QCD matter in heavy ion collisions is the azimuthal anisotropy of produced particles. In order to study the QGP, it is also very important to understand the basic nucleon-nucleon interactions and nucleon-nucleus interactions. At RHIC, we study d+Au collisions to disentangle the initial and final state effects because one does not expect the final state interactions to play a dominant role in such a small system.

This thesis includes the study of identified particle spectra in d+Au collisions, elliptic flow of light nuclei in Au+Au collisions and observation of the antimatter helium-4 nucleus at RHIC. The data sets used for these analyses were taken by the STAR [6] experiment at RHIC. The Time Projection Chamber (TPC), the Forward Time Projection Chamber (FTPC) and the Time-of-Flight (TOF) detector systems were mainly used to identify the hadrons and light nuclei. The details of STAR detector and its subsystems are presented in this thesis.

We present the transverse momentum spectra for ϕ meson and pion in d+Au collisions at $\sqrt{s_{NN}} = 200$ GeV. This data set was taken in the year 2008 with significantly reduced material ($\sim$1/10) and high statistics ($\sim$3) compared to previous runs at RHIC. The measurement of identified particle spectra in d+Au collisions would be helpful to understand the initial Cold Nuclear Matter (CNM) effects such as Cronin effect, shadowing and gluon saturation. The Cronin effect [7], the enhancement of hadron yields at intermediate p_T in p+A collisions as compared to those in p+p collisions, has received renewed interest at RHIC. In order to understand the particle species dependence of Cronin effect and shed light on the initial conditions at RHIC, we have studied the nuclear modification factor (R_{dAu}) of the ϕ meson along with π, K and p in central d+Au collisions at $\sqrt{s_{NN}} = 200$ GeV. The study of ϕ meson is important because it's a meson with the hidden strangeness and mass close to that of light baryons. The measured R_{dAu} of ϕ meson increases above unity and is higher than R_{AuAu} at intermediate p_T. The enhancement of R_{dAu} of ϕ meson at the intermediate p_T is attributed to the Cronin effect. When we compare R_{dAu} of ϕ meson with that of other hadrons, it seems to follow closely the same for other mesons for $2.5 < p_T < 4$ GeV/c. In order to understand the particle production mechanism in forward (d going side) and backward (Au going side) rapidities, we have studied the rapidity asymmetry (Y_{Asym}) of ϕ mesons in the most central d+Au collisions. The Y_{Asym} for ϕ meson is found to be greater than unity in the measured p_T region for both $|y| < 0.5$ and $0.5 < |y| < 1$. Similar to other hadrons, the Y_{Asym} for ϕ meson is found to be larger for $0.5 < |y| < 1$ than for $|y| < 0.5$. This indicates the presence of some rapidity dependence of nuclear effects. No strong particle type dependence observed for Y_{Asym} in the measured p_T region.

The other major topic presented in the thesis is the elliptic flow, v_2, of light nuclei in Au+Au collisions at $\sqrt{s_{NN}} = 200$ GeV and 39 GeV. The Au+Au 200 GeV and 39 GeV data were taken with the STAR detector at RHIC in the year 2007 and 2010, respectively. In relativistic heavy ion collisions, light nuclei and antinuclei are formed through coalescence of produced nucleons and antinucleons or participant nucleons [8]. Since the binding energies of the light nuclei are small, this process can only happen at a late stage of the evolution of the system when interactions between nucleons and other particles are weak. The coalescence probability is related to the local nucleon density. Therefore, the production of light nuclei provides a tool to measure collective motion and freeze-out properties. We have studied v_2 of light nuclei and compared with those of their constituents (nucleons), in order to have better understanding of the coalescence mechanism in general. The measured v_2 for $d(\overline{d})$ and $^3He(\overline{^3He})$ as a function of transverse momentum p_T is found to follow an approximate atomic mass number (A) scaling. The v_2 values for light nuclei are further scaled to the number of constituent quarks (NCQ) of their constituent nucleons and are consistent with NCQ scaled v_2 for baryons and mesons [9]. This indicates that partonic collectivity dominates the expansion dynamics of the nucleus-nucleus collisions at RHIC. We have studied the centrality dependence of v_2 for light nuclei and compared those with that for other hadrons in Au+Au collisions at $\sqrt{s_{NN}} = 200$ GeV. Similar to other hadrons, an increase of p_T integrated v_2 scaled by the participant eccentricity as a function of collision centrality has been observed, which indicates a stronger collective expansion for more central collision. The mass dependence of average transverse momentum ($< p_T >$) and the average v_2 have been studied and compared to Tsallis Blast-Wave (TBW) model [10] predictions. Both v_2 and $< p_T >$ trends are consistent with expectations from TBW model fit. The v_2 of light nuclei measured in Au+Au collisions at $\sqrt{s_{NN}} = 200$ GeV are in good agreement with the dynamical coalescence model calculation [11].

We have observed the antimatter helium-4 nucleus, also known as the anti-α ($\overline{\alpha}$) at the STAR experiment at RHIC [12]. The anti-α consisting of two antiprotons and two antineutrons, is the heaviest antimatter discovered to date. In total 18 $^4\overline{He}$ counts were detected at the STAR experiment in 10^9 recorded Au+Au collisions at $\sqrt{s_{NN}} = 200$ GeV and 62 GeV. Out of those 18 counts, two are from year 2007 Au+Au collisions at 200 GeV and forms a part of this thesis. These two counts are identified by measuring the mean energy loss per unit track length ($\langle dE/dx \rangle$) in the TPC gas. We have done the Tsallis Blast-Wave model calculation to predict the anti-α spectra in Au+Au collisions at $\sqrt{s_{NN}} = 200$ GeV. The observed yield is consistent with expectations from thermodynamic and coalescent nucleosynthesis models, which has implications for future production of even heavier antimatter nuclei, as well as for experimental searches for new phenomena in the cosmos.

References

[1] F. Karsch, Nucl. Phys. A **698**, 199 (2002).

[2] J. Adams *et al.* (STAR Collaboration), Nucl. Phys. A **757**, 102 (2005).

[**3**] K. Adcox *et al.* (PHENIX Collaboration), Nucl. Phys. A **757**, 184 (2005).

[**4**] I. Arsene *et al.* (BRAHMS Collaboration), Nucl. Phys. A **757**, 1 (2005).

[**5**] B. B. Back *et al.* (PHOBOS Collaboration), Nucl. Phys. A **757**, 28 (2005).

[**6**] K. H. Ackermann *et al.* (STAR Collaboration), Nucl. Instr. Meth. A **499**, 624 (2003).

[**7**] J. W. Cronin *et al.*, Phys. Rev. D **11**, 3105 (1975).

[**8**] H. H. Gutbrod *et al.*, Phys. Rev. Lett. **37**, 667 (1976).

[**9**] C. Jena (for the STAR collaboration), Nucl. Phy. A **862-863**, 281 (2011).

[**10**] Z. Tang *et al.*, Phys. Rev. C **79**, 051901 (R) (2009).

[**11**] S. Zhang *et al.*, Phys. Lett. B **684**, 224 (2010).

[**12**] H. Agakishiev *et al.* (STAR Collaboration), Nature **473**, 353 (2011).

Contents

Statement by Author ii

Declaration iii

Acknowledgements v

Selected List of Publications/Preprints x

Synopsis xiv

1 Introduction 15

1.1 Quantum Chromodynamics 17

1.1.1 Deconfinement and QCD Phase Diagram 17

1.2 Relativistic Heavy Ion Collisions 21

1.2.1 The Evolution of a Heavy Ion Collision 22

1.3 Signatures of Quark-Gluon Plasma 24

1.3.1 Hadron Yields and Spectra 24

1.3.2 High p_T Probes 27

1.3.3 Strangeness Enhancement 29

1.3.4 Quarkonia Suppression 31

1.3.5 Photons and Dileptons 32

1.3.6 Azimuthal Anisotropy or Flow 36

1.4 Cold Nuclear Matter Effects 41

1.4.1 Cronin Effect 41

1.4.2 Using ϕ Mesons to Study the Particle Species Dependence of Cronin effect 44

1.5 Light Nuclei Production . . . 45
  1.5.1 Elliptic Flow of Light Nuclei . . . 46
1.6 Organization of the Thesis . . . 46

2 The STAR Experiment **52**
2.1 Relativistic Heavy Ion Collider (RHIC) . . . 52
2.2 The STAR Detector . . . 58
2.3 Trigger Detectors . . . 60
2.4 Electromagnetic Calorimeters . . . 62
  2.4.1 Barrel Electromagnetic Calorimeters . . . 62
  2.4.2 Endcap Electromagnetic Calorimeters . . . 63
2.5 Photon Multiplicity Detector . . . 63
2.6 Time Projection Chamber . . . 66
  2.6.1 Technical Design . . . 66
  2.6.2 Track Reconstruction . . . 68
  2.6.3 Particle Identification Using dE/dx . . . 69
2.7 Forward Time Projection Chamber . . . 71
2.8 Time-of-Flight . . . 72

3 Identified Particle Spectra in d+Au Collisions at $\sqrt{s_{NN}} = 200$ GeV **76**
3.1 Introduction . . . 76
3.2 ϕ Meson Production in d+Au Collisions . . . 77
  3.2.1 Data Set and Analysis Cuts . . . 77
  3.2.2 Event Selection . . . 77
  3.2.3 Centrality Selection . . . 79
  3.2.4 Track Selection . . . 81
  3.2.5 ϕ Meson Reconstruction and Raw Yield Extraction . . . 85
  3.2.6 Efficiency and Acceptance Correction . . . 91
  3.2.7 Results and Discussion . . . 91
    3.2.7.1 Transverse Momentum Spectra . . . 91
    3.2.7.2 Nuclear Modification Factor . . . 94
    3.2.7.3 Rapidity Asymmetry . . . 98
3.3 Pion Production in d+Au Collisions . . . 99

3.3.1 Pion Raw Yield Extraction 99
3.3.2 Efficiency and Acceptance Correction 101
3.3.3 Background Correction 103
3.3.4 Results and Discussion 104
3.3.4.1 Transverse Momentum Spectra 104
3.3.4.2 Antiparticle to Particle Ratio 110

4 Elliptic Flow of Light Nuclei in Au+Au Collisions 114

4.1 Introduction 114
4.2 Data Analysis 115
4.2.1 Data Set and Trigger 115
4.2.2 Event Selection 115
4.2.3 Centrality Selection 116
4.2.4 Track Selection 119
4.2.5 Particle Identification Method with TPC and TOF 121
4.2.6 Event Plane Method and v_2 125
4.2.7 Systematic Uncertainties 131
4.3 Results and Discussion 134
4.3.1 Elliptic Flow Results 134
4.3.2 v_2/n_q vs KE_T/n_q 138
4.3.3 Centrality Dependence 141
4.3.4 Blast-Wave Model and Mass Dependence 145
4.3.5 Collision Energy Dependence 148
4.3.6 Dynamical Coalescence Model 151

5 Search for Anti-Alpha 157

5.1 Introduction 157
5.2 Methods for Searching Anti-Alpha 157
5.3 Anti-Alpha Candidates 160
5.4 Blast-Wave Model Prediction and Invariant Yield 163
5.5 Summary 168

6 Conclusion 170

List of Figures

1.1 The fundamental particles of the standard model and the force mediating gauge bosons. I, II, and III represent the three generations of quarks and leptons. 16

1.2 Summary of measurements of $\alpha_s(Q)$ as a function of the respective energy scale Q and the curves are the QCD predictions [3]. 18

1.3 Lattice QCD calculations for pressure (left) and energy density (right) as a function of temperature for a strongly interacting matter [5]. The dependence on the number of quark flavors are shown in different colored lines. The arrows indicate the Stefan-Boltzmann limit in both the figures. 19

1.4 Schematic QCD phase diagram for nuclear matter [7]. 20

1.5 Collision of two nuclei A and B, with a non-zero impact parameter. The participant and the spectator nucleons are shown in red and yellow colors, respectively. 22

1.6 Space-time diagram and different evolution stages of a relativistic heavy ion collision. 23

1.7 Ratios of the mid-rapidity p_T integrated yields for different hadron species in Au+Au collisions at $\sqrt{s_{NN}} = 200$ GeV. The horizontal lines represent the statistical model fits to the particle ratios. The fit parameters are $T_{ch} = 163 \pm 4 MeV$, $\mu_B = 24 \pm 4 MeV$, $\gamma_s = 0.99 \pm 0.07$ [14]. The inset shows the variation of γ_s with centrality. The figure is taken from [13]. 26

1.8 The χ^2 contours for T_{fo} and $< \beta_T >$ extracted from thermal and radial flow fits for different hadrons produced in Au+Au collisions at $\sqrt{s_{NN}}$ = 200 GeV. The figure is taken from [13]. 26

1.9 Dihadron azimuthal correlations at high p_T for p+p, central d+Au and central Au+Au collisions at $\sqrt{s_{NN}}$ = 200 GeV measured in STAR experiment [13] 27

1.10 $R_{AA}(p_T)$ for charged hadrons for different centralities as measured in the STAR experiment [15]. 28

1.11 Upper panel: The ratio of the yields of K, ϕ, $\bar{\Lambda}$ and $\Xi + \bar{\Xi}$ normalized to $\langle N_{part} \rangle$ in Au+Au and Cu+Cu collisions to corresponding yields in inelastic p+p collisions as a function of $\langle N_{part} \rangle$ at $\sqrt{s_{NN}}$ = 200 GeV. Lower panel: Same as above but for only ϕ mesons in Au+Au and Cu+Cu collisions at $\sqrt{s_{NN}}$ = 200 and 62.4 GeV [20]. The error bars shown here represent the statistical and systematic errors added in quadrature. 30

1.12 Upper panel: J/ψ R_{AA} versus N_{part} for Au+Au collisions at $\sqrt{s_{NN}}$ = 200 GeV. The mid (forward) rapidity data are shown with open (solid) circles. Lower panel: Ratio of forward and mid-rapidity J/ψ R_{AA} as a function of N_{part} [31]. 31

1.13 Invariant cross section and invariant yield of direct photons as a function of p_T in p+p and Au+Au collisions at $\sqrt{s_{NN}}$ = 200 GeV, respectively [38]. The three curves on the p+p data represent NLO pQCD calculations, and the dashed curves show a modified power-law fit to the p+p data, scaled by T_{AA}. The black solid curves are exponential plus the T_{AA} scaled p+p fit. The red dotted curve near the 0-20% centrality data is a theory calculation [40] 34

1.14 Theoretical calculations of thermal photon emission are compared with the direct photon data in central 0-20% Au+Au collisions from PHENIX experiment [41]. 35

1.15 Schematic diagram showing the transformation of initial coordinate space anisotropy into a momentum space anisotropy in a non-central heavy ion collision. 36

1.16 The centrality dependence of p_T integrated v_2 as measured by the NA49 experiment at SPS [44] and STAR experiment at RHIC [45, 46]. 37

1.17 The p_T dependence of the elliptic flow parameter, v_2 in Au+Au collisions at $\sqrt{s_{NN}} = 200$ GeV as measured by the STAR experiment. The hydrodynamic calculations are shown as dot-dashed lines. This figure is taken from [46]. 38

1.18 v_2 as a function of p_T for different hadrons in minimum bias Au+Au collisions at $\sqrt{s_{NN}} = 200$ GeV [46]. Hydrodynamical calculations are shown by solid and dotted curves [47]. 39

1.19 Upper Panel: v_2/n vs. p_T/n for identified particles measured by the STAR experiment. n is the number of constituent quarks. The dashed-dotted line is the polynomial fit to the data. Lower Panel: The data from the upper panel is divided by the polynomial fit as a function of p_T/n [46]. 40

1.20 v_2 as a function of p_T and $m_T - m$ for identified particles in Au+Au collisions at $\sqrt{s_{NN}} = 200$ GeV, and also v_2/n_q vs $(m_T - m)/n_q$ in the last panel [49]. 40

1.21 The dependence of exponent α as a function of p_T for the production of different hadrons by 300 GeV protons in a fixed target experiment [52]. 43

1.22 Nuclear modification factors for the identified particles from d+Au collisions at $\sqrt{s_{NN}} = 200$ GeV, measured by the STAR (left) and PHENIX (right) experiments at RHIC [54, 55]. Nuclear modification factors calculated from the per-beam nucleon cross sections reported for $\sqrt{s_{NN}} = 27.4$ GeV p + A collisions are also shown for the comparison (right) [52]. 44

2.1 Schematic diagram showing the various stages of acceleration of ions at the RHIC. 54

2.2 Overview of the RHIC accelerator complex at Brookhaven National Laboratory, Upton, New York. 57

2.3 Perspective view of the STAR detector, with a cutaway for viewing inner detector systems [7]. 59

2.4 A cutaway side view of the STAR detector [3]. 59

2.5 Picture of the PMD after complete installation at the STAR experiment. 64
2.6 Schematic diagram showing the working principle of PMD. 65
2.7 Three dimensional schematic diagram indicating the main structural elements of the STAR TPC [10]. 66
2.8 A sector of the TPC anode plane indicating the inner and outer subsectors and their respective padrows [10]. 68
2.9 The energy loss distribution for charged particles in the STAR TPC as a function of momentum [10]. 70
2.10 Schematic diagram of an FTPC at the STAR experiment. 71
2.11 Geometry of TOF trays, modules and pads. 72
2.12 TOF $1/\beta$ as a function of momentum from run 9 p+p collisions at $\sqrt{s_{NN}} = 200$ GeV. 73

3.1 Event-by-event distribution of the Z-position of the primary vertex (V_z) in d+Au collisions at $\sqrt{s_{NN}} = 200$ GeV. 78
3.2 Left panel: Mean multiplicity from east FTPC as a function of day number in d+Au collisions at $\sqrt{s_{NN}} = 200$ GeV. Right panel: Multiplicity distributions from east FTPC for three different run periods in d+Au collisions at $\sqrt{s_{NN}} = 200$ GeV. 80
3.3 The multiplicity distributions from east FTPC (black circles) and the simulated multiplicity distributions using Monte Carlo Glauber calculation (red lines) for three different run periods in d+Au collisions at $\sqrt{s_{NN}} = 200$ GeV. Both the multiplicity distributions are normalized for multiplicity greater than 15 for each run period. 82
3.4 Number of primary tracks in TPC with $\chi^2 < 6$ (open circle) and without χ^2 cut (open triangles) as a function of BBC coincidence rate in d+Au collisions at $\sqrt{s_{NN}} = 200$ GeV. 84
3.5 Left panel: TPC dE/dx as a function of momentum for charged tracks in d+Au collisions at $\sqrt{s_{NN}} = 200$ GeV. Different color lines are expected dE/dx values for different charged tracks as predicted by the Bichsel function [11]. Right Panel: TPC dE/dx as a function of rigidity for charged tracks. Selected kaon candidates are shown in red bands. 85

3.6 Same-event (blue line) and mixed-event (red line) K^+K^- invariant mass distributions in 0-20% d+Au collisions at $\sqrt{s_{NN}} = 200$ GeV. ϕ meson mass from PDG is shown in black dotted lines [9]. 88

3.7 The ϕ meson mass peaks after subtracting the background for different p_T bins in 0-20% d+Au collisions at $\sqrt{s_{NN}} = 200$ GeV. Black curves show a Breit-Wigner + linear background function fit. Red curves and Green lines stand for a Breit-Wigner function and a linear function, respectively. 90

3.8 Reconstruction efficiency including acceptance of ϕ meson as a function of p_T in minimum bias d+Au collisions at $\sqrt{s_{NN}} = 200$ GeV. 92

3.9 ϕ meson transverse momentum spectrum in 0-20% d+Au collisions at $\sqrt{s_{NN}} = 200$ GeV. The dotted curve represents the Levy function fit to the distribution. Errors are statistical only. 93

3.10 Left panel: ϕ meson transverse momentum spectrum in 0-20% d+Au collisions at $\sqrt{s_{NN}} = 200$ GeV from year 2008 (run 8) and year 2003 (run 3). Right panel: The ratio of ϕ meson yield from run 8 and run 3 as a function of transverse momentum. 95

3.11 p_T dependence of the nuclear modification factor R_{AB} for ϕ meson in 0-20% d+Au and 0-5% Au+Au [16] collisions at $\sqrt{s_{NN}} = 200$ GeV. Errors are statistical only. The normalization uncertainties for 0-20% d+Au and 0-5% Au+Au collisions are shown in red and blue rectangular bands, respectively. 96

3.12 The nuclear modification factor R_{dAu} for ϕ meson as a function of p_T in 0-20% d+Au collisions at $\sqrt{s_{NN}} = 200$ GeV. The R_{dAu} for pions and protons are shown in brown and green bands, respectively [24]. The STAR preliminary data for K^0_S and $\Lambda + \bar{\Lambda}$ are taken from the Ref. [25]. Errors are statistical only. The gray shaded band represents the normalization uncertainty of 18%. 97

3.13 Rapidity asymmetry factor (Y_{asym}) for ϕ meson at $|y| < 0.5$ (left panel) and $0.5 < |y| < 1$ (right panel) in 0-20% d+Au collisions at $\sqrt{s_{NN}} =$ 200 GeV. For comparison, $\pi^+ + \pi^-$ (open squares) and $p + \bar{p}$ (solid triangles) results from STAR [32] are also shown. 99

3.14 The dE/dx distributions for positively charged (left) and negatively charged (right) hadrons in the TPC, normalized by the expected pion dE/dx at $0.25 < p_T < 0.3$ GeV/c and $|y| < 0.1$ in d+Au collisions at $\sqrt{s_{NN}} = 200$ GeV. The curves are Gaussian fits representing contributions from pions (dot-dashed, red), electrons (dashed, green), kaons (dot-dashed, blue), and protons (dotted, magenta). Errors are statistical only. 100

3.15 Reconstruction efficiency including detector acceptance for π^+ (red open squares) and π^- (black solid circles) as a function of p_T in minimum bias d+Au collisions at $\sqrt{s_{NN}} = 200$ GeV. The curves (red dashed line for π^+ and black solid line for red π^-) are parameterizations to the efficiency data and are used for corrections in the analysis. 102

3.16 Percentage of pion background contribution estimated from HIJING+GEANT as a function of p_T in d+Au collisions at $\sqrt{s_{NN}} = 200$ GeV. The curve is the parameterization to the pion background contribution and is used for correction in the analysis. 103

3.17 Transverse momentum spectra for π^- and π^+ at mid-rapidity ($|y| < 0.1$) in 0-20% d+Au collisions at $\sqrt{s_{NN}} = 200$ GeV. Spectra for π^+ is scaled by a factor 5 for clarity. Errors shown are statistical only. The curves are the Bose-Einstein function fit to the spectra. 105

3.18 Comparison of transverse momentum spectra for $\pi^\pm$ at mid-rapidity ($|y| < 0.1$) in 0-20% d+Au collisions at $\sqrt{s_{NN}} = 200$ GeV, obtained from year 2008 and year 2003. Errors are statistical only. 109

3.19 Variation of π^-/π^+ ratio as a function of p_T in 0-20% d+Au collisions at $\sqrt{s_{NN}} = 200$ GeV. Errors are statistical only. 110

4.1 Event-by-event distribution of the Z-position of the primary vertex (V_Z) in Au+Au collisions at $\sqrt{s_{NN}} = 200$ GeV (left) and 39 GeV (right).116

4.2 Left Column: Event-by-event distribution of $gRefMult$ for $0 < V_z < 2$ cm and $14 < V_z < 16$ cm compared with the multiplicity distribution from Glauber Monte Carlo simulation. Right Column: The ratio of simulated multiplicity distribution to real data $gRefMult$ distribution for $0 < V_z < 2$ cm and $14 < V_z < 16$ cm. 118

4.3 $gRefMult$ distribution before and after the re-weighting correction for $|V_z| < 30$ cm compared with the multiplicity distribution from MC Glauber simulation. 119

4.4 TPC reference multiplicity distribution for Au+Au collisions at $\sqrt{s_{NN}}$ = 39 GeV. The $RefMult$ cuts for different centrality bins are shown in different dashed blue lines. 120

4.5 TPC dE/dx as a function of rigidity. Different color lines are expected dE/dx values for different charged tracks predicted by the Bichsel function [4]. 122

4.6 Z distribution of ^3He (open square) and $\overline{^3He}$ (open circle) for $1.4 \leq p_T < 6$ GeV/c in Au+Au collisions at $\sqrt{s_{NN}} = 200$ GeV. 123

4.7 Left panel: Z distribution of $\overline{d}$ for $0.7 < p_T < 1.0$ GeV/c from Au+Au collisions at $\sqrt{s_{NN}} = 200$ GeV, fitted with a Gaussian (dashed, red line) plus an exponential (dot-dashed, green line) background function. Right panel: Z distribution of $\overline{d}$ for $1.6 < p_T < 1.9$ GeV/c from Au+Au collisions at $\sqrt{s_{NN}} = 39$ GeV, fitted with a double Gaussian function. 124

4.8 Left panel: TOF $1/\beta$ as a function of momentum from Au+Au collisions at $\sqrt{s_{NN}} = 39$ GeV. Different lines are the expected $1/\beta$ for different particles. Right panel: m^2 as a function of momentum for all charged tracks. 125

4.9 The distribution of second harmonic event plane angle (Ψ_2) from TPC in Au+Au collisions at $\sqrt{s_{NN}} = 200$ GeV (left) and 39 GeV (right). The red curves show a fit to the event plane angle distribution in both plots. 127

4.10 The distribution of second harmonic event plane angle (Ψ_2) from FTPC in Au+Au collisions at $\sqrt{s_{NN}} = 200$ GeV. The red curve shows a fit to the event plane angle distribution. 129

4.11 Event plane resolution as a function of centrality for TPC (solid square) and FTPC (open square) event plane in Au+Au collisions at $\sqrt{s_{NN}}$ = 200 GeV (left) and for TPC event plane in Au+Au collisions at $\sqrt{s_{NN}}$ = 39 GeV (right). See the text for details. 131

4.12 $\phi - \Psi$ distribution for ^3He in different p_T bins from minimum bias Au+Au collisions at $\sqrt{s_{NN}}$ = 200 GeV. Black curve is the fit to the $\phi - \Psi$ distribution. 132

4.13 $\phi - \Psi$ distribution for d in different p_T bins from minimum bias Au+Au collisions at $\sqrt{s_{NN}}$ = 200 GeV. Black curve is the fit to the $\phi - \Psi$ distribution. 132

4.14 $\phi - \Psi$ distribution for ^3He in different p_T bins from minimum bias Au+Au collisions at $\sqrt{s_{NN}}$ = 39 GeV. Black curve is the fit to the $\phi - \Psi$ distribution. 132

4.15 $\phi - \Psi$ distribution for d in different p_T bins from minimum bias Au+Au collisions at $\sqrt{s_{NN}}$ = 39 GeV. Black curve is the fit to the $\phi - \Psi$ distribution. 133

4.16 Left panel: Variation of v_2 for ^3He+$\overline{^3He}$ with the variation of dca cut in minimum bias Au+Au collisions at $\sqrt{s_{NN}}$ = 200 GeV. Right panel: Ratio of measured v_2 for ^3He+$\overline{^3He}$ with $dca < 0.5$ cm and $dca < 1$ cm. 134

4.17 Left panel: Variation of v_2 for ^3He+$\overline{^3He}$ with the variation of $nHitsFit$ cut in minimum bias Au+Au collisions at $\sqrt{s_{NN}}$ = 200 GeV. Right panel: Ratio of measured v_2 for ^3He+$\overline{^3He}$ with $nHitsFit \geq 25$ and $nHitsFit \geq 20$. 135

4.18 Left panel: Variation of v_2 for ^3He+$\overline{^3He}$ with the variation of Z range to identify ^3He candidates in minimum bias Au+Au collisions at $\sqrt{s_{NN}}$ = 200 GeV. Right panel: Ratio of measured v_2 for ^3He+$\overline{^3He}$ with $|Z(^3He)| < 0.2$ and $-0.05 < Z(^3He) < 0.2$. 135

4.19 v_2 as a function of p_T for $d(\overline{d})$, $\overline{t}$, and ^3He+$\overline{^3He}$ from 0-80% of the collision centrality in Au+Au collisions at $\sqrt{s_{NN}}$ = 200 GeV. The light nuclei v_2 measured in run 4 Au+Au 200 GeV are shown in the plot as a comparison [16]. 136

4.20 v_2 as a function of p_T for $\overline{d}$ and ^3He from 0-80% of the collision centrality in Au+Au collisions at $\sqrt{s_{NN}} = 39$ GeV. v_2 of $\overline{p}$ is shown in the plot as a comparison [18]. 137

4.21 $d(\overline{d})$ and ^3He+$\overline{^3He}$ v_2 as a function of KE_T, both v_2 and KE_T have been scaled by A. $\overline{p}$ (open square) and $\Lambda + \overline{\Lambda}$ (solid inverted triangle) v_2 are shown in the plot as a comparison. The dotted line is a fit to the v_2 of $\overline{p}$. The ratio of ^3He+$\overline{^3He}$ to $\overline{p}$ is shown in the lower panel of the plot. 139

4.22 $\overline{d}$ and ^3He v_2 as a function of KE_T, both v_2 and KE_T have been scaled by A. $\overline{p}$ (open square) v_2 are shown in the plot as a comparison. The dotted line is a fit to the v_2 of $\overline{p}$. The ratio of $\overline{d}$ to $\overline{p}$ and ^3He to $\overline{p}$ is shown in the lower panel of the plot. 140

4.23 v_2/n_q as a function of KE_T/n_q for different particles in minimum bias Au+Au collisions at $\sqrt{s_{NN}} = 200$ GeV. The inset is the ratio of ^3He+$\overline{^3He}$ to $p + \overline{p}$. 141

4.24 v_2/n_q as a function of KE_T/n_q for different particles in minimum bias Au+Au collisions at $\sqrt{s_{NN}} = 39$ GeV. 142

4.25 v_2 as a function of centrality for ^3He in Au+Au collisions at $\sqrt{s_{NN}} =$ 200 GeV. The shown errors are statistical only. 143

4.26 v_2/ε as a function of centrality for different particles in Au+Au collisions at $\sqrt{s_{NN}} = 200$ GeV [22], the ^3He value is scaled down by a factor of 3. The errors shown here are statistical only. 144

4.27 The transverse momentum spectra for identified particles including light nuclei ($d(\overline{d})$ and $^3He(\overline{^3He})$) in minimum bias ($0 - 80\%$ centrality) Au+Au collisions at $\sqrt{s_{NN}} = 200$ GeV. The symbols represent experiment data points. The curves represent the TBW fit for the hadrons. The curves for the light nuclei are the TBW prediction using parameters from the fit to other hadrons. 146

4.28 v_2 as a function of p_T for identified particles including light nuclei ($d(\overline{d})$ and $^3He(\overline{^3He})$) in minimum bias ($0-80\%$ centrality) Au+Au collisions at $\sqrt{s_{NN}}$ = 200 GeV. The symbols represent experiment data points. The curves represent the TBW fit for the hadrons. The curves for the light nuclei are the TBW prediction using parameters from the fit to other hadrons. 147

4.29 Mean v_2 and mean transverse momenta for identified particles (π, K, p, ϕ, d and ^3He) as a function of particle mass in minimum bias Au+Au collisions at $\sqrt{s_{NN}}$ = 200 GeV. Blast-Wave model calculations are also shown as shaded bands. 149

4.30 v_2 as a function of p_T for $d(\overline{d})$ and $^3He(\overline{^3He})$ from 0-80% of the collision centrality in Au+Au collisions at $\sqrt{s_{NN}}$ = 200 GeV and 39 GeV. v_2 of $\overline{p}$ at the two energies are shown for the comparison [18, 19]. 150

4.31 v_2 as a function of p_T for $d(\overline{d})$, $\overline{t}$, and ^3He+$\overline{^3He}$ from 0-80% of the collision centrality. v_2 of $\overline{p}$ is shown in the plot as a comparison [19]. The lines are calculations using a dynamical coalescence model [33]. See text for details. 153

5.1 TPC dE/dx as a function of rigidity. Different color lines are expected dE/dx values for different charged tracks predicted by the Bichsel function [4]. The two $^4\overline{He}$ candidates are encircled by an ellipse. 158

5.2 Tracks in TPC from an event which contains first $^4\overline{He}$ candidate (Track A) are shown in STAR event display with the beam axis normal to the page (left) and with the beam axis horizontal (right). The $^4\overline{He}$ candidate is highlighted in bold red line. 161

5.3 Tracks in TPC from an event which contains second $^4\overline{He}$ candidate (Track B) are shown in STAR event display with the beam axis normal to the page (left) and with the beam axis horizontal (right). The $^4\overline{He}$ candidate is highlighted in bold red line. 162

5.4 The top two panels show the dE/dx in units of multiples of $\sigma_{dE/dx}$, $n_{\sigma_{dE/dx}}$, of negatively charged particles (first panel) and positively charged particles (second panel) as a function of mass measured by the TOF system. The masses of ^{3}He ($^{3}\overline{He}$) and ^{4}He ($^{4}\overline{He}$) are indicated by the vertical lines at 2.81 GeV/c^2 and 3.73 GeV/c^2, respectively. The horizontal line marks the position of zero deviation from the expected value of dE/dx ($n_{\sigma_{dE/dx}} = 0$) for ^{4}He ($^{4}\overline{He}$). The rectangular boxes highlight areas for ^{4}He ($^{4}\overline{He}$) selections : $-2 < n_{\sigma_{dE/dx}} < 3$ and $3.35\,\mathrm{GeV/c^2} < \mathrm{mass} < 4.04\,\mathrm{GeV/c^2}$ (corresponding to a $\pm3\sigma$ window in mass). The bottom panel shows a projection of entries in the upper two panels onto the mass axis for particles in the window of $-2 < \sigma_{dE/dx} < 3$. 164

5.5 The transverse momentum spectra for identified particles including light nuclei ($d(\overline{d})$, $^{3}He(^{3}\overline{He})$, and $^{4}He(^{4}\overline{He})$) in 0-10% Au+Au collisions at $\sqrt{s_{NN}} = 200$ GeV. The spectra for light nuclei are predicted by TBW model using parameters from the fit to other hadrons. . . . 165

5.6 Differential invariant yields as a function of baryon number B, evaluated at $p_T/|B| = 0.875$ GeV/c, in central 200 GeV Au+Au collisions. The lines represent fits with the exponential formula $\propto e^{-r|B|}$ for positive and negative particles separately, where r is the production reduction factor. Errors are statistical only. Systematic errors are smaller than the symbol size, and are not plotted. 167

List of Tables

2.1 Summary of RHIC operating modes and total integrated luminosity delivered to all experiments [2]. 53

2.2 Some of the designed parameters and performance information of the RHIC. 57

3.1 Selection criteria to get a stable charged particle multiplicity distribution from east FTPC for centrality determination in run 8 d+Au collisions at $\sqrt{s_{NN}}$ = 200 GeV. 80

3.2 Centrality definitions in run 8 d+Au collisions at $\sqrt{s_{NN}}$ = 200 GeV using the multiplicity from east FTPC. 81

3.3 Initial geometric quantities for various collision centrality in run 8 d+Au collisions at $\sqrt{s_{NN}}$ = 200 GeV. 82

3.4 Track selection criteria for the ϕ meson study in run 8 d+Au collisions at $\sqrt{s_{NN}}$ = 200 GeV. 83

3.5 Values of fit parameters and χ^2/ndf from Levy function fit to the p_T spectrum of ϕ meson in 0-20% d+Au collisions at $\sqrt{s_{NN}}$ = 200 GeV. For comparison, the values of fit parameters and χ^2/ndf from fits to the p_T spectrum of ϕ meson for p+p, d+Au (run 3) and Au+Au collisions in different centralities at $\sqrt{s_{NN}}$ = 200 GeV are also listed [16]. Only statistical errors are shown. 94

3.6 Track selection criteria for the pion spectra analysis in run 8 d+Au collisions at $\sqrt{s_{NN}}$ = 200 GeV. 100

3.7 Fit parameters for π^+ and π^- efficiencies in minimum bias d+Au collisions at $\sqrt{s_{NN}}$ = 200 GeV. 102

3.8 Fit parameters from the polynomial fit to pion background contribution in d+Au collisions at $\sqrt{s_{NN}}$ = 200 GeV. 104
3.9 Values of fit parameters and χ^2/ndf from Bose-Einstein function fit to the p_T spectra for π^- and π^+ at mid-rapidity ($|y| < 0.1$) in 0-20% d+Au collisions at $\sqrt{s_{NN}}$ = 200 GeV. 106
3.10 Extrapolated average transverse momenta, $\langle p_T \rangle$ in GeV/c, of π^- and π^+ in 0-20% d+Au collisions at $\sqrt{s_{NN}}$ = 200 GeV. For comparison, $\langle p_T \rangle$ of π^- and π^+ for various collision systems and centralities are also listed [33]. Quoted errors are the quadratic sum of statistical and systematic uncertainties for all collision systems and centralities except for run 8 d+Au collisions, where only statistical errors are shown. . . 107
3.11 Integrated multiplicity rapidity density, dN/dy, of π^- and π^+ in 0-20% d+Au collisions at $\sqrt{s_{NN}}$ = 200 GeV. For comparison, dN/dy of π^- and π^+ for various collision systems and centralities are also listed [33]. Quoted errors are the quadratic sum of statistical and systematic uncertainties for all collision systems and centralities except for run 8 d+Au collisions, where only statistical errors are shown. . . 108

4.1 Centrality definitions in run 7 Au+Au 200 GeV collisions using $gRefMult$.117
4.2 Centrality definitions in run 10 Au+Au 39 GeV collisions using $RefMult$.120
4.3 Track selection criteria for the analysis presented in this chapter. . . . 121
4.4 Track selection criteria for flow tracks used in the event plane reconstruction 127
4.5 Fit parameters from the fit to the v_2 of $\overline{p}$ in Au+Au collisions at $\sqrt{s_{NN}}$ = 200 GeV and 39 GeV. 138
4.6 Initial geometric quantities for various collision centrality in Au+Au collisions at $\sqrt{s_{NN}}$ = 200 GeV [22]. 142
4.7 Values of parameters and best χ^2 from TBW fit to identified particle p_T spectra and v_2 in minimum bias Au+Au collisions at $\sqrt{s_{NN}}$ = 200 GeV. 146

5.1 Track selection criteria for identification of light nuclei. 159

5.2 Track information of the two $^4\overline{He}$ candidates in year 2007 minimum bias Au+Au collisions data at $\sqrt{s_{NN}} = 200$ GeV. 160

5.3 Values of parameters from TBW fit to identified particle transverse spectra for different centralities in Au+Au collisions at $\sqrt{s_{NN}} = 200$ GeV. Quoted errors are quadratical sum of statistical and uncorrelated systematic errors. 165

5.4 Values of yield ratios from TBW model in 0-10% Au+Au collisions at $\sqrt{s_{NN}} = 200$ GeV. 166

Chapter 1

Introduction

The goal of elementary particle physics is to understand the nature of matter at the most fundamental level, specifically to identify the basic constituents of matter and to understand their properties and interactions. In the past, people believed that atoms are indivisible and they are the fundamental building blocks of matter. Then, it was discovered that atoms themselves are made up of three kinds of smaller particles, called protons, neutrons and electrons. We now know that protons and neutrons are not the fundamental particles like electrons, because they consist of sets of point like particles called quarks held together by the exchange of messenger particles called gluons. Collectively these quarks and gluons are called "partons".

The fundamental structure of matter as well as the fundamental interactions can be well described by the "Standard Model"of particle physics. It is a gauge theory concerning three of the four known fundamental interactions between the elementary particles such as the electromagnetic, weak, and strong interactions. The gravitational interaction has not yet been incorporated in this model. The Standard Model of particle physics contains 12 flavors of elementary fermions (6 quarks and 6 leptons), plus their corresponding antiparticles, as well as elementary bosons that mediate the forces. These 12 fundamental fermionic flavors are divided into three generations of four particles each. The grouping of elementary particles of the Standard Model and the force mediating gauge bosons are shown in the Fig. 1.1. Here, photons carry the electromagnetic force, gluons carry the strong force, and weak bosons ($W^{\pm}$ and Z^0) carry the weak force.

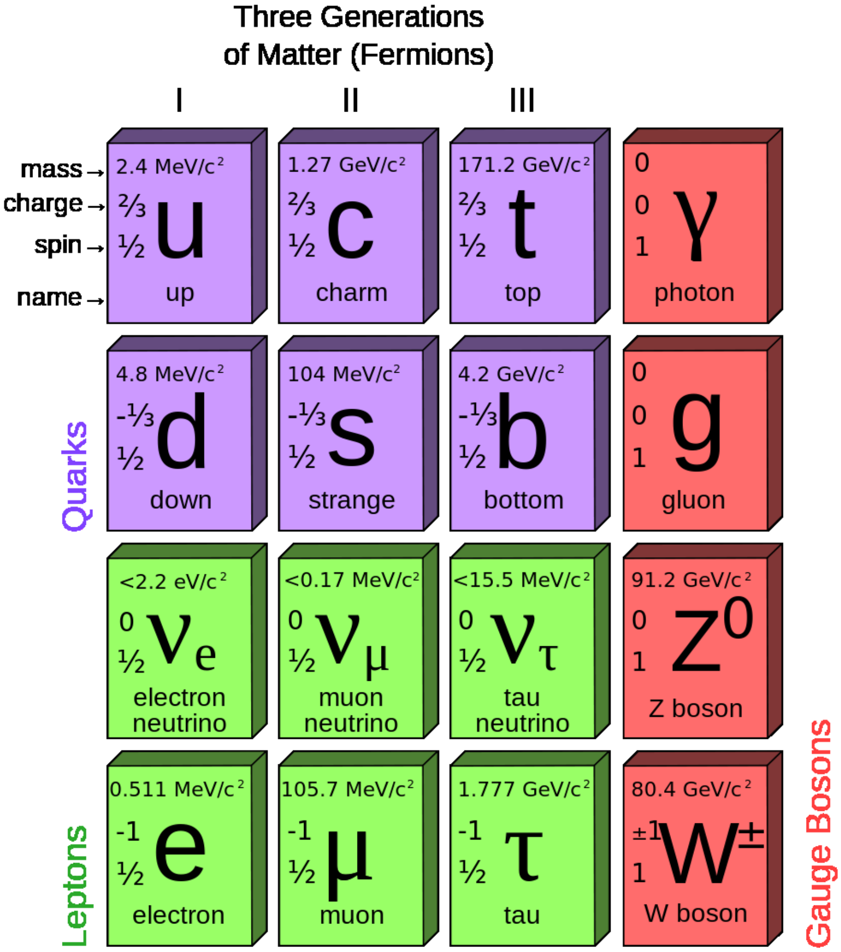

Figure 1.1: The fundamental particles of the standard model and the force mediating gauge bosons. I, II, and III represent the three generations of quarks and leptons.

1.1 Quantum Chromodynamics

Quantum Chromodynamics (QCD) is the theory of the strong interaction, one of the four fundamental forces in nature [1, 2]. It describes the interactions between quarks and gluons which bind together to form hadrons. The charges responsible for QCD interactions are called “color charges”, hence the “chromo”component of the theory’s name. There are two key features of QCD such as confinement and asymptotic freedom, which can be understood from the expression of strong interaction coupling constant, α_s, given by:

$$\alpha_s(Q^2) \approx \frac{12\pi}{(33 - (2N_f)ln(Q^2/\Lambda^2_{QCD}))}, \tag{1.1}$$

where Q^2 is the momentum transfer, N_f is the number of quark flavors and Λ is the scale parameter. The typical value of Λ, obtained from scattering experiments is about 200 MeV. The values of α_s has been extracted from different experimental results and compared with perturbative QCD (pQCD) predictions [3]. The pQCD has been very successful in predicting and describing various processes observed in different experiments as illustrated in Fig. 1.2.

At large distances or small momentum transfers, α_s is large and increases as the distance between two quarks is increased. This property is called “Confinement”and is the reason that quarks are never found alone but are instead always bound together in groups of three in the form of baryons or as quark-antiquark pairs in the form of mesons. For sufficiently short distances or large momentum transfers, α_s tends to zero and quarks behave as free non-interacting particles. As a consequence, QCD medium at very high temperatures is predicted to be a gas of free quarks and gluons. This property, where the interactions between the quarks becomes arbitrarily weak at length scales that asymptotically goes to zero, is known as “Asymptotic Freedom”. This was discovered in 1973 by David Gross, Frank Wilczek, and David Politzer who were awarded the Nobel Prize in Physics in 2004.

1.1.1 Deconfinement and QCD Phase Diagram

It was suggested by Collins and Perry in 1975, soon after the discovery of asymptotic freedom in non-abelian gauge theories, that the dense nuclear matter at the center

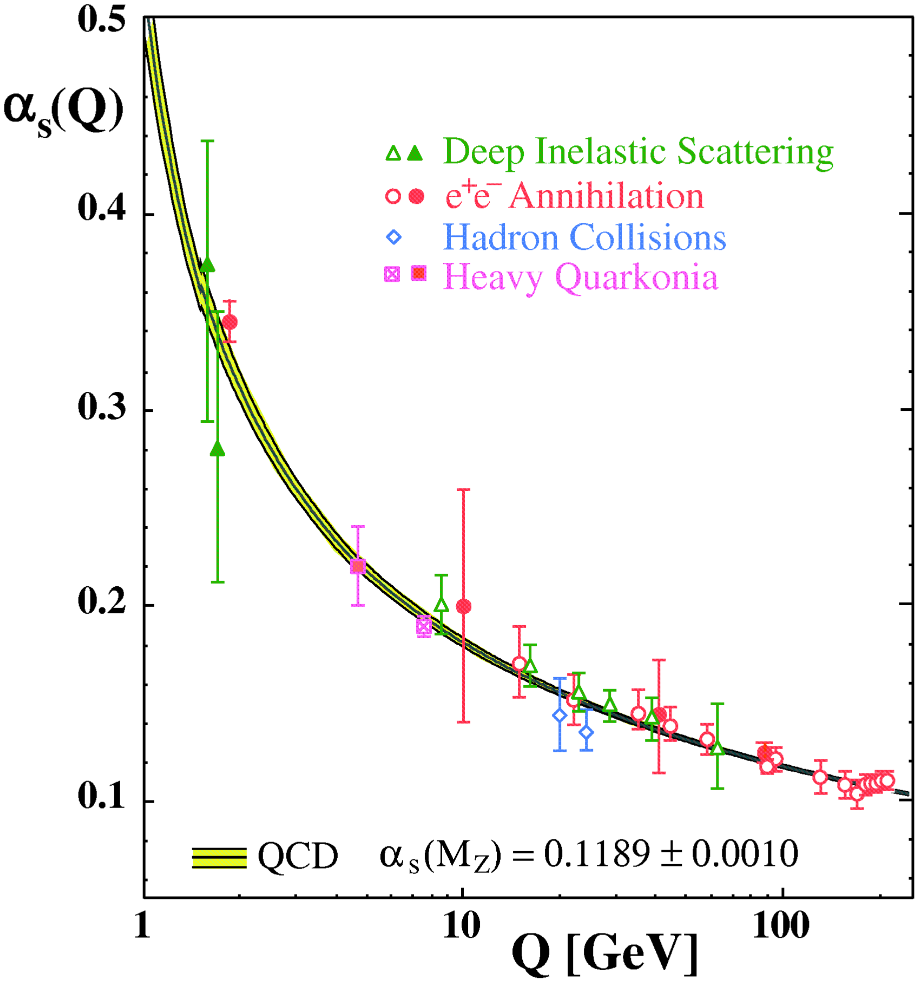

Figure 1.2: Summary of measurements of $\alpha_s(Q)$ as a function of the respective energy scale Q and the curves are the QCD predictions [3].

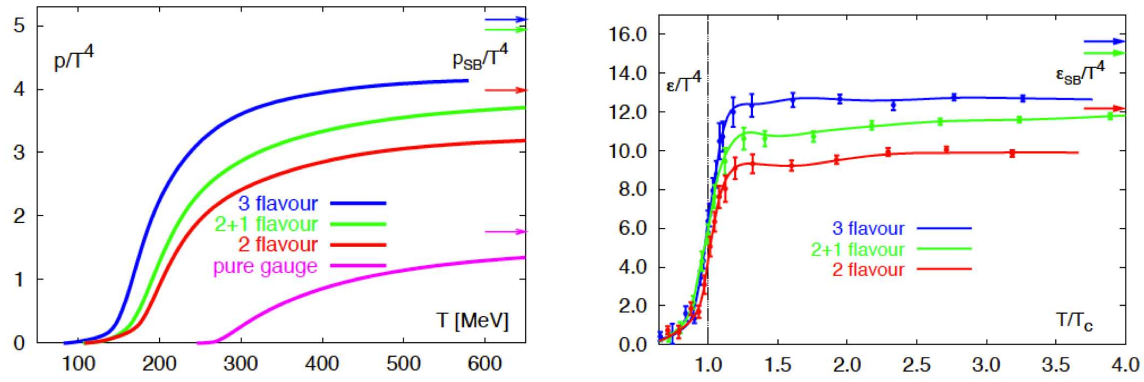

Figure 1.3: Lattice QCD calculations for pressure (left) and energy density (right) as a function of temperature for a strongly interacting matter [5]. The dependence on the number of quark flavors are shown in different colored lines. The arrows indicate the Stefan-Boltzmann limit in both the figures.

of neutron stars could consist of deconfined quarks and gluons [4]. The lattice QCD calculations predicts a phase transition from a confined hadronic matter to a deconfined state of quarks and gluons at a critical temperature of $T_c \sim 170$ MeV and an energy density of $\epsilon \sim 1$ GeV$/fm^3$ [5, 6]. This predicted state of matter containing deconfined quarks and gluons is called the Quark-Gluon Plasma (QGP), which is believed to have existed a few microseconds after the creation of the universe in the Big Bang. This plasma also exhibits the so-called "Chiral Symmetry"which in normal nuclear matter is spontaneously broken, resulting in effective quark masses which are much larger than the actual masses. Figure 1.3 shows the temperature dependence of pressure (p) and energy density (ϵ) as obtained from lattice QCD calculations [5]. These calculations are performed for non-zero temperatures and non-zero chemical potentials. The ϵ/T^4 is proportional to the number of degrees of freedom in the thermodynamic system. The sharp increase of ϵ/T^4 around critical temperature indicates a transition in the system to a state where the quarks and gluons have become relevant degrees of freedom. The pressure changes slowly at T_c compared to the rapid increase of the energy density, which means the pressure gradient in the system is significantly reduced during the phase transition.

Figure 1.4 shows the schematic phase diagram of strongly interacting matter, which depicts possible phases of nuclear matter depending on its temperature (T) and the baryon chemical potential (μ_{B}). At a larger T and smaller μ_{B}, lattice QCD

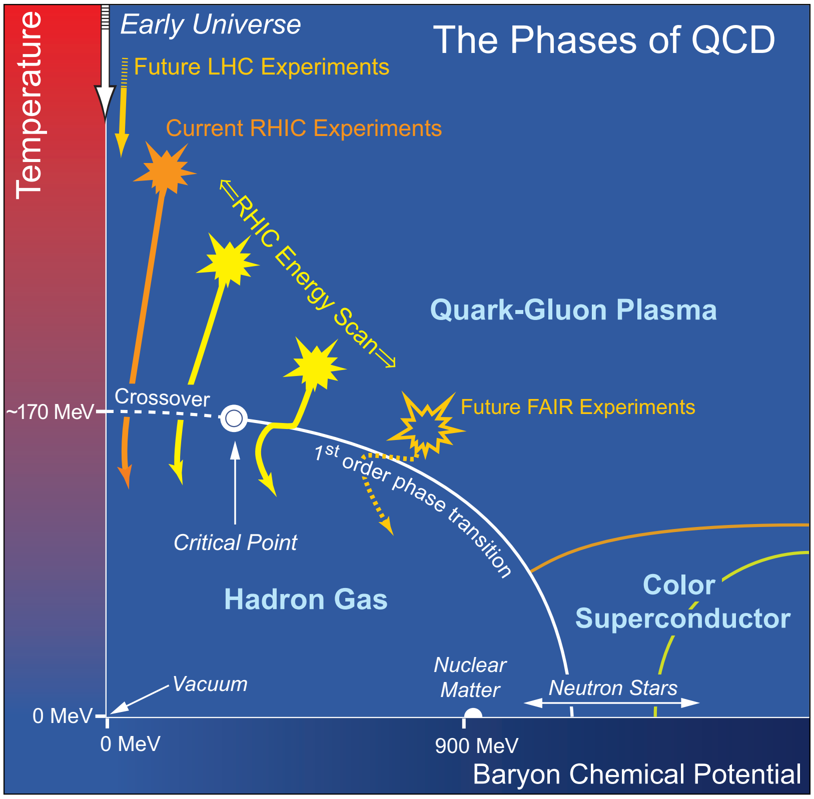

Figure 1.4: Schematic QCD phase diagram for nuclear matter [7].

predicts a smooth crossover between phases [8], while theoretical calculations show that at smaller T and larger μ_{B} a first order phase transition may take place between hadron gas and quark-gluon plasma [9]. The point in the QCD phase diagram where the first order phase transition ends would be the QCD critical point. The scenario of very high temperature and almost zero net baryon density is very similar to the early universe, where as high net baryon density and very low temperature scenario has similarity to the inner core of the neutron star. At larger μ_{B} and relatively low T, color superconducting phase is predicted to exist.

1.2 Relativistic Heavy Ion Collisions

The primary motivation for colliding heavy ions at ultrarelativistic energies is the belief that it is possible to create macroscopic volumes of nuclear matter at such extreme conditions of temperature and energy density that a phase transition will occur from a confined hadronic matter to a plasma of deconfined quarks and gluons. The first heavy ion collision experiment at modestly relativistic conditions was started in the early 1970s at the Bevalac at Lawrence Berkeley National Laboratory (LBNL). This Bevalac facility permitted the acceleration of nuclear projectiles to about 1 A GeV/c, which yields compressed nuclear matter at few times normal nuclear density. The success of initial heavy ion experimental program, specifically the demonstration of the possibility of studying the properties of compressed and excited matter led to several heavy ion collision experiments at BNL (Brookhaven National Laboratory) and CERN (European Organization for Nuclear Research). The Alternating Gradient Synchrotron (AGS) at BNL and the Super Proton Synchrotron (SPS) at CERN have run fixed target heavy ion collision experiments at top center of mass energies of $\sqrt{s_{NN}}$ = 4.86 GeV and $\sqrt{s_{NN}}$ = 17.3 GeV, respectively. The Relativistic Heavy Ion Collider (RHIC) at BNL is the first machine in the world capable of colliding ions as heavy as gold. Since its start of operation in the year 2000, RHIC has collided a variety of beams such as p+p, d+Au, Cu+Cu, Cu+Au, Au+Au, and U+U at center of mass energies ranging from 7.7 GeV to 500 GeV. RHIC is now the second highest energy heavy ion collider in the world. On 7 November 2010, the Large Hadron Collider (LHC) at CERN became the worlds most energetic heavy ion accelerator when lead

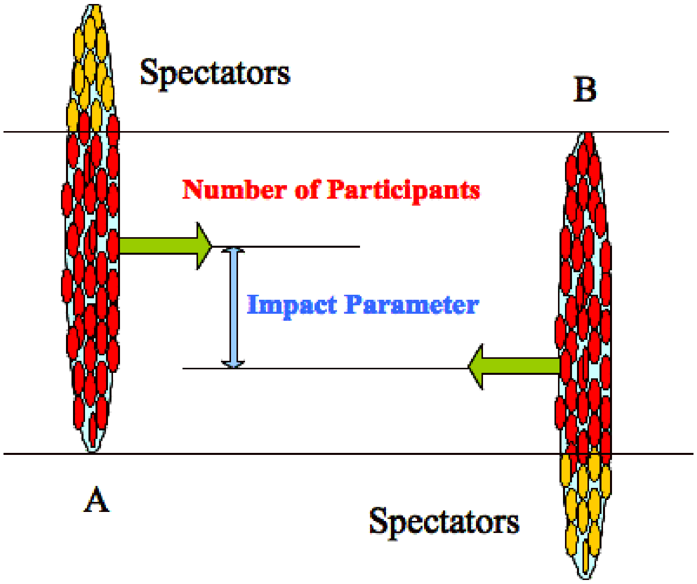

Figure 1.5: Collision of two nuclei A and B, with a non-zero impact parameter. The participant and the spectator nucleons are shown in red and yellow colors, respectively.

(Pb) nuclei collided at a centre of mass energy $\sqrt{s_{NN}} = 2.76$ TeV per colliding nucleon pair. Although the LHC physics program is mainly based on proton-proton collisions to search for the elusive Higgs boson, it will operate with heavy ions for about one month per year to investigate QGP.

1.2.1 The Evolution of a Heavy Ion Collision

In relativistic heavy ion collisions, two nuclei are accelerated to nearly the speed of light in opposite directions. The nuclei traveling at relativistic velocities appear Lorentz contracted along the beam direction (z-axis) and take on a pancake shape. Figure 1.5 shows a schematic diagram of a collision between two nuclei at very high energy. The region of overlap between the incoming nuclei, is usually characterized by the impact parameter (b) of the collision. Central collisions are events with small impact parameters, while peripheral collisions have large impact parameters. Nucleons in the overlap region that interact are called "participants"and non-interacting nucleons are called "spectators". The number of interacting participant nucleons and non-interacting spectators depend on the overlap between the incident nuclei and hence the impact parameter of the collision.

The space-time evolution of the medium created in an ultrarelativistic heavy ion

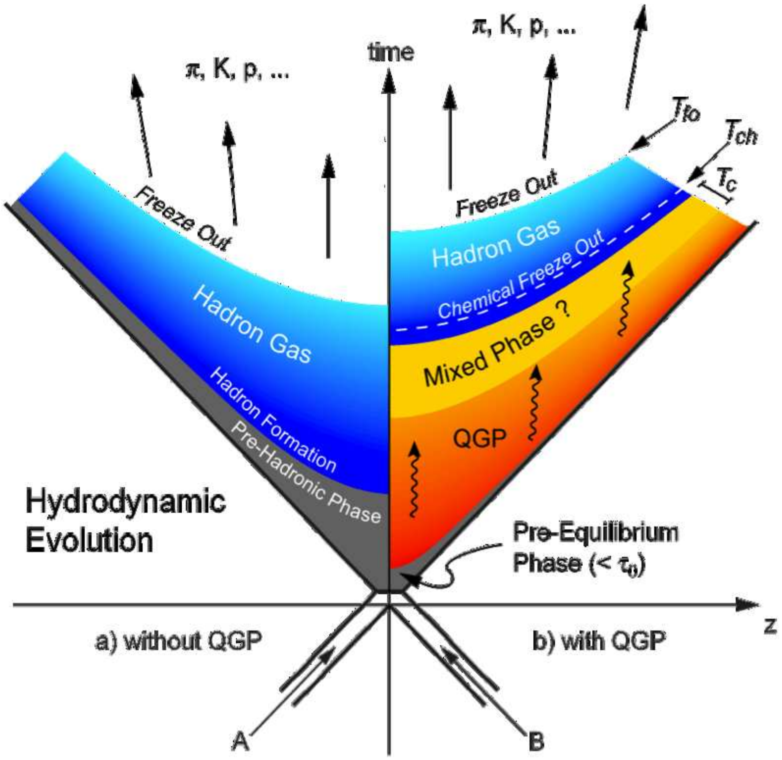

Figure 1.6: Space-time diagram and different evolution stages of a relativistic heavy ion collision.

collision is depicted schematically in Fig. 1.6. Let us consider the head-on collision of two Lorentz contracted nuclei, A and B, along the beam direction (z-axis), in the center of mass frame. At the point $(z, t) = (0,\ 0)$, collisions of the nucleons of the projectile nucleus with the nucleons of the target nucleus take place. In this collision, a large amount of the energy is deposited in the interaction region, which may lead to at least two possible scenarios. If the energy density created in the collision does not reach the critical value necessary for QGP formation, then the system will be composed of a gas of hadrons as shown on the left-hand side of Fig. 1.6. However, the other possibility is that the initial energy density is large enough and the temperature of the created system exceeds the critical temperature T_c, a phase transition is expected to occur and a fireball of deconfined quarks and gluons is formed. This scenario is shown on the right-hand side of Fig. 1.6. The fireball initially may not be in thermal equilibrium, but subsequent interactions among quarks and gluons may bring it to local equilibrium at the proper time τ_0. This phase of matter can be identified as the QGP. The subsequent expansion of the medium is then governed by the relativistic hydrodynamics. As the system expands and cools to the critical temperature T_c, hadronization takes place and the quarks and gluons become confined. If the phase transition from quarks and gluons to hadrons is of first order then it will go through a mixed phase, in which quarks and gluons co-exist with hadrons. The expansion is likely to be isothermal in this phase and latent heat is used to convert the quarks and gluons to hadrons. As the system of hadrons continues to expand, "chemical freeze-out"occurs at a temperature T_{ch}, where the inelastic interactions between the hadrons cease and the relative abundances for hadron species do not change any more. The expansion continues until a temperature T_{fo}, where the mean free path of hadrons becomes larger than the system size and the elastic interactions between the hadrons cease. This is called as "thermal freeze-out"or "kinetic freeze-out". At this stage, the particles come out of the system freely and get detected in the detectors.

1.3 Signatures of Quark-Gluon Plasma

The hot and dense medium created in heavy ion collisions is extremely short-lived ($\sim 5-10$ fm/c) and only the final state particles are measured in the detectors of experiments. Therefore, one has to use various experimental observables to characterize the properties of the system created in these collisions. Many signatures of QGP formation and associated characteristics of the medium have been proposed [10, 11]. In the following sections, we briefly discuss some of the proposed signatures of QGP formation.

1.3.1 Hadron Yields and Spectra

In high energy heavy ion collisions, the transverse momentum (p_T) spectra of identified particles is very useful in extracting initial conditions like chemical and kinetic freeze-out properties. The p_T spectra are usually studied by calculating the invariant cross section given by:

$$E\frac{d^3N}{dp^3} = \frac{1}{2\pi p_T}\frac{d^2N}{dp_T dy}, \tag{1.2}$$

where E is the particle energy and d^2N/dp_Tdy represents an event-wise yield density. The p_T spectra can be characterized by extracting yield (dN/dy), inverse slope parameter (T) and average transverse momentum ($\langle p_T \rangle$).

The particle yields measured in high energy nucleus-nucleus collisions can provide information about the system at chemical freeze-out, when the chemical composition of different particle species stops changing. Statistical Models use the particle ratios to constrain the system temperature and the baryonic chemical potential, μ_B, at chemical freeze-out, under the assumption that the system is in thermal and chemical equilibrium at that stage [12]. Figure 1.7 shows a comparison of the experimental p_T integrated hadron yield ratios, as measured by STAR at mid-rapidity for Au+Au collisions at $\sqrt{s_{NN}} = 200$ GeV, with statistical model fits [13]. The excellent fit obtained to the ratios indicates that the light flavors have reached chemical equilibrium at a temperature, $T_{ch} = 163 \pm 4$ MeV. This temperature is essentially equal to the critical value for a QGP to hadron gas transition predicted by lattice QCD. The inset in Fig. 1.7 shows the variation of the strangeness suppression factor, γ_s, with centrality. The value of γ_s reaches unity for most central collisions, indicating that the system created in central collisions at RHIC is in chemical equilibrium.

The characteristics of the system at kinetic freeze-out can be explored by analyzing the spectra of various hadron species. Kinetic equilibration is thought to prevail over the transverse degrees of freedom, therefore transverse momentum (p_T) or transverse mass (m_T) distribution are used to extract the kinetic freeze-out temperature (T_{fo}). The spectra are usually fitted by hydrodynamics motivated models to extract model parameters such as the kinetic freeze-out temperature T_{fo} and the radial flow velocity β_T. Figure 1.8 depicts the values of T_{fo} and $< \beta_T >$ extracted from thermal and radial flow fits for different centrality bins and hadron species as obtained in Au+Au collisions at $\sqrt{s_{NN}} = 200$ GeV [13]. We observe that bulk of the system consisting of pions, kaons and protons become cooler at kinetic freeze-out and develop a stronger collective flow. This indicates that there is a rapid expansion after chemical freeze-out which is seen to increase with centrality. The results obtained with ϕ and Ω indicate reduced hadronic interactions after chemical freeze-out.

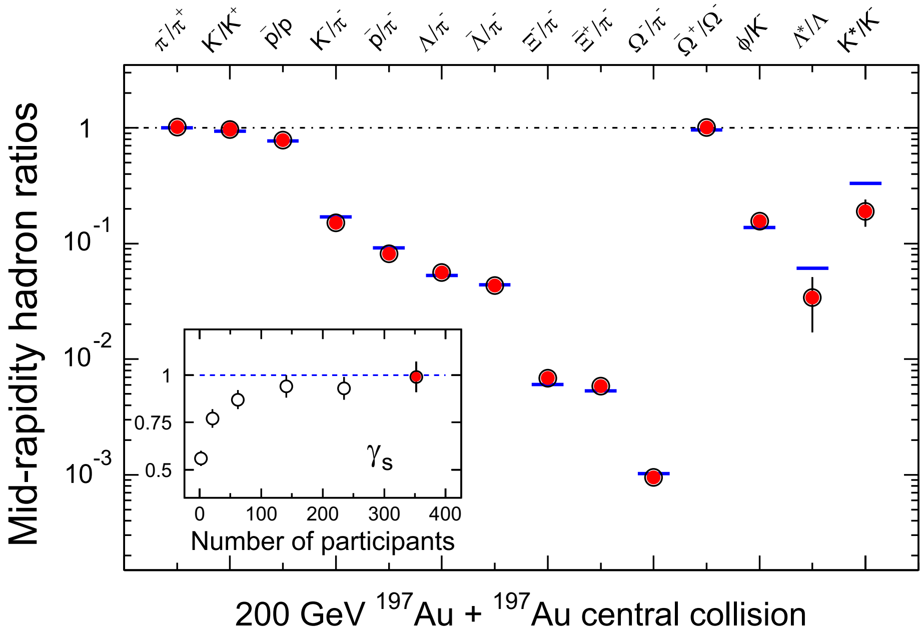

Figure 1.7: Ratios of the mid-rapidity p_T integrated yields for different hadron species in Au+Au collisions at $\sqrt{s_{NN}} = 200$ GeV. The horizontal lines represent the statistical model fits to the particle ratios. The fit parameters are $T_{ch} = 163 \pm 4MeV$, $\mu_B = 24 \pm 4MeV$, $\gamma_s = 0.99 \pm 0.07$ [14]. The inset shows the variation of γ_s with centrality. The figure is taken from [13].

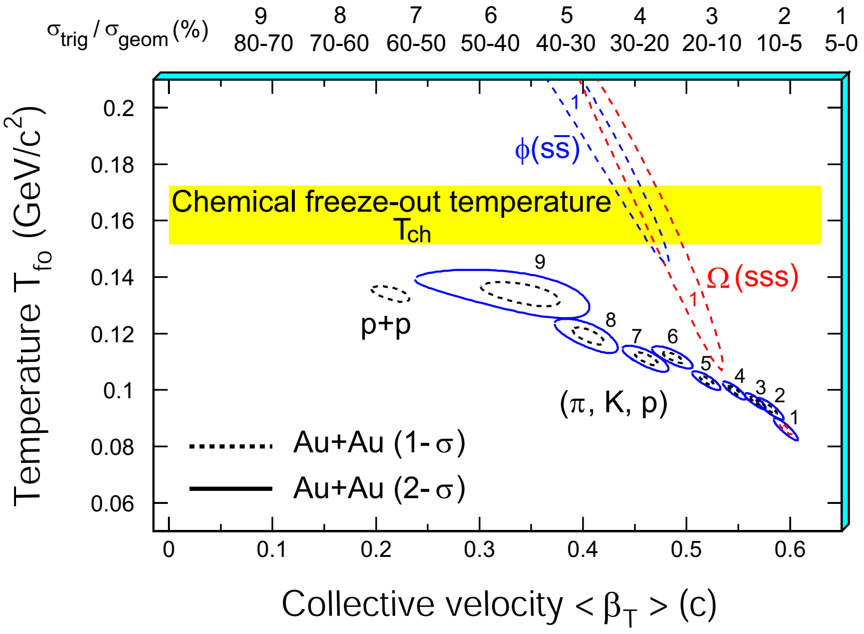

Figure 1.8: The χ^2 contours for T_{fo} and $< \beta_T >$ extracted from thermal and radial flow fits for different hadrons produced in Au+Au collisions at $\sqrt{s_{NN}} = 200$ GeV. The figure is taken from [13].

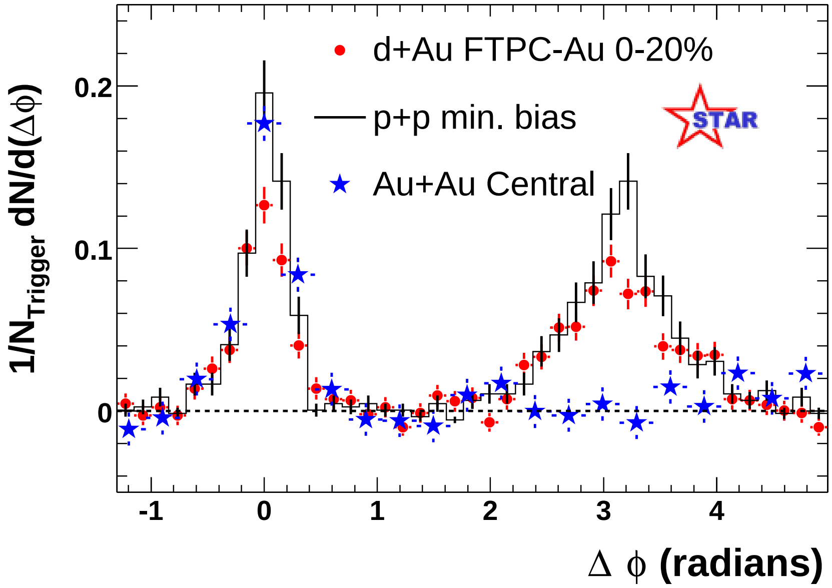

Figure 1.9: Dihadron azimuthal correlations at high p_T for p+p, central d+Au and central Au+Au collisions at $\sqrt{s_{NN}}$ = 200 GeV measured in STAR experiment [13]

.

1.3.2 High p_T Probes

Partonic energy loss is a very sensitive probe of the matter created in high energy heavy ion collisions. A high momentum parton traversing a dense colored medium is predicted to experience substantial energy loss through induced gluon radiation [16, 25]. The energetic partons in the high density system originate from the initial hard scattering of partons from the incoming nuclei. After a hard scattering, the parton fragments to create a high energy cluster (jets) of particles. The significant softening and broadening of jets in the dense partonic medium, is known as the phenomenon of *jet-quenching*.

Figure 1.9 shows the STAR measurements of azimuthal distribution of hadrons with $p_T > 2$ GeV/c relative to a trigger hadron with $p_T^{trig} > 4$ GeV/c [13]. A hadron pair drawn from a single jet generate an enhanced correlation at $\Delta\phi \approx 0$, as observed for p+p, d+Au and Au+Au collisions. In contrast, a hadron pair drawn from back-to-back di-jets will generate an enhanced correlation at $\Delta\phi \approx \pi$, as observed for p+p and for d+Au collisions with a broader width than the near-side correlation peak. In central Au+Au collisions, the back-to-back dihadron correlation is absent. The strong suppression of back-to-back correlations for di-jet events in central Au+Au collisions

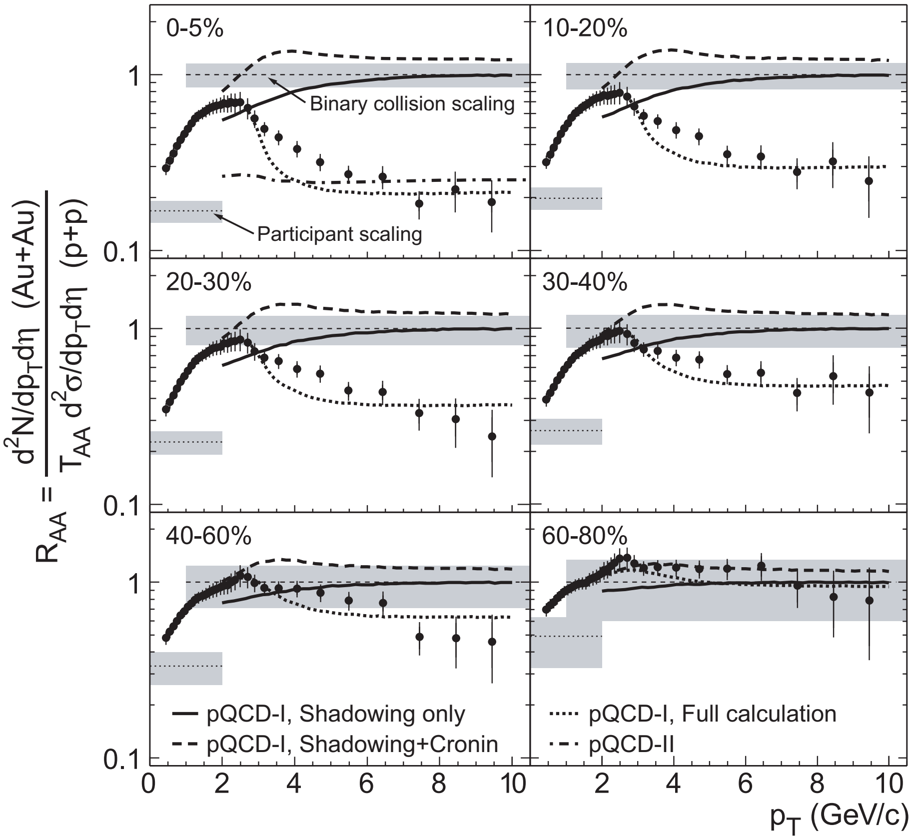

Figure 1.10: $R_{AA}(p_T)$ for charged hadrons for different centralities as measured in the STAR experiment [15].

is due to final state interactions of hard scattered partons or their fragmentation products in the dense medium generated in such collisions [21, 22].

In order to understand the effects of the medium on particle production, it is necessary to compare the hadron spectra from nucleus-nucleus (AA) collisions with the same obtained from nucleon-nucleon (NN) collisions. The observable used to measure such effects is called the Nuclear Modification Factor (R_{AA}), which is defined as

$$R_{AA} = \frac{d^2N^{AA}/dp_T d\eta}{T_{AA} d^2\sigma^{NN}/dp_T d\eta}, \tag{1.3}$$

where $T_{AA} = \langle N_{bin} \rangle / \sigma^{NN}_{inel}$ is the nuclear thickness function. N_{bin} is the average number of binary NN inelastic collisions as estimated from Glauber calculation [23, 24]. In the absence of medium effects, an AA collision could be viewed simply as a superposition of individual NN collisions, where the R_{AA} factor would be unity, above a certain p_T threshold. Figure 1.10 shows the measured $R_{AA}(p_T)$ for unidentified charged hadrons at $\sqrt{s_{NN}} = 200$ GeV for centrality-selected Au+Au spectra relative to the measured p+p spectrum [15]. We observe that for $6 < p_T < 10$ GeV/c, $R_{AA}(p_T)$ is suppressed for each collision centrality except for most peripheral collisions. The $R_{AA}(p_T)$ is much more suppressed in central Au+Au relative to p+p collisions. As can be seen from the Fig. 1.10, the Cronin enhancement and shadowing alone cannot explain the suppression, which is reproduced only if parton energy loss in dense matter is included. The suppression of $R_{AA}(p_T)$ at high p_T was predicted to be one of the signature of QGP formation [16, 17]. The peripheral $R_{AA}(p_T)$ is in agreement with p+p measurement indicating that strong medium effects are only taking place in central collisions.

1.3.3 Strangeness Enhancement

The enhanced production of strange particles in AA collisions, relative to NN collisions, has been proposed as a signature of QGP formation [18]. The strange particles are of particular interest because the initial strangeness content of the colliding nuclei is very small and there is no net strangeness. This means that all strange hadrons must be formed in the matter produced. In QGP, the production and equilibration of strangeness is very efficient due to a large gluon density and a low energy threshold for dominant QCD processes of $s\bar{s}$ production i.e. $gg \rightarrow s\bar{s}$. In contrast, in a hadronic system, e.g., in pp, the higher threshold for strangeness production was argued to make the strangeness yield considerably smaller and the equilibration time much longer than in QGP [19].

The strangeness enhancement measured in experiments is defined as the ratio of the yield of a strange particle per participating nucleon in the large AA system (e.g. Au+Au at RHIC) to the yield of the same strange particle in a the small reference system (e.g. p+p at RHIC). Figure 1.11 shows the strangeness enhancement as a function of average number of participating nucleons ($\langle N_{part} \rangle$) for K, ϕ, $\bar{\Lambda}$ and $\Xi + \bar{\Xi}$ for Au+Au and Cu+Cu collisions relative to p+p collisions at $\sqrt{s_{NN}} = 200$ and 62.4 GeV in the STAR experiment [20]. These experimental data indicate the formation of a dense partonic medium in heavy ion collisions where strange quark production is enhanced.

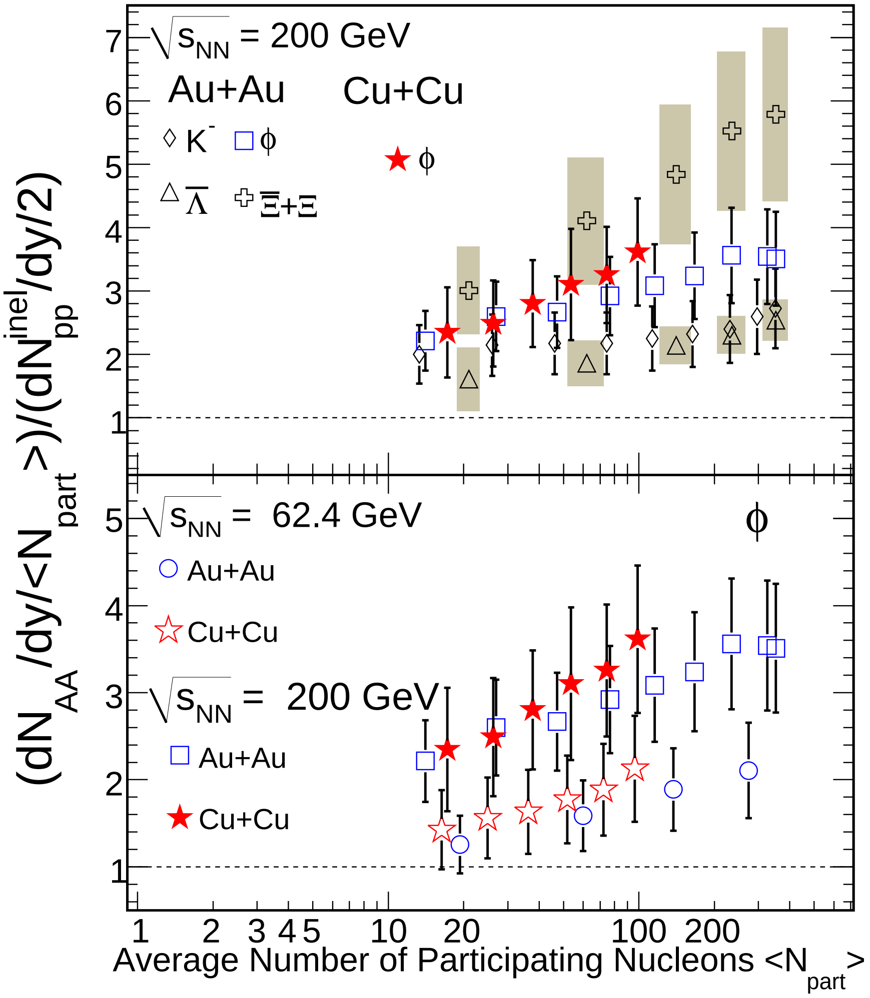

Figure 1.11: Upper panel: The ratio of the yields of K, ϕ, $\bar{\Lambda}$ and $\Xi + \bar{\Xi}$ normalized to $\langle N_{part} \rangle$ in Au+Au and Cu+Cu collisions to corresponding yields in inelastic p+p collisions as a function of $\langle N_{part} \rangle$ at $\sqrt{s_{NN}}$ = 200 GeV. Lower panel: Same as above but for only ϕ mesons in Au+Au and Cu+Cu collisions at $\sqrt{s_{NN}}$ = 200 and 62.4 GeV [20]. The error bars shown here represent the statistical and systematic errors added in quadrature.

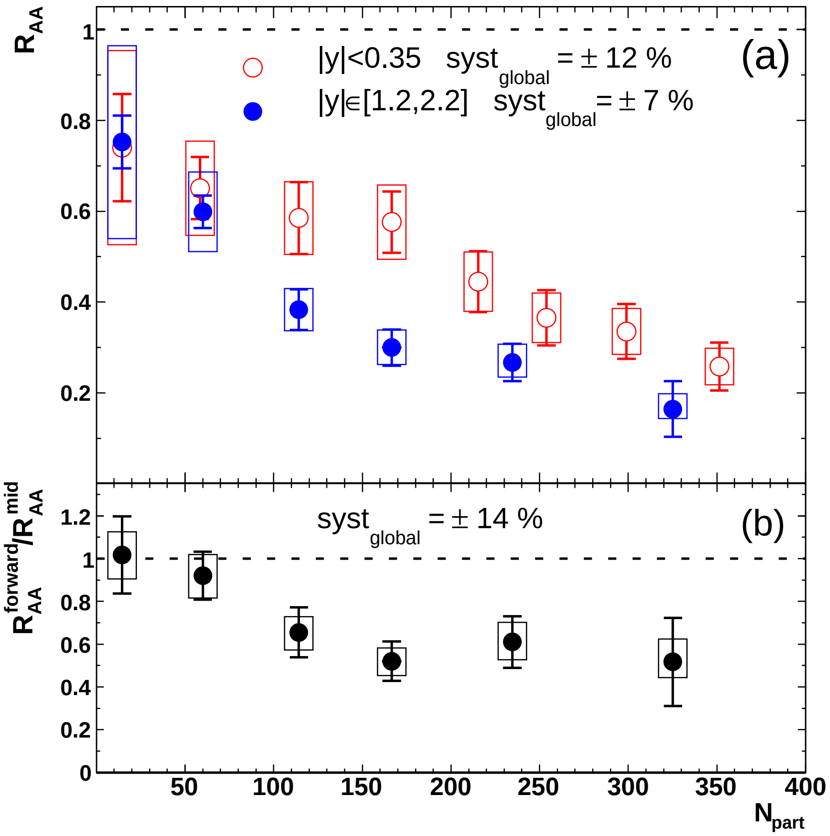

Figure 1.12: Upper panel: J/ψ R_{AA} versus N_{part} for Au+Au collisions at $\sqrt{s_{NN}} = 200$ GeV. The mid (forward) rapidity data are shown with open (solid) circles. Lower panel: Ratio of forward and mid-rapidity J/ψ R_{AA} as a function of N_{part} [31].

1.3.4 Quarkonia Suppression

In 1986, Matsui and Satz predicted that the suppression of quarkonia production in ultrarelativistic heavy ion collisions was expected to be an unambiguous signature for the formation of a QGP [26]. In the deconfined state, the attraction between heavy quarks and antiquarks is predicted to be reduced due to the color screening effects, leading to the suppression of heavy quarkonia yield. The magnitude of the suppression depends on the binding energies of the quarkonia and the temperature of the system. Therefore, studies of J/Ψ particle, which is a bound state of charm quark c and charm antiquark $\bar{c}$, can reveal the thermodynamic properties of the medium.

The suppression of J/Ψ production has been studied in detail at the CERN SPS and RHIC experiments. At the CERN SPS, the NA38, NA50 and NA60 experiments have already studied J/Ψ production in various colliding systems and energies. The

NA50 experiment observed a suppression of J/Ψ production as a function of collision centrality in Pb+Pb collisions at $\sqrt{s_{NN}} = 17.3$ GeV that exceeds expectations based on the measurements of cold nuclear matter (CNM) effects in p+A collisions [27, 28]. The NA60 experiment also observed similar behavior in In+In collisions at the same energy [29]. The PHENIX experiment at RHIC has characterized effects of the nuclear medium on J/Ψ production at $\sqrt{s_{NN}} = 200$ GeV [30, 31, 32, 33]. Figure 1.12 shows the p_T integrated R_{AA} versus N_{part} at mid and forward rapidity in Au+Au collisions at $\sqrt{s_{NN}} = 200$ GeV. A significant J/ψ suppression relative to the binary scaling of p+p collisions has been observed for central Au+Au collisions at RHIC. The magnitude of suppression is greater than that expected by extrapolating the CNM effects measured in d+Au collisions [33]. The suppression at mid-rapidity is similar to that observed at the SPS [27] and it is significantly larger at forward rapidity. Models of quarkonia suppression based on the local energy density of the medium predict a greater suppression at RHIC than at SPS as the energy density reached at RHIC is larger than the one reached at SPS. Further, compared to mid-rapidity, a reduced suppression is expected at forward rapidity because the energy density at mid-rapidity is higher than that in the forward rapidity. Both trends are contradicted by the data. A number of explanations have been put forth, including sequential melting, where Ψ' and χ_c are dissociated leading to suppression of feed down components of J/Ψ yield [34] and gluon saturation, which leads to a lower charm quark yield at forward rapidity [35]. At RHIC, more than 10 $c\bar{c}$ pairs are expected to be produced in a central Au+Au collision and these uncorrelated charm quark pairs can recombine to form J/ψs. This regeneration approach for J/Ψ production has also been used to describe the R_{AA} of J/Ψ [36].

1.3.5 Photons and Dileptons

Electromagnetic probes such as photons and dileptons are very useful probes of the hot and dense matter formed in relativistic heavy ion collisions. In the QGP phase, the production processes of direct photons are annihilation ($q\bar{q} \to \gamma g$) and Compton scattering ($qg \to q\gamma$, $\bar{q}g \to \bar{q}\gamma$). In addition, direct photons are produced through fragmentation of hard partons. These are also called bremsstrahlung photons. The dilepton production is mainly from quark and antiquark annihilation ($q\bar{q} \to \gamma^* \to l^- l^+$

) i.e. a quark can interact with an antiquark to form a virtual photon (γ^*) and the virtual photon subsequently decays into a lepton l^- and an antilepton l^+. The photons and dileptons interact with medium or other particles only electromagnetically and are largely unaffected by final state interactions due to their large mean free path. Therefore, they retain the information of early times more efficiently compared to hadronic signals, where the hadrons interact strongly and thus tend to erase the information of early time. However, the measurements involving the detection of direct photons are very challenging because the production rate is small and the background from hadronic decays is large.

Direct photon measurements have been made at the CERN SPS [37] and RHIC [38]. Figure 1.13 compares the direct photon spectra obtained by the PHENIX experiment at RHIC [38] with the Next to Leading Order pQCD (NLO pQCD) calculations [39]. The pQCD calculation is consistent with the p+p data within the theoretical uncertainties for $p_T > 2$ GeV/c. The Au+Au data are above the p+p fit curve scaled by T_{AA} (dashed curves) for $p_T < 2.5$ GeV/c, indicating that in the low p_T range the direct photon yield increases faster than the binary NN collision scaled p+p cross section. In central Au+Au collisions, the shape of the direct photon spectrum above the T_{AA}-scaled p+p spectrum is exponential in p_T, with an inverse slope $T = 221 \pm 19^{\text{stat}} \pm 19^{\text{syst}}$ MeV. If the direct photons in Au+Au collisions are of thermal origin, the inverse slope T is related to the initial temperature T_{init} of the dense matter. In hydrodynamical models, T_{init} is 1.5 to 3 times T due to the space-time evolution. The red dotted curve in Fig. 1.13 shows a thermal photon spectrum in central Au+Au collisions calculated with $T_{\text{init}} = 370$ MeV [40]. Figure 1.14 shows a comparison of the direct photon data in central 0-20% Au+Au collisions with results of several theoretical calculations of thermal photon emission added to the pQCD calculations [41]. These hydrodynamical models which assume the formation of a hot system with initial temperature ranging from $T_{\text{init}} = 300$ MeV at thermalization time $\tau_0 = 0.6$ fm/c to $T_{\text{init}} = 600$ MeV at $\tau_0 = 0.15$ fm/c, provide results in qualitative agreement with the data. Lattice QCD predicts a phase transition from hadronic phase to quark-gluon plasma at a critical temperature $T_c \sim$170 MeV [5, 6].

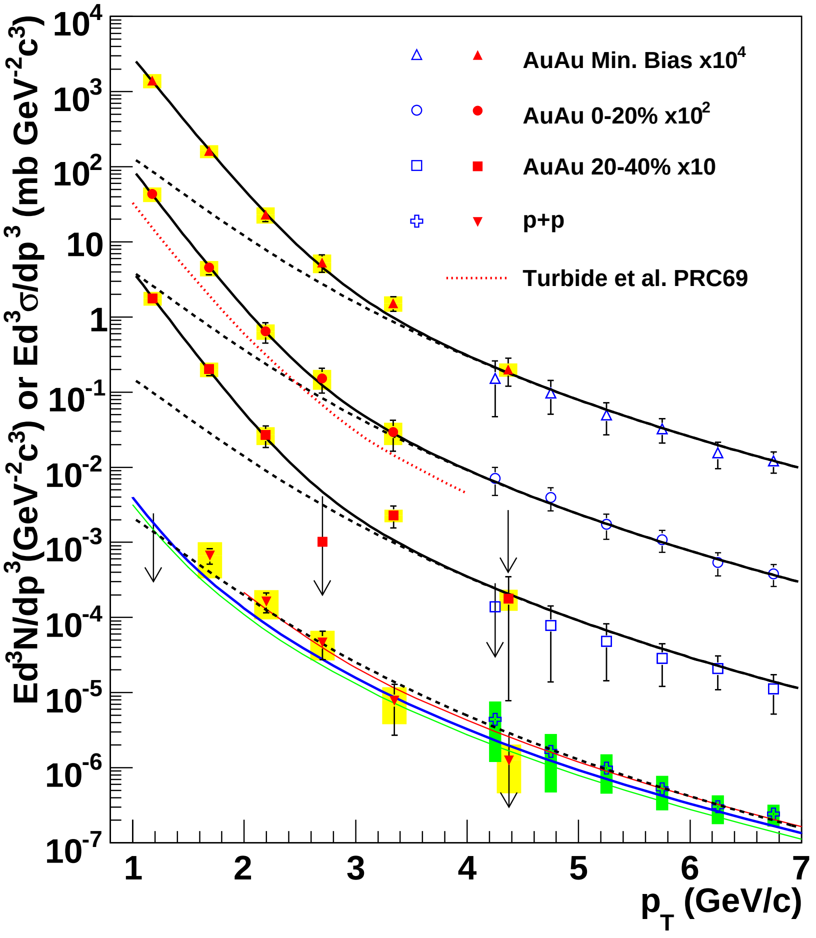

Figure 1.13: Invariant cross section and invariant yield of direct photons as a function of p_T in p+p and Au+Au collisions at $\sqrt{s_{NN}} = 200$ GeV, respectively [38]. The three curves on the p+p data represent NLO pQCD calculations, and the dashed curves show a modified power-law fit to the p+p data, scaled by T_{AA}. The black solid curves are exponential plus the T_{AA} scaled p+p fit. The red dotted curve near the 0-20% centrality data is a theory calculation [40]

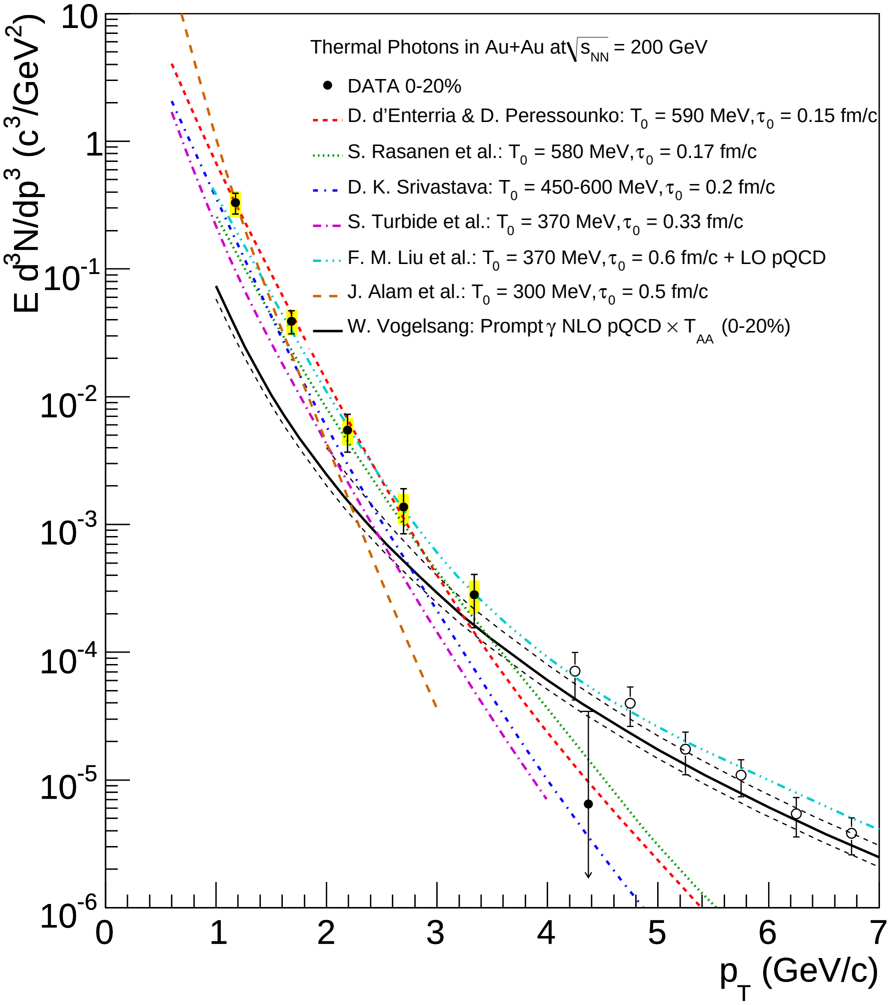

Figure 1.14: Theoretical calculations of thermal photon emission are compared with the direct photon data in central 0-20% Au+Au collisions from PHENIX experiment [41].

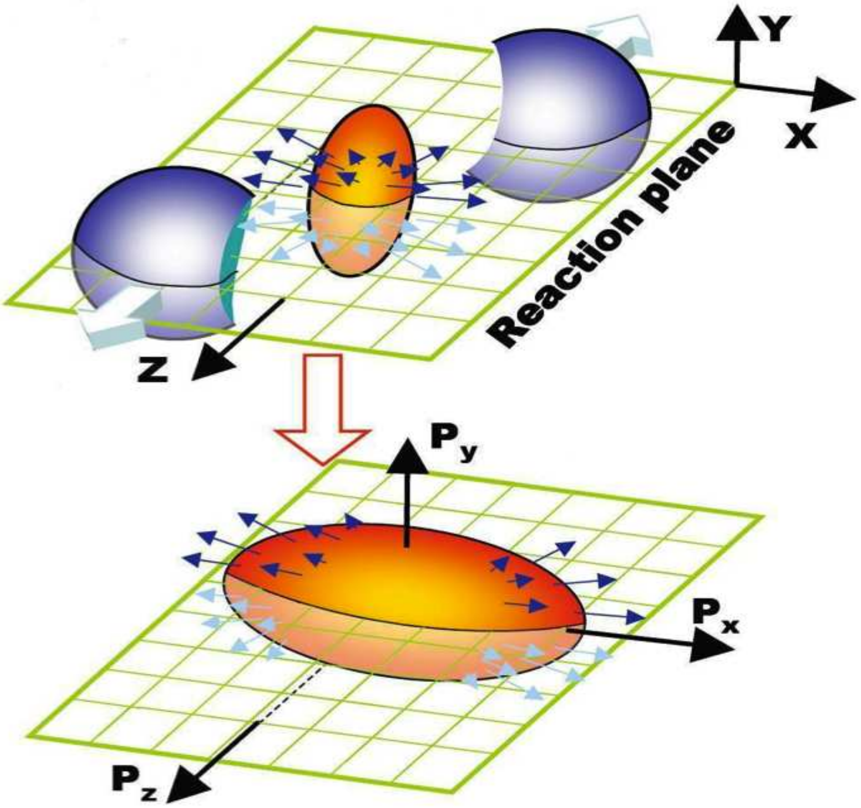

Figure 1.15: Schematic diagram showing the transformation of initial coordinate space anisotropy into a momentum space anisotropy in a non-central heavy ion collision.

1.3.6 Azimuthal Anisotropy or Flow

In non-central heavy ion collisions, the overlap region of two colliding nuclei is spatially asymmetric with an almond-like shape as shown in the Fig. 1.15. The interactions among constituents of the system generate a pressure gradient, which is larger along the short axis than along the long axis of the almond-shaped collision region. Therefore, the initial spatial anisotropy causes the nuclear matter to also have a momentum anisotropy. Consequently, the azimuthal distribution of produced particles may carry information about the pressure of the nuclear matter produced in the early stage of the heavy ion collisions [42].

The azimuthal anisotropy can be quantified by studying the Fourier expansion of azimuthal angle distribution of produced particles with respect to the reaction plane

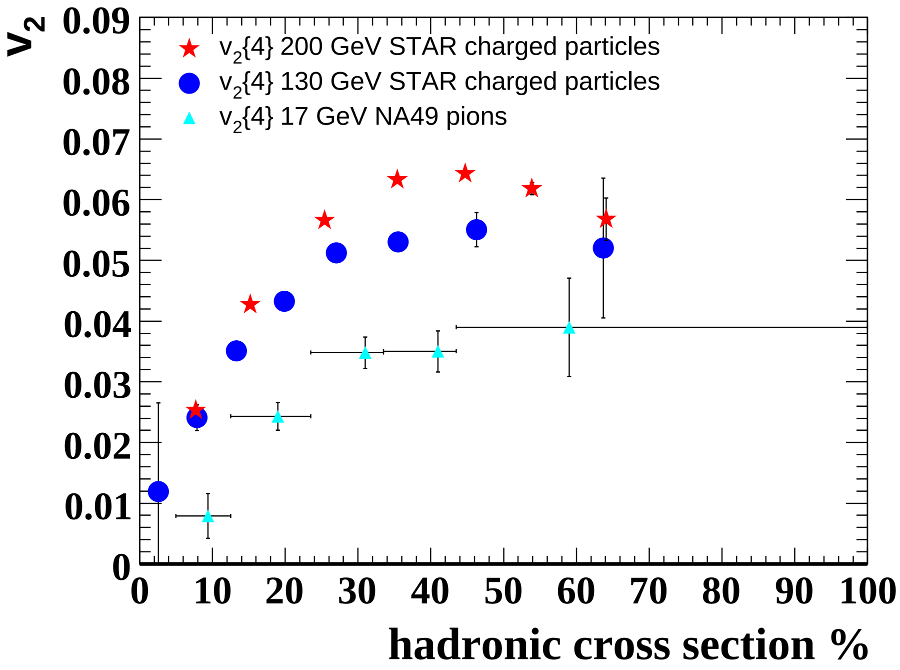

Figure 1.16: The centrality dependence of p_T integrated v_2 as measured by the NA49 experiment at SPS [44] and STAR experiment at RHIC [45, 46].

(the plane spanned by the beam direction and impact parameter vector) [43]:

$$E\frac{d^3N}{d^3p} = \frac{1}{2\pi}\frac{d^2N}{p_T dp_T dy}(1 + \sum_{n=1}^{\infty} 2v_n cos[n(\phi - \Psi_r)]), \tag{1.4}$$

where ϕ is the azimuthal angle of the particle, Ψ_r is the reaction plane angle and v_n is the n^{th} harmonic coefficient. The first harmonic coefficient, v_1, is called the directed flow and the second harmonic coefficient, v_2, is called the elliptic flow. Figure 1.16 shows the p_T integrated mid-rapidity elliptic flow coefficient, v_2, as a function of collision centrality for SPS [44] and RHIC [45, 46] energies. We can observe the characteristic centrality dependence that reflects the increase of the initial spatial eccentricity of the collision overlap geometry with increasing impact parameter. The integrated elliptic flow value for produced particles increases about 70% from the top SPS energy to the top RHIC energy.

At low p_T ($\leq$ 2 GeV/c), the differential elliptic flow $v_2(p_T)$ for different hadrons has been observed to scale with particle mass. Figure 1.17 shows the measured low p_T v_2 distributions for different identified particles in Au+Au collisions at $\sqrt{s_{NN}} = 200$ GeV [46]. The hadron mass ordering of v_2 is seen in the low p_T region, where at a given

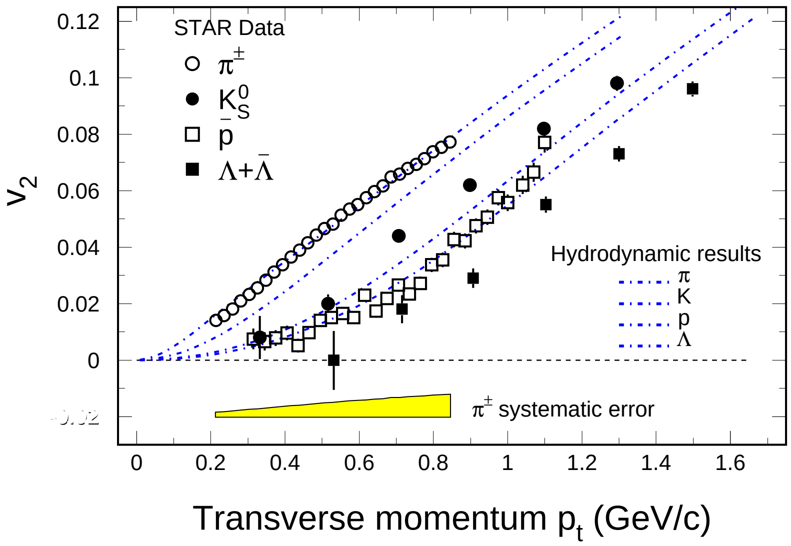

Figure 1.17: The p_T dependence of the elliptic flow parameter, v_2 in Au+Au collisions at $\sqrt{s_{NN}}$ = 200 GeV as measured by the STAR experiment. The hydrodynamic calculations are shown as dot-dashed lines. This figure is taken from [46].

p_T, the higher is the hadron mass the lower is the value of v_2. This mass dependence, as well as the absolute magnitude of v_2, is well reproduced by the hydrodynamic calculations [47]. The agreement with the hydrodynamic calculation, which assume early thermalization and ideal relativistic fluid expansion, is one of the centerpieces of the discovery of QGP, as claimed at RHIC.

Figure 1.18 presents the v_2 measurements for identified hadrons in minimum bias Au+Au collisions at $\sqrt{s_{NN}} = 200$ GeV [46]. For $p_T > 2$ GeV/c, it can be seen that the observed values of v_2 saturate and the level of the saturation differs substantially for mesons and baryons. This provides some important information regarding the origin of baryon-meson difference which characterize this p_T range. The hydrodynamic calculations over predict the data for $p_T > 2$ GeV/c. If we divide the v_2 values with the number of constituent quarks, n (i.e. $n = 2$ for mesons and $n = 3$ for baryons), we observe a scaling for $p_T/n > 1$ GeV/c, which is called the Number of Constituent Quark (NCQ) scaling.

The upper panel in Fig. 1.19 shows the STAR results on v_2/n as a function of

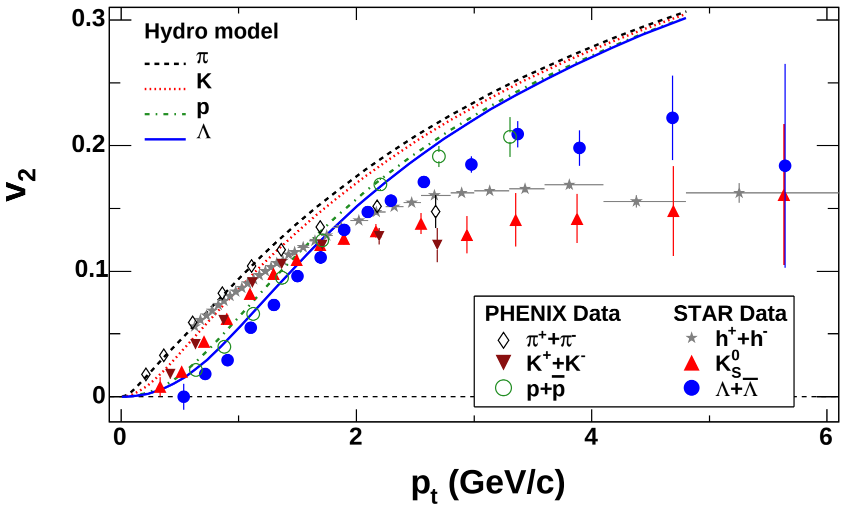

Figure 1.18: v_2 as a function of p_T for different hadrons in minimum bias Au+Au collisions at $\sqrt{s_{NN}} = 200$ GeV [46]. Hydrodynamical calculations are shown by solid and dotted curves [47].

p_T/n for identified hadrons in minimum bias Au+Au collisions at $\sqrt{s_{NN}} = 200$ GeV. Here n stands for the number of constituent quarks. The dashed-dotted line denotes a polynomial fit to the data. To investigate the quality of agreement between particle species, the data from the top panel are scaled by the fitted polynomial function and plotted in the bottom panel of Fig. 1.19. This shows that in the intermediate p_T range ($0.6 < p_T/n < 2$ GeV/c), the v_2 of the identified hadrons (except pion) scales with the number of constituent quarks. The large resonance decay contribution to pion production has been suggested as a possible explanation for the apparent deviation from this scaling [48]. This observation of NCQ scaling, is of particular interest and importance, as it indicates that the system is in a deconfined stage. In a more general sense, it appears that high energy nuclear collisions provide an opportunity to prove that hadron production indeed happens via coalescence of the constituent quarks [50]. The constituent quarks carry their own substantial azimuthal anisotropy which is later summed up to give the hadronic flow.

Figure 1.20 shows that plotting v_2 as a function of transverse kinetic energy $KE_T = m_T - m$, where $m_T = \sqrt{p_T^2 + m^2}$, results in the formation of distinct branches for mesons and baryons at intermediate p_T. If we scale with the number of constituent quarks n_q then the two branches merge into one curve. At the moment there is no

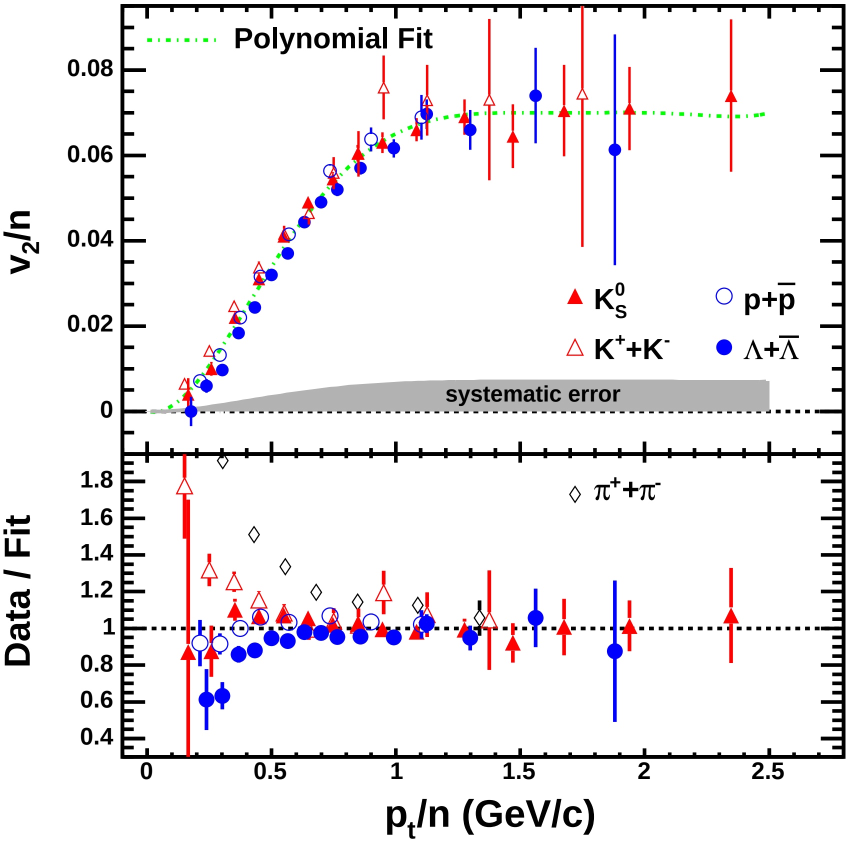

Figure 1.19: Upper Panel: v_2/n vs. p_T/n for identified particles measured by the STAR experiment. n is the number of constituent quarks. The dashed-dotted line is the polynomial fit to the data. Lower Panel: The data from the upper panel is divided by the polynomial fit as a function of p_T/n [46].

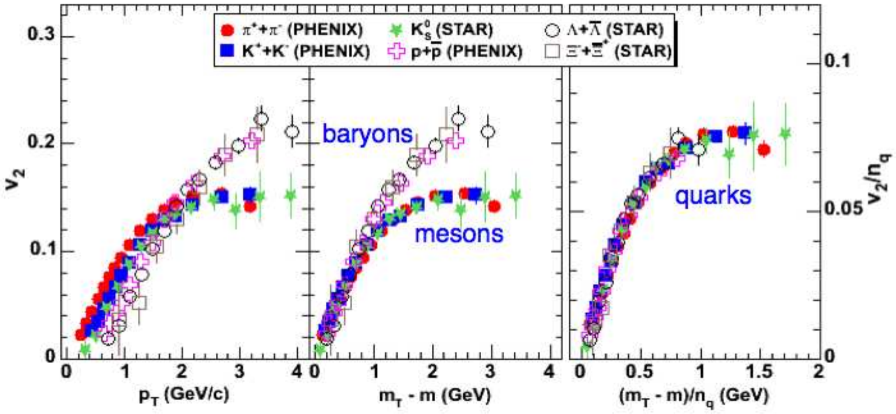

Figure 1.20: v_2 as a function of p_T and $m_T - m$ for identified particles in Au+Au collisions at $\sqrt{s_{NN}} = 200$ GeV, and also v_2/n_q vs $(m_T - m)/n_q$ in the last panel [49].

agreement on the reason for such a universal scaling except that re-plotting the data as a function of transverse kinetic energy to some extent compensates for the effect of radial flow [49].

1.4 Cold Nuclear Matter Effects

As we have discussed earlier, a strong jet quenching and suppression of high p_T hadron spectra in central Au+Au collisions relative to p+p collisions at $\sqrt{s_{NN}} = 200$ GeV have been observed at RHIC [15]. It is very important to check whether this high p_T suppression is due to initial state or final state effects. In the environment of heavy ion collisions, the initial cold nuclear matter (CNM) effects play an important role. Therefore, in order to disentangle the final state effects, one has to carefully estimate the initial state effects in an environment where the transition to a QGP phase is unlikely e.g. d+Au collisions at RHIC. These d+Au collisions are important because the initial state nuclear effects are present in both d+Au and Au+Au collisions, where as the final state effects are expected only in Au+Au collisions. The measurement of identified particle spectra in d+Au and p+p collisions provide the reference for Au+Au collisions and also helpful to understand the initial CNM effects such as *Cronin effect* in $p + A$ collisions. In addition to Cronin effect, other known initial state effects are nuclear shadowing and gluon saturation [51].

1.4.1 Cronin Effect

The enhancement of hadron yields at intermediate p_T in p+A collisions as compared to those in p+p collisions is commonly referred to as the Cronin effect. This was first observed by Cronin *et al.* in 1974 [52], for a low energy fixed target experiment, using a 300 GeV proton beam on Be, Ti and W targets. The atomic weight (A) dependence of the invariant cross section per nucleus is parameterized in the following form

$$E\frac{d^3\sigma}{dp^3}(p_T, A) = E\frac{d^3\sigma}{dp^3}(p_T, 1)A^{\alpha(p_T)}. \tag{1.5}$$

It was found that the exponent α is significantly larger than unity at intermediate p_T for all particles, indicating an enhancement of the production cross section. A strong particle species dependence of α has also been observed, which is shown in Fig. 1.21.

The enhancement for proton and antiproton are larger than that for kaon and the enhancement for kaon is larger than that of pion. The Cronin effect was observed and studied in detail in fixed target $p + A$ collisions with center of mass energy up to $\sqrt{s_{NN}} = 38.8$ GeV [53]. The lower energy data suggest the exponent α decreases with increase in energy. So, it is interesting to study the Cronin effect at higher energy such as in d+Au collisions at $\sqrt{s_{NN}} = 200$ GeV.

At RHIC energies, studies are being carried out to quantify the Cronin effect. Figure 1.22 shows the variation of nuclear modification factors (R_{dAu}) with p_T for the identified particles from d+Au collisions at $\sqrt{s_{NN}} = 200$ GeV as measured by both STAR (left) and PHENIX (right) experiments at RHIC [54, 55]. The R_{dAu} of the identified particles has characteristics of the Cronin effect in particle production with R_{dAu} less than unity at low p_T and above unity at $p_T > 1.0$ GeV/c. The R_{dAu} of protons rise faster than R_{dAu} of pions and kaons. This is consistent with the observed species dependence of the enhancement in lower energy collisions. The Cronin enhancement is usually attributed to momentum broadening due to multiple initial state soft or semi-hard scattering [56]. Such models typically do not predict the particle species dependence observed in the data. There is also an alternative explanation provided by Hwa and collaborators [57] that the recombination of soft and shower partons in the final state could explain the particle species dependent enhancement. This model predicts a larger enhancement for protons than for pions at intermediate p_T. There is no distinction of the hadronization mechanism in this model if hot or cold nuclear matter is produced. However, the inclusion of recombination from deconfined partons requires a high energy density in initial state, which may not be justified in d+Au collisions.

The magnitude of the enhancement for pions at $p_T > 3$ GeV/c is larger at $\sqrt{s_{NN}}$ = 27.4 GeV than at 200 GeV as shown in the right panel of Fig. 1.22. Protons and antiprotons yields are also more enhanced at the lower beam energy. This energy dependence of the Cronin effect for pions has been interpreted as evidence for a different production mechanism for high p_T hadrons at RHIC energies compared to lower energies [58]. In this model, high p_T hadrons are produced incoherently on different nucleons at low energy, while in higher energy collisions the production amplitudes can interfere because the process of gluon radiation is long compared to

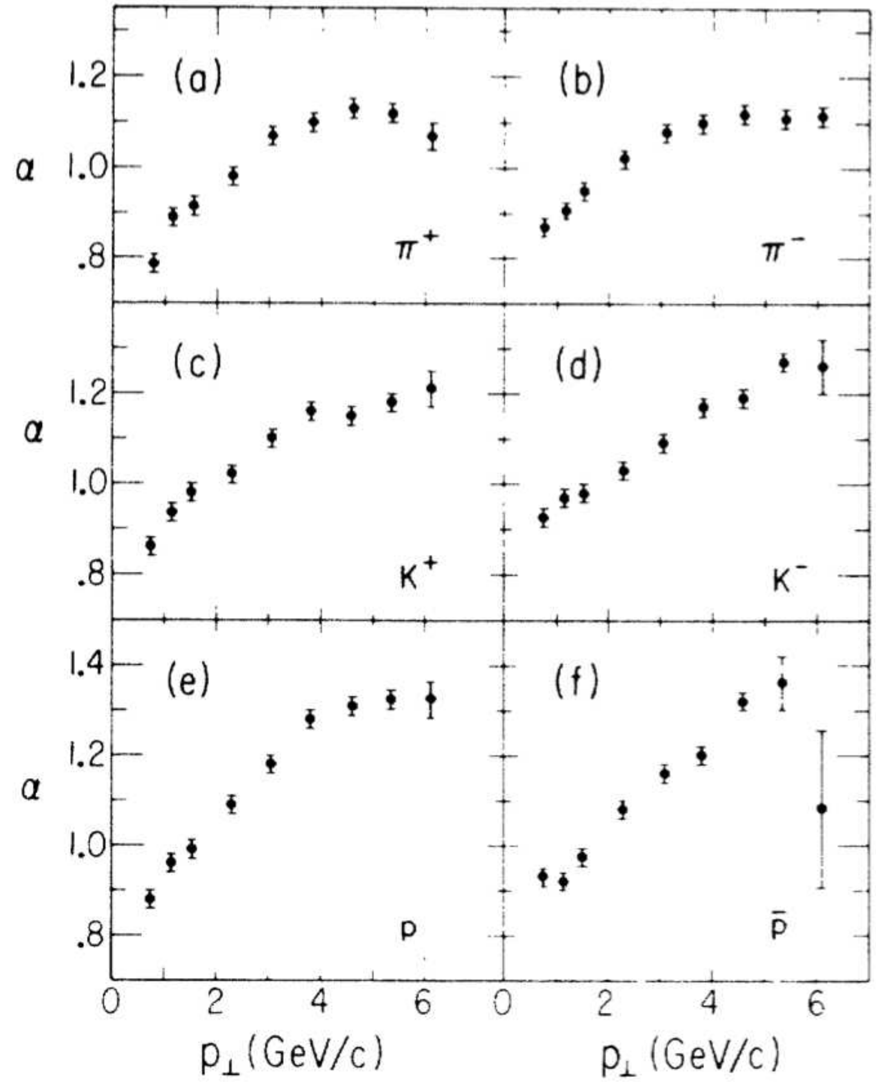

Figure 1.21: The dependence of exponent α as a function of p_T for the production of different hadrons by 300 GeV protons in a fixed target experiment [52].

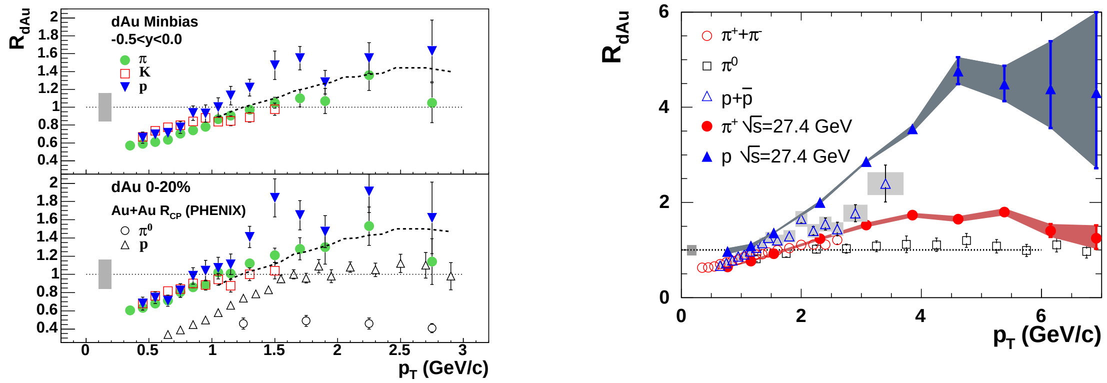

Figure 1.22: Nuclear modification factors for the identified particles from d+Au collisions at $\sqrt{s_{NN}}$ = 200 GeV, measured by the STAR (left) and PHENIX (right) experiments at RHIC [54, 55]. Nuclear modification factors calculated from the per-beam nucleon cross sections reported for $\sqrt{s_{NN}}$ = 27.4 GeV p + A collisions are also shown for the comparison (right) [52].

the binary collision time. Coherent radiation from different nucleons is subject to Landau-Pomeranchuk suppression. However, the difference between the baryon and meson Cronin effects is not predicted by this model.

1.4.2 Using ϕ Mesons to Study the Particle Species Dependence of Cronin effect

The ϕ(1020) meson's properties and its transport in the nuclear medium have been of interest since its discovery [59]. The lifetime of the ϕ meson is about 45 fm/c and it decays into charged kaons K^+K^- with a branching ratio of 49.2% and more rarely into the dilepton pairs e^+e^- and $\mu^+\mu^-$. The ϕ meson, consisting of strange quarks $s\bar{s}$, is a good probe to study the effect of final state hadronic rescatterings due to its small hadronic cross sections with other non-strange particles. The effect of hadronic rescatterings on ϕ meson is thought to be small. Most of the ϕ mesons are directly produced from the collision process, the feed-down contribution from other hadrons to ϕ meson being less than $\sim$ 1%. The ϕ meson is an interesting vector meson as it's mass is very close to the mass of light baryons such as proton and Λ. So, the ϕ meson is very useful to understand the particle species dependence of Cronin effect i.e. whether the enhancement is due to meson-baryon effect and mass effect. The ϕ meson results when compared to those from π, K, and p will also tell us the role of hadronic re-scattering towards the understanding the Cronin effect. Some results on the measurement of π and ϕ meson transverse momentum spectra in d+Au collisions at $\sqrt{s_{NN}} = 200$ GeV will be discussed in chapter 3.

1.5 Light Nuclei Production

According to the Big Bang theory, matter and antimatter existed in equal abundance at the early stage of the universe. It remains a mystery how this symmetry got lost in the evolution of the universe reaching a stage with no significant amounts of antimatter being present. High energy nuclear collisions create an energy density similar to that of the universe microseconds after the Big Bang, where nearly equal abundance of matter and antimatter are formed in the central rapidity region [60]. The production of light nuclei and antinuclei are closely related to the matter-antimatter symmetry at high energies.

In relativistic heavy ion collisions, production of nuclei and antinuclei is possible via two mechanisms. The first mechanism is direct production of nucleus-antinucleus pairs in elementary NN or parton-parton interactions. Since their binding energies are small, the directly produced nuclei or antinuclei are likely to be dissociated in the medium before escaping. The second and presumably the dominant mechanism for nucleus and antinucleus production is via final state coalescence of produced nucleons and antinucleons or participant nucleons [61, 62]. In this process, nucleons and antinucleons merge to form light nuclear and antinuclear clusters during the final stages of kinetic freeze-out. The formation probability is proportional to the product of the phase space densities of its constituent nucleons [63]. Therefore, the production of light nuclei provides information about the size of the emitting system and its space-time evolution.

The invariant yields of nuclei can be related to the primordial invariant yields of nucleons as

$$E_A \frac{d^3N_A}{d^3p_A} = B_A (E_p \frac{d^3N_p}{d^3p_p})^Z (E_n \frac{d^3N_n}{d^3p_n})^{A-Z} \approx B_A (E_p \frac{d^3N_p}{d^3p_p})^A, \tag{1.6}$$

where N_A, N_p, and N_n denote the yields of the particular nucleus, and of its constituent protons and neutrons, respectively. A and Z being the atomic mass number and atomic number, respectively. Here, it is assumed that protons and neutrons are produced with identical momentum spectra and $p_A = A \cdot p_p$. B_A is the coalescence parameter, which is related to the freeze-out correlation volume [61]: $B_A \propto V_f^{1-A}$. The coalescence parameter,B_A, can be used to infer the space-time geometry of the system [64].

1.5.1 Elliptic Flow of Light Nuclei

As we have discussed earlier, the elliptic flow of identified hadrons measured at RHIC, are seen to follow a constituent quark number scaling at intermediate transverse momentum. This scaling behavior of hadron elliptic flow is consistent with the predictions of the quark coalescence model for hadron production from produced QGP in relativistic heavy ion collisions [65]. In the quark coalescence model, two nearest quark and antiquark are combined into mesons and three nearest quarks or antiquarks are combined into baryons or antibaryons that are closest to the invariant masses of these parton combinations. Since the partons are not directly observable in experiments, it is difficult to study the role of local correlations and energy in partonic coalescence. The light nuclei and antinuclei production in heavy ion collisions could be described by the final state coalescence of nucleons and antinucleons [61, 62]. In this case, both the nuclei and their constituent nucleons are directly observable in experiments. So, it is important to study the elliptic flow of light nuclei and compare the same with their constituents. This will provide valuable information for studying the freeze-out dynamics and coalescence mechanism. The measurement of elliptic flow of light nuclei in Au+Au collisions at $\sqrt{s_{NN}}$ = 200 GeV and 39 GeV will be discussed in chapter 4.

1.6 Organization of the Thesis

The work presented in this thesis involve the study of various observables to understand the particle production mechanisms in high energy heavy ion collisions and to study the properties of QGP. The data reported here were taken by the STAR experiment at RHIC. A brief overview of the RHIC and the STAR detector systems are presented in Chapter 2. In Chapter 3, we discuss in detail about the analysis techniques and methods used to study the production of ϕ meson and pion in d+Au collisions at $\sqrt{s_{NN}} = 200$ GeV. The results on transverse momentum spectra, nuclear modification factor, and rapidity asymmetry for ϕ meson are presented. In Chapter 4, we discuss the measurement of elliptic flow, v_2, of light nuclei in Au+Au collisions at $\sqrt{s_{NN}} = 200$ GeV and 39 GeV. The v_2 of light nuclei in Au+Au collisions at $\sqrt{s_{NN}} =$ 200 GeV are compared with a dynamical coalescence model calculation. In Chapter 5, we present the observation of two anti-α candidates in the Au+Au collisions at $\sqrt{s_{NN}} = 200$ GeV, data set collected in the year 2007. This is followed by conclusions in Chapter 6.

Bibliography

[1] H. Kastrup, P. Zerwas, eds., QCD 20 yrs later World Scientific, Singapore (1993).

[2] D. J. Gross and F. Wilczek, Phys. Rev. Lett. **30**, 1343 (1973); H. Politzer, Phys. Rev. Lett. **30**, 1346 (1973).

[3] S. Bethke, Prog. Part. Nucl. Phys. **58**, 351 (2007).

[4] J. C. Collins and M. J. Perry, Phys. Rev. Lett. **34**, 1353 (1975).

[5] F. Karsch, Nucl. Phys. A **698**, 199 (2002).

[6] S. Gupta *et al.* Science **332**, 1525 (2011).

[7] M. M. Aggarwal *et al.* (STAR Collaboration), arXiv:nucl-ex/1007.2613 (2010).

[8] F.R. Brown *et al.*, Phys. Rev. Lett. **65**, 2491 (1990).

[9] Y. Hatta and T. Ikeda, Phys. Rev. D **67**, 014028 (2003) and references therein.

[10] J. W. Harris and B. Muller, Ann. Rev. Nucl. Part. Sci. **46**, 71 (1996).

[11] S. A. Bass *et al.*, J. Phys. G **25** R1 (1999).

[12] J. Cleymans and K. Redlich, Phys. Rev. C **60**, 054908 (1999); P. Braun-Munzinger *et al.*, Phys. Lett. B **518**, 41 (2001); N. Xu and M. Kaneta, Nucl. Phys. A **698**, 306 (2002).

[13] J. Adams *et al.* (STAR Collaboration), Nucl. Phys. A **757**, 102 (2005).

[14] O. Barannikova (for the STAR Collaboration), nucl-ex/0403014.

[15] J. Adams *et al.*, Phys. Rev. Lett. **91**, 172302 (2003).

[16] M. Gyulassy and M. Plumer, Phys. Lett. B **243**, 432 (1990).

[17] X. N. Wang, Nucl. Phys. A **715**, 775 (2003).

[18] J.Rafelski and B.Muller, Phys. Rev. Lett. **48**, 1066 (1982).

[19] J. Cleymans, K. Redlich and E. Suhonen, Z. Phys. C **51**, 137 (1991); F. Becattini and G. Pettini, Phys.Rev. C **67**, 015205 (2003).

[20] B. I. Abelev *et al.* (STAR Collaboration), Phys. Lett. B **673**, 183 (2009).

[21] C. Adler *et al.* (STAR Collaboration), Phys. Rev. Lett. **90**, 082302 (2003).

[22] J. Adams *et al.* (STAR Collaboration), Phys. Rev. Lett. **91**, 072304 (2003).

[23] R. J. Glauber, Lectures in Theoretical Physics (Interscience, New York, 1958), Vol. I, p. 315.

[24] T. Adachi and T. Kotani, Prog. Theor. Phys. **39**, 430 (1968).

[25] X. N. Wang and M. Gyulassy, Phys. Rev. Lett. **68**, 1480 (1992).

[26] T. Matsui and H. Satz, Phys. Lett B **178**, 416 (1986).

[27] B. Alessandro *et al.* (NA50 Collaboration), Euro. Phys. J. C **39**, 335 (2005).

[28] B. Alessandro *et al.* (NA50 Collaboration), Eur. Phys. J. C **48**, 329 (2006).

[29] R. Arnaldi *et al.* (NA60 Collaboration), Phys. Rev. Lett. **99**, 132302 (2007).

[30] A. Adare *et al.* (PHENIX Collaboration), Phys. Rev. Lett. **98**, 232002 (2007).

[31] A. Adare *et al.* (PHENIX Collaboration), Phys. Rev. Lett. **98**, 232301 (2007).

[32] A. Adare *et al.* (PHENIX Collaboration), Phys. Rev. Lett. **101**, 122301 (2008).

[33] A. Adare *et al.* (PHENIX Collaboration), Phys. Rev. Lett. **96**, 012304 (2006).

[34] F. Karsch *et al.*, Phys. Lett. B **637**, 75 (2006).

[35] K. Tuchin, J. Phys. G **30**, S1167 (2004).

[36] L. Yan, P. Zhuang, and N. Xu, Phys. Rev. Lett. **97**, 232301 (2006).

[37] M. M. Aggarwal *et al.* (WA98 Collaboration), Phys. Rev. Lett. **85**, 3595 (2000).

[38] A. Adare *et al.* (PHENIX Collaboration), Phys. Rev. Lett. **104**, 132301 (2010) and references therein.

[39] L. E. Gordon and W. Vogelsang, Phys. Rev. D **48**, 3136 (1993).

[40] S. Turbide, R. Rapp, and C. Gale, Phys. Rev. C **69**, 014903 (2004).

[41] A. Adare *et al.* (PHENIX Collaboration), Phys. Rev. C **81**, 034911 (2010) and references therein.

[42] J.-Y. Ollitrault, Phys. Rev. D **46**, 229 (1992).

[43] S. Voloshin and Y. Zhang, Z. Phys. C **70**, 665 (1996).

[44] C. Alt *et al.* (NA49 Collaboration), Phys. Rev. **C 68**, 034903 (2003).

[45] C. Adler *et al.* (STAR Collaboration), Phys. Rev. **C 66**, 034904 (2002).

[46] J. Adams *et al.* (STAR Collaboration), Phys. Rev. C 72, 014904 (2005).

[47] P. Huovinen *et al.*, Phys. Lett. B **503**, 58 (2001).

[48] X. Dong *et al.*, Phys. Lett. B **597**, 328 (2004).

[49] S. A. Voloshin, A. M. Poskanzer, and R. Snellings, arXiv:nucl-ex/0809.2949 (2008).

[50] D. Molnar and S. A. Voloshin, Phys. Rev. Lett. **91**, 092301 (2003); S. A. Voloshin, Nucl. Phys. A **715**, 379 (2003).

[51] D. Kharzeev, E. Levin, and L. McLerran, Phys. Lett. B **561**, 93 (2003).

[52] J. W. Cronin *et al.*, Phys. Rev. D **11**, 3105 (1975).

[53] P. B. Straub *et al.*, Phys. Rev. Lett. **68**, 452 (1992).

[54] J. Adams *et al.* (STAR Collaboration), Phys. Lett. B **616**, 8 (2005).

[55] S. S. Adler *et al.* (PHENIX Collaboration), Phys. Rev. C **74**, 024904 (2006).

[56] M. Lev and B. Petersson, Z. Phys. C **21**, 155 (1983); A. Accardi and M. Gyulassy, Phys. Lett. B **586**, 244 (2004); G. Papp, P. Levai, and G. Fai, Phys. Rev.C **61**, 021902(R) (1999); X. N. Wang, Phys. Rev. C 61, 064910 (2000).

[57] R. C. Hwa and C. B. Yang, Phys. Rev. Lett. **93**, 082302 (2004); R. C. Hwa and C. B. Yang, Phys. Rev. C **70**, 037901 (2004).

[58] B. Z. Kopeliovich *et al.*, Phys. Rev. Lett. **88**, 232303 (2002).

[59] L. Bertanza *et al.*, Phys. Rev. Lett. **9**, 180 (1962).

[60] B. I. Abelev *et al.* (STAR Collaboration), Phys. Rev. C **79**, 034909 (2009); A. K. Aamodt *et al.* (ALICE Collaboration), Phys. Rev. Lett. **105**, 072002 (2010).

[61] H.H. Gutbrod *et al.*, Phys. Rev. Lett. **37**, 667 (1976).

[62] S.T. Butler and C.A. Pearson, Phys. Rev. **129**, 836 (1963); R. Scheibl and U. Heinz, Phys. Rev. C **59**, 1585 (1999); W.J. Llope *et al.*, Phys. Rev. C **52**, 2004 (1995).

[63] L. P. Csernai and J. I. Kapusta, Phys. Rep. **131**, 223 (1986); A. Z. Mekjian, Phys. Rev. C **17**, 1051 (1978).

[64] A.Z. Mekjian, Phys. Rev. C **17**, 1051 (1978); S. Das Gupta and A.Z. Mekjian, Phys. Rep. **72**, 131 (1981).

[65] D. Molnar and S. A. Voloshin, Phys. Rev. Lett. **91**, 092301 (2003); R. C. Hwa and C. B. Yang, Phys. Rev. C **67**, 064902 (2003); R. J. Fries *et al.*, Phys. Rev. Lett. **90**, 202303 (2003).

Chapter 2

The STAR Experiment

2.1 Relativistic Heavy Ion Collider (RHIC)

The Relativistic Heavy Ion Collider (RHIC) at Brookhaven National Laboratory [1] is the first machine in the world, designed to accelerate and collide the heavy ion beams at relativistic speed to explore the matter at early universe. RHIC is a versatile accelerator, capable of operating with both polarized protons and a variety of ion species over a broad range of energies. It can accelerate heavy ions up to $\sqrt{s_{\mathrm{NN}}} = 200$ GeV, and polarized protons up to $\sqrt{s_{\mathrm{NN}}} = 500$ GeV. The polarized proton-proton collisions at RHIC is a part of spin physics program with the aim of studying the spin structure of the nucleon. The RHIC construction was completed at BNL in 1999 and the first commissioning runs with Au+Au collisions took place in 2000. Since 2000, RHIC has been used to collide various particle species at a number of collision energies as summarized in Table 2.1.

Figure 2.1 shows a schematic diagram of the RHIC together with all other accelerators used to bring the heavy ions up to the RHIC injection energy. The various steps required to produce collisions of heavy ions (e.g. Au) at the top RHIC energy of $\sqrt{s_{\mathrm{NN}}} = 200$ GeV are described below.

1. **Tandem Van de Graaff:** The Tandem Van de Graaff accelerator produces the initial acceleration of Au ions after their extraction from a pulsed sputter ion source. The Au ions which enter into Tandem are negatively charged. Here the ions are accelerated in two stages through a 14 MV potential, while passing

Table 2.1: Summary of RHIC operating modes and total integrated luminosity delivered to all experiments [2].

Run	Year	Species	$\sqrt{s_{\text{NN}}}$ (GeV)	Delivered Luminosity
1	2000	Au+Au	56	$< 0.001\ \mu\text{b}^{-1}$
		Au+Au	130	$20\ \mu\text{b}^{-1}$
2	2001/02	Au+Au	200	$258\ \mu\text{b}^{-1}$
		Au+Au	19.6	$0.4\ \mu\text{b}^{-1}$
		p+p	200	$1.4\ \text{pb}^{-1}$
3	2002/03	d+Au	200	$73\ \text{nb}^{-1}$
		p+p	200	$5.5\ \text{pb}^{-1}$
4	2003/04	Au+Au	200	$3.53\ \text{nb}^{-1}$
		Au+Au	62.4	$67\ \mu\text{b}^{-1}$
		p+p	200	$7.1\ \text{pb}^{-1}$
5	2004/05	Cu+Cu	200	$42.1\ \text{nb}^{-1}$
		Cu+Cu	62.4	$1.5\ \text{nb}^{-1}$
		Cu+Cu	22.4	$0.02\ \text{nb}^{-1}$
		p+p	200	$29.5\ \text{pb}^{-1}$
		p+p	409.8	$0.1\ \text{pb}^{-1}$
6	2006	p+p	200	$88.6\ \text{pb}^{-1}$
		p+p	62.4	$1.05\ \text{pb}^{-1}$
7	2006/07	Au+Au	200	$7.25\ \text{nb}^{-1}$
		Au+Au	9.2	small
8	2007/08	d+Au	200	$437\ \text{nb}^{-1}$
		p+p	200	$38.4\ \text{pb}^{-1}$
		Au+Au	9.2	small
9	2008/09	p+p	500	$110\ \text{pb}^{-1}$
		p+p	200	$114\ \text{pb}^{-1}$
		$pp2pp$	200	$0.6\ \text{nb}^{-1}$
10	2009/10	Au+Au	200	$10.3\ \text{nb}^{-1}$
		Au+Au	62.4	$544\ \mu\text{b}^{-1}$
		Au+Au	39	$206\ \mu\text{b}^{-1}$
		Au+Au	7.7	$4.23\ \mu\text{b}^{-1}$
		Au+Au	11.5	$7.8\ \mu\text{b}^{-1}$

Run	Year	Species	$\sqrt{s_{\mathrm{NN}}}$ (GeV)	Delivered Luminosity
11	2010/11	p+p	500	166 pb^{-1}
		Au+Au	19.6	33.2 $\mu\mathrm{b}^{-1}$
		Au+Au	200	9.79 nb^{-1}
		Au+Au	27	63.1 $\mu\mathrm{b}^{-1}$
12	2011/12	p+p	200	74 pb^{-1}
		p+p	500	277 pb^{-1}
		U+U	193	736 $\mu\mathrm{b}^{-1}$
		Cu+Au	200	27 nb^{-1}

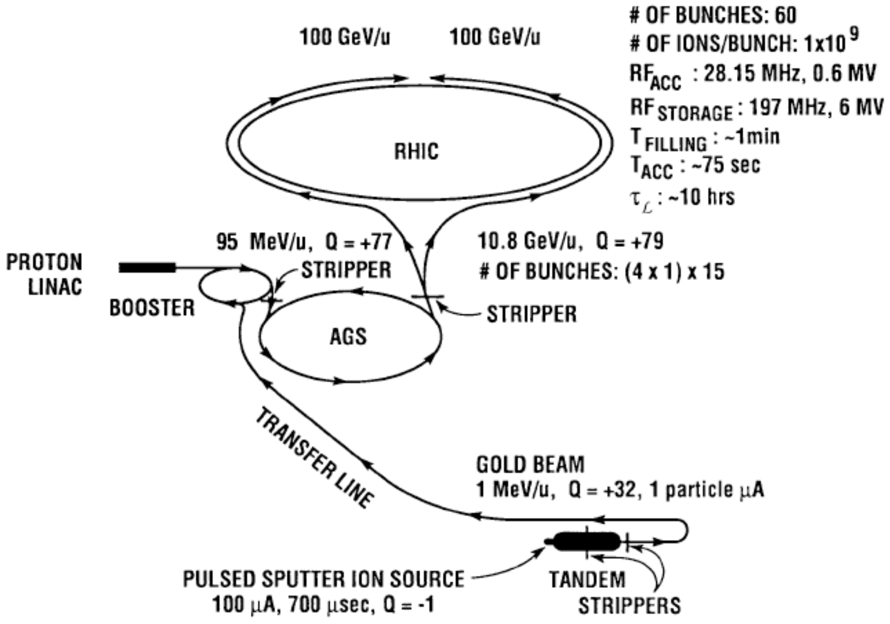

Figure 2.1: Schematic diagram showing the various stages of acceleration of ions at the RHIC.

through stripping foils that remove electrons off the ions, leaving them with a charge state of 32+ and kinetic energy of 1 MeV/u as they exit the Tandem.

2. **Tandem-to-Booster line (TTB):** From the Tandem, the bunches of Au^{32+} ions enter the 850 m long Tandem-to-Booster beam line, which carries them through a vacuum via a magnetic field to the Booster Synchrotron.
3. **Linear Accelerator (Linac):** For collision of proton beams at RHIC, the energetic protons are supplied by the 200 MeV Linac. Protons from the Linac are transfered to the Booster Synchrotron.
4. **Booster Synchrotron:** The Booster synchrotron is a powerful circular accelerator that provides the ions more energy, by having them "surf ride" on the downhill slope of radio frequency electromagnetic waves. The ions are propelled forward at higher and higher speeds, getting closer and closer to the speed of light. The Booster synchrotron accelerates the ions to 95 MeV/u and the ions are further stripped to reach the charge state of Au^{77+} at the exit of the Booster. The Booster then feeds the beam into the Alternating Gradient Synchrotron (AGS).
5. **Alternating Gradient Synchrotron:** The AGS is filled with 24 ion bunches in 4 Booster cycles. The bunches are then debunched and rebunched into four final bunches, and then accelerated, so that each bunch holds ions equivalent to one Booster filling. The AGS accelerates the Au^{77+} ions to 10.8 GeV/u. After passing through a final stripping foil, the gold ions are fully stripped to a charge state of 79+ at the exit of the AGS.
6. **AGS-to-RHIC Line:** When the ion beam is travelling at top speed (about 99.7% speed of light) in the AGS, it is passed through another beam line called the AGS-To-RHIC (ATR) transfer line. At the end of this line, there is a "fork in the road", where a switching magnet sends the ion bunches down one of two beam lines. Bunches are directed either left to travel clockwise in the RHIC ring or right to travel anticlockwise in the second RHIC ring.
7. **RHIC Rings:** The RHIC is an intersection storage ring particle accelerator. It consists of two independent quasi-circular concentric accelerator/storage rings

> of superconducting magnets, each with a circumference of 3.8 km. Out of these two rings one is called as the “Blue Ring”, where the beam moves in a clockwise direction and the other one is known as the “Yellow Ring”, where the beam moves in a counter-clockwise direction. The rings share a common horizontal plane inside the tunnel, with each ring having an independent set of bending and focusing magnets as well as radio frequency acceleration cavities. This allows independent tuning of the magnetic fields in each ring which is required to achieve equal rotation frequencies of the different particle/ion species in each ring. In the RHIC, the counter-rotating beams of heavy ions are accelerated to the top energy of 100 GeV/u and can be collided into one another at as many as six interaction points.

Another important aspect of RHIC is to provide beams of very high luminosities, which makes possible to measure rare processes having small cross sections. For a process with the cross section σ_i, the event rate (R_i) is given by $R_i = \sigma_i \cdot \mathcal{L}$. The luminosity $\mathcal{L}$ is given by $\mathcal{L}= fn\frac{N_1 N_2}{A}$, where N_1 and N_2 are the number of particles contained in each bunch, A is the cross-sectional area of the overlap between the two colliding beams of particles, f is the frequency of revolution, and n is the number of bunches per beam. High luminosities can therefore be achieved by maximizing f, n and decreasing the beam profile. Table 2.2 lists some of the designed parameters of the RHIC.

The four main experiments located at the four intersection points at RHIC are Solenoidal Tracker At RHIC (STAR) [3], Pioneering High Energy Nuclear Interaction eXperiment (PHENIX) [4], Broad RAnge Hadron Magnetic Spectrometers (BRAHMS) [5] and PHOBOS (not an acronym, but named after moon of Mars) [6]. If RHIC is thought to be a clock, then four experiments BRAHMS, STAR, PHENIX, and PHOBOS are located at 2 o’clock, 6 o’clock, 8 o’clock, and 10 o’clock positions, respectively as shown in Fig. 2.2. The two large experiments STAR and PHENIX are still operational at RHIC, while the two small experiments PHOBOS and BRAHMS have completed their operation in the year 2005 and 2006, respectively.

Table 2.2: Some of the designed parameters and performance information of the RHIC.

Parameter	Value
Luminosity (Au+Au)	$2 \times 10^{26}\mathrm{cm}^{-2}\mathrm{s}^{-1}$
Luminosity (p+p)	$4 \times 10^{30}\mathrm{cm}^{-2}\mathrm{s}^{-1}$
No. of bunches per ring	60
Revolution frequency	78 kHz
Ions (Au) per bunch	10^9
Ions (p) per bunch	10^{11}
Beam life time	10 hours
Ring circumference	3833.845 m

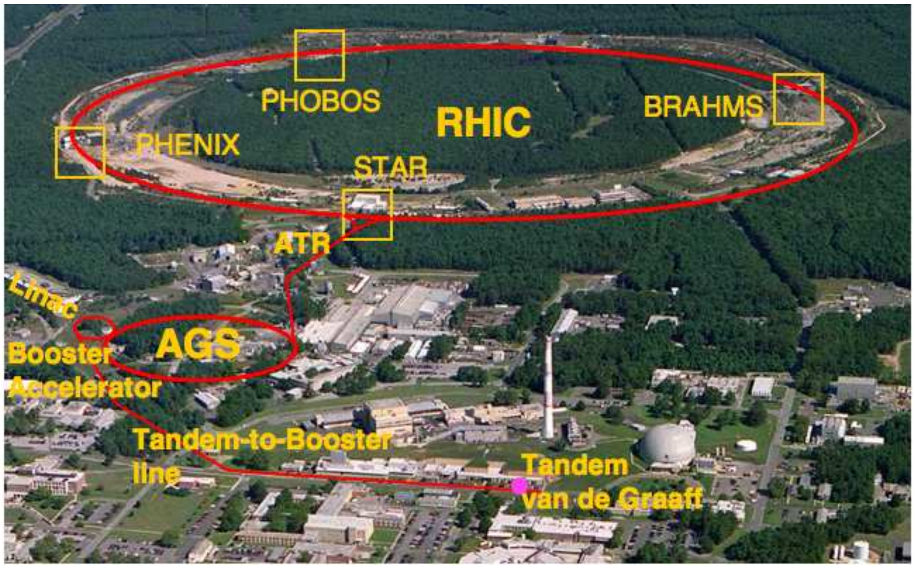

Figure 2.2: Overview of the RHIC accelerator complex at Brookhaven National Laboratory, Upton, New York.

2.2 The STAR Detector

The STAR detector [3] is one of the two large detector systems constructed at RHIC. The main motivation to build the STAR detector was to investigate the behavior of strongly interacting matter at high energy density and to search for the signatures of QGP. The goal is to obtain a fundamental understanding of the microscopic structure of these hadronic interactions at high energy densities. In order to accomplish this, STAR was designed primarily for measurements of hadron production over a large solid angle, featuring detector systems for high precision tracking, momentum analysis, and particle identification at the central rapidity region. STAR measures many observables simultaneously to study signatures of a possible phase transition from hadronic matter to QGP and to understand the space-time evolution of the collision process in ultrarelativistic heavy ion collisions. The large acceptance of STAR detector makes it well suited for event-by-event characterizations of heavy ion collisions and for the detection of hadron jets [3]. In addition to the heavy ion physics program at STAR, there is also an active spin physics program ongoing with the aim of studying the spin structure of the nucleon.

Figure 2.3 shows a three dimensional view of the STAR detector along with the subsystems, and Fig. 2.4 shows the cross-sectional side view of the STAR detector [3, 7]. The whole detector is enclosed in a solenoidal magnet that provides a uniform magnetic field of maximum value 0.5 T parallel to the beam direction. The uniform magnetic field provides ability to perform momentum measurements of charged particles. The charged particle tracking close to the interaction region is accomplished by a Silicon Vertex Tracker (SVT) [8] and a Silicon Strip Detectors (SSD) [9]. The silicon detectors cover a pseudorapidity range $|\eta| \leq 1$ with complete azimuthal symmetry ($\Delta\phi = 2\pi$). Silicon tracking close to the interaction point allows precision localization of the primary interaction vertex and identification of secondary vertices from weak decays of Λ, Ξ, and Ω etc. After the 2007 run, the SVT and SSD has been taken out of the STAR to reduce considerable amount of material budget. The heart of the STAR detector is the Time Projection Chamber (TPC) [10] which is used for the charged particle tracking and particle identification. The TPC is 4.2 meters long and it covers a pseudorapidity range $|\eta| \leq 1.8$ for tracking with complete

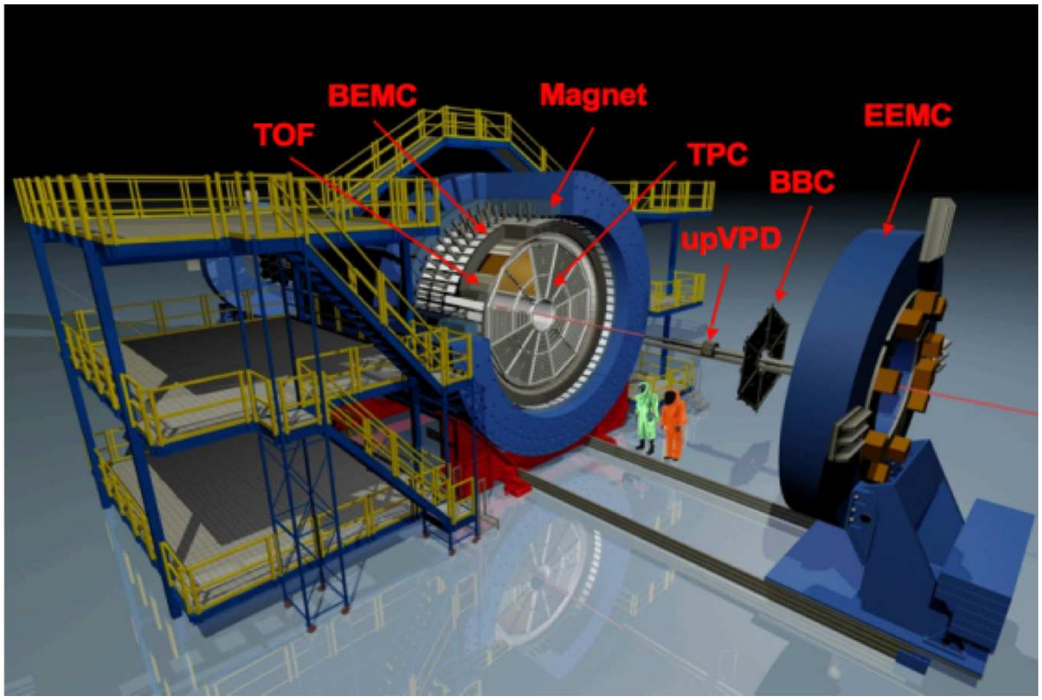

Figure 2.3: Perspective view of the STAR detector, with a cutaway for viewing inner detector systems [7].

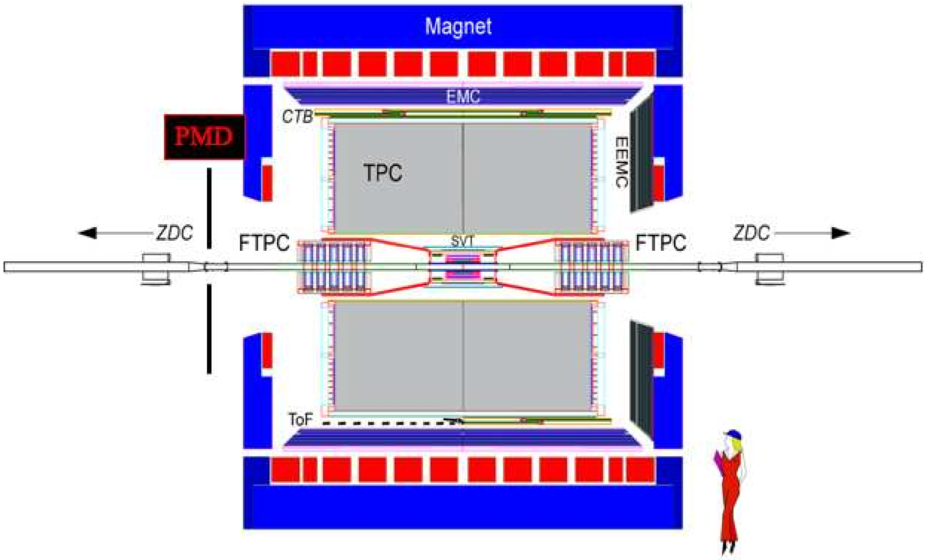

Figure 2.4: A cutaway side view of the STAR detector [3].

azimuthal symmetry ($\Delta\phi = 2\pi$). To extend the tracking to the forward region, two Forward Time Projection Chambers (FTPC) [11] are installed covering $2.5 < |\eta| < 4$, on either side of the TPC in forward and backward rapidity and with complete azimuthal coverage.

A Ring Imaging CHerenkov (RICH) detector [12] covering $|\eta| < 0.3$ and $\Delta\phi = 0.11\pi$, and a Time-of-Flight patch (TOFp) [13] covering $-1 < \eta < 0$ and $\Delta\phi = 0.04\pi$ were installed at STAR in 2001 to extend the particle identification to larger momenta over a small solid angle. In 2010, a barrel Time-of-Flight (TOF) detector based on Multi-gap Resistive Plate Chamber (MRPC) technique [14] was fully installed in STAR. The TOF consists of a total of 120 trays spanning a pseudorapidity range $|\eta| \leq 0.9$ with full azimuth coverage. The trigger system of the TOF detector is the two upgraded Pseudo Vertex Position Detectors (upVPD) [13], each staying 5.7 m away from the TPC center along the beam line. They provide the start timing information for TOF detectors.

For detection of electromagnetic particles STAR has a set of calorimeters. The full Barrel Electro Magnetic Calorimeter (BEMC) [15] covers $|\eta| < 1$ and Endcap ElectroMagnetic Calorimeter (EEMC) [16] covers $1 < \eta \leq 2$. Both these detectors are azimuthally symmetric. These calorimeters include shower-maximum detectors (SMD) to distinguish between energy deposited by single photons or from photon pairs arising from neutral pion (π^0) or η meson decays. The EMC can also be employed to provide prompt charged particle signals essential to discriminate against pile-up tracks in TPC. The STAR detector is also capable of detecting photons at forward rapidity using the Photon Multiplicity Detector (PMD) [17]. The PMD covers a pseudorapidity range $-3.7 < \eta < -2.3$ with full azimuthal coverage.

We will describe briefly these detectors in the later sections. The TPC, FTPC and the TOF are the main detectors, central to results and discussions presented in this thesis. We will discuss these detectors in detail in the later part of this chapter.

2.3 Trigger Detectors

The interaction rates at RHIC for the highest luminosity beams can approach ~ 10 MHz. Since some of the detector subsystems in STAR can only operate at rates of

$\sim$ 100 Hz, not all events can be recorded by the data acquisition system (DAQ). Therefore, the STAR trigger system, which is based on input from the fast detectors, controls the selection of events. In addition, the trigger is used to select events with rare or specific signals of interest to increase the recorded statistics of these events. STAR detector consists of some fast detectors, which are employed to provide trigger for the slow detectors in order to record data. The main triggering detectors for STAR are: Zero Degree Calorimeter (ZDC), Central Trigger Barrel (CTB), Beam Beam Counter (BBC), and Electro Magnetic Calorimeters (BEMC and EEMC).

In order to provide some universal characterization of heavy ion collisions, all four RHIC experiments have one common detector subsystem, namely a pair of ZDCs [18]. The ZDCs at STAR are situated at $\pm$ 18 m from the center of the STAR detector and subtend an angle of $\theta < 2$ mrad with respect to the beam direction. Each ZDC consists of three modules. Each module consists of a series of tungsten plates alternating with layers of wavelength shifting fibres which are connected to a photomultiplier tube (PMT). The ZDCs are hadronic calorimeters designed to measure the energy of spectator neutrons from the colliding nuclei after the collision. Since they are positioned on the other side of the DX magnets to the interaction region, the charged fragments are bent away from the zero degree region and are not measured in the ZDCs. The real collisions can be distinguished from the background events by selecting events with ZDC coincidence from the two beam directions. This makes ZDC as a useful event trigger and a luminosity monitor detector. The energy deposited by the neutrons are correlated to the particle multiplicity and can be used to measure collision centrality. The ZDCs are also used to locate the interaction vertex by using the time delay between the coincidences. Hence, ZDCs are very useful for the beam monitoring, triggering, and locating interaction vertices. In order to study the spatial distribution of the neutron hits on the transverse plane of the ZDCs, a Shower Maximun Detector (SMD) was installed between the first and second modules of each existing STAR ZDC in the year 2004. The addition of ZDC-SMD to the STAR experiment enhances its capability in different areas of physics such as anisotropic flow, strangelet searching, ultra-peripheral collisions, and spin physics [19].

The CTB [20] was installed surrounding the outer cylinder of the TPC. CTB consists of 240 scintillator slats of plastic scintillator with $0 \leq \phi \leq 2\pi$ and $|\eta| \leq 1$

coverage. Each slat consists of a scintillator, light guide, and mesh dynode PMT. As charged particles travel through the tiles the generated scintillation photons are collected by PMTs, digitized and converted into electric signals. The amplitude of the signal is proportional to the multiplicity of the charged particles. The response time of the CTB is fast (260 ns), therefore in combination with the ZDC signal (which detect the neutrons), it provides a powerful charged particle multiplicity trigger. Now CTB is replaced by the barrel TOF system at STAR.

The BBC consists of a hexagonal scintillator array structure, mounted around the beam pipe beyond the east and west pole-tips of the STAR magnet at about 3.5 m from the center of nominal interaction region. It covers $3.3 < |\eta| < 5.0$ in pseudorapidity. The non-single diffractive (NSD) p+p events are triggered by the coincidence of two BBCs. The timing difference between the two counters is used to get information of the primary vertex position. BBC coincidences are also used to reject beam gas events, to measure the absolute luminosity $\mathcal{L}$ with 15% precision, and to measure the relative luminosities R for different proton spin orientations with high precisions. Apart from the above applications, the small tiles of BBC are used to reconstruct the first order event plane for flow analysis.

2.4 Electromagnetic Calorimeters

The Electromagnetic Calorimeters allow STAR to trigger on and study rare and high p_T processes like jets, leading hadrons, direct photons and heavy quarks. They provide large acceptance for photons, electrons along with neutral pions and η mesons in all collision systems spanning from polarized p+p to Au+Au collisions. Other applications include general event characterization in heavy ion collisions including ultra-peripheral collisions. In order to achieve these goals, STAR has installed two electromagnetic calorimeters i.e. Barrel Electromagnetic Calorimeter and Endcap Electromagnetic Calorimeter. A discussion on these is given below.

2.4.1 Barrel Electromagnetic Calorimeters

The BEMC [15] is located inside the aluminium coil of the STAR solenoid and covers the pseudorapidity region $|\eta| < 1$ with full azimuthal angle. It is basically a sampling calorimeter which consists of alternate layers of lead and scintillator planes. It has 20 layers of lead plates and 21 layers of scintillator. The full BEMC consists of 120 calorimeter modules, each covering 6^0 ($\sim$0.1 radian) in $\Delta\phi$ and 1.0 unit in $\Delta\eta$. Each module is further segmented into 40 towers, 2 in ϕ and 20 in η, with each tower having a granularity of 0.05 in both $\Delta\phi$ and $\Delta\eta$. There exists a SMD located about 5 radiation lengths (X_0) from the front of the lead-scintillator stack in each module. The SMD is used to provide fine spatial resolution in a calorimeter which has segmentations (towers) significantly larger than an electromagnetic shower size. Using BEMC, it is possible to reconstruct neutral pions at relatively high $p_T \approx$ 25–30 GeV/c and also to identify single electrons and pairs in dense hadron backgrounds from the heavy vector mesons, W and Z bosons decays.

2.4.2 Endcap Electromagnetic Calorimeters

The EEMC [16] is situated on the west pole-tip of the STAR detector. It covers the pseudorapidity region $1 \leq \eta \leq 2$ with full azimuthal angle, supplementing the BEMC as described in the previous subsection. Within this acceptance, it enhances STAR's capability to detect photons and electromagnetically decaying mesons (π^0, η), to identify electrons and positrons, and to trigger on high energy particles of these types. The construction of EEMC includes a SMD optimized to discriminate between photons and π^0 or η mesons over the energy region 10–40 GeV. It also consists of preshower and postshower layers used to discriminate between electrons and hadrons. In addition, the EEMC enhances the acceptance and triggering capabilities for jets in STAR.

2.5 Photon Multiplicity Detector

The PMD [17] was installed on east wall of the wide angle hall in the STAR experiment. It was installed at 540 cm from the center of the TPC outside the STAR magnet. It covers a pseudorapidity region $-3.7 < \eta < -2.3$ with full azimuthal angle. The PMD was designed to measure photon multiplicity in the forward rapidity region, where the calorimeters are not efficient due to high particle density. It can detect photons with p_T as low as 20 MeV/c [21]. Figure 2.5 shows a picture of the

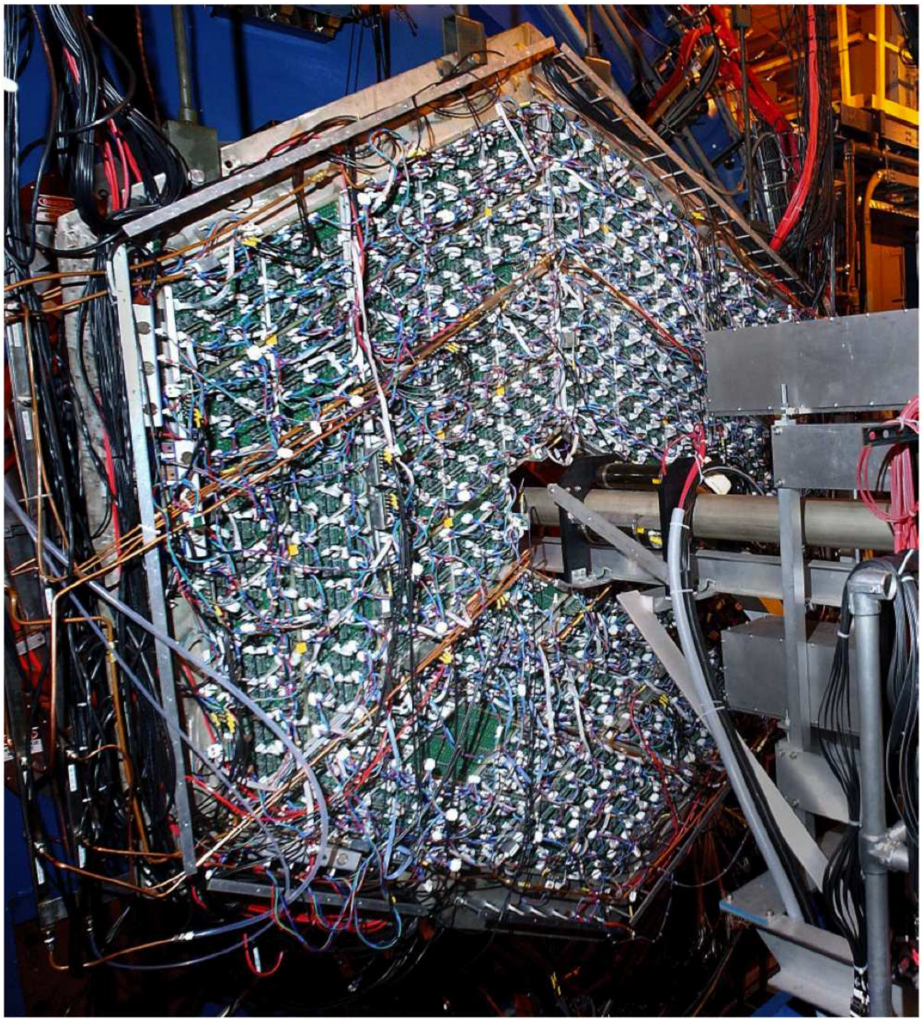

Figure 2.5: Picture of the PMD after complete installation at the STAR experiment.

PMD as installed at the STAR experiment.

The PMD consists of a Charged Particle Veto (CPV) plane and a Preshower detector plane with $3X_0$ thick lead converter in between. Each plane consists of 12 super modules arranged in the form of a hexagon and has 41,472 hexagonal honeycomb cells. The detector is based on a proportional counter design using $Ar + CO_2$ gas mixture in ratio 70:30 by weight. Figure 2.6 shows the schematic diagram on the working principle of the PMD. A photon passing through the converter produces an electromagnetic shower. These shower particles produce signals in several cells of the sensitive volume of the detector. Charged hadrons usually affect only one cell and produce a signal resembling those of Minimum Ionizing Particles (MIPs). The thickness of converter is optimized such that the conversion probability of photons is high

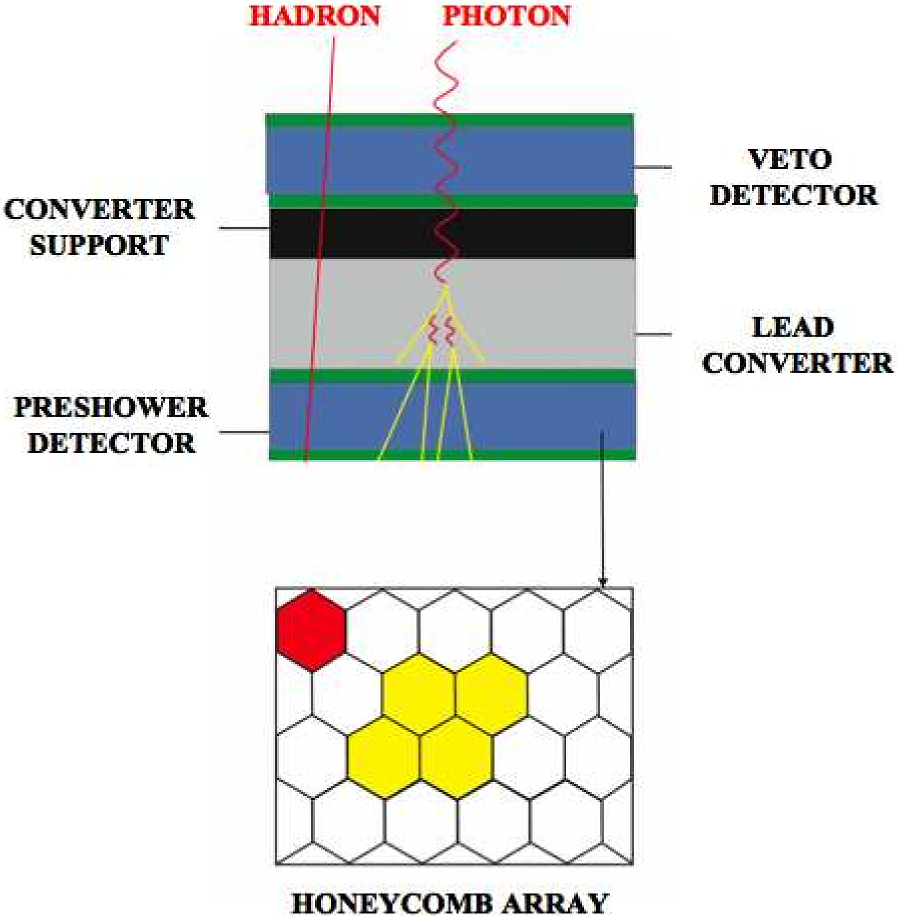

Figure 2.6: Schematic diagram showing the working principle of PMD.

and transverse shower spread is small to minimize shower overlap in high multiplicity environment. The CPV plane is used for the hadron rejection.

The PMD measures the spatial distribution and multiplicity of photons on an event by event basis. Using these information on photons and combining the information from other detectors, the PMD is capable of addressing the following broad topics in physics:

(a) Critical phenomena near the phase boundary leading to fluctuations in global observables like multiplicity and pseudorapidity distributions,

(b) Signals of chiral symmetry restoration (e.g., disoriented chiral condensates) using information on charged particles from FTPC, and

(c) Determination of reaction plane and probe thermalization via studies of azimuthal anisotropy and flow.

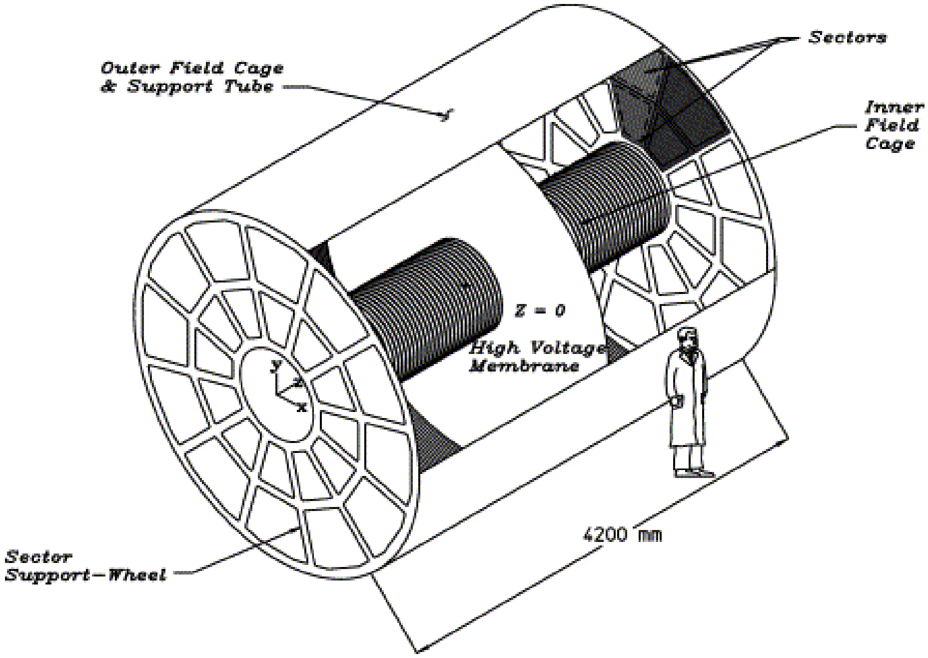

Figure 2.7: Three dimensional schematic diagram indicating the main structural elements of the STAR TPC [10].

The PMD has completed data taking at the STAR experiment in the year 2011.

2.6 Time Projection Chamber

The TPC [10, 22] is the primary tracking device in the STAR experiment. It records the tracks of charged particles, measures their momenta, and identifies the charged particles by measuring their ionization energy loss (dE/dx). The TPC covers a pseudorapidity region $|\eta| < 1.8$ with full azimuthal angle coverage. It can measure the charged particle's momenta from 100 MeV/c to 30 GeV/c and identify them over a momentum range from 100 MeV/c to greater than 1 GeV/c.

2.6.1 Technical Design

Figure 2.7 shows the schematic diagram of STAR TPC. The TPC is placed inside a large solenoidal magnet which provides a uniform magnetic field of 0.5 T along the length of the TPC. It is in the form of a cylinder 4.2 m in length and 4 m in diameter. It consists of one outer field cage (OFC), one inner field cage (IFC), and two end caps as shown in the Fig. 2.7. The inner and outer radii of the active volume are

0.5 m and 2.0 m respectively and the cylinder is concentric with the beam pipe. A thin conductive Central Membrane (CM) made of 70 μm thick carbon coated kapton divides the TPC into two equal halves. This central membrane is maintained at a voltage of -28 kV with respect to the detection planes and acts as cathode. The end caps providing the readout system are at ground potential act as anodes. A uniform electric field of $\sim$135 V/cm is maintained between the central membrane and the readout end caps. A chain of 183 resistors and equipotential rings along the concentric field cage cylinders help to maintain this uniformity of the electric field which is critical for uniform electron drift [10]. An outer support hoop mounted on the outer field cage keeps the CM taut and secured under tension. Attached on each side of the CM, there are 36 Al stripes which act as targets emitting electrons for the TPC Laser Calibration System. Since the position of the narrow stripes are precisely measured, the emitted electrons, which are photo-ejected when an ultraviolet laser beam hits a stripe, can be used for spatial calibration.

The TPC volume is filled with P10 gas (90% Ar and 10% CH_4) regulated at a pressure of 2 mbar above the atmospheric pressure. The P10 gas has an advantage of fast drift velocity which peaks at a low electric field. Operating on the peak of the velocity curve makes the drift velocity stable and insensitive to small variations in temperature and pressure. Lower field strengths require lower voltages which simplify the design of the detector. The electron drift velocity in P10 is relatively fast, 5.45 cm/μs at 130 V/cm drift field.

The TPC readout endcap planes are multi-wire proportional counter (MWPC) chambers with pad readout and are positioned on the support wheels. The MWPC chambers consist of three wire planes and a pad plane each. For each endcap there are 12 readout sectors which are positioned radially with respect to the hole defined by the inner field-cage with 3 mm gaps between each sector. Each sector is subdivided into inner and outer subsectors characterized by a change in the readout padrow geometry. Each inner sector contains a large number of small pads, distributed in 13 pad rows, to maximize the position and two-track resolution in a region with high particle density. The pads of the outer sectors are densely packed in 32 rows per sector to optimize the measure of energy loss by ionization in a region with lower particle densities. One full sector of the anode pad plane is shown in Fig. 2.8. Therefore, a

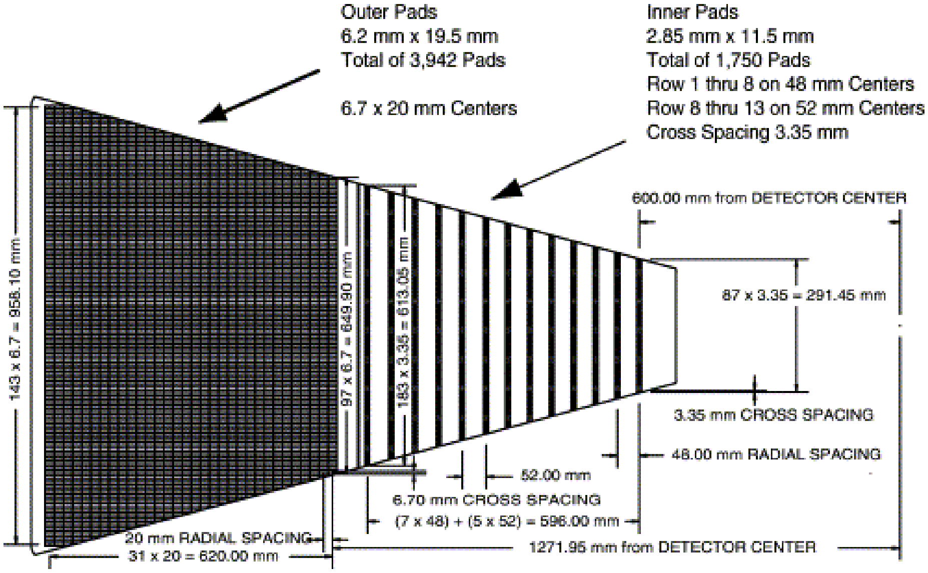

Figure 2.8: A sector of the TPC anode plane indicating the inner and outer subsectors and their respective padrows [10].

track in the TPC can be sampled a maximum of 45 times if it crosses all 45 padrows.

2.6.2 Track Reconstruction

The TPC track reconstruction starts by identifying the three dimensional space coordinate points. When a charged particle traverses through the volume of the TPC, it ionizes the gas atoms and molecules along its path leaving behind a cluster of electrons. The $x-y$ position of each cluster is found by measuring the signal in adjacent pads (along a single padrow). The drift time from point of origin of the cluster to the endcap is measured and the z-position of the cluster is determined by dividing the drift time by the average drift velocity. Once the positions of the clusters are found, a Time Projection Chamber Tracker (TPT) algorithm is used to reconstruct the tracks by a helical trajectory fit. Each track is a helix to first order, but there can be deviations from the helical shape due to energy loss in the gas and multiple Coulomb scattering. The resulting track information collected from the TPC together with additional tracking information from other inner detectors (SVT, SSD) are then refit by application of the Kalman Fit Method [23] to find a global track. The z-position of the primary collision vertex is determined by extrapolating the trajectories of the reconstructed global tracks back to the origin. If a global track has a distance of closest approach (dca) (with respect to the primary vertex), less than 3 cm, then the track is refitted to include the primary vertex as an additional space point. These tracks are called primary tracks. The reconstruction efficiency for primary tracks depends on the track quality cuts, particle type and track multiplicity.

2.6.3 Particle Identification Using dE/dx

Identification of the charged particles can be achieved by TPC through their energy loss (dE/dx) due to interactions in the medium inside the TPC. If a particle travels through the entire TPC volume, it will provide 45 dE/dx points on the 45 pad rows. However, the ionization fluctuations are large and the length over which the particle energy loss is measured is short, it is not possible to measure the average dE/dx accurately. Hence we measure the most probable dE/dx. This is done by removing 30% of the largest ionization clusters and then calculating the truncated mean of the remaining clusters.

For a given track momentum and particle mass, the ionization energy loss can be described by the Bichsel function [24], which is an extension of the Bethe-Bloch formula [25]:

$$-\frac{dE}{dx} = Kz^2\frac{Z}{A}\frac{1}{\beta^2}\left[\frac{1}{2}\ln\left(\frac{2m_ec^2\beta^2\gamma^2T_{\max}}{I}\right) - \beta^2 - \frac{\delta^2}{2}\right], \tag{2.1}$$

where z is the integral charge of the particle, K is a constant, Z is the atomic number of the absorber, A is the atomic mass of the absorber, m_e is the electron mass, c is the speed of light in vacuum, I is the average ionization energy of the material, $T_{\max}$ is the maximum kinetic energy that can be given to a free electron in an interaction, δ is a correction based on the electron density, and $\beta\gamma = p/mc$, where p is the momentum and m is the mass of the charged particle. The above equation shows that dE/dx is mass dependent and hence useful in particle identification. Figure 2.9 shows energy loss for primary and secondary particles in the TPC as a function of particle momentum. The red lines are the theoretical predictions from Bichsel function for different particle species and the bands represent the measured values of dE/dx. The TPC dE/dx resolution of around 7–8% allows identification of charged

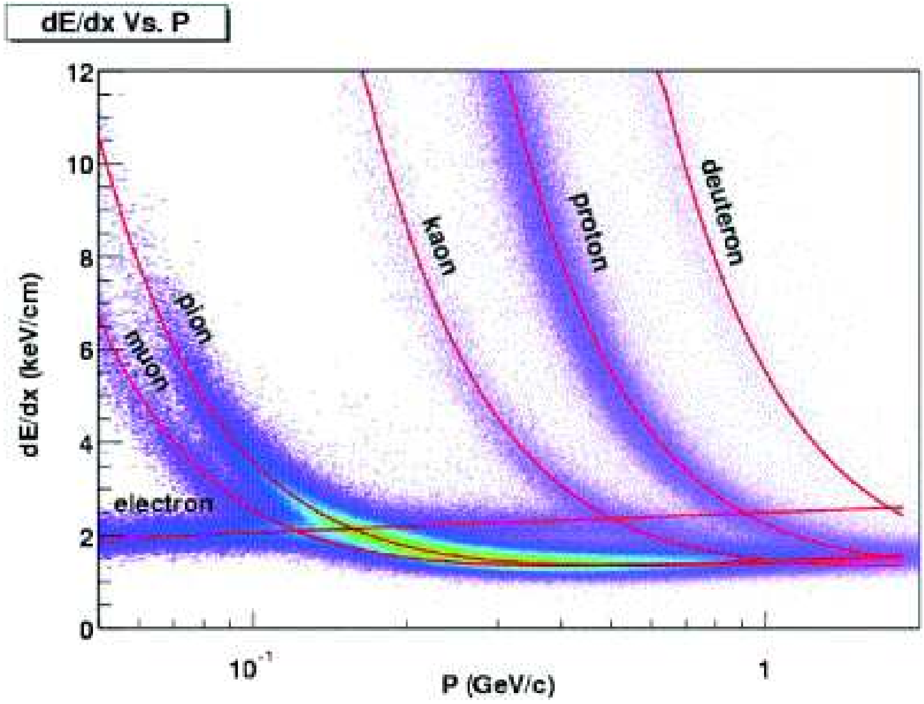

Figure 2.9: The energy loss distribution for charged particles in the STAR TPC as a function of momentum [10].

pions and kaons up to about a transverse momentum of 0.75 GeV/c. Protons and antiprotons can be identified up to about 1.1 GeV/c.

The particle identification can be quantitatively described by the variable $n\sigma$, which corresponds to the standard deviation of a Gaussian between the measured track and its expected value. The $n\sigma_X$ is defined as:

$$n\sigma_X = \frac{1}{R}\log\frac{< dE/dx > |_{measured}}{< dE/dx >_X |_{expected}}, \tag{2.2}$$

where X is the particle type (e, π, K, or p), $< dE/dx > |_{measured}$ is the measured energy loss of a track, $< dE/dx >_X |_{expected}$ is the expected mean energy loss of particle X at a given momentum and R is the dE/dx resolution which is found to range between 6% to 10%. Similarly, another variable Z is also used to identify the particles, which is defined as

$$Z_i = \ln\left(\frac{< dE/dx > |_{measured}}{< dE/dx >_i |_{expected}}\right), \tag{2.3}$$

where $< dE/dx > |_{measured}$ is the measured mean energy loss of a track and $< dE/dx >_i |_{expected}$ is the expected mean energy loss calculated using a Bichsel function for the given particle type i ($i = d$, t and ^3He).

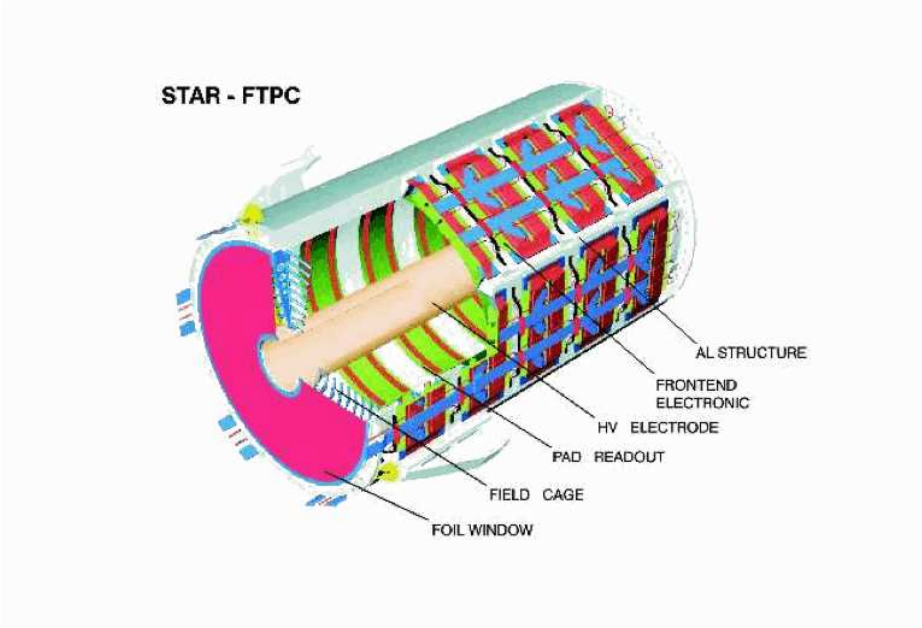

Figure 2.10: Schematic diagram of an FTPC at the STAR experiment.

2.7 Forward Time Projection Chamber

In order to extend the phase space coverage of the STAR experiment to the forward region of $2.5 < |\eta| < 4.0$, two cylindrical FTPC's were constructed [11]. The increased acceptance improves the event characterization and allows the study of asymmetric systems. The full two-component system measures the momenta and production rates of charged particles. Figure 2.10 shows a schematic diagram of the FTPC. The FTPCs are situated on both sides from center of the TPC along the beam pipe. Each of the FTPCs is a 120 cm cylindrical structure, 75 cm in diameter with a radial drift field. It has readout chambers located in five rings on the outer cylinder surface. This radial configuration improves the two track separation in the highest particle density region (close to the beam pipe). The front-end electronics (FEE) boards are mounted on the back of readout chambers. The ionization electrons drift to the anode sense wires. The induced signals on the adjacent cathode surface are read out by 9600 pads (each of area $1.6 \times 20\ mm^2$). Curved readout chambers are used to keep the radial field as ideal as possible. The low electron diffusion and the radial drift in principle result in the required 2-track separation of about 1 mm. The two FTPC's have 19,200 channels of electronics, capable of measuring the charge drifting to the

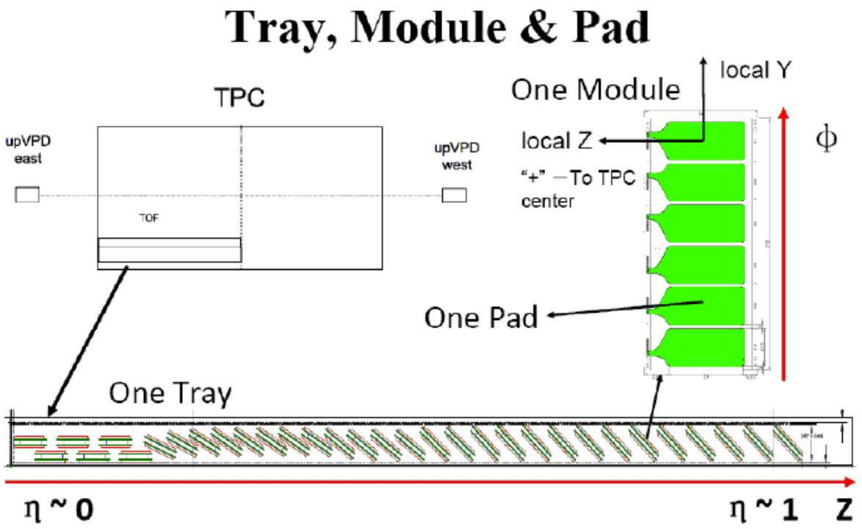

Figure 2.11: Geometry of TOF trays, modules and pads.

readout chambers in short time samples. The FTPC's use a mixture Ar and CO_2 with $Ar : CO_2 :: 50 : 50$. The track points are calculated from the charge distribution measured by the readout electronics. These track points are grouped to tracks which, together with magnetic field maps, can be used to get the particle momenta. In high multiplicities, event-by-event observables like $\langle p_T \rangle$, fluctuations of charged particle multiplicity, and collective flow anisotropies can be studied using FTPC.

2.8 Time-of-Flight

The main goal of the TOF [14] system was to extend the particle identification capabilities of the experiment to the higher momentum region. STAR has performed the upgrade of full barrel TOF detector based on the Multigap Resistive Plate Chamber (MRPC) technology since the year 2009. The TOF consists of a total of 120 trays (60 on east side and 60 on west side) that cover the full azimuth and have a pseudorapidity range $|\eta| < 0.9$. Each tray covers 6 degree in azimuthal direction (ϕ) around the TPC.

Figure 2.11 shows the detailed geometry and the definition of local coordinate system on each pad of TOF subsystem. There are 32 MRPC modules in each tray, placed along beam (Z) direction. In each module, there are 6 read-out strips (called as pad or channel) along the azimuthal direction. To provide a starting time for

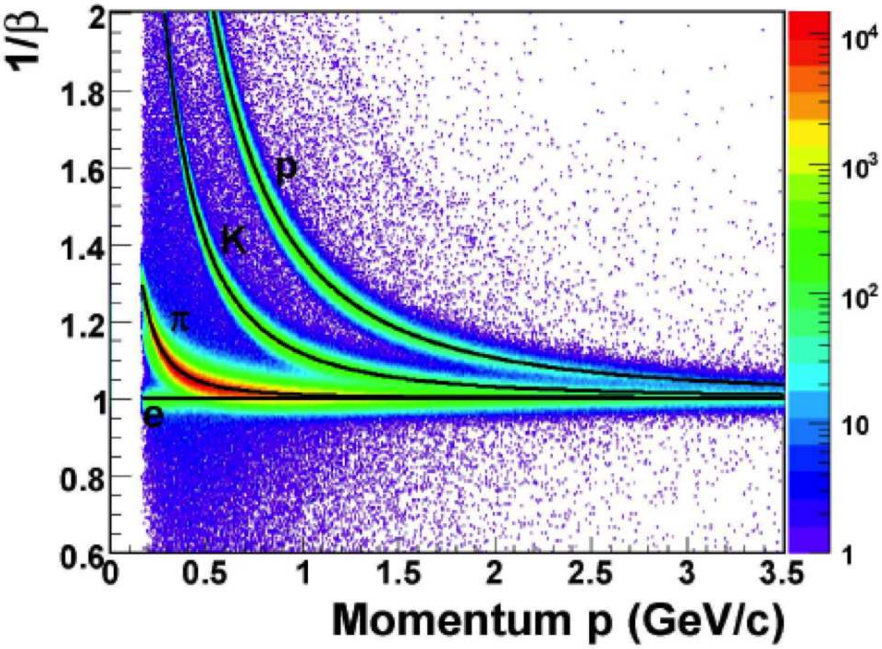

Figure 2.12: TOF $1/\beta$ as a function of momentum from run 9 p+p collisions at $\sqrt{s_{NN}}$ = 200 GeV.

TOF detectors, two VPDs are also installed. Each VPD lies at a distance of 5.4 m from the center of the TPC along the beam direction. The VPD has 19 channels on the east side and 19 channels on the west side. Apart from providing the start time information, the VPD can also provide the independent Z component of the vertex. The timing resolution for each VPD and TOF tray is on nano second level before any calibration. The timing resolution can be improved by an order of magnitude after the calibration. Figure 2.12 shows $1/\beta$ from TOF measurement as a function of momentum (p) in run 9 p+p collisions at $\sqrt{s_{NN}} = 200$ GeV. This shows the hadron identification capability of TOF subsystem at higher momentum.

Bibliography

[1] http://www.bnl.gov/rhic/.

[2] http://www.agsrhichome.bnl.gov/RHIC/Runs/. RHIC Collider Accelerator Department.

[3] K. H. Ackermann *et al.* (STAR Collaboration), Nucl. Instr. Meth. A **499**, 624 (2003).

[4] K. Adcox *et al.* (PHENIX Collaboration), Nucl. Instr. Meth. A **499**, 469 (2003).

[5] M. Adamczyk *et al.* (BRAHMS Collaboration), Nucl. Instr. Meth. A**499**, 437 (2003).

[6] B. B. Back *et al.* (PHOBOS Collaboration), Nucl. Inst. Meth. A **499**, 603 (2003).

[7] 3D picture of STAR detector by Alex Schmah and Maria.

[8] R. Bellwied *et al.*, Nucl. Instrum. Meth. A **499**, 640 (2003).

[9] L. Arnold *et al.*, Nucl. Instrum. Meth. A **499**, 652 (2003).

[10] M. Anderson *et al.*, Nucl. Instr. Meth. A **499**, 659 (2003).

[11] K. H. Ackermann *et al.*, Nucl. Instr. Meth. A **499**, 713 (2003).

[12] A. Braem *et al.*, Nucl. Instr. Meth. A **499**, 720 (2003).

[13] W. J. Llope *et al.*, Nucl. Instr. Meth. A **522**, 252 (2004).

[14] B. Bonner *et al.*, Nucl. Instr. Meth. A **508**, 181 (2003); M. Shao *et al.*, Nucl. Instr. Meth. A **492**, 344 (2002).

[15] M. Beddo *et al.*, Nucl. Instrum. Meth. A **499**, 725 (2003).

[16] C. E. Allgower *et al.*, Nucl. Instrum. Meth. A **499**, 740 (2003).

[17] M. M. Aggarwal *et al.*, Nucl. Instr. Meth. A **499**, 751 (2003).

[18] C. Adler *et al.*, Nucl. Instrum. Meth. A **470**, 488 (2001).

[19] B. I. Abelev *et al.* (STAR Collaboration), Phys. Rev. Lett. **101**, 252301 (2008); STAR ZDC-SMD proposal, STAR Note SN-0448 (2003).

[20] F. S. Bieser *et al.*, Nucl. Instrum. Meth. A **499**, 766 (2003).

[21] “A Preshower PMD for STAR Experiment”, STAR Note **310** (1997).

[22] H. Wieman *et al.*, IEEE Trans. Nuc. Sci. **44**, 671 (1997); J. Thomas *et al.*, Nucl. Instum Meth. A **478**, 166 (2002).

[23] D. Liko, STAR Note **00087**, 1–15 (1992).

[24] H. Bichsel, Nucl. Instr. Meth. A **562** 154 (2006).

[25] W. M. Yao *et al.*, J. Phys. G: Nucl. Part. Phys. **33**, 1 (2006).

Chapter 3

Identified Particle Spectra in d+Au Collisions at $\sqrt{s_{NN}} = 200$ GeV

3.1 Introduction

The d+Au collision at RHIC is very important to disentangle initial and final state effects in heavy ion collisions. The measurement of identified particle spectra in d+Au collisions would be helpful to understand the initial Cold Nuclear Matter (CNM) effects such as Cronin effect, shadowing and gluon saturation. The Cronin effect [1], the enhancement of yields of hadrons at intermediate p_T in p+A collisions as compared to those in p+p collisions, has received renewed interest at RHIC. It is thought that this effect may reflect on the early parton scatterings in high energy nuclear collisions. It is also observed that the Cronin effect is more prominent for protons compared to pions [1, 2]. However, the particle species dependence of Cronin effect in p+A collisions is not well understood. We study the nuclear modification factor of the ϕ meson along with π, K and p in order to differentiate between mass and particle species ordering. The ϕ meson is very useful because it is a meson with mass close to that of light baryons. It also provides important information on strangeness enhancement in nucleus-nucleus collisions relative to p+p collisions due to its hidden strangeness. The study of particle production in d+Au collisions in forward and backward rapidities will help in constraining the various particle production models based on initial multiple partonic scattering, nuclear shadowing, parton saturation, recombination and energy loss in cold nuclear matter [3]. In order to further investigate these observations, and shed light on the initial conditions at RHIC, our goal is to analyze the p_T and rapidity dependence of various identified hadron production in d+Au collisions at RHIC.

3.2 ϕ Meson Production in d+Au Collisions

3.2.1 Data Set and Analysis Cuts

The data set used in the presented analysis are from d+Au collisions at $\sqrt{s_{NN}} = 200$ GeV taken in the year 2008 using the STAR [4] detector at RHIC. This data set is taken with a minimum bias trigger. The trigger detectors used are the Zero Degree Calorimeter (ZDC) [5] and Vertex Position Detector (VPD) [6]. A minimum bias trigger was defined by requiring at least one beam-rapidity neutron in the Au beam outgoing direction depositing energy in the East Zero Degree Calorimeter (ZDCE), which is assigned negative pseudorapidity (η). It additionally requires an online vertex Z cut of ± 30 cm from VPD. The VPD determines the vertex Z position by measuring the time difference between the signals detected at its east and west positions. It has low efficiency in triggering peripheral events compared to central events and it's online vertex Z resolution is worse for peripheral events relative to the central ones. This leads to a trigger bias for peripheral events and brings difficulties for centrality determination, which will be discussed in more detail later in this chapter.

3.2.2 Event Selection

The analyzed events were required to have a primary vertex Z position, V_z, within ± 30 cm from the center of the TPC along the beam line. The primary vertex for each minimum bias event is determined by finding the best point of common origin of the tracks measured in the TPC. This value was chosen to ensure nearly uniform detector acceptance because the events with primary vertex, far away from the TPC center, have a significantly non-uniform acceptance. The V_z distribution from run 8 d+Au collisions at $\sqrt{s_{NN}} = 200$ GeV is shown in Fig. 3.1.

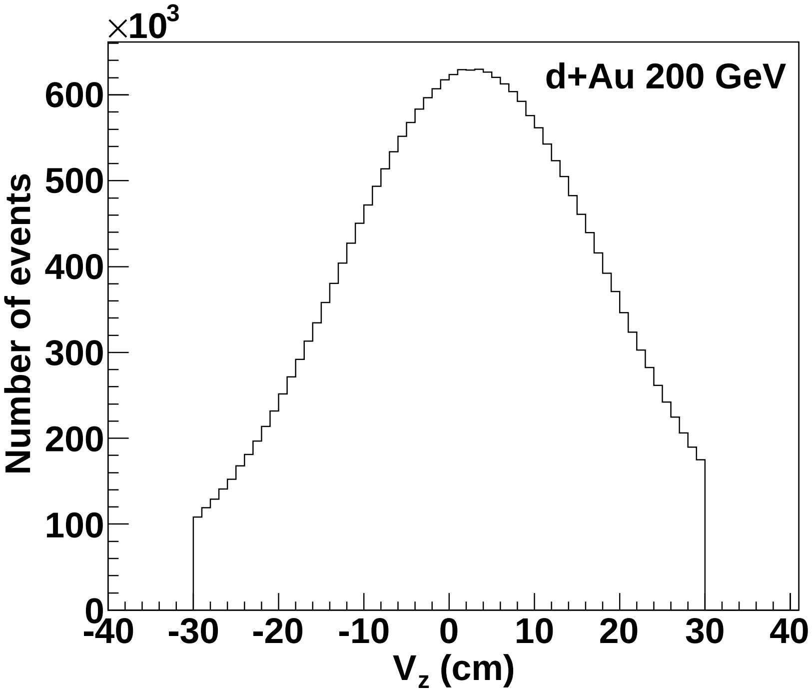

Figure 3.1: Event-by-event distribution of the Z-position of the primary vertex (V_z) in d+Au collisions at $\sqrt{s_{NN}}$ = 200 GeV.

3.2.3 Centrality Selection

The collision centralities represent the fractions of the full cross section in a collision. In d+Au collisions, centralities are selected based on the charged particle multiplicity measured in the East Forward Time Projection Chamber (FTPCE) [7] within the pseudorapidity range of $-3.8 < \eta \leq -2.8$. The reason to use the FTPC multiplicity instead of the TPC mid-rapidity multiplicity for centrality selection is to avoid autocorrelation between centrality and the measurements of charged particles in the TPC. In run 8, the FTPC data are studied carefully because it had a number of non-functional readout (RDO) boards, which changed over time, and it also had serious pile-up effect due to the higher luminosity (reflected in higher coincidence rate for ZDCs) [8]. In a high luminosity environment, there are two or more nucleus-nucleus collisions recorded as a single event, which is called pile-up effect. After extensive tests it has been found that the standard $RefMult$ from east FTPC is not so stable as a function of beam luminosity. The standard $RefMult$ from east FTPC is defined as the uncorrected charged particle multiplicity measured in the FTPC in the pseudorapidity region $-3.8 < \eta \leq -2.8$ with distance of closest approach (dca) less than 3 cm from the primary vertex position and at least 6 hits out of 11 maximum hits ($6 \leq nHitsFit \leq 11$) in the FTPC including the primary vertex. Additionally, the transverse momentum is required to not exceed 3 GeV/c because of the reduced momentum resolution and a significant background contamination at high p_T [7]. So to get a stable multiplicity distribution from east FTPC we need to use the cuts listed in Table 3.1. Here $nBEMCmatch$ represents the number of tracks used in the vertex finding with matching BEMC hits. This cut is used to reject pile-up vertices. The $nFTPCERefMult$ is the number of uncorrected charged particles measured from east FTPC. The flag of a track is used to record the status of the track fitting at the track reconstruction stage. It is required to be greater than 0 to avoid tracks with bad fitting and smaller than 1000 to reject Post Crossing Tracks (PCTs). The Post Crossing Tracks crossed the central membrane of the TPC after the event was triggered, so these are pile-up tracks.

In run 8 d+Au collisions, there is a strong run number (time) dependence of east FTPC multiplicity due to dead RDO boards in the FTPC during the data taking. The day dependence of mean multiplicity from east FTPC is shown in the left panel

Table 3.1: Selection criteria to get a stable charged particle multiplicity distribution from east FTPC for centrality determination in run 8 d+Au collisions at $\sqrt{s_{NN}} =$ 200 GeV.

Event cuts	**Track cuts**
$\lvert V_z \rvert < 30$ cm	$-3.8 < \eta \leq -2.8$
$nBEMCmatch \geq 1$	$0 < flag < 1000$
$nFTPCERefMult > 0$	$6 \leq nHitsFit \leq 11$
	$p_T < 3$ GeV/c
	$dca < 2$ cm

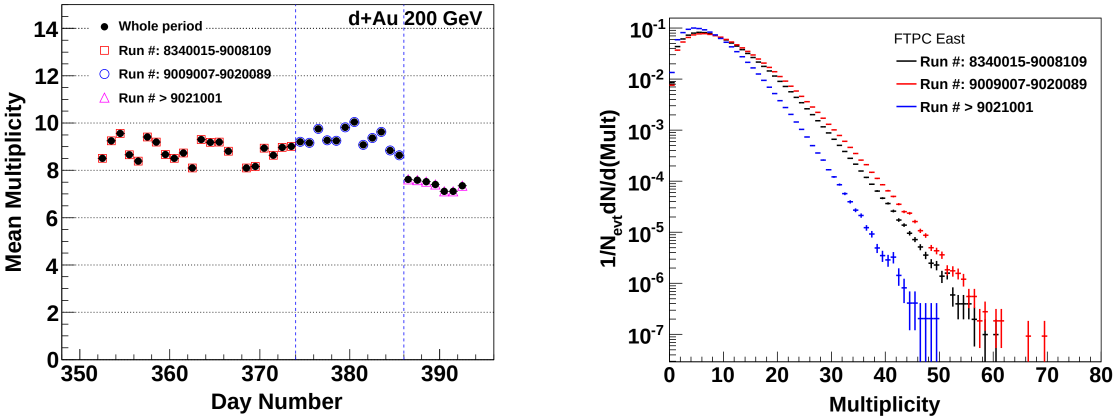

Figure 3.2: Left panel: Mean multiplicity from east FTPC as a function of day number in d+Au collisions at $\sqrt{s_{NN}} = 200$ GeV. Right panel: Multiplicity distributions from east FTPC for three different run periods in d+Au collisions at $\sqrt{s_{NN}} = 200$ GeV.

Table 3.2: Centrality definitions in run 8 d+Au collisions at $\sqrt{s_{NN}} = 200$ GeV using the multiplicity from east FTPC.

% cross section	$RunP1$ $(8340015 - 9008109)$	$RunP2$ $(9009007 - 9020089)$	$RunP3$ (> 9021001)
0-20	$M_{FTPCE} > 10$	$M_{FTPCE} > 10$	$M_{FTPCE} > 8$
20-40	$6 < M_{FTPCE} \leq 10$	$6 < M_{FTPCE} \leq 10$	$4 < M_{FTPCE} \leq 8$
40-100	$M_{FTPCE} \leq 6$	$M_{FTPCE} \leq 6$	$M_{FTPCE} \leq 4$

of Fig. 3.2. The right panel shows the variation of the east FTPC multiplicity distribution for three different run periods. The shape of the multiplicity distributions for three different run periods are different, so the centrality determination has been done for each run period independently. There is also a strong V_z dependence of mean multiplicity for each run period. This V_z dependent bias in multiplicity distribution require a re-weighting correction to be applied as a function of V_z in 2 cm bins for each run period. A Monte Carlo based Glauber model is generally used to simulate the multiplicity distribution and to calculate geometrical quantities in the initial state of nucleus-nucleus collisions. In run 8 d+Au collisions, Monte Carlo Glauber simulation has been done for three different run periods using the east FTPC multiplicity distribution for $0 < V_z < 2$ cm as shown in the Fig. 3.3. The various centrality bins are calculated as a fraction of this simulated multiplicity distribution starting from the highest multiplicities. Table 3.2 lists the east FTPC multiplicity values for each centrality in run 8 d+Au collisions at $\sqrt{s_{NN}} = 200$ GeV. The initial geometric quantities such as the average number of participating nucleons ($\langle N_{part} \rangle$), the average number of binary collisions ($\langle N_{coll} \rangle$) and the average impact parameter ($\langle b \rangle$) for each centrality are listed in Table 3.3. The errors shown here are statistical only. The $\langle N_{part} \rangle$, $\langle N_{coll} \rangle$ and $\langle b \rangle$ have been obtained from Monte Carlo Glauber calculations.

3.2.4 Track Selection

The tracks used in the present analysis are primary tracks which means the primary vertex is included as one of the fit point for track reconstruction. To ensure optimal particle identification and momentum resolution, various quality cuts are required to be applied to each track measured in the TPC. The track quality cuts for ϕ meson

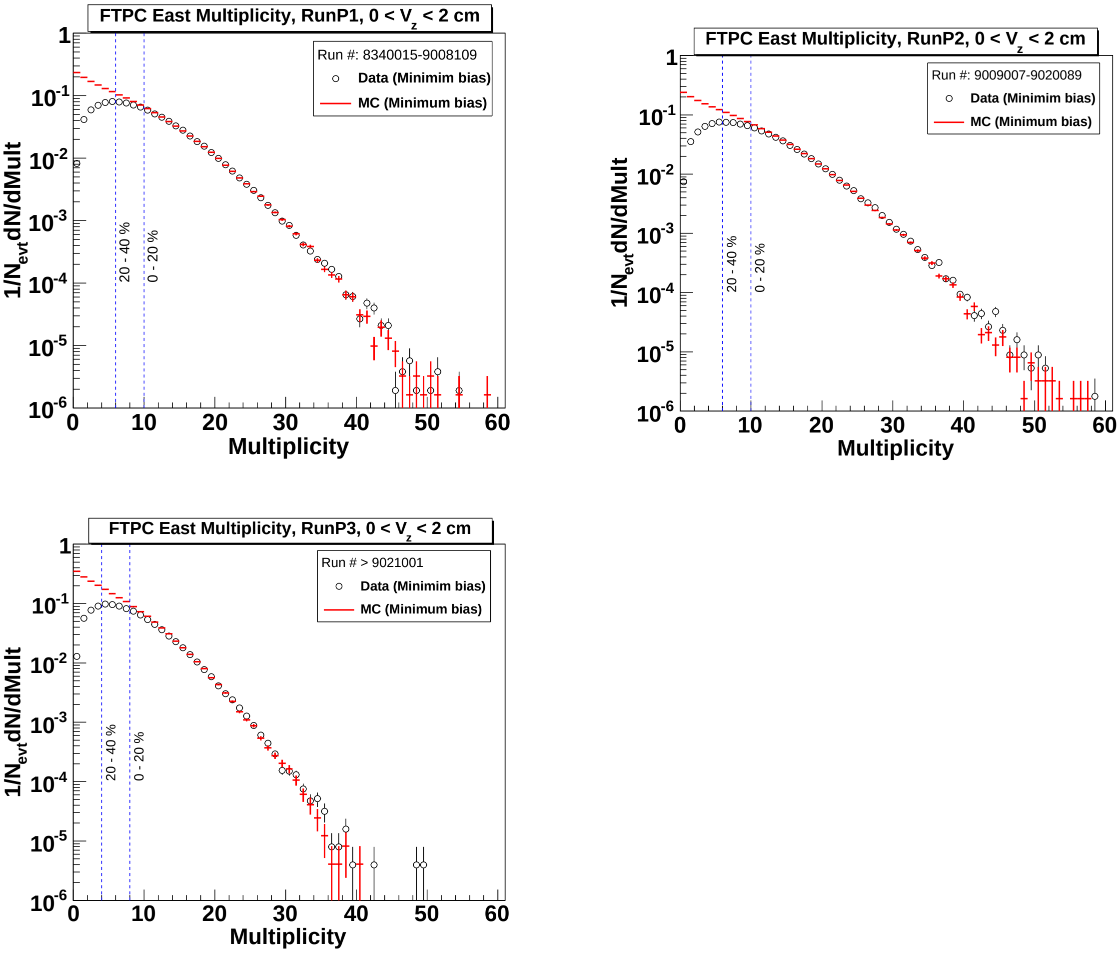

Figure 3.3: The multiplicity distributions from east FTPC (black circles) and the simulated multiplicity distributions using Monte Carlo Glauber calculation (red lines) for three different run periods in d+Au collisions at $\sqrt{s_{NN}}$ = 200 GeV. Both the multiplicity distributions are normalized for multiplicity greater than 15 for each run period.

Table 3.3: Initial geometric quantities for various collision centrality in run 8 d+Au collisions at $\sqrt{s_{NN}}$ = 200 GeV.

% cross section	$\langle N_{part} \rangle$	$\langle N_{coll} \rangle$	$\langle b \rangle$ (fm)
0-20	15.218 ± 0.006	14.591 ± 0.007	3.57 ± 0.002
20-40	11.365 ± 0.006	10.752 ± 0.006	4.571 ± 0.002
40-100	5.646 ± 0.003	4.752 ± 0.003	6.652 ± 0.002

Table 3.4: Track selection criteria for the ϕ meson study in run 8 d+Au collisions at $\sqrt{s_{NN}} = 200$ GeV.

Cut Description	**Value**
$\lvert\eta\rvert$	< 1.0
dca	< 3 cm
$nHitsFit$	≥ 15
$nHitsFit/nHitsPoss$	> 0.52 and < 1.02
Transverse Momentum	$0.15 < p_T < 12$ GeV/c
Momentum	$0.15 < p < 12$ GeV/c
Track Fitting Flag	$0 < flag < 1000$
χ^2	< 6
$n\sigma$ cut on dE/dx	$\lvert n\sigma_K\rvert < 2$

study are presented in Table 3.4. In order to have uniform detector performance, a pseudorapidity cut of $|\eta| < 1.0$ is applied in the data. To avoid admixture of tracks from secondary vertices, a constraint is imposed on the distance of closest approach (dca) between each track and the event vertex. In order to ensure good track momentum resolution, short tracks are avoided by requiring all tracks to have a minimum number of 15 fit points in the reconstruction of the track. The effect of track splitting is minimized by requiring that the number of fit points is more than half the number of total possible hit points for a track. Tracks can have a maximum of 45 hits in the TPC. The low momentum tracks ($p_T \leq 0.15$ GeV/c) can not traverse the entire TPC due to their large track curvature inside the solenoidal magnetic field. So, those tracks are avoided by requiring all tracks to have p_T and p greater than 0.15 GeV/c. The flag of a track is required to be greater than 0 to avoid tracks with bad fitting and smaller than 1000 to reject pile-up tracks. In order to further remove pile-up tracks, a requirement is placed on the χ^2 of the primary tracks. Since pile-up tracks do not belong to the primary vertex, the χ^2 of the fit to their hit points including the vertex is larger than that of tracks belonging to the primary vertex. The maximum allowed χ^2 of primary tracks is taken to be less than 6 as obtained by studying the stability of mean multiplicity as a function of beam luminosity as illustrated in Fig. 3.4.

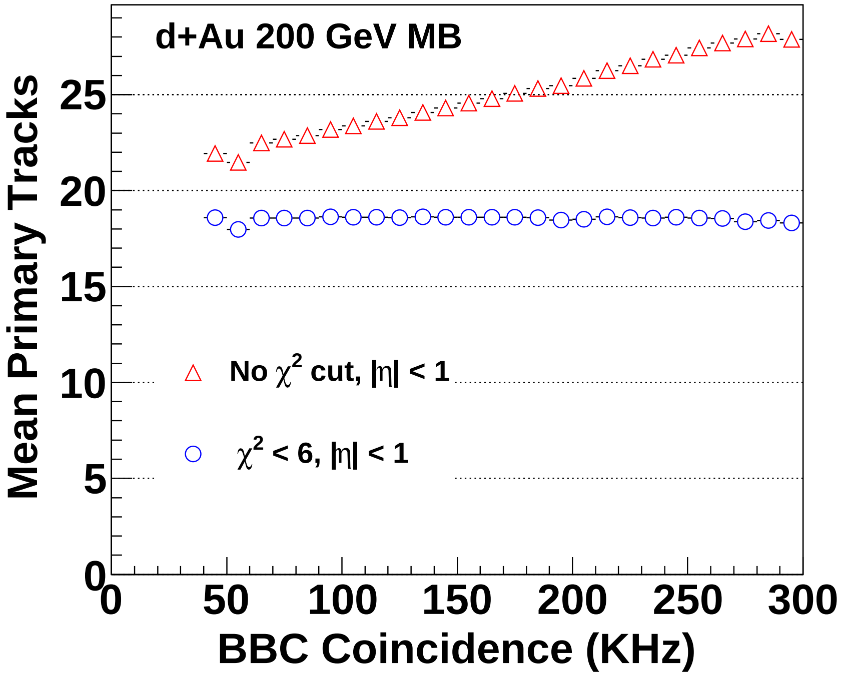

Figure 3.4: Number of primary tracks in TPC with $\chi^2 < 6$ (open circle) and without χ^2 cut (open triangles) as a function of BBC coincidence rate in d+Au collisions at $\sqrt{s_{NN}} = 200$ GeV.

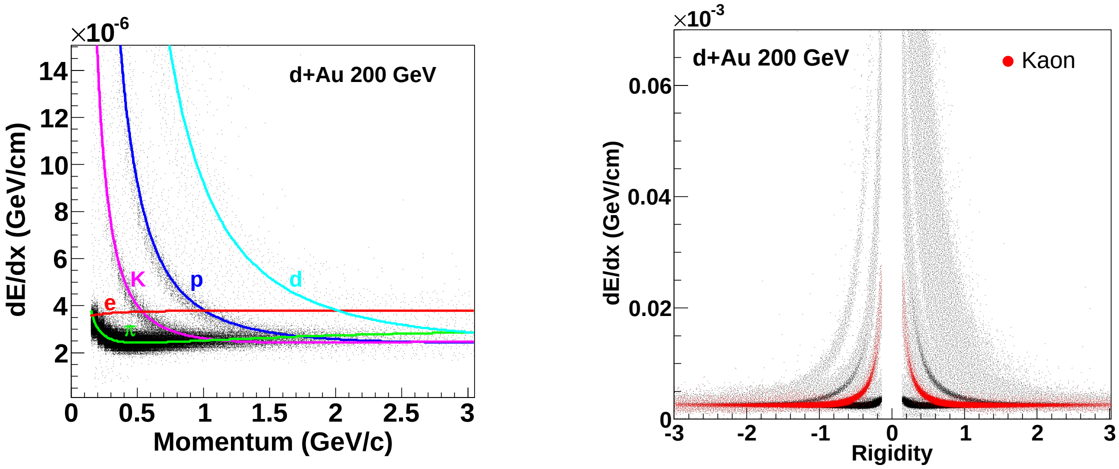

Figure 3.5: Left panel: TPC dE/dx as a function of momentum for charged tracks in d+Au collisions at $\sqrt{s_{NN}} = 200$ GeV. Different color lines are expected dE/dx values for different charged tracks as predicted by the Bichsel function [11]. Right Panel: TPC dE/dx as a function of rigidity for charged tracks. Selected kaon candidates are shown in red bands.

In this analysis, ϕ mesons are measured through the decay channel $\phi \rightarrow K^+K^-$ (branching ratio $= 49.2 \pm 0.6\%$) [9]. As has been mentioned earlier the TPC provides particle identification and momentum information of the charged particles by measuring their ionization energy loss (dE/dx) [10]. The left panel of Fig. 3.5 shows the dE/dx of charged tracks as a function of momentum measured by the TPC. The expected dE/dx values for different particles as predicted by the Bichsel function [11] are shown in different color lines. A charged track in the TPC is accepted as a kaon candidate if its dE/dx value falls within 2 standard deviations ($|n\sigma_K| < 2$) of the predicted value by Bichsel function for kaons in the TPC gas. The right panel of Fig. 3.5 shows the dE/dx of charged tracks as a function of rigidity (= momentum/charge). The selected kaon candidates are shown in red bands.

3.2.5 ϕ Meson Reconstruction and Raw Yield Extraction

After selecting the K^+ and K^- samples, the ϕ meson was reconstructed by calculating the invariant mass (m_{inv}) for all possible K^+K^- pairs in an event. Since not all charged kaons in an event originate from ϕ meson decays, the ϕ meson signal reconstructed this way sits on top of a large combinatorial background. Therefore, one must subtract the large combinatorial background from the resulting same-event invariant mass distribution to observe the ϕ meson signal. An event-mixing technique [12, 13] was applied to calculate the combinatorial background from the uncorrelated K^+K^- pairs, where the invariant mass was calculated by pairing two kaons from two different events with same primary vertex and multiplicity bins (mixed-event). The data sample was divided into 3 bins in multiplicity and 4 bins in collision vertex position, V_z, along the beam direction. The pairs from events with similar multiplicity and V_z were selected for mixing. These requirements ensure that the two events used in mixing have similar event structure, so the mixed-event invariant mass distribution can better represent the combinatorial background in the same-event invariant mass distribution. In order to reduce statistical uncertainty in the mixed-event, each event was mixed with 20 other events.

To extract the ϕ meson signal, first the mixed-event and the same-event K^+K^- invariant mass distributions were accumulated, and the mixed-event distribution was normalized to the same-event distribution in the ϕ mass region by employing an iterative scaling procedure [14]. In this normalization method, the background distribution was scaled by the ratio of the integral of the signal to the integral of the background distribution in a fixed invariant mass region including the ϕ mass peak ($0.99 < m_{inv} < 1.05$ GeV/c^2). The background distribution was then subtracted from the signal distribution and the remaining signal was fitted with a Breit-Wigner function plus a straight line. The signal integral was then set to be the signal integral in the ϕ mass range minus the integral of the Breit-Wigner function, the ratio was recalculated and the background rescaled. Six iterations were needed to stabilize the final scaling factor. Then the normalized mixed-event invariant mass distribution was subtracted from the same-event invariant mass distribution in each p_T and y (rapidity) bin for every collision centrality.

Although the mixed-event background gives a good estimation of the combinatorial background due to uncorrelated kaon pairs, it cannot account for the real correlated background from decay pairs due to Coulomb interactions, photon conversions ($\gamma \to e^+e^-$) and particle decays such as $K^{0*} \to K^+\pi^-$, $\rho^0 \to \pi^+\pi^-$, $K^0_S \to \pi^+\pi^-$, and $\Lambda \to p\pi^-$. For example, when both pions from a K^0_S decay are misidentified as kaons, the real correlation from decay will remain in the same-event as a broad distribution but will not be reproduced by the event-mixing method.

Due to overlap of dE/dx bands for kaons and electrons around $p = 0.5$ GeV/c, the electrons/positrons are misidentified as kaons in this momentum range. This leads to a residual background in the K^+K^- invariant mass distribution near the threshold from correlated e^+e^- pairs, mainly from photon conversions ($\gamma \rightarrow e^+ + e^-$). The δ-dip-angle between the photon converted electron and positron is usually very small. The δ-dip-angle is calculated from

$$\delta\text{–}dip\text{–}angle = cos^{-1}[\frac{p_{T1}p_{T2} + p_{z1}p_{z2}}{p_1 p_2}], \tag{3.1}$$

where p_1, p_2 represent the momenta of the two tracks, the other parameters with subscripts T and z representing the transverse and the longitudinal components, respectively. This δ-dip-angle represents the opening angle of a pair in the p_z-p_T plane. We required the δ-dip-angle to be greater than 0.04 radians for the kaon candidate pairs. This cut is very effective in removing the photon conversion background. Figure 3.6 shows the K^+K^- invariant mass distributions from same-event (blue line) and mixed-event (red line) in 0-20% d+Au collisions at $\sqrt{s_{NN}} = 200$ GeV. Here, the ϕ meson peak is clearly visible before background subtraction.

After subtracting the scaled mixed-event background distributions from the same-event K^+K^- invariant mass distributions, the remaining distribution consists of the ϕ mass peak plus some residual background. To determine the raw yields for ϕ meson, this distribution is fitted with a Breit-Wigner function superimposed on a linear background function

$$\frac{dN}{dM_{inv}} = \frac{A\Gamma}{(M_{inv} - m_0)^2 + \Gamma^2/4} + B(M_{inv}), \tag{3.2}$$

where A is the area under the peak corresponding to the number of ϕ mesons, Γ is the full width at half maximum (FWHM) of the peak, and m_0 is the resonance mass position. $B(M_{inv})$ denotes a linear $[B(M_{inv}) = p_0 + p_1 M_{inv}]$ residual background function. The parameters p_0 and p_1 of $B(M_{inv})$ and A, m_0 and Γ are free parameters in this fitting. The mixed-event background subtracted invariant mass distributions for different p_T bins in 0-20% d+Au collisions are shown in the Fig. 3.7.

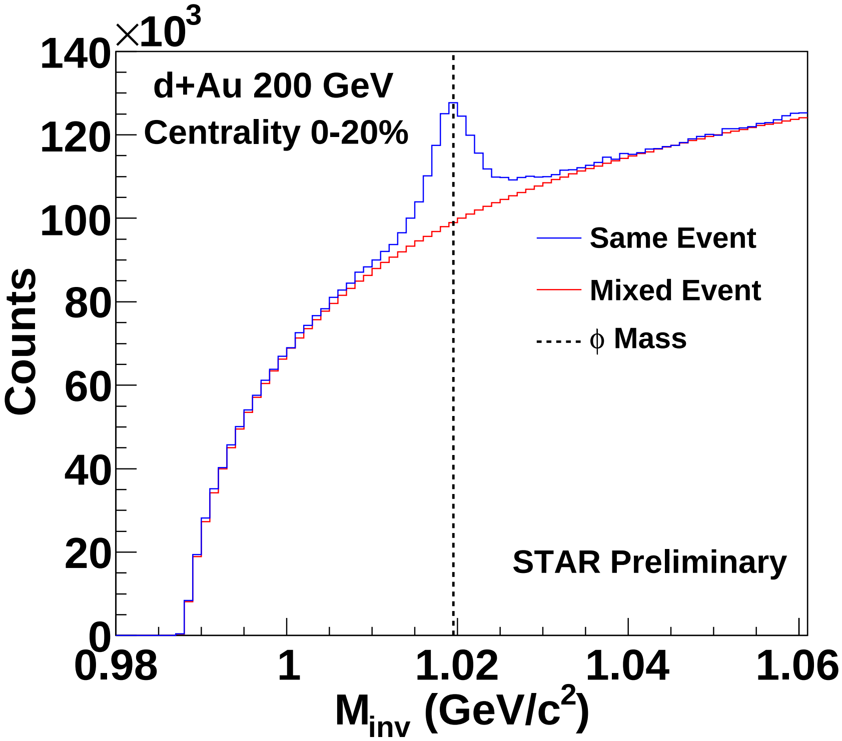

Figure 3.6: Same-event (blue line) and mixed-event (red line) K^+K^- invariant mass distributions in 0-20% d+Au collisions at $\sqrt{s_{NN}} = 200$ GeV. ϕ meson mass from PDG is shown in black dotted lines [9].

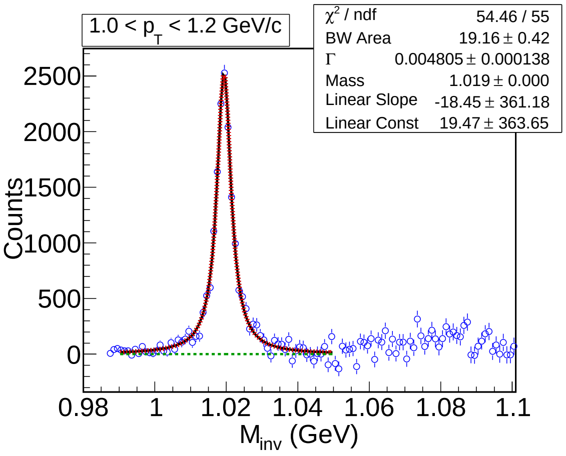
1.0 < p_T < 1.2 GeV/c
χ² / ndf 54.46 / 55
BW Area 19.16 ± 0.42
Γ 0.004805 ± 0.000138
Mass 1.019 ± 0.000
Linear Slope -18.45 ± 361.18
Linear Const 19.47 ± 363.65
Counts
2500
2000
1500
1000
500
0
0.98
1
1.02
1.04
1.06
1.08
1.1
M_inv (GeV)

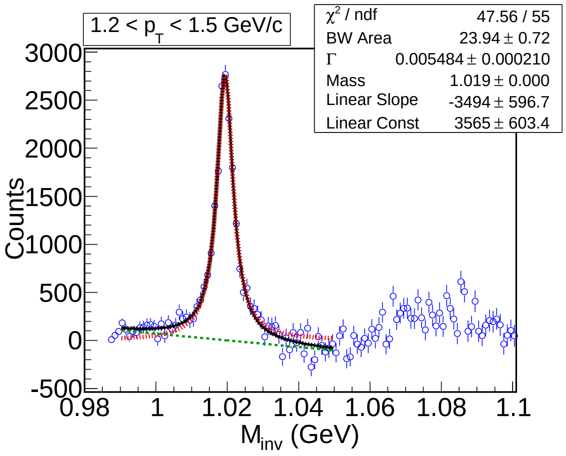
1.2 < p_T < 1.5 GeV/c
χ² / ndf 47.56 / 55
BW Area 23.94 ± 0.72
Γ 0.005484 ± 0.000210
Mass 1.019 ± 0.000
Linear Slope -3494 ± 596.7
Linear Const 3565 ± 603.4
Counts
3000
2500
2000
1500
1000
500
0
-500
0.98
1
1.02
1.04
1.06
1.08
1.1
M_inv (GeV)

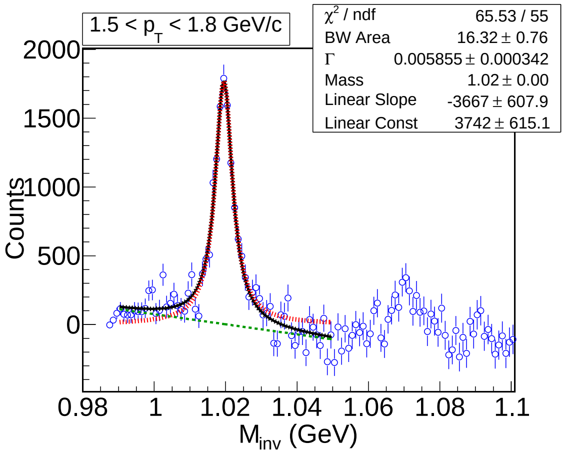
1.5 < p_T < 1.8 GeV/c
χ² / ndf 65.53 / 55
BW Area 16.32 ± 0.76
Γ 0.005855 ± 0.000342
Mass 1.02 ± 0.00
Linear Slope -3667 ± 607.9
Linear Const 3742 ± 615.1
Counts
2000
1500
1000
500
0
0.98
1
1.02
1.04
1.06
1.08
1.1
M_inv (GeV)

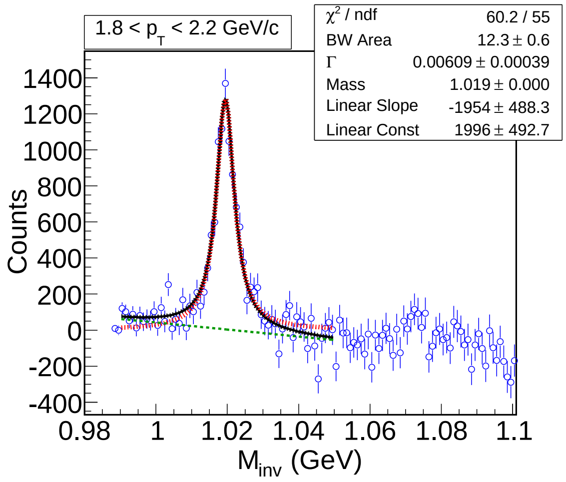
1.8 < p_T < 2.2 GeV/c
χ² / ndf 60.2 / 55
BW Area 12.3 ± 0.6
Γ 0.00609 ± 0.00039
Mass 1.019 ± 0.000
Linear Slope -1954 ± 488.3
Linear Const 1996 ± 492.7
Counts
1400
1200
1000
800
600
400
200
0
-200
-400
0.98
1
1.02
1.04
1.06
1.08
1.1
M_inv (GeV)

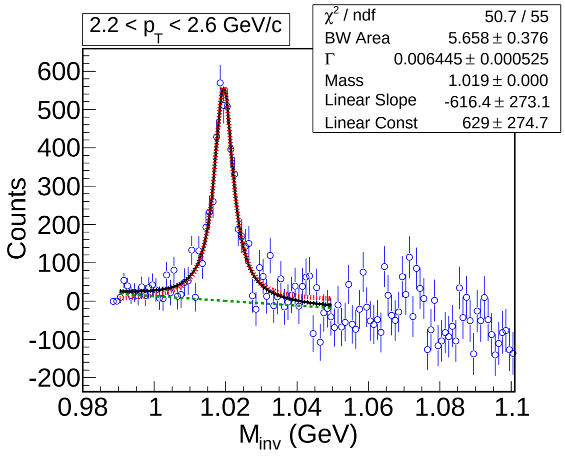
2.2 < p_T < 2.6 GeV/c
χ² / ndf 50.7 / 55
BW Area 5.658 ± 0.376
Γ 0.006445 ± 0.000525
Mass 1.019 ± 0.000
Linear Slope -616.4 ± 273.1
Linear Const 629 ± 274.7
Counts
600
500
400
300
200
100
0
-100
-200
0.98
1
1.02
1.04
1.06
1.08
1.1
M_inv (GeV)

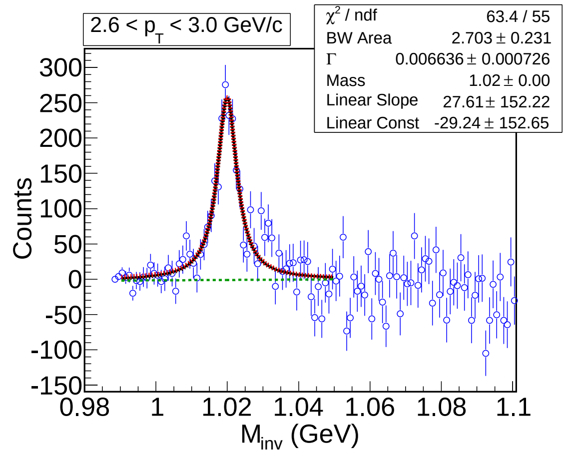
2.6 < p_T < 3.0 GeV/c
χ² / ndf 63.4 / 55
BW Area 2.703 ± 0.231
Γ 0.006636 ± 0.000726
Mass 1.02 ± 0.00
Linear Slope 27.61 ± 152.22
Linear Const -29.24 ± 152.65
Counts
300
250
200
150
100
50
0
-50
-100
-150
0.98
1
1.02
1.04
1.06
1.08
1.1
M_inv (GeV)

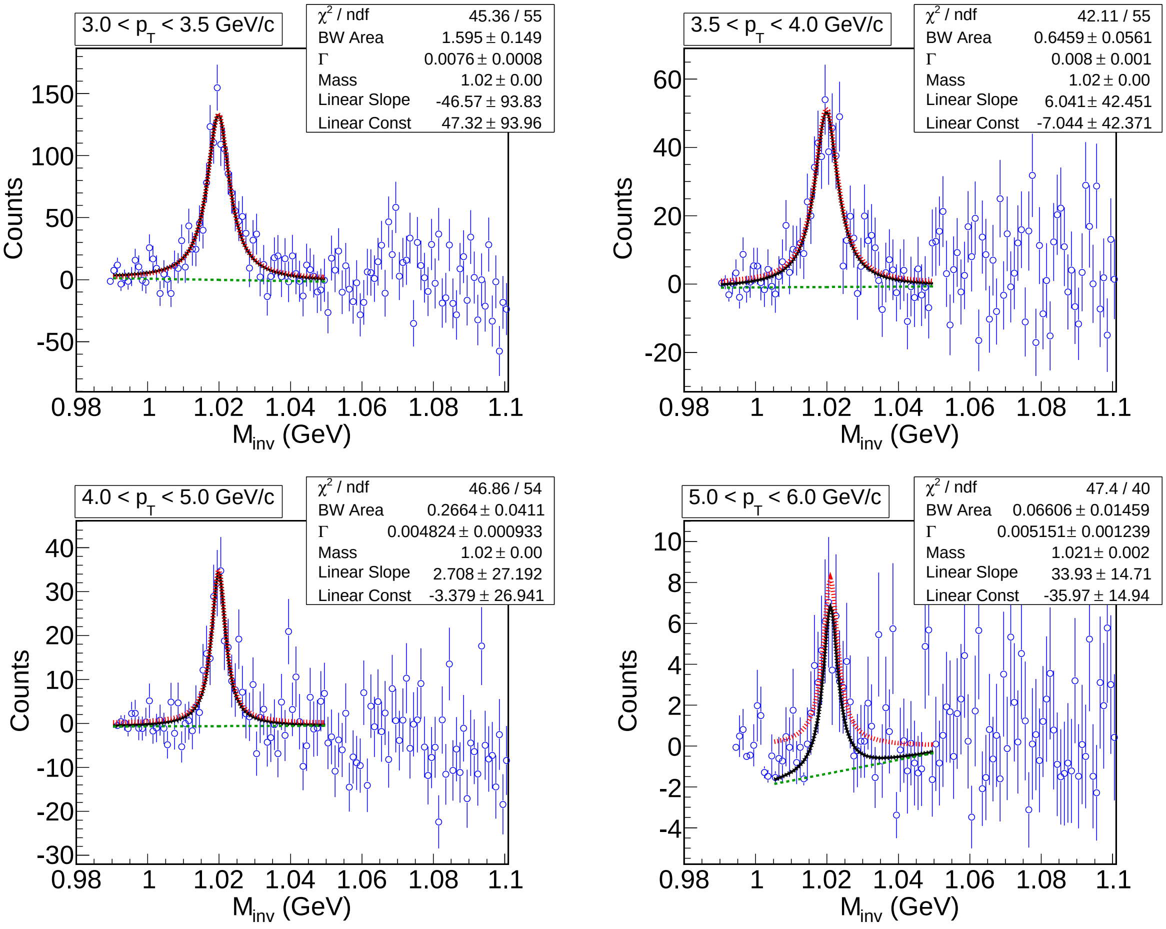

Figure 3.7: The ϕ meson mass peaks after subtracting the background for different p_T bins in 0-20% d+Au collisions at $\sqrt{s_{NN}} = 200$ GeV. Black curves show a Breit-Wigner + linear background function fit. Red curves and Green lines stand for a Breit-Wigner function and a linear function, respectively.

3.2.6 Efficiency and Acceptance Correction

The raw ϕ meson yields, as obtained for various p_T bins, need to be corrected for detector acceptance and tracking efficiency. The ϕ meson acceptance and reconstruction efficiency are calculated using an embedding technique, in which Monte Carlo (MC) simulated tracks are embedded into real events. One simulated ϕ meson track is embedded for each event. The ϕ meson decay ($\phi \rightarrow K^+K^-$) and the detector response are simulated by the GEANT program package [15] and the simulated output signals are embedded into real events before being processed by the standard STAR event reconstruction code. Embedded data are then analyzed to reconstruct the ϕ meson. A ϕ meson is counted as being reconstructed if both its decay daughters are reconstructed by the track reconstruction code and passes all analysis cuts that are applied in the real data analysis. As the first step in reconstructing the input ϕ mesons, we need to identify the reconstructed primary tracks which are associated to the input MC kaons in the embedding events. This process of matching or associating the reconstructed information of decay daughters of ϕ meson with the MC information is called Association. A cut of 10 common hit points was applied on the number of common hit points in the TPC between reconstructed and the input simulated tracks. The decay daughter kaons of Monte Carlo ϕ meson are also subjected to the same cuts that are applied in the real data analysis. The tracking efficiencies and detector acceptance (tracking efficiency × acceptance) is then calculated by dividing the number of reconstructed ϕ mesons by the number of input ϕ mesons. Figure 3.8 shows the efficiency×acceptance for our analysis as a function of ϕ meson p_T in minimum bias d+Au collisions at $\sqrt{s_{NN}} = 200$ GeV. The reconstruction efficiency slightly decreases at high p_T due to the δ-dip-angle cut used in the analysis.

3.2.7 Results and Discussion

3.2.7.1 Transverse Momentum Spectra

The differential invariant yield of ϕ meson is calculated by correcting the extracted raw yield by tracking efficiency, detector acceptance, $n\sigma$ cut efficiency and the decay branching ratio of ϕ to charged kaons. Figure 3.9 shows the ϕ meson transverse momentum spectrum at mid-rapidity ($|y| < 0.5$) in 0-20% d+Au collisions at $\sqrt{s_{NN}}$

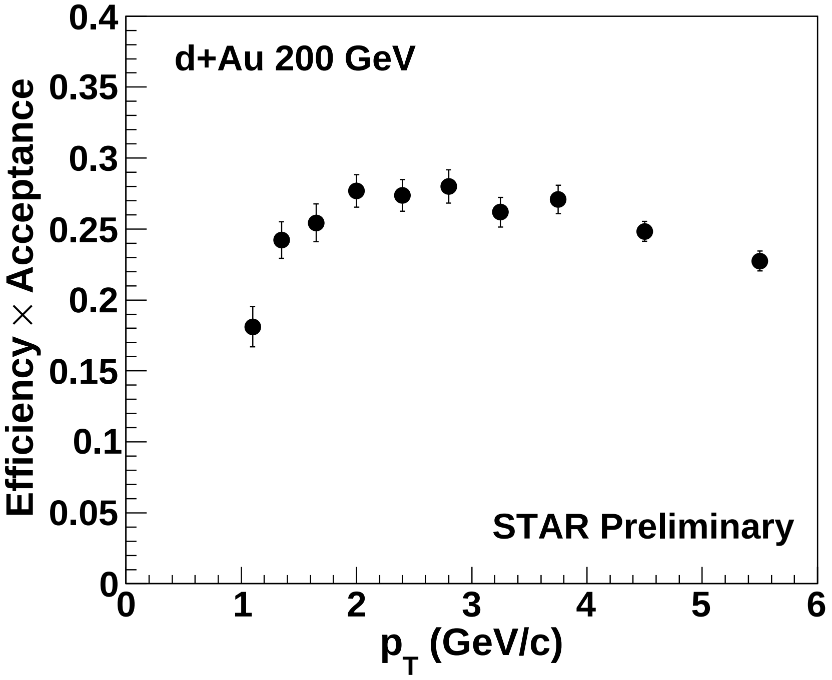

Figure 3.8: Reconstruction efficiency including acceptance of ϕ meson as a function of p_T in minimum bias d+Au collisions at $\sqrt{s_{NN}} = 200$ GeV.

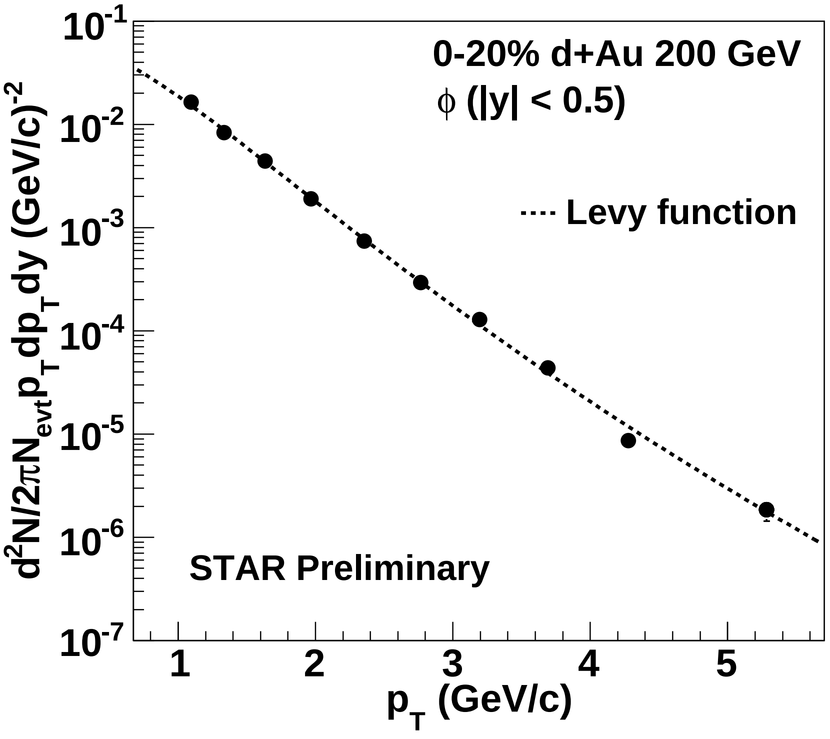

Figure 3.9: ϕ meson transverse momentum spectrum in 0-20% d+Au collisions at $\sqrt{s_{NN}} = 200$ GeV. The dotted curve represents the Levy function fit to the distribution. Errors are statistical only.

= 200 GeV. The dotted curve in Fig. 3.9 is the Levy function fit of the form:

$$\frac{1}{2\pi p_T}\frac{d^2N}{dp_T dy} = \frac{dN/dy(n-1)(n-2)}{2\pi n T_{Levy}(nT_{Levy} + m_0(n-2))} \times (1 + \frac{m_T - m_0}{nT_{Levy}})^{-n}, \tag{3.3}$$

where n, the slope parameter T_{Levy}, and yield dN/dy are free parameters. The ϕ meson transverse momentum spectrum in 0-20% d+Au collisions is well described by a Levy function, due to the power-law tail at intermediate and high p_T [16]. The values of the fit parameters T_{Levy}, n and dN/dy as well as the χ^2/ndf of the Levy function fit are listed in Table 3.5. For comparison, the values of fit parameters and χ^2/ndf from fits to the p_T spectrum of ϕ meson for p+p, d+Au (run 3) and Au+Au collisions in different centralities at $\sqrt{s_{NN}} = 200$ GeV are also listed [16]. The difference in the values of the fit parameters T_{Levy}, n and dN/dy between run 8 and run 3 d+Au collisions may be due to the difference in p_T acceptances. In run 3, the p_T spectrum of ϕ meson has been studied for $0.4 < p_T < 6$ GeV/c, whereas in

Table 3.5: Values of fit parameters and χ^2/ndf from Levy function fit to the p_T spectrum of ϕ meson in 0-20% d+Au collisions at $\sqrt{s_{NN}}$ = 200 GeV. For comparison, the values of fit parameters and χ^2/ndf from fits to the p_T spectrum of ϕ meson for p+p, d+Au (run 3) and Au+Au collisions in different centralities at $\sqrt{s_{NN}}$ = 200 GeV are also listed [16]. Only statistical errors are shown.

System	Centrality	Fit Function	$T_{Exp/Levy}$ (MeV)	n	dN/dy	χ^2/ndf
d+Au 200 GeV (run 8)	0-20%	Levy	304 ± 16	18.0 ± 2.6	0.188 ± 0.012	10.15/12
p+p 200 GeV	0-100%	Levy	202 ± 14	8.3 ± 1.2	0.018 ± 0.001	10.1/10
d+Au 200 GeV (run 3)	0-20%	Levy	323 ± 20	15.5 ± 3.9	0.146 ± 0.005	4.7/11
	20-40%	Levy	316 ± 19	16.9 ± 4.7	0.103 ± 0.003	13.6/11
	40-100%	Levy	263 ± 15	12.2 ± 2.1	0.040 ± 0.001	12.4/11
	0-100% (MB)	Levy	297 ± 11	13.9 ± 1.8	0.071 ± 0.001	17.5/11
Au+Au 200 GeV	0-5%	Exp.	357 ± 3	-	7.95 ± 0.11	11.0/12
	0-10%	Exp.	359 ± 5	-	7.42 ± 0.14	10.2/12
	10-20%	Exp.	373 ± 4	-	5.37 ± 0.09	9.7/12
	20-30%	Exp.	387 ± 4	-	3.47 ± 0.06	26.7/12
	30-40%	Exp.	371 ± 4	-	2.29 ± 0.04	21.1/12
	40-50%	Levy	315 ± 11	22.7 ± 4.3	1.44 ± 0.03	17.4/11
	50-60%	Levy	290 ± 13	13.8 ± 1.9	0.82 ± 0.02	6.9/11
	60-70%	Levy	291 ± 13	18.6 ± 3.6	0.45 ± 0.01	7.4/11
	70-80%	Levy	243 ± 15	13.0 ± 2.3	0.20 ± 0.01	5.5/11

run 8 it has been studied for $1 < p_T < 6$ GeV/c due to pile-up issues at low p_T.

The left panel of Fig. 3.10 shows the comparison of ϕ meson p_T spectrum obtained from 0-20% d+Au collisions at $\sqrt{s_{NN}}$ = 200 GeV in the year 2008 (run 8) with the STAR published p_T spectrum from year 2003 (run 3) data [16]. The ϕ meson p_T spectrum for $p_T > 1$ GeV/c from run 8 is consistent with run 3 results within the statistical errors. The ratio of ϕ meson yield from run 8 and run 3 as a function of p_T is shown in the right panel of Fig. 3.10.

3.2.7.2 Nuclear Modification Factor

The measurement of the nuclear modification factor, R_{AB}, provides a sensitive tool to probe the production dynamics and hadronization process in relativistic heavy ion collisions [17, 18]. The variable R_{AB} corresponds to the ratio of the invariant yields of the produced particles in nucleus (A) + nucleus (B) collisions to those in inelastic p+p collisions scaled by the number of nucleon-nucleon binary collisions. It is defined

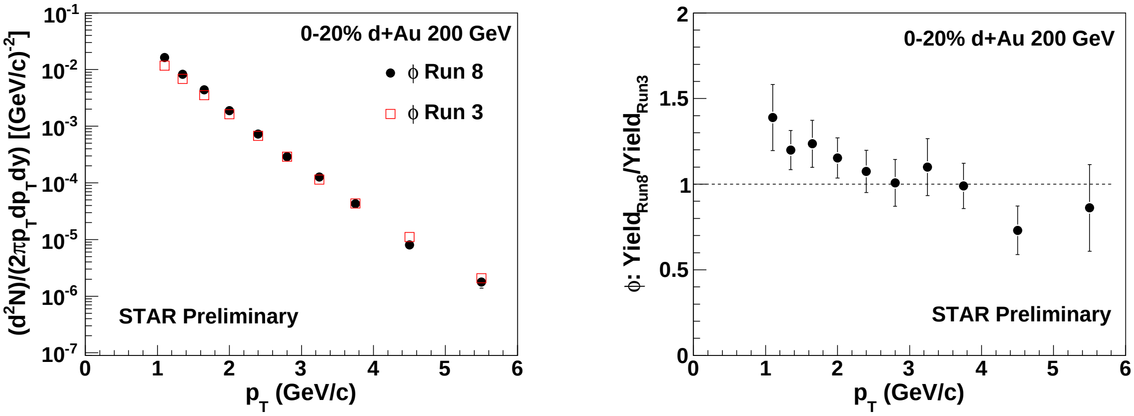

Figure 3.10: Left panel: ϕ meson transverse momentum spectrum in 0-20% d+Au collisions at $\sqrt{s_{NN}} = 200$ GeV from year 2008 (run 8) and year 2003 (run 3). Right panel: The ratio of ϕ meson yield from run 8 and run 3 as a function of transverse momentum.

as

$$R_{AB}(p_T) = \frac{d^2N^{AB}/dydp_T}{T_{AB} \cdot d^2\sigma^{pp}/dydp_T}, \tag{3.4}$$

where $T_{AB} = \langle N_{bin} \rangle / \sigma_{inel}^{pp}$ is the nuclear thickness function. $\langle N_{bin} \rangle$ is the average number of binary nucleon-nucleon inelastic collisions, as estimated from Glauber model calculations. The total inelastic cross section for p+p collisions at $\sqrt{s_{NN}} = 200$ GeV used in the Glauber model calculations is $\sigma_{inel} = 42$ mb. However, STAR only triggers on Non-Singly Diffractive (NSD) p+p events with measured cross section $\sigma_{NSD} = 30$ mb. Thus the NSD p+p spectrum was normalized to the inelastic yield by a correction factor of 30/42. We expect the $R_{AB}(p_T)$ to be unity if nucleus-nucleus collisions are just simple superpositions of nucleon-nucleon collisions at high p_T. Deviation of this ratio from unity would imply contributions from nuclear effects.

Figure 3.11 shows the p_T dependence of the nuclear modification factor R_{AB} in 0-20% d+Au and 0-5% Au+Au [16] collisions at $\sqrt{s_{NN}} = 200$ GeV. The R_{dAu} of ϕ meson increases above unity and is higher than R_{AuAu} at intermediate p_T. The enhancement of R_{dAu} of ϕ meson at the intermediate p_T is attributed to the Cronin effect [1, 2]. The Cronin enhancement may result either from momentum broadening due to multiple soft or semi-hard scattering in the initial state [19, 20, 21, 22] or from final state interactions as suggested in the recombination model [23]. These mechanisms lead to different particle type and/or mass dependence in the nuclear modification factors as

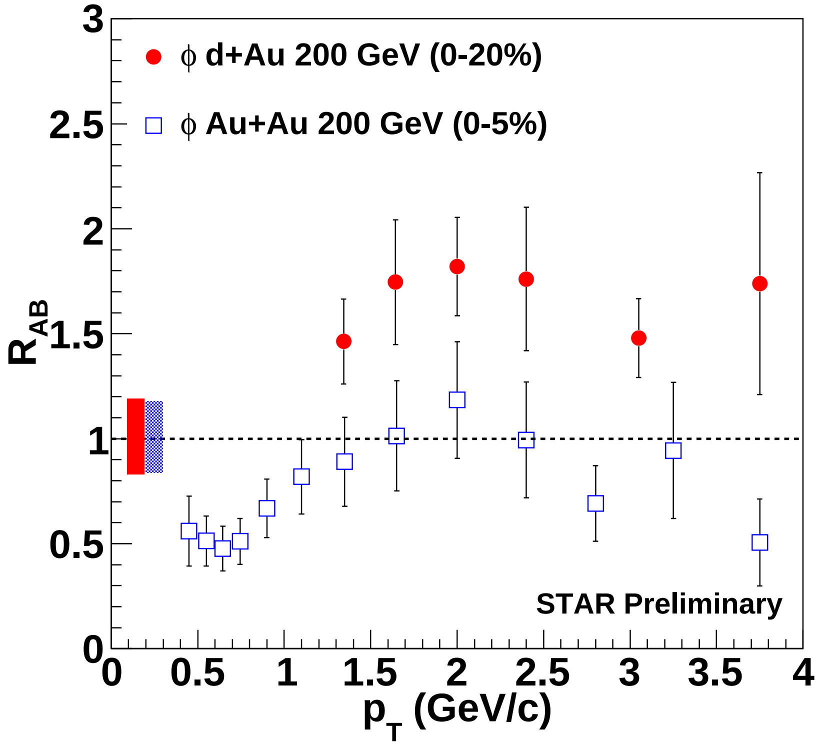

Figure 3.11: p_T dependence of the nuclear modification factor R_{AB} for ϕ meson in 0-20% d+Au and 0-5% Au+Au [16] collisions at $\sqrt{s_{NN}} = 200$ GeV. Errors are statistical only. The normalization uncertainties for 0-20% d+Au and 0-5% Au+Au collisions are shown in red and blue rectangular bands, respectively.

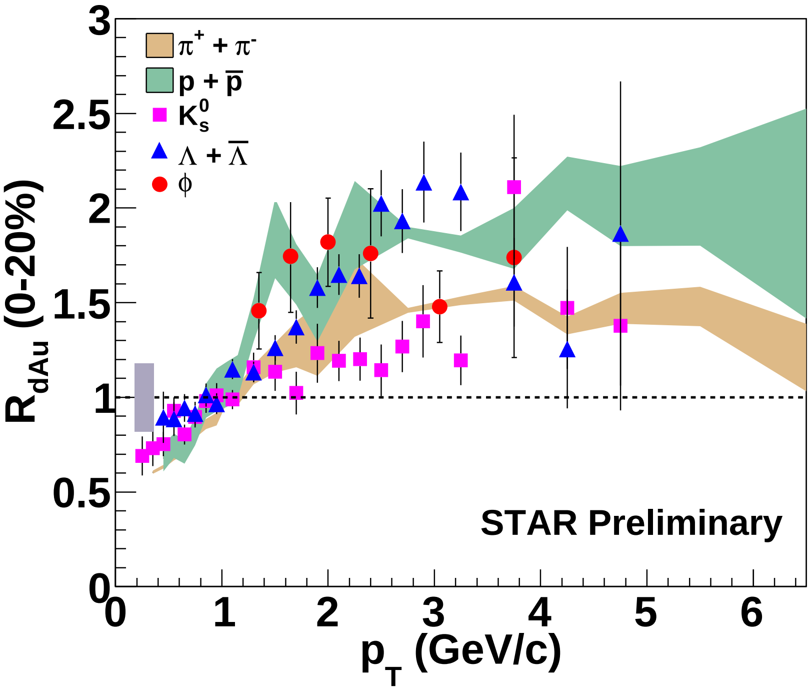

Figure 3.12: The nuclear modification factor R_{dAu} for ϕ meson as a function of p_T in 0-20% d+Au collisions at $\sqrt{s_{NN}} = 200$ GeV. The R_{dAu} for pions and protons are shown in brown and green bands, respectively [24]. The STAR preliminary data for K^0_S and $\Lambda + \bar{\Lambda}$ are taken from the Ref. [25]. Errors are statistical only. The gray shaded band represents the normalization uncertainty of 18%.

a function of p_T. To understand the particle production mechanism we have studied the particle species dependence of Cronin effect.

Figure 3.12 shows a comparison of R_{dAu} of ϕ meson with that of $\pi^+ + \pi^-$, $p + \bar{p}$, K^0_S and $\Lambda + \bar{\Lambda}$ [24, 25]. Due to large statistical uncertainties in R_{dAu} of ϕ meson, it is very difficult to differentiate particle dependence scenarios. We need high precision measurement of R_{dAu} to differentiate very well between different particles and particle production scenarios. However, the R_{dAu} of ϕ meson seems to follow the same for other mesons for $2.5 < p_T < 4$ GeV/c. This result favors coalescence as the mechanism for particle production at mid-rapidity and intermediate p_T in most central d+Au collisions.

3.2.7.3 Rapidity Asymmetry

In case of asymmetric systems such as d+Au collision, the particle production mechanism may be different at forward and backward rapidities. The partons from the deuteron-side (forward rapidity) are expected to undergo multiple scattering while traversing the gold nucleus, where as those on the gold-side (backward rapidity) are likely to be affected by the properties of the nucleus. A comparative study of particle production at forward and backward rapidity can be carried out using a ratio called the rapidity asymmetry (Y_{Asym}), which is defined as,

$$Y_{Asym}(p_T) = \frac{Y_B(p_T)}{Y_F(p_T)}, \tag{3.5}$$

where Y_F and Y_B are forward and backward particle yields, respectively. The Y_{Asym} may provide some information to determine the relative contributions of various physics processes to particle production in d+Au collisions.

Models based on Color Glass Condensate (CGC) [26, 27], HIJING [28], multiphase transport (AMPT) [29] and parton coalescence [30] predict specific rapidity and centrality dependence of produced particles. These models incorporating different physics process such as parton saturation, multiple scattering, nuclear shadowing and recombination of thermal partons have been able to describe qualitatively the pseudorapidity asymmetry for inclusive charged hadrons in d+Au collisions [31]. The Y_{Asym} of identified hadrons (π and p) in d+Au collisions has been able to provide some definitive insight on the particle production mechanism [32]. The present study is mainly focused on the particle type (baryon/meson) dependence of Y_{Asym} in d+Au collisions at $\sqrt{s_{NN}} = 200$ GeV.

Figure 3.13 shows the p_T dependence of Y_{Asym} for ϕ meson at $|y| < 0.5$ (left panel) and $0.5 < |y| < 1$ (right panel) in 0-20% d+Au collisions at $\sqrt{s_{NN}} = 200$ GeV. For comparison, the Y_{Asym} for $\pi^+ + \pi^-$ and $p + \bar{p}$ are also shown in the figure [32]. The Y_{Asym} for ϕ meson is greater than unity in the measured p_T region for both $|y| < 0.5$ and $0.5 < |y| < 1$. Similar to other hadrons, the Y_{Asym} for ϕ meson is found to be larger for $0.5 < |y| < 1$ than for $|y| < 0.5$. This may indicate the presence of some rapidity dependence of nuclear effects. No strong particle type dependence is observed for Y_{Asym} in the measured p_T region.

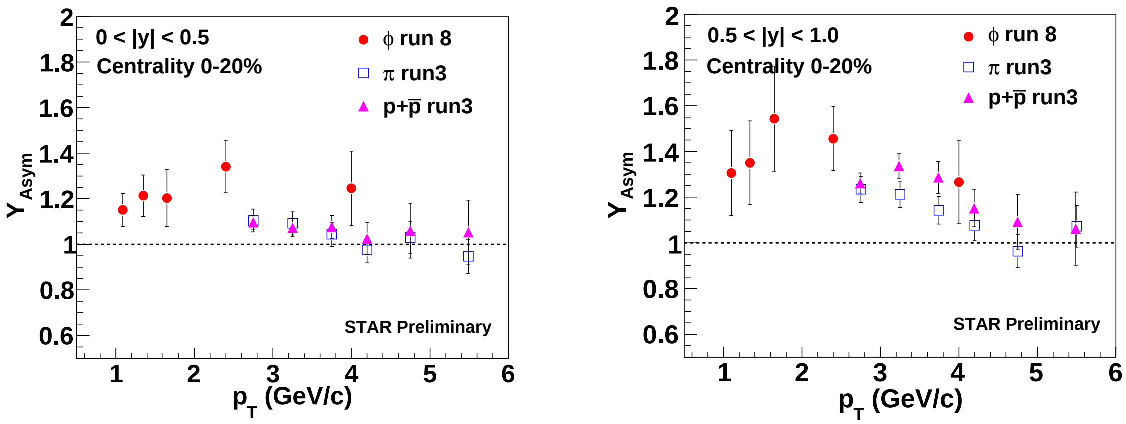

Figure 3.13: Rapidity asymmetry factor (Y_{asym}) for ϕ meson at $|y| < 0.5$ (left panel) and $0.5 < |y| < 1$ (right panel) in 0-20% d+Au collisions at $\sqrt{s_{NN}} = 200$ GeV. For comparison, $\pi^+ + \pi^-$ (open squares) and $p+\bar{p}$ (solid triangles) results from STAR [32] are also shown.

3.3 Pion Production in d+Au Collisions

3.3.1 Pion Raw Yield Extraction

As discussed earlier, the main TPC in STAR is used for tracking and identification of charged particles. Measurements of the ionization energy loss (dE/dx) of charged tracks in the TPC gas are used to identify pion, kaon, proton and their antiparticles. Track selection criteria used for this analysis are presented in Table 3.6. To extract the pion raw yield in a given p_T bin, we perform four-Gaussian fits to the normalized dE/dx distributions of positively charged and negatively charged hadrons. The normalized dE/dx in general is defined as

$$n\sigma_X = \frac{1}{R}\log\frac{< dE/dx > |_{measured}}{< dE/dx >_X |_{expected}}, \tag{3.6}$$

where X is the particle type ($e^{\pm}, \pi^{\pm}, K^{\pm}$, p or $\bar{p}$), $< dE/dx > |_{measured}$ is the measured energy loss of a track, $< dE/dx >_X |_{expected}$ is the expected mean energy loss of particle X at a given momentum as obtained from Bichsel function [11] and R is the dE/dx resolution of the TPC, which is a function of the track length in the TPC. Figure 3.14 shows dE/dx distributions for positively charged and negatively charged hadrons in the TPC, normalized to the pion dE/dx (referred to as the $n\sigma_\pi$) at $0.25 < p_T < 0.3$ GeV/c and $|y| < 0.1$ in d+Au collisions at $\sqrt{s_{NN}} = 200$ GeV.

Table 3.6: Track selection criteria for the pion spectra analysis in run 8 d+Au collisions at $\sqrt{s_{NN}} = 200$ GeV.

Cut Description	**Value**
$\lvert y \rvert$	< 1.0
dca	< 3 cm
$nHitsFit$	≥ 25
$nHitsdEdx$	≥ 15
Transverse Momentum	> 0.15 GeV/c
Momentum	> 0.15 GeV/c
Track Fitting Flag	$0 < flag < 1000$
χ^2	< 6

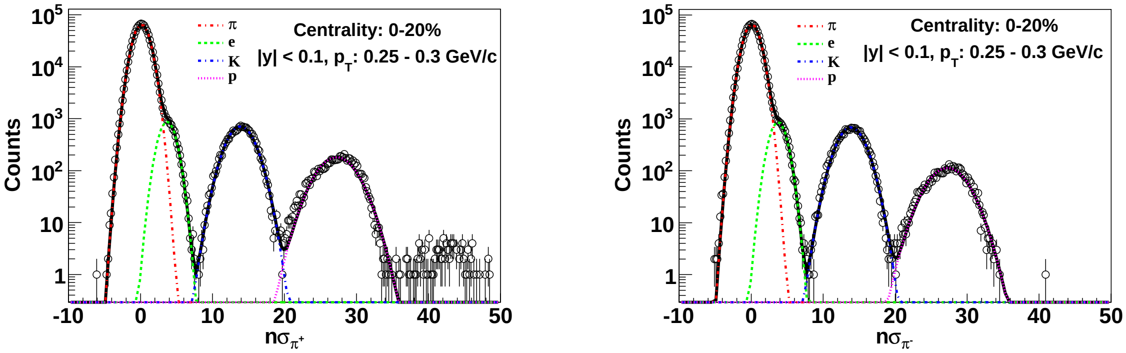

Figure 3.14: The dE/dx distributions for positively charged (left) and negatively charged (right) hadrons in the TPC, normalized by the expected pion dE/dx at $0.25 < p_T < 0.3$ GeV/c and $\lvert y \rvert < 0.1$ in d+Au collisions at $\sqrt{s_{NN}} = 200$ GeV. The curves are Gaussian fits representing contributions from pions (dot-dashed, red), electrons (dashed, green), kaons (dot-dashed, blue), and protons (dotted, magenta). Errors are statistical only.

The counts under the Gaussian about $n\sigma_\pi \sim 0$ give the yield of pions for a particular p_T range. A similar procedure is followed to obtain yields for other p_T ranges. Further details of extracting raw yields of identified hadrons from normalized dE/dx distributions can be found in Ref. [33].

3.3.2 Efficiency and Acceptance Correction

The raw yields are corrected for detector acceptance and tracking efficiency which are obtained from the MC embedding method. In this method, simulated MC tracks are embedded into real events at the raw data level. The MC tracks are simulated with primary vertex position taken from the real events. The MC track kinematics are taken from flat distributions in y and p_T. The flat p_T distribution is used in order to have similar statistics in different p_T bins. One simulated track is embedded in each event. The tracks are propagated through the full simulation of the STAR detector and geometry using the GEANT program package [15]. The real events with the embedded MC track are referred as mixed-events and are processed through the standard STAR event reconstruction chain. Then an association map is created between the input MC tracks and the reconstructed tracks of the mixed-event to find the matched tracks. The reconstruction efficiency is obtained by the ratio of the number of matched MC tracks to the number of input MC tracks.

Figure 3.15 shows the product of tracking efficiency and detector acceptance for pions as a function of the input MC p_T in minimum bias d+Au collisions at $\sqrt{s_{NN}}$ = 200 GeV. The efficiencies for π^+ and π^- are similar and are independent of p_T for $p_T > 0.2$ GeV/c. The curves superimposed in Fig. 3.15 are parameterizations to the efficiencies for π^+ and π^-. The fit function used for these parametrizations is defined as

$$f(p_T) = P_0 \; exp[-(P_1/p_T)^{P_2}], \tag{3.7}$$

where P_0, P_1 and P_2 are free parameters. Table 3.7 lists the value of the fit parameters for π^+ and π^- efficiencies in minimum bias d+Au collisions at $\sqrt{s_{NN}}$ = 200 GeV. These parameterizations are used for efficiency corrections to get the correct p_T spectra for pions.

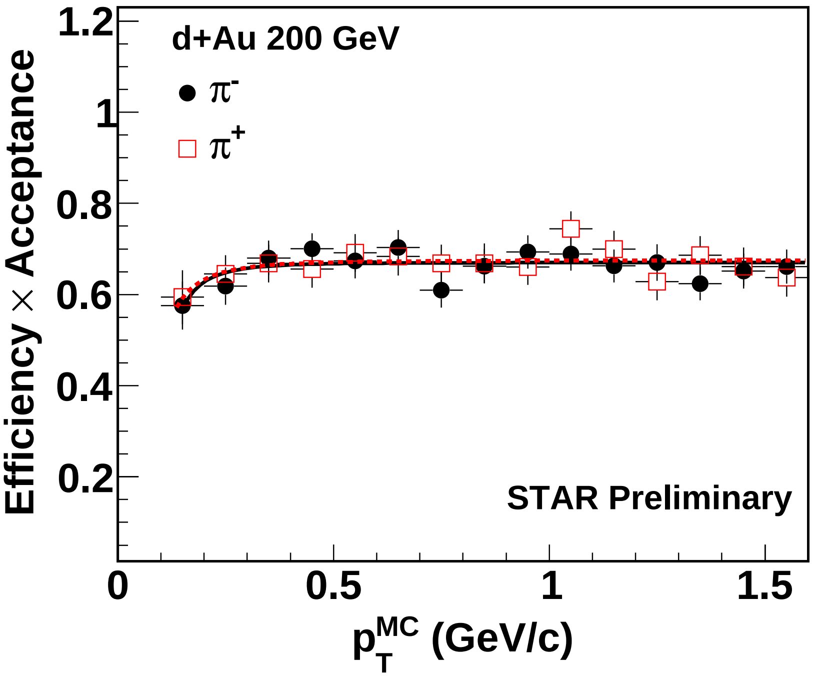

Figure 3.15: Reconstruction efficiency including detector acceptance for π^+ (red open squares) and π^- (black solid circles) as a function of p_T in minimum bias d+Au collisions at $\sqrt{s_{NN}} = 200$ GeV. The curves (red dashed line for π^+ and black solid line for red π^-) are parameterizations to the efficiency data and are used for corrections in the analysis.

Table 3.7: Fit parameters for π^+ and π^- efficiencies in minimum bias d+Au collisions at $\sqrt{s_{NN}} = 200$ GeV.

Particle	P_0	P_1	P_2
π^+	0.675 ± 0.009	0.066 ± 0.064	2.46 ± 2.4
π^-	0.670 ± 0.006	0.083 ± 0.042	3.11 ± 2.3

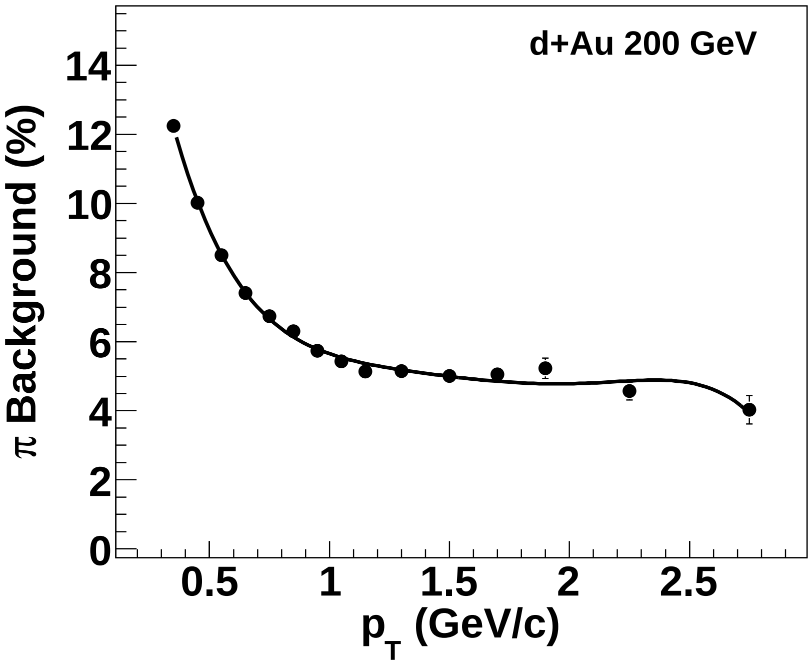

Figure 3.16: Percentage of pion background contribution estimated from HIJING+GEANT as a function of p_T in d+Au collisions at $\sqrt{s_{NN}} = 200$ GeV. The curve is the parameterization to the pion background contribution and is used for correction in the analysis.

3.3.3 Background Correction

The pion spectra are corrected for feed-downs from weak decays, muon contamination, and background pions produced in the detector materials. These corrections are obtained from MC simulations of HIJING events, with the STAR geometry and a realistic description of the detector response using GEANT. The simulated events are reconstructed in the same way as the real data. The weak decay daughter pions are mainly from K_S^0 and are identified by the parent particle information accessible from the simulation. The muons from pion decay can be misidentified as primordial pions because of the similar masses of muon and pion. This contamination is obtained from MC simulations by identifying the decay, which is also accessible in simulation. The total background rate for pion, which is dominated by weak decays and muon contamination, obtained from the MC simulations is shown in Fig. 3.16. This pion background contribution is obtained from the Ref. [34]. The curve superimposed in Fig. 3.16 is the parameterization to the pion background contribution using a 5th

Table 3.8: Fit parameters from the polynomial fit to pion background contribution in d+Au collisions at $\sqrt{s_{NN}}$ = 200 GeV.

Parameters	**Values**
P_0	26.87 ± 0.65
P_1	-63.57 ± 3.58
P_2	76.70 ± 7.01
P_3	-46.85 ± 6.12
P_4	14.2 ± 2.41
P_5	-1.69 ± 0.35

order polynomial. The fit parameters are listed in Table 3.8. This parameterization is used for pion background correction to get the final p_T spectra for pions.

3.3.4 Results and Discussion

3.3.4.1 Transverse Momentum Spectra

Figure 3.17 shows the transverse momentum spectra for π^- and π^+ at mid-rapidity ($|y| < 0.1$) in 0-20% d+Au collisions at $\sqrt{s_{NN}}$ = 200 GeV. The dotted curves in Fig. 3.17 are the Bose-Einstein function fit to the spectra and have the following functional form:

$$\frac{1}{2\pi p_T}\frac{d^2N}{dp_T dy} = \frac{A}{\exp(m_T/T_{BE}) - 1}, \tag{3.8}$$

where A and T_{BE} are fit parameters, and $m_T = \sqrt{m^2 + p_T^2}$ is the transverse mass. The values of the fit parameters A and T_{BE} as well as the χ^2/ndf of the Bose-Einstein function fit to the spectra are listed in Table 3.9. Since the p_T spectra for pions are well described by the Bose-Einstein function, the same is used for extrapolating the spectra into unmeasured regions at low p_T ($p_T < 0.2$ GeV/c) and high p_T ($p_T > 0.7$ GeV/c). To further characterize the spectra, the average transverse momenta $\langle p_T \rangle$ and the integrated particle multiplicity densities dN/dy have been extracted from the measured spectra using the Bose-Einstein function. The extracted $\langle p_T \rangle$ of π^- and π^+ are found to be 0.371 ± 0.003 and 0.371 ± 0.002, respectively. Similarly, the extracted dN/dy of π^- and π^+ are found to be 8.72 ± 0.36 and 8.74 ± 0.33, respectively. The quoted errors are statistical only. These $\langle p_T \rangle$ and dN/dy of π^- and π^+ in 0-20% d+Au

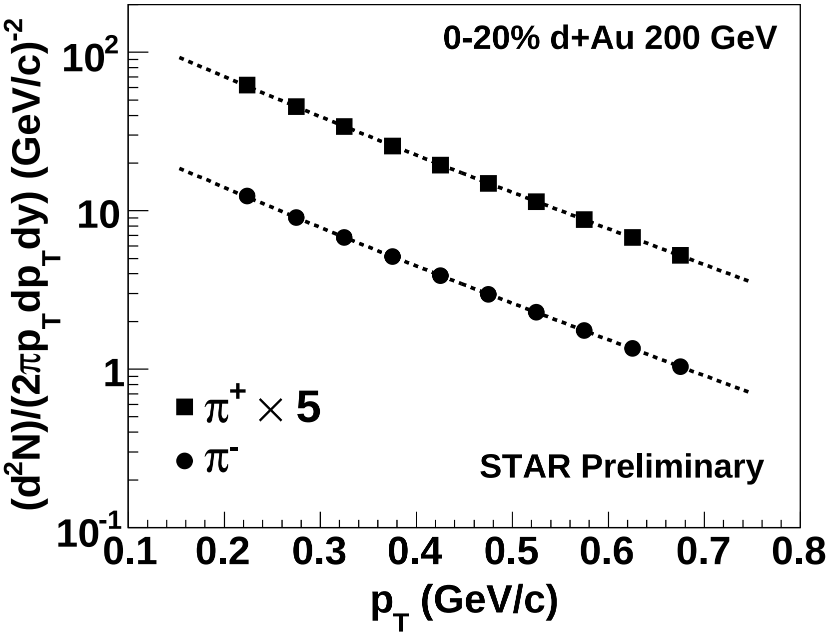

Figure 3.17: Transverse momentum spectra for π^- and π^+ at mid-rapidity ($|y| < 0.1$) in 0-20% d+Au collisions at $\sqrt{s_{NN}} = 200$ GeV. Spectra for π^+ is scaled by a factor 5 for clarity. Errors shown are statistical only. The curves are the Bose-Einstein function fit to the spectra.

Table 3.9: Values of fit parameters and χ^2/ndf from Bose-Einstein function fit to the p_T spectra for π^- and π^+ at mid-rapidity ($|y| < 0.1$) in 0-20% d+Au collisions at $\sqrt{s_{NN}} = 200$ GeV.

Particle	A	$T_{BE}(MeV)$	χ^2/ndf
π^-	223.46 ± 5.05	193.4 ± 1.4	0.445/8
π^+	223.40 ± 4.12	193.6 ± 1.4	0.622/8

collisions at $\sqrt{s_{NN}} = 200$ GeV are listed in Table 3.10 and Table 3.11, respectively. For comparison, $\langle p_T \rangle$ and dN/dy of π^- and π^+ for p+p, d+Au (run 3) and Au+Au collisions in different centralities at $\sqrt{s_{NN}} = 200$ GeV are also listed [33]. The $\langle p_T \rangle$ and dN/dy of π^- and π^+ from run 3 and run 8 d+Au collisions are found to be consistent with each other.

One interesting observation is that the $\langle p_T \rangle$ of pions in central d+Au collisions is found to be larger than that in peripheral Au+Au collisions. This can be due to jets, k_T broadening, and multiple scattering [35]. These effects can be stronger in d+Au collisions than in peripheral Au+Au collisions, because nucleons in the deuteron suffer multiple collisions traversing the incoming Au nucleus in central d+Au collisions while peripheral Au+Au collisions are close to simple superposition of multiple p+p collisions. On the other hand, $\langle p_T \rangle$ of pions in central d+Au collisions are smaller than that in central Au+Au collisions. This larger $\langle p_T \rangle$ in central Au+Au collisions cannot be only due to the effects already present in d+Au collisions, as random-walk models argue [35], but also be due to other effects including transverse radial flow, due to thermodynamic pressure, and remaining contributions from (semi-)hard scatterings [33].

Figure 3.18 shows the comparison of pion p_T spectra for 0-20% d+Au collisions at $\sqrt{s_{NN}} = 200$ GeV in the year 2008 (run 8) with the previously published STAR results from the year 2003 (run 3) data [33]. The p_T spectra for π^- and π^+ from run 8 are consistent with run 3 results within the statistical errors. The shape of the p_T spectra for π^- and π^+ are similar in both cases.

Table 3.10: Extrapolated average transverse momenta, $\langle p_T \rangle$ in GeV/c, of π^- and π^+ in 0-20% d+Au collisions at $\sqrt{s_{NN}} = 200$ GeV. For comparison, $\langle p_T \rangle$ of π^- and π^+ for various collision systems and centralities are also listed [33]. Quoted errors are the quadratic sum of statistical and systematic uncertainties for all collision systems and centralities except for run 8 d+Au collisions, where only statistical errors are shown.

System	Centrality	π^-	π^+
d+Au 200 GeV (run 8)	0-20%	0.371 ± 0.003	0.371 ± 0.002
p+p 200 GeV	min. bias	0.348 ± 0.018	0.348 ± 0.018
d+Au 200 GeV (run 3)	min. bias	0.367 ± 0.027	0.369 ± 0.027
	40-100%	0.359 ± 0.024	0.364 ± 0.025
	20-40%	0.363 ± 0.031	0.370 ± 0.031
	0-20%	0.378 ± 0.028	0.378 ± 0.028
Au+Au 200 GeV	70-80%	0.363 ± 0.018	0.367 ± 0.018
	60-70%	0.377 ± 0.019	0.377 ± 0.019
	50-60%	0.389 ± 0.020	0.389 ± 0.020
	40-50%	0.395 ± 0.020	0.395 ± 0.020
	30-40%	0.402 ± 0.021	0.404 ± 0.021
	20-30%	0.408 ± 0.021	0.411 ± 0.021
	10-20%	0.416 ± 0.021	0.421 ± 0.021
	5-10%	0.418 ± 0.021	0.422 ± 0.021
	0-5%	0.422 ± 0.022	0.427 ± 0.022

Table 3.11: Integrated multiplicity rapidity density, dN/dy, of π^- and π^+ in 0-20% d+Au collisions at $\sqrt{s_{NN}} = 200$ GeV. For comparison, dN/dy of π^- and π^+ for various collision systems and centralities are also listed [33]. Quoted errors are the quadratic sum of statistical and systematic uncertainties for all collision systems and centralities except for run 8 d+Au collisions, where only statistical errors are shown.

System	Centrality	π^-	π^+
d+Au 200 GeV (run 8)	0-20%	8.72 ± 0.36	8.74 ± 0.33
p+p 200 GeV	min. bias	1.42 ± 0.11	1.44 ± 0.11
d+Au 200 GeV (run 3)	min. bias	4.63 ± 0.31	4.62 ± 0.31
	40-100%	2.89 ± 0.20	2.87 ± 0.21
	20-40%	6.06 ± 0.41	6.01 ± 0.41
	0-20%	8.42 ± 0.57	8.49 ± 0.58
Au+Au 200 GeV	70-80%	10.9 ± 0.8	10.8 ± 0.8
	60-70%	21.1 ± 1.6	21.1 ± 1.6
	50-60%	36.3 ± 2.8	36.2 ± 2.7
	40-50%	58.9 ± 4.5	58.7 ± 4.5
	30-40%	89.6 ± 6.8	89.2 ± 6.8
	20-30%	136 ± 10	135 ± 10
	10-20%	196 ± 15	194 ± 15
	5-10%	261 ± 20	257 ± 20
	0- 5%	327 ± 25	322 ± 25

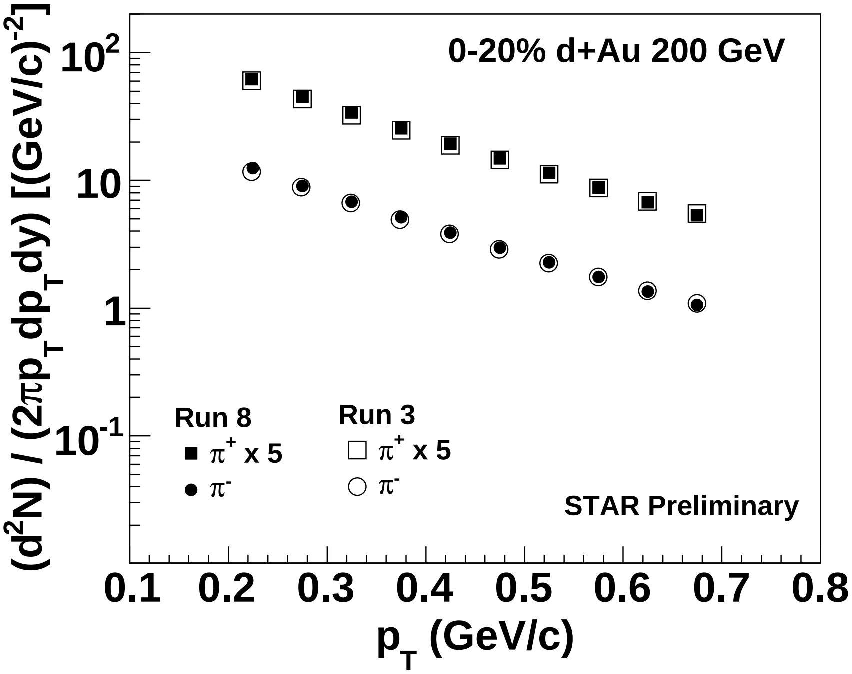

Figure 3.18: Comparison of transverse momentum spectra for $\pi^{\pm}$ at mid-rapidity ($|y| < 0.1$) in 0-20% d+Au collisions at $\sqrt{s_{NN}}$ = 200 GeV, obtained from year 2008 and year 2003. Errors are statistical only.

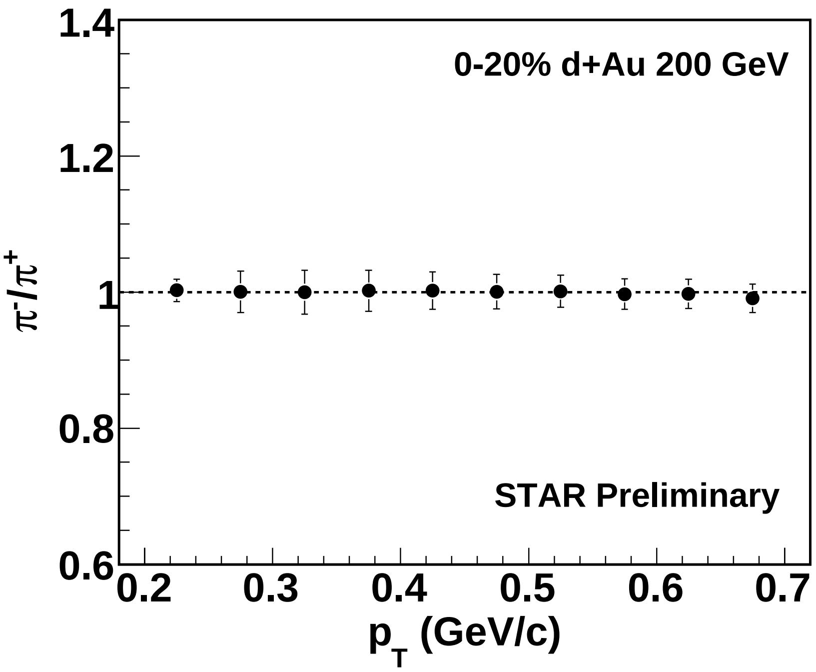

Figure 3.19: Variation of π^-/π^+ ratio as a function of p_T in 0-20% d+Au collisions at $\sqrt{s_{NN}}$ = 200 GeV. Errors are statistical only.

3.3.4.2 Antiparticle to Particle Ratio

Figure 3.19 shows the π^-/π^+ ratio as a function of p_T in 0-20% d+Au collisions at $\sqrt{s_{NN}}$ = 200 GeV. The π^-/π^+ ratio is approximately unity and is independent of p_T. Similar behavior has been observed for different collision energies and collision systems as well [33].

Bibliography

[1] J.W. Cronin *et al.*, Phys. Rev. D **11**, 3105 (1975); P. B. Straub *et al.*, Phys. Rev. Lett. **68**, 452 (1992).

[2] J. Adams *et al.* (STAR Collaboration), Phys. Lett. B **616**, 8 (2005); S. S. Adler *et al.* (PHENIX Collaboration), Phys. Rev. C **74**, 024904 (2006).

[3] B. I. Abelev *et al.* (STAR Collaboration), Phys. Rev. C **76**, 054903 (2007).

[4] K.H.Ackermann *et.al.* (STAR Collaboration), Nucl. Instrum. Methods A **499**, 624 (2003).

[5] F. S. Bieser *et al.*, Nucl. Instrum. Methods A **499**, 766 (2003).

[6] W. J. Llope *et al.*, Nucl. Instrum. Methods A **522**, 252 (2004).

[7] K. H. Ackermann *et al.*, Nucl. Instrum. Methods A **499**, 713 (2003).

[8] Run 8 d+Au 200 GeV centrality selection. http://www.star.bnl.gov/protected/lfspectra/cjena/run8_dAu200GeV/dAu_centrality/documentation/centrality_run8_dAu200GeV.html

[9] W. M. Yao *et al.*, J. Phys. G **33**, 1 (2006).

[10] M. Anderson *et al.*, Nucl. Instrum. Methods A **499**, 659 (2003).

[11] H. Bichsel, Nucl. Instrum. Methods A **562**, 154 (2006).

[12] D. L'Hote, Nucl. Instrum. Methods A **337**, 544 (1994); D. Drijard, H. G. Fischer, and T. Nakada, Nucl. Instrum. Methods A **225**, 367 (1984).

[13] B. I. Abelev *et al.* (STAR Collaboration), Phys. Rev. C **79**, 064903 (2009).

[14] S. L. Blyth, Ph.D. Thesis 2007, University of Capetown, Capetown. http://drupal.star.bnl.gov/STAR/files/startheses/2007/blyth_sarah.ps

[15] F. Carminati *et al.*, GEANT 3.21: Detector Description 38 and Simulation Tool, CERN Program Library Long Writeup W5013 (1993).

[16] B. I. Abelev *et al.* (STAR Collaboration), Phys. Rev. C **79**, 064903 (2009).

[17] Z. W. Lin and C.M. Ko, Phys. Rev. Lett. **89**, 202302 (2002).

[18] R. J. Fries *et al.*, Phys. Rev. Lett. **90**, 202303 (2003).

[19] M. Lev and B. Petersson, Z. Phys. C **21**, 155 (1983).

[20] A. Accardi and M. Gyulassy, Phys. Lett. B **586**, 244 (2004).

[21] I. Vitev and M. Gyulassy, Phys. Rev. Lett. **89**, 252301 (2002).

[22] X.-N. Wang, Phys. Rev. C **61**, 064910 (2000).

[23] R. C. Hwa and C. B. Yang, Phys. Rev. Lett. **93**, 082302 (2004).

[24] J. Adams *et al.* (STAR Collaboration), Phys. Lett. B **637**, 161 (2006).

[25] X. Zhu (for the STAR Collaboration), Proceedings for Quark Matter 2009.

[26] D. Kharzeev, Nucl. Phys. A **730**, 448 (2004); D. Kharzeev, Y. Kovchegov, and K. Tuchin, Phys. Lett. B **599**, 23 (2004).

[27] J. Jalilian-Marian *et al.*, Phys. Lett. B **577**, 54 (2003); J. L. Albacete *et al.*, Phys. Rev. Lett. **92**, 082001 (2004); R. Baier *et al.*, Phys. Rev. D **68**, 054009 (2003).

[28] X. N. Wang, Phys. Lett. B **565**, 116 (2003).

[29] Z. Lin and C. M. Ko, Phys. Rev. C **68**, 054904 (2003).

[30] R. C. Hwa, C. B. Yang, and R. J. Fries, Phys. Rev. C **71**, 024902 (2005).

[31] J. Adams *et al.* (STAR Collaboration), Phys. Rev. C **70**, 064907 (2004).

[32] B. I. Abelev *et al.* (STAR Collaboration), Phys. Rev. C **76**, 054903 (2007).

[33] B. I. Abelev *et al.* (STAR Collaboration), Phys. Rev. C **79**, 034909 (2009).

[34] Lijuan Ruan, Ph.D. Thesis 2004, University of Science and Technology of China (USTC).
http://drupal.star.bnl.gov/STAR/files/startheses/2004/ruan_lijuan.pdf

[35] A. Leonidov, M. Nardi, and H. Satz, Z. Phys. C **74**, 535 (1997).

Chapter 4

Elliptic Flow of Light Nuclei in Au+Au Collisions

4.1 Introduction

One of the most important experimental findings at RHIC has been the signature of coalescence as the mechanism of particle production. The differences in baryons and mesons at the intermediate transverse momentum ($1.5 < p_T < 5$ GeV/c) in nuclear modification factor and the elliptic flow have been observed [1]. These are considered as the signatures of quark coalescence as a mechanism of hadron production. However, it is experimentally difficult to study how local correlations and energy/entropy play a role in coalescence since the partonic constituents are not directly observable. In relativistic heavy ion collisions, light nuclei and antinuclei are formed through coalescence of nucleons and antinucleons [2, 3, 4]. The binding energies of the light nuclei are small ($\sim$ MeV), hence this formation process can only happen at a late stage of the evolution of the system when interactions between nucleons and other particles are weak. This process is called final state coalescence [2, 5]. The coalescence probability is related to the local nucleon density. Therefore, the production of light nuclei provides an interesting tool to measure collective motion and freeze-out properties. The advantage of nucleons over the partonic coalescence phenomena is that both the nuclei and the constituent nucleon space-momentum distributions are measurable quantities in heavy ion collisions. By studying the elliptic flow of nuclei and comparing to those of their constituents (nucleons), we will have a better understanding of coalescence process for hadronization.

4.2 Data Analysis

In the following subsections, we discuss the data sets and different criteria that are used for data set selection.

4.2.1 Data Set and Trigger

The data sets used in the presented analysis are from Au+Au collisions at $\sqrt{s_{NN}}$ = 200 GeV and 39 GeV. The Au+Au 200 GeV and 39 GeV data were taken with the STAR detector at RHIC in the year 2007 (run 7) and 2010 (run 10), respectively. The run 7 Au+Au 200 GeV data set consisted of minimum bias (MB) trigger only. The minimum bias trigger requires a coincidence of two zero degree calorimeters (ZDCs) [6], which are located at ± 18 m from the center of the interaction region along the beam line. It additionally requires the Vertex Position Detector (VPD) [7] with an online vertex Z position cut of ± 5 cm. The VPD is more efficient at triggering on central events relative to peripheral and its vertex Z resolution is worse for peripheral events relative to central. This leads to a trigger bias for peripheral events, which will be discussed in more detail later in this chapter. The run 10 Au+Au 39 GeV data set consisted of MB trigger only.

4.2.2 Event Selection

The primary vertex for each minimum bias event is determined by finding the best point of common origin of the tracks measured in the TPC. The analyzed events were required to have a primary vertex Z position, V_Z, within ± 30 cm for run 7 Au+Au 200 GeV data set and ± 40 cm for run 10 Au+Au 39 GeV data set from the center of the TPC along the beam line. This value was chosen to ensure nearly uniform detector acceptance in the η range studied. The V_Z distribution for the different collision energies are shown in Fig. 4.1. In order to reject events which involves beam

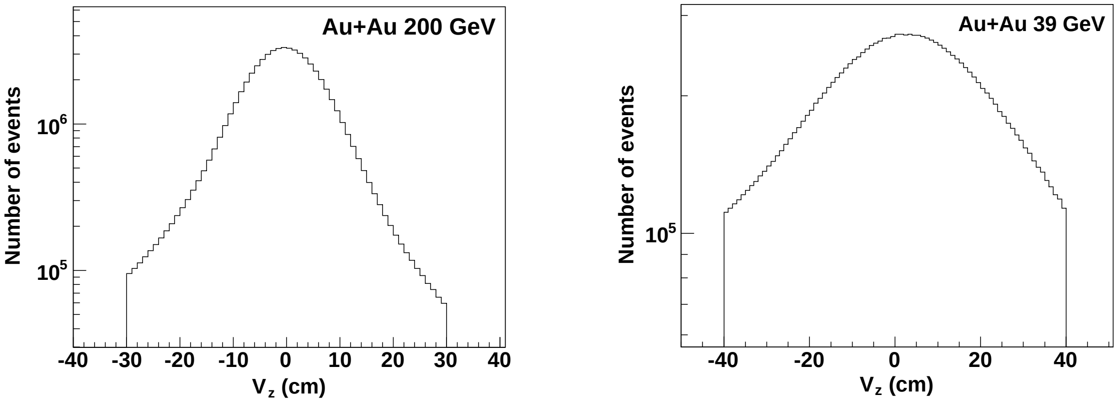

Figure 4.1: Event-by-event distribution of the Z-position of the primary vertex (V_Z) in Au+Au collisions at $\sqrt{s_{NN}}$ = 200 GeV (left) and 39 GeV (right).

pipe and beam-gas interactions, the event vertex radius (defined as $\sqrt{V_x^2 + V_y^2}$, where V_x and V_y are the vertex positions along the x and y directions) is required to be less than 2 cm. The approximate number of events analyzed after imposing these cuts are 62 M and 16 M for Au+Au collisions at 200 GeV and 39 GeV, respectively.

4.2.3 Centrality Selection

The collision centralities represent the fractions of the full hadronic cross section in a collision. In Au+Au collisions, the collision centrality is determined by using the TPC reference multiplicity ($RefMult$). The TPC $RefMult$ is defined as the uncorrected charged particle multiplicity measured in the TPC in the pseudorapidity region $|\eta| < 0.5$ with distance of closest approach (dca) less than 3 cm from the primary vertex position and at least 10 hits ($nHitsFit \geq 10$) in the TPC including the primary vertex. In run 7 Au+Au 200 GeV, the inclusion of inner tracking detectors rendered reference multiplicity a poor method to determine centrality [12]. There is a dependence on the primary vertex position for the reconstruction efficiency in the $|V_z| < 30$ cm region. The dependence was generally absent for TPC only tracking used in many of the previous productions and is undesirable since it requires the centrality cuts to change as a function of V_z. Therefore, another variable is proposed to determine the centrality called global reference multiplicity ($gRefMult$), which counts global tracks with $|\eta| < 0.5$, $dca < 3$ cm and $nHitsFit \geq 10$. After extensive

Table 4.1: Centrality definitions in run 7 Au+Au 200 GeV collisions using $gRefMult$.

% cross section	$gRefMult$
0-5	≥ 485
5-10	$399 - 484$
10-20	$269 - 398$
20-30	$178 - 268$
30-40	$114 - 177$
40-50	$69 - 113$
50-60	$39 - 68$
60-70	$21 - 38$
70-80	$10 - 20$

checks, $gRefMult$'s reconstruction efficiency was determined to be stable as function of V_z and run number. The high end of the $gRefMult$ distribution is fitted with a Monte Carlo Glauber simulation. The various centrality bins are calculated as a fraction of this simulated multiplicity distribution starting from the highest multiplicities. Table 4.1 lists the $gRefMult$ values for each centrality in run 7 Au+Au collisions at $\sqrt{s_{NN}} = 200$ GeV.

The other issues in run 7 Au+Au 200 GeV are biases on multiplicity distribution introduced by the online cut of $|V_z| < 5$ cm. The biases come from two sources. Firstly, over the full range in V_z, the VPD efficiency is higher for more central events compared to peripheral ones which leads to a general deficit in peripheral events for a given data sample. Secondly, a centrality dependence of the VPD's online V_z resolution which is worse for peripheral events relative to central events. Therefore, the events at the higher $|V_z|$ are more likely to be peripheral whereas the events at the lower $|V_z|$ are more likely to be central. This effect is demonstrated on Fig. 4.2. The V_z dependent biases in multiplicity distribution require a re-weighting correction to be applied for all analysis. The correction has to be applied as a function of V_z in 2 cm bins for acceptance reasons. In a given V_z bin, the weights are determined by normalizing the 1D global reference multiplicity distribution by the number of events with $gRefMult > 500$. The ideal multiplicity distribution from MC Glauber then divided by the normalized global reference multiplicity distribution to calculate

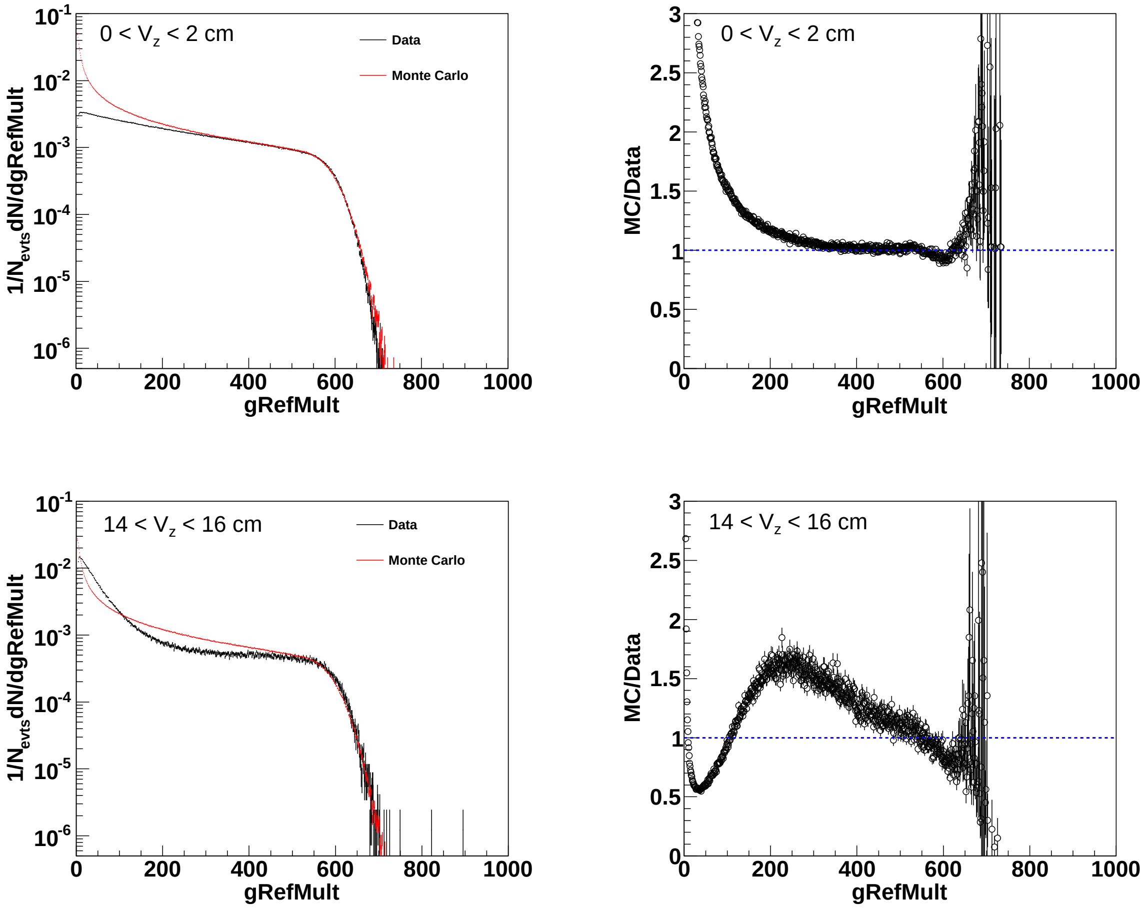

Figure 4.2: Left Column: Event-by-event distribution of $gRefMult$ for $0 < V_z < 2$ cm and $14 < V_z < 16$ cm compared with the multiplicity distribution from Glauber Monte Carlo simulation. Right Column: The ratio of simulated multiplicity distribution to real data $gRefMult$ distribution for $0 < V_z < 2$ cm and $14 < V_z < 16$ cm.

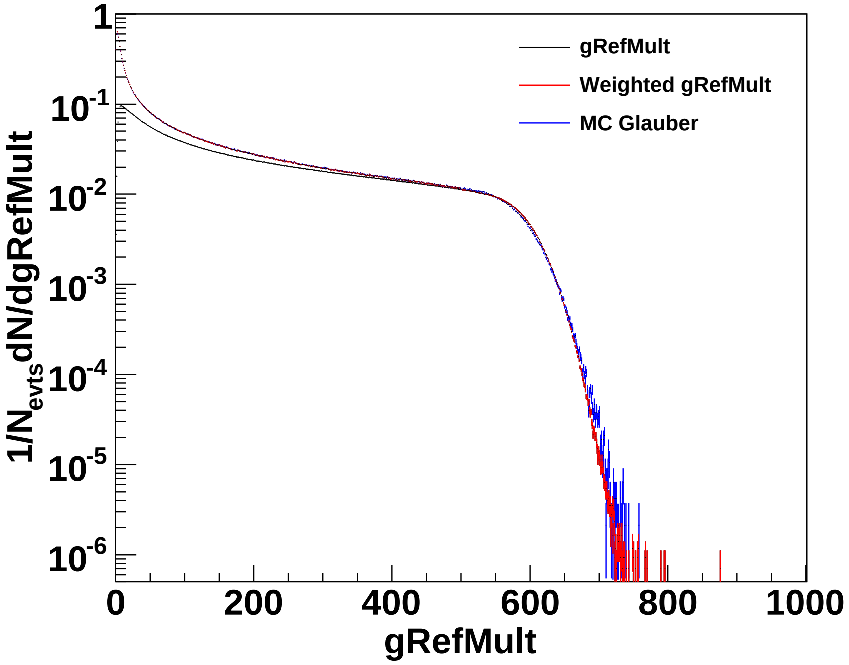

Figure 4.3: $gRefMult$ distribution before and after the re-weighting correction for $|V_z| < 30$ cm compared with the multiplicity distribution from MC Glauber simulation.

the weights. Figure 4.3 shows the comparison of $gRefMult$ distribution before and after the re-weighting correction for $|V_z| < 30$ cm. After applying the re-weighting correction which were determined in smaller V_z bins, the $gRefMult$ distribution matches with the multiplicity distribution from MC Glauber simulation.

In run 10 Au+Au 39 GeV, the collision centrality is determined by using the TPC reference multiplicity. Table 4.2 lists the $RefMult$ values for each centrality in run 10 Au+Au collisions at $\sqrt{s_{NN}} = 39$ GeV. Figure 4.4 shows the TPC $RefMult$ distribution with centrality cuts for each centrality.

4.2.4 Track Selection

In the present analysis, the tracks used in all the data sets are primary tracks. To select good tracks, various quality cuts are required to be applied to each track measured in the TPC. The track quality cuts are presented in the Table 4.3. In order to have uniform detector performance, a pseudorapidity cut of $|\eta| < 1.0$ is applied

Table 4.2: Centrality definitions in run 10 Au+Au 39 GeV collisions using $RefMult$.

% cross section	$gRefMult$
0-5	≥ 317
5-10	$266 - 316$
10-20	$186 - 265$
20-30	$126 - 185$
30-40	$82 - 125$
40-50	$51 - 81$
50-60	$29 - 50$
60-70	$16 - 28$
70-80	$8 - 15$

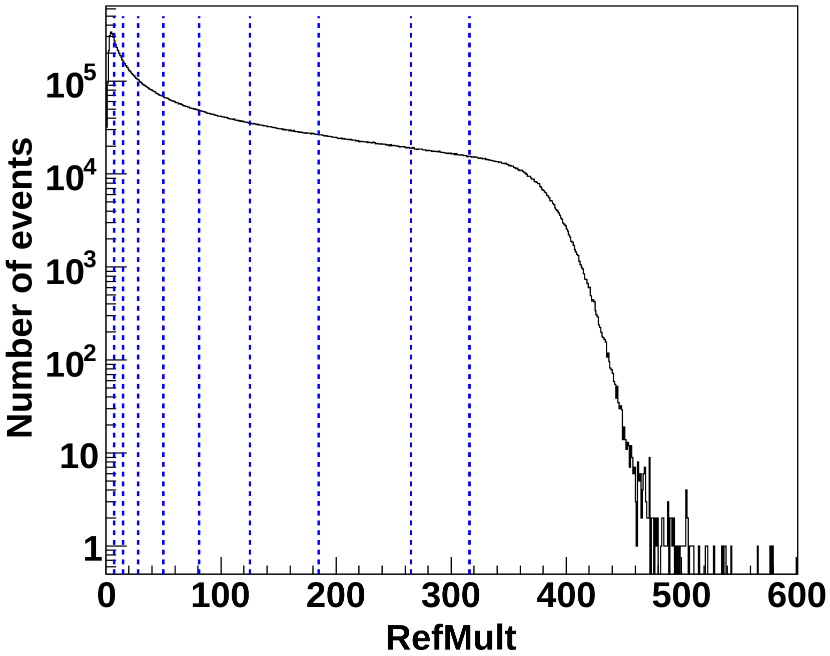

Figure 4.4: TPC reference multiplicity distribution for Au+Au collisions at $\sqrt{s_{NN}} =$ 39 GeV. The $RefMult$ cuts for different centrality bins are shown in different dashed blue lines.

Table 4.3: Track selection criteria for the analysis presented in this chapter.

Cut Description	**Value**
$\|\eta\|$	< 1.0
dca	< 0.5 cm (^3He), < 1 cm (d)
$nHitsFit$	≥ 25
$nHitsFit/nHitsPoss$	> 0.52 and < 1.02
$nHitsdEdx$	≥ 15
p_T	> 0.15 GeV/c

in the data. To avoid admixture of tracks from secondary vertices, a requirement is placed on the distance of closest approach (dca) between each track and the event vertex. The multiple counting of split tracks is avoided by requiring all tracks to have a minimum number of 25 fit points used in the reconstruction of the track. The effect of track splitting is minimized by further requiring that the number of fit points is more than half the number of total possible hit points for a track. Tracks can have a maximum of 45 hits in the TPC. In order to ensure tracks have good $\langle dE/dx \rangle$ values, a condition is placed on the number of hits used to calculate $\langle dE/dx \rangle$ of the track i.e. $nHitsdEdx \geq 15$. The low momentum tracks ($p_T \leq 0.15$ GeV/c) can not traverse the entire TPC due to their large track curvature inside the solenoidal magnetic field. So, those tracks are avoided by requiring all tracks to have $p_T > 0.15$ GeV/c.

4.2.5 Particle Identification Method with TPC and TOF

In run 7 Au+Au 200 GeV, STAR's main TPC [3] was used for tracking and identification of charged particles. Measurements of the ionization energy loss (dE/dx) of charged tracks in the TPC gas are used to identify protons, deuterons, tritons, ^3He and their antiparticles. Figure 4.5 shows the ionization energy loss (dE/dx) of charged tracks as a function of rigidity (= momentum/charge) measured by the TPC. It can be seen that the light nuclei (d, t and ^3He) and their antiparticles can be identified very well using TPC. We have also observed two $^4\overline{He}$ candidates in this data set which is discussed in detail in Chapter 5.

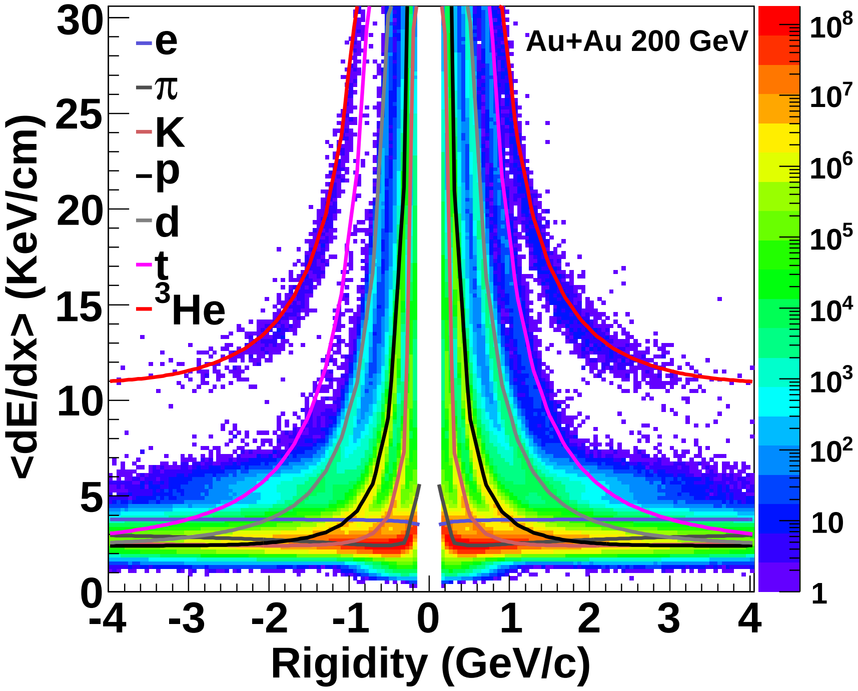

Figure 4.5: TPC dE/dx as a function of rigidity. Different color lines are expected dE/dx values for different charged tracks predicted by the Bichsel function [4].

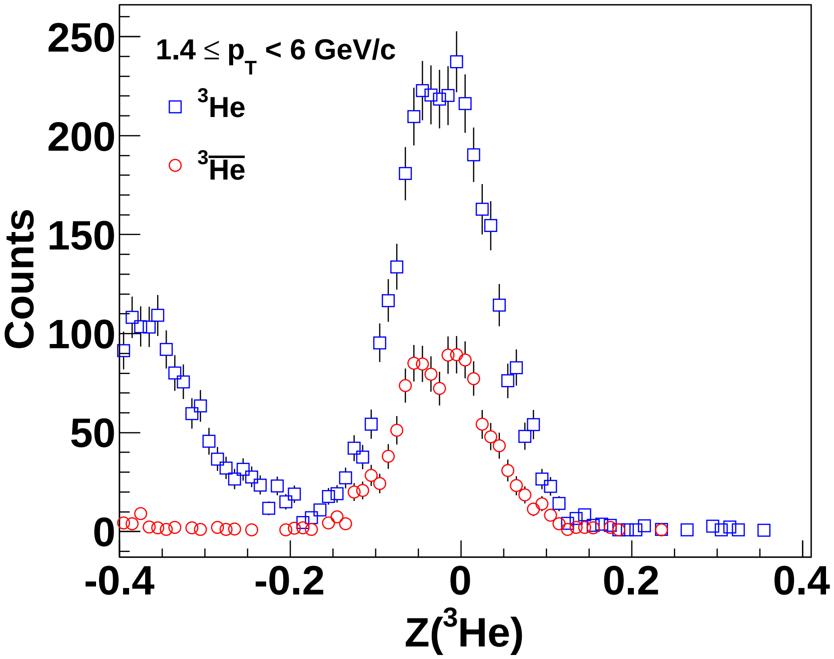

Figure 4.6: Z distribution of ^3He (open square) and $\overline{^3He}$ (open circle) for $1.4 \leq p_T < 6$ GeV/c in Au+Au collisions at $\sqrt{s_{NN}}$ = 200 GeV.

In order to identify light nuclei a variable Z is defined as

$$Z_i = \ln\left(\frac{(dE/dx)|_{measure}}{(dE/dx)_i|_{predict}}\right), \tag{4.1}$$

where $(dE/dx)|_{measure}$ is the measured mean energy loss of a track and $(dE/dx)_i|_{predict}$ is the mean energy loss predicted by Bichsel function for the given particle type i (i = d, t and ^3He) [4, 10]. The expected value of Z_i for the particle in study is around zero. Figure 4.6 shows a typical Z distribution for ^3He and $\overline{^3He}$ signals for $1.4 \leq p_T < 6$ GeV/c in Au+Au collisions at $\sqrt{s_{NN}}$ = 200 GeV. After track quality selections, the $^3He(\overline{^3He})$ signals are essentially background free. We derive the yields by counting $^3He(\overline{^3He})$ candidates with $|Z(^3He)| < 0.2$. The left panel of Fig. 4.7 shows the Z distribution of $\overline{d}$ for $0.7 < p_T < 1.0$ GeV/c in Au+Au collisions at $\sqrt{s_{NN}}$ = 200 GeV. The Z distribution of $\overline{d}$ is fitted with a Gaussian plus an exponential background function to extract the yield. In Au+Au 39 GeV, the Z distribution of $\overline{d}$ is fitted with a double Gaussian function (one is for signal and the other one is for background) to extract the yield, as shown in the right panel of Fig. 4.7.

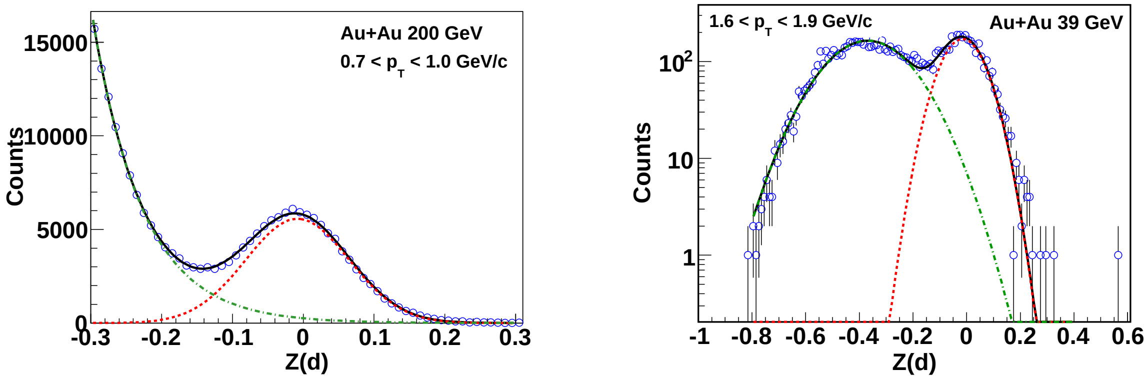

Figure 4.7: Left panel: Z distribution of $\bar{d}$ for $0.7 < p_T < 1.0$ GeV/c from Au+Au collisions at $\sqrt{s_{NN}} = 200$ GeV, fitted with a Gaussian (dashed, red line) plus an exponential (dot-dashed, green line) background function. Right panel: Z distribution of $\bar{d}$ for $1.6 < p_T < 1.9$ GeV/c from Au+Au collisions at $\sqrt{s_{NN}} = 39$ GeV, fitted with a double Gaussian function.

In run 10 Au+Au 39 GeV, full coverage of the Time-of-Flight (TOF) [9] detector based on multi-gap resistive plate chamber (MRPC) technology was installed at STAR. Both TPC and TOF were used for the identification of charged particles. The time of flight (t) information from TOF and the path length (L) from TPC can be used to calculate the velocity $\beta(= v/c)$ of the particle. The mass square ($m^2 = p^2(1/\beta^2 - 1)$) of the charged tracks is calculated using $1/\beta$ from TOF and momentum (p) from TPC. The left panel of Fig. 4.8 shows $1/\beta$ from TOF measurement as a function of momentum calculated from TPC tracking. The right panel of Fig. 4.8 shows m^2 as a function of momentum for all charged tracks. The TOF allows identification of particles at higher momenta than by using the TPC alone. In this analysis, deuterons and antideuterons are identified by the TPC for $p_T < 1$ GeV/c, and by both TPC and TOF in the range $1 < p_T < 4$ GeV/c. However, at low p_T (< 1 GeV/c), primary deuterons are overwhelmed by background from knock-out deuterons from the beam pipe and inner detector material, which are difficult to separate from collision products. As a result, only antideuterons are counted as collision products in this analysis. Measurements of the dE/dx of charged tracks in the TPC gas are alone used to identify $^3He(\overline{^3He})$ for $1 < p_T < 5$ GeV/c in minimum bias Au+Au collisions at $\sqrt{s_{NN}} = 39$ GeV.

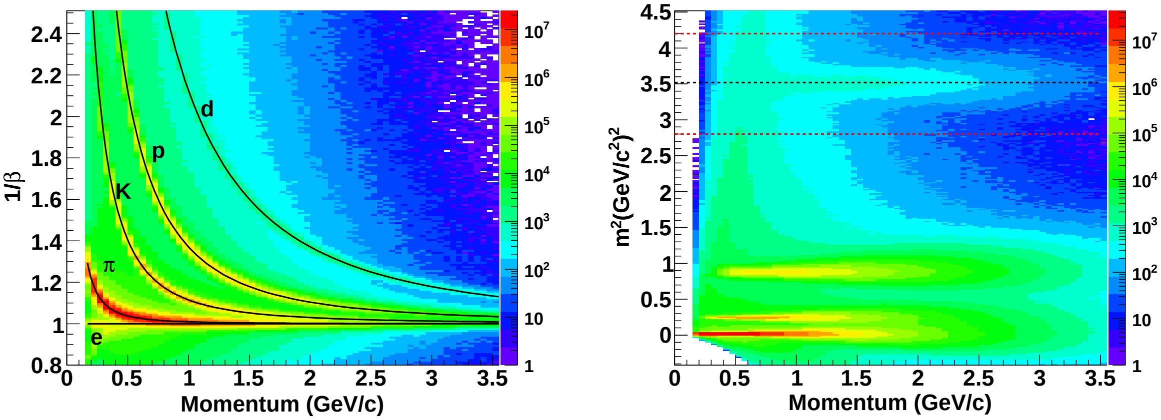

Figure 4.8: Left panel: TOF $1/\beta$ as a function of momentum from Au+Au collisions at $\sqrt{s_{NN}} = 39$ GeV. Different lines are the expected $1/\beta$ for different particles. Right panel: m^2 as a function of momentum for all charged tracks.

4.2.6 Event Plane Method and v_2

In relativistic heavy ion collisions, the azimuthal distributions of particles can be described using a Fourier expansion in terms of the particle emission azimuthal angle measured with respect to the reaction plane in the collision [13] as:

$$E\frac{d^3N}{d^3p} = \frac{1}{2\pi}\frac{d^2N}{p_T dp_T dy}(1 + \sum_{n=1}^{\infty} 2v_n cos[n(\phi - \Psi_r)]), \tag{4.2}$$

where the coefficients $v_n = \langle\cos(n(\phi - \Psi_r))\rangle$ are used for a quantitative characterization of the event anisotropy, and the angle brackets mean an average over all particles in all events. The sine terms are not present in the above equation because of symmetry with respect to the reaction plane. The coefficient v_1 is called directed flow and v_2 is known as elliptic flow.

The reaction plane angle, Ψ_r, can not be directly measured in high energy nuclear collisions, but can be estimated from the particle azimuthal distribution on an event-by-event basis. The estimated reaction plane is usually called the event plane. In the standard event plane method [13] the anisotropic flow itself used to determine the event plane. The event plane angle can be calculated in terms of the event flow vector Q_n as:

$$Q_n \cos(n\Psi_n) = \sum_i w_i \cos(n\phi_i), \tag{4.3}$$

$$Q_n \sin(n\Psi_n) = \sum_i w_i \sin(n\phi_i), \tag{4.4}$$

where the sum goes over all particles i used in the event plane calculation. The quantities ϕ_i and w_i are the lab azimuthal angle and weight for particle i. The event plane angle for each harmonic of the anisotropic flow is defined as:

$$\Psi_n = \left(\tan^{-1} \frac{\sum_i w_i \sin(n\phi_i)}{\sum_i w_i \cos(n\phi_i)}\right) /n. \tag{4.5}$$

In this analysis the event plane angle from second harmonic (Ψ_2) is used, which is in the range $0 \leq \Psi_2 < \pi$. The primary tracks used to calculate the event plane is known as flow tracks. Table 4.4 lists the selection criteria for flow tracks used in the second harmonic event plane reconstruction. The weights (w_i) used in this analysis include both p_T-weight and ϕ-weight i.e. $w_i = p_{Ti} \times w_\phi$. The transverse momentum (p_T) is a common choice as a weight because often v_2 increases with p_T. The p_T-weight is taken as the p_T of the particle for $p_T \leq 2$ GeV/c and constant (= 2) for $p_T > 2$ GeV/c. The ϕ-weight is necessary to correct for detector acceptance effects which can lead to anisotropic particle distributions in the lab frame. Therefore, it is necessary to ensure that the event plane angle distribution over all events is isotropic. This is achieved by finding the azimuthal distribution of all particles to be used in the event plane determination over many events and taking the inverse of the azimuthal distribution as the ϕ-weight. In order to remove autocorrelation effects, the tracks used for the calculation of v_2 are excluded from the event plane calculation.

Figure 4.9 shows the event plane angle distribution from TPC after all weighting in Au+Au collisions at $\sqrt{s_{NN}} = 200$ GeV (left) and 39 GeV (right). The distributions are fitted with a function $f(\Psi_2) = p_0(1 + 2p_1 cos(2\Psi_2))$ to check the flatness of the distribution. In both cases the event plane angle distributions are flat and the anisotropy of these distributions are negligible i.e. $p_1 \approx 0$.

In run 7 Au+Au 200 GeV, both east and west Forward Time Projection Chambers (FTPCs) are also used to determine the event plane. The FTPCs cover the pseudorapidity range of $2.5 \leq |\eta| \leq 4.0$. The η gap between two FTPCs helps to reduce non-flow effects due to short range correlations. Non-flow are correlations not associated with the reaction plane. Included in non-flow effects are jets, resonance decay, short-range correlations such as the Hanbury-Brown Twiss (HBT) effect, and momentum conservation [14].

Table 4.4: Track selection criteria for flow tracks used in the event plane reconstruction

Cut Description	Value
$\|\eta\|$	< 1.0
dca	< 2 cm
$nHits$	> 15
$nHits/nHitsPoss$	> 0.52
p_T	$0.15 < p_T < 2$ GeV/c

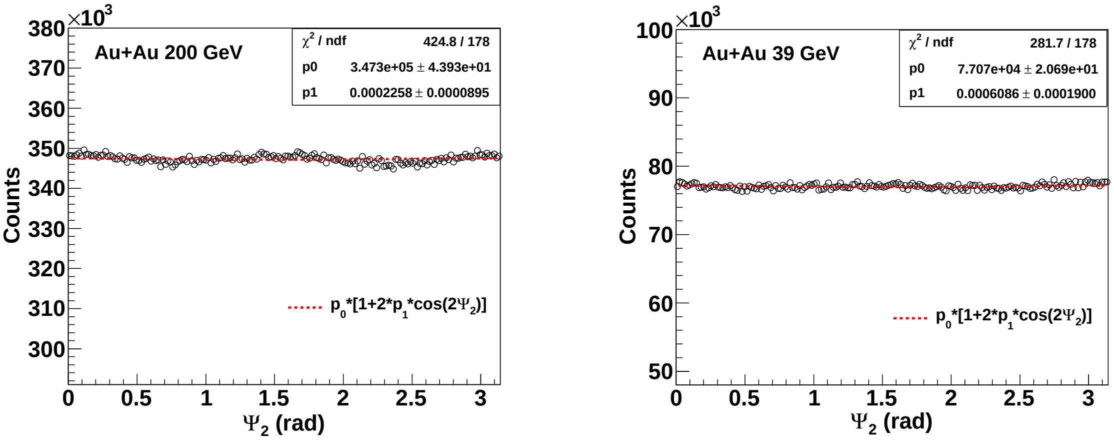

Figure 4.9: The distribution of second harmonic event plane angle (Ψ_2) from TPC in Au+Au collisions at $\sqrt{s_{NN}} = 200$ GeV (left) and 39 GeV (right). The red curves show a fit to the event plane angle distribution in both plots.

Because of the serious loss of acceptance for FTPCs due to partially non-functional readout electronics, the ϕ-weight method is not enough to generate a flat event plane distribution. Thus, further corrections are applied after ϕ-weight corrections using the shifting method [15]. The formula for the shift correction is as given below

$$\Psi^{'} = \Psi + \sum_{n} \frac{1}{n}[-\langle\sin(2n\Psi)\rangle\cos(2n\Psi) + \langle\cos(2n\Psi)\rangle\sin(2n\Psi)]. \tag{4.6}$$

The averages in Eq. 4.6 are taken from a large sample of events. In this analysis, the correction is done up to the 20th harmonic. The second harmonic event plane angle distributions from FTPC east (Ψ_2^{East}) and west (Ψ_2^{West}) are separately flattened and then the event plane angle distribution for full event is flattened. Accordingly, the observed v_2 and resolution are calculated using the shifted (sub)event plane azimuthal angles. Figure 4.10 shows the second harmonic event plane angle distribution from FTPC after shift corrections are applied. The distributions are fitted with a function $f(\Psi_2) = p_0(1 + 2p_1 cos(2\Psi_2))$ to check the flatness of the distribution. In this case the event plane angle distribution is flat and hence the v_2 measurement is free from detector acceptance bias.

A finite number of particles are used to calculate the event plane in an event, which leads to a limited resolution in the measured event plane angle. Therefore, the observed v_2 has to be corrected for the event plane resolution as

$$v_2 = \frac{v_2^{\mathrm{obs}}}{\langle\cos[2(\Psi_2 - \Psi_r)]\rangle}, \tag{4.7}$$

where v_2, v_2^{obs}, Ψ_2 and Ψ_r refer to the real v_2, observed v_2, the event plane angle and the real reaction plane angle. The denominator in the Eq. 4.7, $\langle\cos[2(\Psi_2 - \Psi_r)]\rangle$, is the event plane resolution [13]. The event plane resolution can be expressed as

$$\langle\cos[2(\Psi_2 - \Psi_r)]\rangle = \frac{\pi}{2\sqrt{2}}\chi_2 exp(-\chi_2^2/4) \times [I_0(\chi_2^2/4) + I_1(\chi_2^2/4)], \tag{4.8}$$

where $I_{0(1)}$ is the modified Bessel function of order 0(1) and

$$\chi_2 \equiv v_2/\sigma \text{ and } \sigma^2 = \frac{1}{2N}\frac{\langle w^2\rangle}{\langle w\rangle^2}, \tag{4.9}$$

where N is the number of particles used to calculate the event plane angle and w are the weights discussed previously.

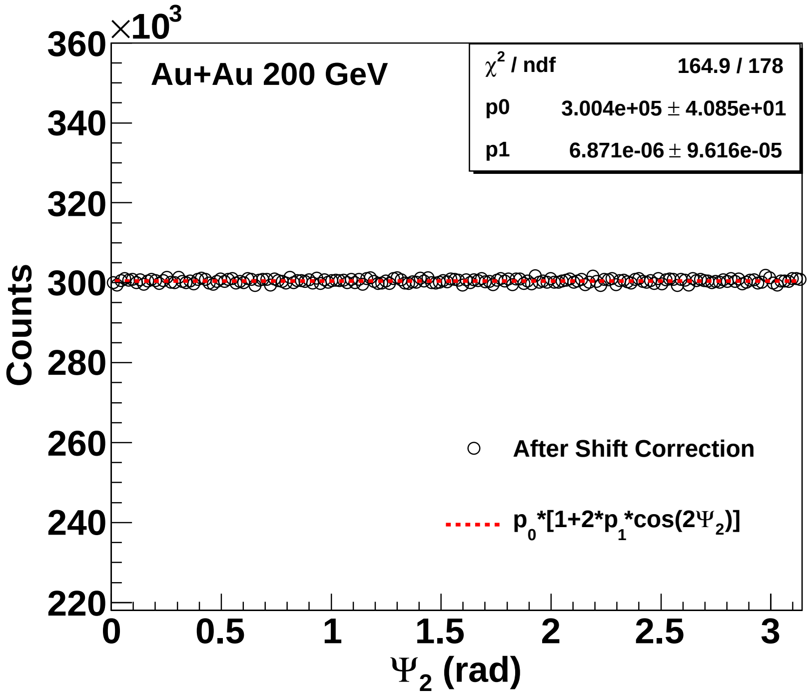

Figure 4.10: The distribution of second harmonic event plane angle (Ψ_2) from FTPC in Au+Au collisions at $\sqrt{s_{NN}}$ = 200 GeV. The red curve shows a fit to the event plane angle distribution.

The event plane resolution can be estimated by using the correlation of the event planes calculated from two independent sub-events of nearly equal multiplicity. The criteria which have been used for dividing the event into sub-events are random and pseudorapidity. Since the multiplicity of each sub-event A and B are approximately equal, their respective resolutions are expected to be equal. The resolution of each of them is given by:

$$\langle \cos[2(\Psi_2^A - \Psi_r)] \rangle \ = \sqrt{\langle \cos[2(\Psi_2^A - \Psi_2^B)] \rangle}. \tag{4.10}$$

To calculate the full event plane resolution, first the sub-event plane resolution i.e. $\langle \cos[2(\Psi_2^A - \Psi_r)] \rangle$ is calculated from Eq. 4.10. Then the sub-event plane resolution is used in Eq. 4.8 to extract the sub-event χ_2^A. Since the full event has twice as many particles as the sub-events, the full event χ_2 will be $\sqrt{2}$ times that of χ_2^A i.e. $\chi_2 = \sqrt{2}\chi_2^A$. The full event plane resolution is then calculated by putting this χ_2 value in Eq. 4.8.

Since the event plane resolution is dependent on the number of particles used in the calculation, it decreases for more peripheral collisions. Again the event plane is calculated using the anisotropic flow of the event itself, for more central collisions the resolution also reduces because the event anisotropy is small for more central collisions. In this analysis, the event plane resolution is calculated for small centrality bins $(0-5\%, 5-10\%, 10-20\%, 20-30\%, 30-40\%, 40-50\%, 50-60\%, 60-70\%, 70-80\%)$ within the minimum bias data set individually. The resolution for minimum bias $(0-80\%)$ collision is calculated by weighting the resolution of each centrality bin with the raw yield of the particle. The left panel of Fig. 4.11 shows the event plane resolution for TPC and FTPC event plane using pseudorapidity sub-events in Au+Au collisions at $\sqrt{s_{NN}} = 200$ GeV. The right panel of Fig. 4.11 shows the event plane resolution for TPC event plane using random sub-events in Au+Au collisions at $\sqrt{s_{NN}} = 39$ GeV. The resolution for minimum bias collisions is calculated by weighting the resolution of each centrality bin with ^3He raw yield, which is shown as the first data point (centrality below 0%) in each plot.

The ϕ-binning method was used to obtain the v_2 of nuclei in Au+Au collisions at $\sqrt{s_{NN}} = 200$ GeV and 39 GeV. In this method the raw yield of the identified particle (nuclei) is measured in different $\phi - \Psi$ bins, where ϕ is the azimuthal angle of the

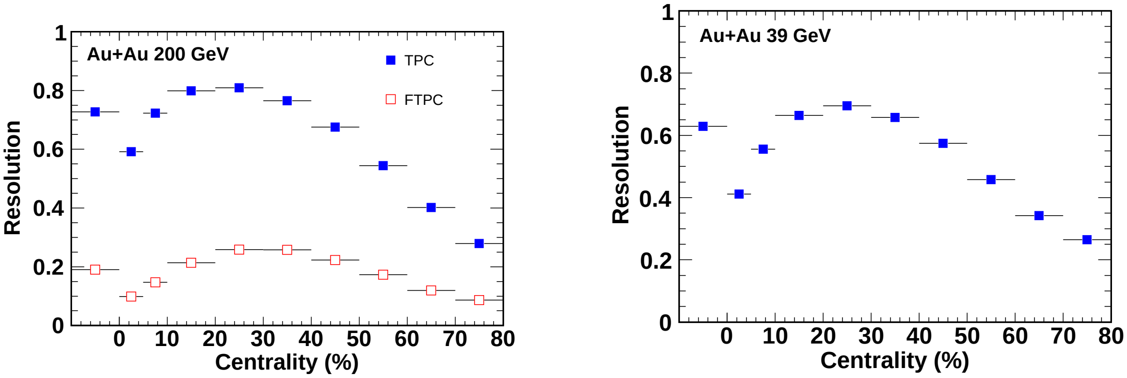

Figure 4.11: Event plane resolution as a function of centrality for TPC (solid square) and FTPC (open square) event plane in Au+Au collisions at $\sqrt{s_{NN}}$ = 200 GeV (left) and for TPC event plane in Au+Au collisions at $\sqrt{s_{NN}}$ = 39 GeV (right). See the text for details.

particle in the laboratory frame and Ψ is the event plane angle. Then the $\phi - \Psi$ distribution can be fitted with a functional form as

$$\frac{dN}{d(\phi - \Psi)} = p_0(1 + 2p_1 cos(2(\phi - \Psi))), \tag{4.11}$$

where the fit parameter p_1 is the observed v_2 (v_2^{obs}). The v_2^{obs} is then divided by the appropriate event plane resolution correction factor to obtain the final v_2. The p_T dependence of the elliptic flow can be measured by repeating the procedure in different p_T ranges. Figure 4.12 and Fig. 4.13 show the $\phi - \Psi$ distribution for ^3He and d in different p_T bins from minimum bias Au+Au collisions at $\sqrt{s_{NN}}$ = 200 GeV, respectively. Similarly, the $\phi - \Psi$ distribution for ^3He and d in different p_T bins from minimum bias Au+Au collisions at $\sqrt{s_{NN}}$ = 39 GeV are shown in Fig. 4.14 and Fig. 4.15, respectively.

4.2.7 Systematic Uncertainties

Systematic uncertainties on the v_2 measurement are estimated by varying the track cuts and the Z range to identify the light nuclei. In addition, two different detectors are used to determine the event plane for the measurement of v_2 of light nuclei. The systematic uncertainties on the v_2 for ^3He+$\overline{^3He}$ due to the variation of dca and $nHitsFit$ cut are of the order of 10% and 2% as shown in the Fig. 4.16 and Fig. 4.17, respectively. An additional systematic uncertainty on the v_2 for ^3He+$\overline{^3He}$ due to the

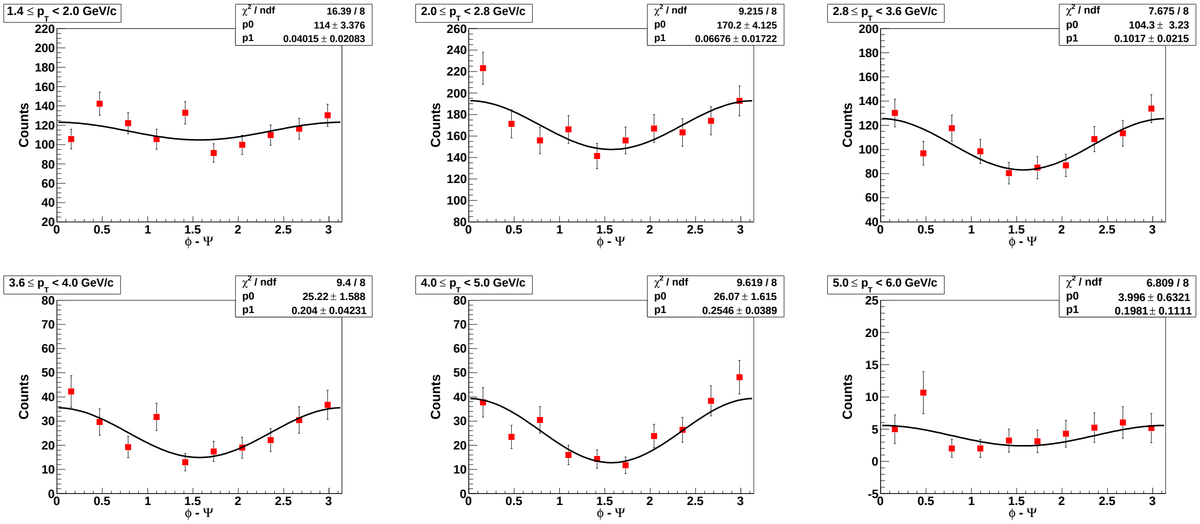

Figure 4.12: $\phi - \Psi$ distribution for ^3He in different p_T bins from minimum bias Au+Au collisions at $\sqrt{s_{NN}}$ = 200 GeV. Black curve is the fit to the $\phi - \Psi$ distribution.

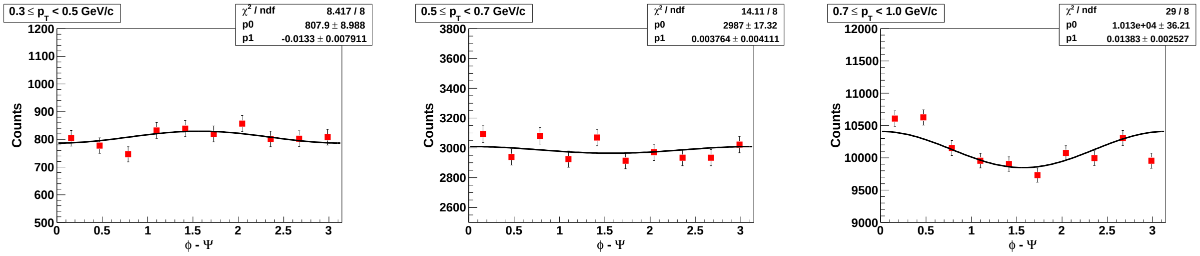

Figure 4.13: $\phi - \Psi$ distribution for d in different p_T bins from minimum bias Au+Au collisions at $\sqrt{s_{NN}}$ = 200 GeV. Black curve is the fit to the $\phi - \Psi$ distribution.

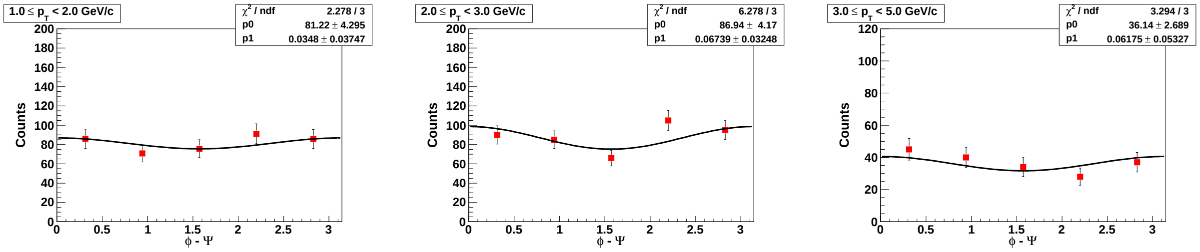

Figure 4.14: $\phi - \Psi$ distribution for ^3He in different p_T bins from minimum bias Au+Au collisions at $\sqrt{s_{NN}}$ = 39 GeV. Black curve is the fit to the $\phi - \Psi$ distribution.

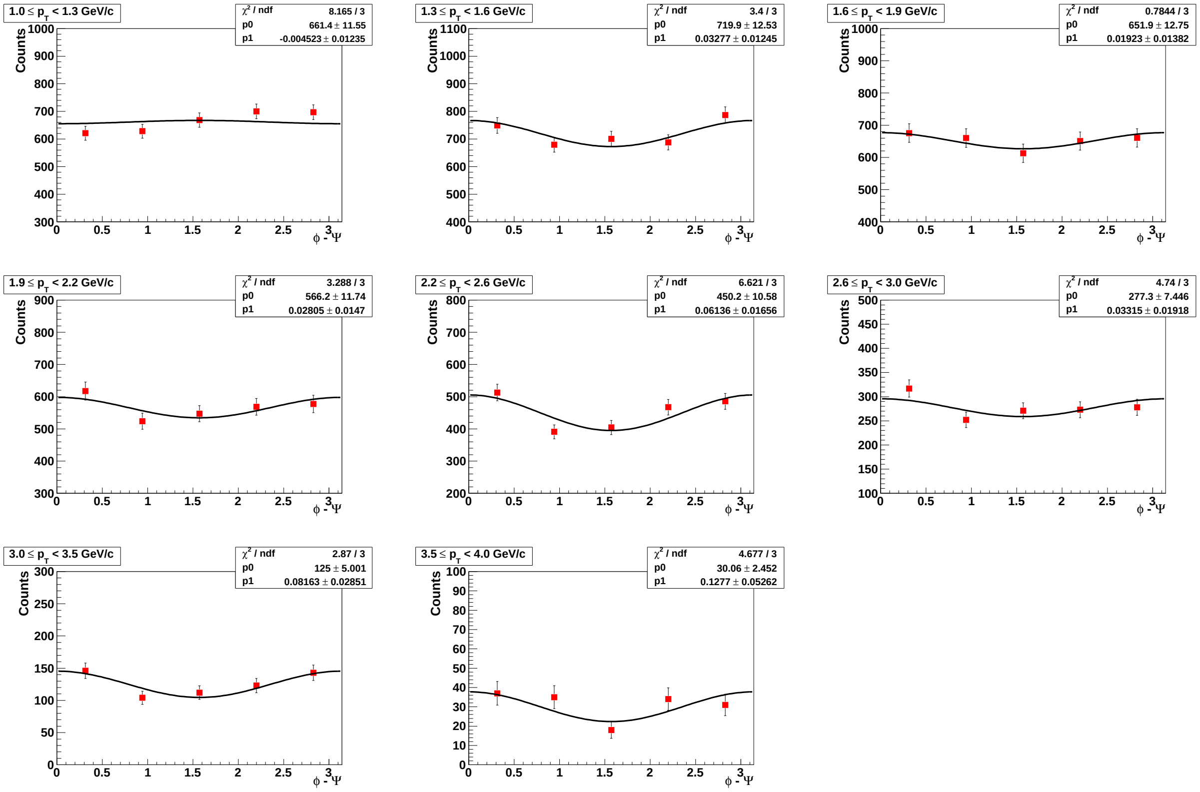

Figure 4.15: $\phi - \Psi$ distribution for d in different p_T bins from minimum bias Au+Au collisions at $\sqrt{s_{NN}}$ = 39 GeV. Black curve is the fit to the $\phi - \Psi$ distribution.

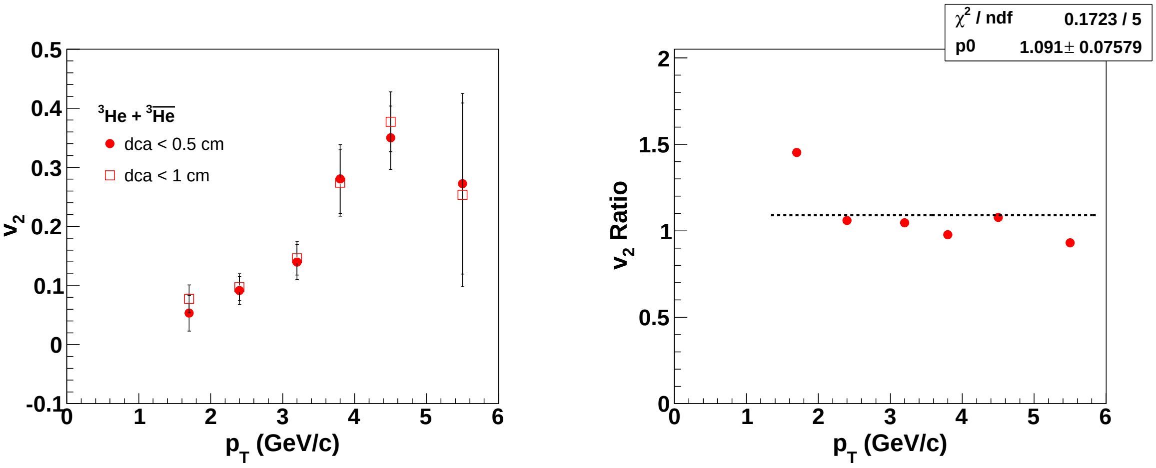

Figure 4.16: Left panel: Variation of v_2 for ^3He+$\overline{^3He}$ with the variation of dca cut in minimum bias Au+Au collisions at $\sqrt{s_{NN}} = 200$ GeV. Right panel: Ratio of measured v_2 for ^3He+$\overline{^3He}$ with $dca < 0.5$ cm and $dca < 1$ cm.

variation of Z range is of the order of 5% as shown in the Fig. 4.18. The statistical errors ($> 15\%$) on v_2 for ^3He+$\overline{^3He}$ is much larger than the estimated systematic errors.

4.3 Results and Discussion

4.3.1 Elliptic Flow Results

The light nuclei ($\overline{d}$, $\overline{t}$ and ^3He+$\overline{^3He}$) differential elliptic flow, $v_2(p_T)$, measured in Au+Au collisions at $\sqrt{s_{NN}} = 200$ GeV for minimum bias ($0-80\%$) collisions is shown in the Fig. 4.19. The v_2 of light nuclei measured by the STAR in year 2004 (run 4) Au+Au 200 GeV are also shown for the comparison [16]. The errors are statistical only. The v_2 of $\overline{d}$ is measured in low p_T ($p_T < 1$ GeV/c) only, since there was no TOF in run 7 Au+Au 200 GeV to improve particle identification at high p_T. The measured light nuclei v_2 from run 7 Au+Au 200 GeV is consistent with the previous results obtained from run 4 Au+Au 200 GeV with improved statistical uncertainties. The negative v_2 of $\overline{d}$ is observed in the low transverse momentum region. This negative v_2 at low p_T range is consistent with a large radial flow, as the Blast-Wave calculations show [16]. That is because the large radial flow pushes low p_T particles to high p_T and depleted low p_T particles, predominantly in the event plane [17]. The v_2 of $\overline{t}$ is shown

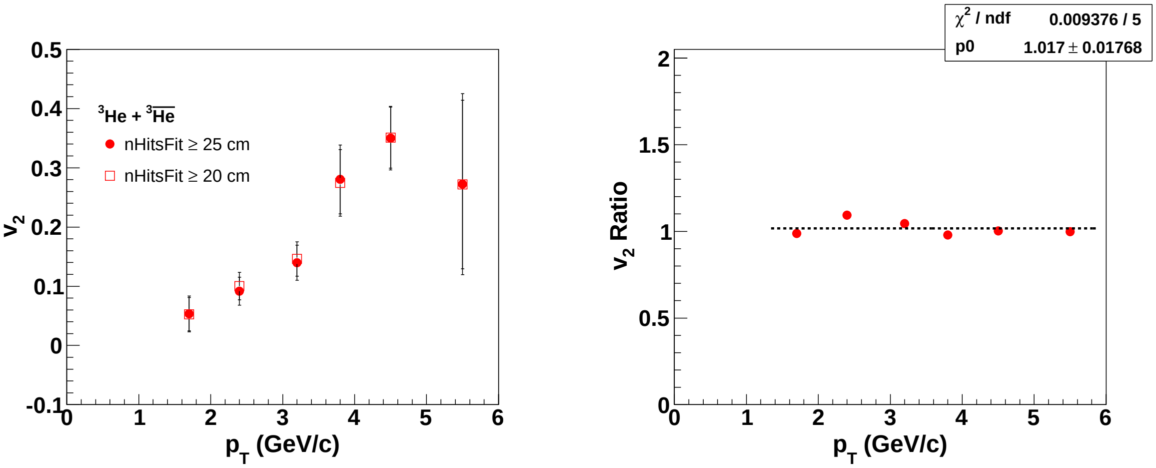

Figure 4.17: Left panel: Variation of v_2 for ^3He+$\overline{^3He}$ with the variation of $nHitsFit$ cut in minimum bias Au+Au collisions at $\sqrt{s_{NN}}$ = 200 GeV. Right panel: Ratio of measured v_2 for ^3He+$\overline{^3He}$ with $nHitsFit \geq 25$ and $nHitsFit \geq 20$.

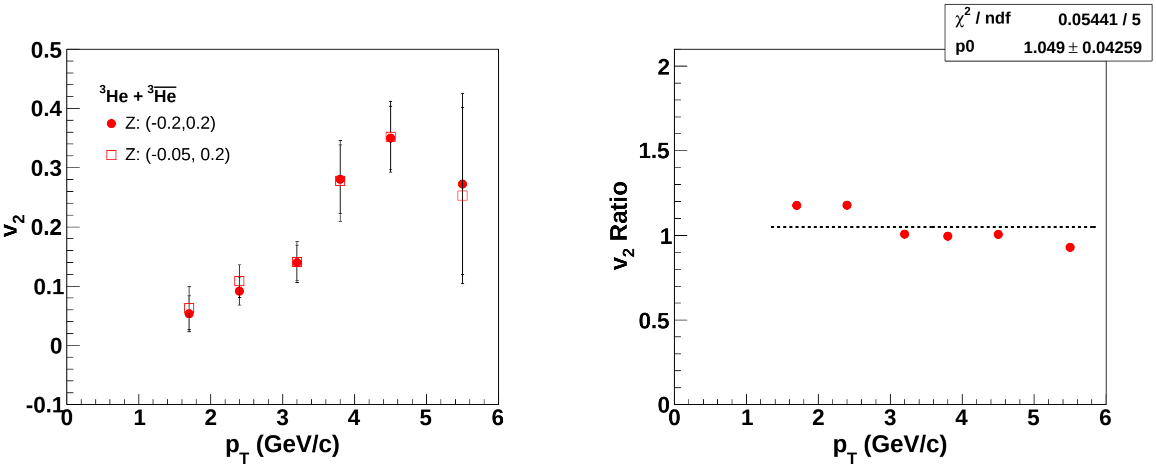

Figure 4.18: Left panel: Variation of v_2 for ^3He+$\overline{^3He}$ with the variation of Z range to identify ^3He candidates in minimum bias Au+Au collisions at $\sqrt{s_{NN}}$ = 200 GeV. Right panel: Ratio of measured v_2 for ^3He+$\overline{^3He}$ with $|Z(^3He)| < 0.2$ and $-0.05 < Z(^3He) < 0.2$.

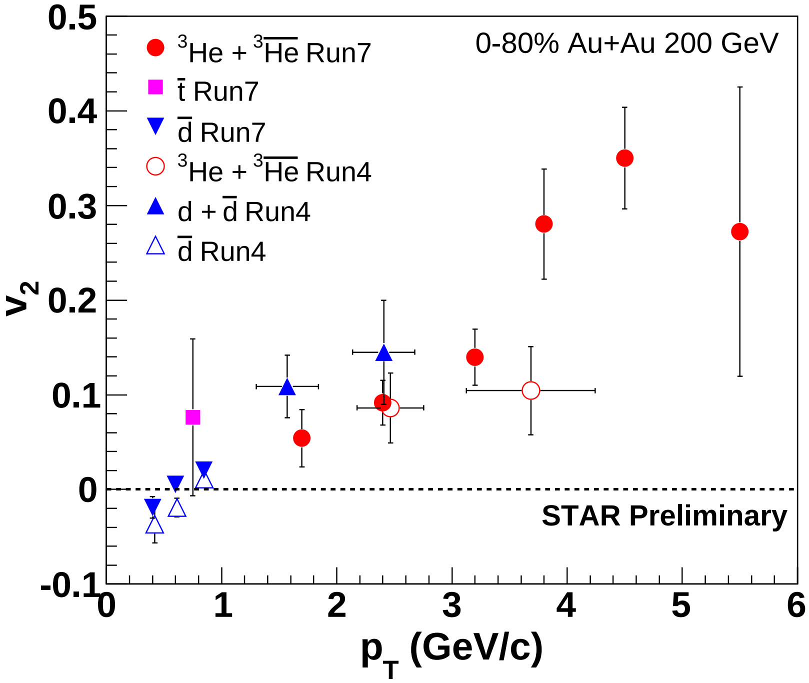

Figure 4.19: v_2 as a function of p_T for $d(\bar{d})$, $\bar{t}$, and ^3He+$\overline{^3He}$ from 0-80% of the collision centrality in Au+Au collisions at $\sqrt{s_{NN}}$ = 200 GeV. The light nuclei v_2 measured in run 4 Au+Au 200 GeV are shown in the plot as a comparison [16].

only for $0.3 < p_T < 1.2$ GeV/c. In future, high statistics data sets and good particle identification using STAR TPC and TOF will allow us to study the p_T dependence of v_2 for $t(\bar{t})$.

Figure 4.20 shows v_2 as a function of p_T for $\bar{d}$ and ^3He measured in Au+Au collisions at $\sqrt{s_{NN}}$ = 39 GeV for minimum bias $(0 - 80\%)$ collisions. At lower p_T (p_T < 1 GeV/c), v_2 of $\bar{d}$ is measured using TPC only, where as at higher p_T ($1 < p_T < 4$ GeV/c) both TPC and TOF are used. In case of ^3He, only TPC is used for the measurement of v_2 in the range $1 < p_T < 5$ GeV/c. The v_2 of $\bar{p}$ measured by the STAR is also shown for the comparison [18].

The results with both v_2 and transverse kinetic energy $KE_T = m_T - m$, where $m_T = \sqrt{p_T^2 + m^2}$ scaled by the mass number (A) for Au+Au collisions at $\sqrt{s_{NN}}$ = 200 GeV are shown in the Fig. 4.21. As a comparison, the v_2 of $\bar{p}$ and $\Lambda + \overline{\Lambda}$ are superimposed on the plot [19]. The dotted line is a fit to the v_2 of $\bar{p}$ using a fit

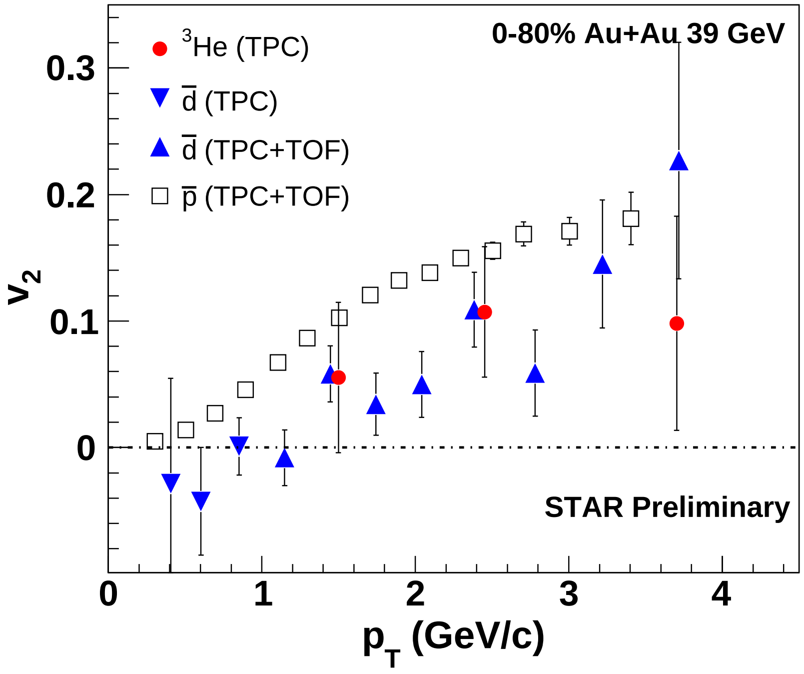

Figure 4.20: v_2 as a function of p_T for $\overline{d}$ and ^3He from 0-80% of the collision centrality in Au+Au collisions at $\sqrt{s_{NN}}$ = 39 GeV. v_2 of $\overline{p}$ is shown in the plot as a comparison [18].

Table 4.5: Fit parameters from the fit to the v_2 of $\overline{p}$ in Au+Au collisions at $\sqrt{s_{NN}}$ = 200 GeV and 39 GeV.

Parameters and χ^2/ndf	**Au+Au 200 GeV**	**Au+Au 39 GeV**
n	3.0 (fixed)	3.0 (fixed)
a	0.0453 ± 0.0191	0.2854 ± 0.0432
b	0.3593 ± 0.0569	0.2221 ± 0.1133
c	0.080 ± 0.022	0.5059 ± 0.0652
d	$-3.307 \times 10^{-4} \pm 1.548 \times 10^{-3}$	0.1158 ± 0.0372
χ^2/ndf	0.938/24	7.46/11

function (NCQ inspired function [20]) as mentioned in the Eq. 4.12.

$$f_{v_2}(n) = \frac{an}{1 + exp(-(p_T/n - b)/c)} - dn, \tag{4.12}$$

where a, b, c, and d are free parameters and n is fixed at 3. The values of the fit parameters n, a, b, c, and d as well as the χ^2/ndf of the above mentioned fit are listed in Table 4.5. The ratio of v_2/A of ^3He+$\overline{^3He}$ to $\overline{p}$ is close to unity. This suggests that the $^3He(\overline{^3He})$, $d(\overline{d})$ and baryon v_2 seem to follow the A scaling within errors, indicating that the light nuclei are formed through the coalescence of nucleons just before thermal freeze-out. Figure 4.22 shows the results with both v_2 and KE_T scaled by A for light nuclei in Au+Au collisions at $\sqrt{s_{NN}}$ = 39 GeV. The v_2 of $\overline{p}$ is superimposed on the plot [18], which is fitted with the same function as defined in the Eq. 4.12. The values of the fit parameters as well as the χ^2/ndf of this fit are listed in Table 4.5. The data suggest v_2 of ^3He and $\overline{d}$ seem to follow a weak mass number dependence in Au+Au collisions at $\sqrt{s_{NN}}$ = 39 GeV.

4.3.2 v_2/n_q vs KE_T/n_q

Figure 4.23 and Figure 4.24 show v_2/n_q as a function of KE_T/n_q for different hadrons including the nuclei and antinuclei in minimum bias Au+Au collisions at $\sqrt{s_{NN}}$ = 200 GeV and 39 GeV, respectively. Here n_q is the number of constituent quarks. The value of n_q used for $d(\overline{d})$ and $^3He(\overline{^3He})$ are 6 and 9 respectively, to account for their composite nature. The scaled results for v_2 versus KE_T for the light nuclei and antinuclei are consistent with the experimentally observed NCQ scaling of v_2 for

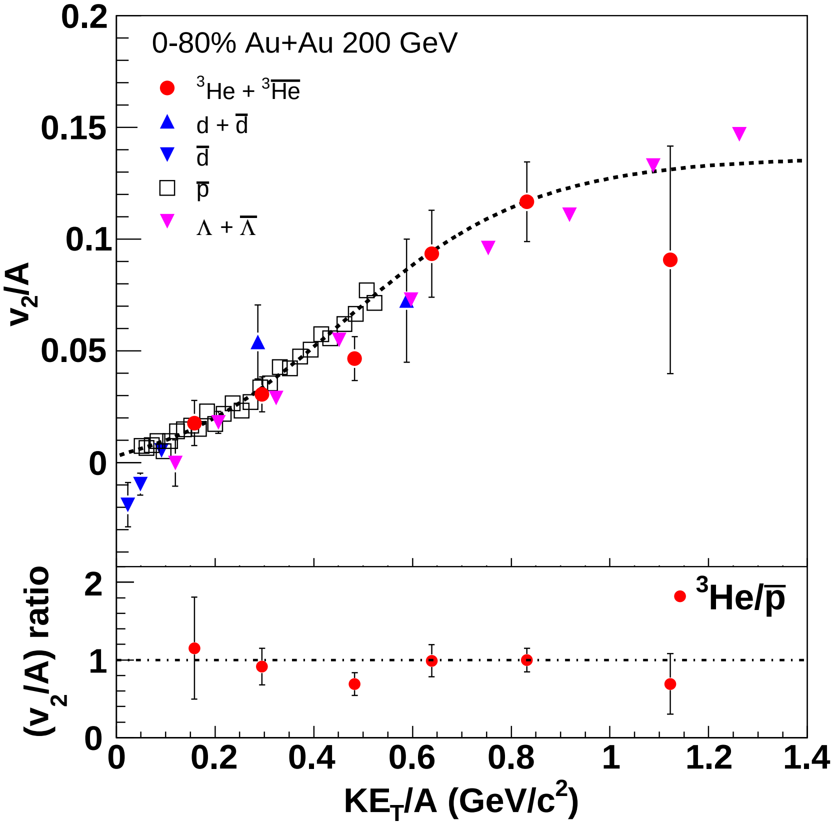

Figure 4.21: $d(\overline{d})$ and ^3He+$\overline{^3He}$ v_2 as a function of KE_T, both v_2 and KE_T have been scaled by A. $\overline{p}$ (open square) and $\Lambda + \overline{\Lambda}$ (solid inverted triangle) v_2 are shown in the plot as a comparison. The dotted line is a fit to the v_2 of $\overline{p}$. The ratio of ^3He+$\overline{^3He}$ to $\overline{p}$ is shown in the lower panel of the plot.

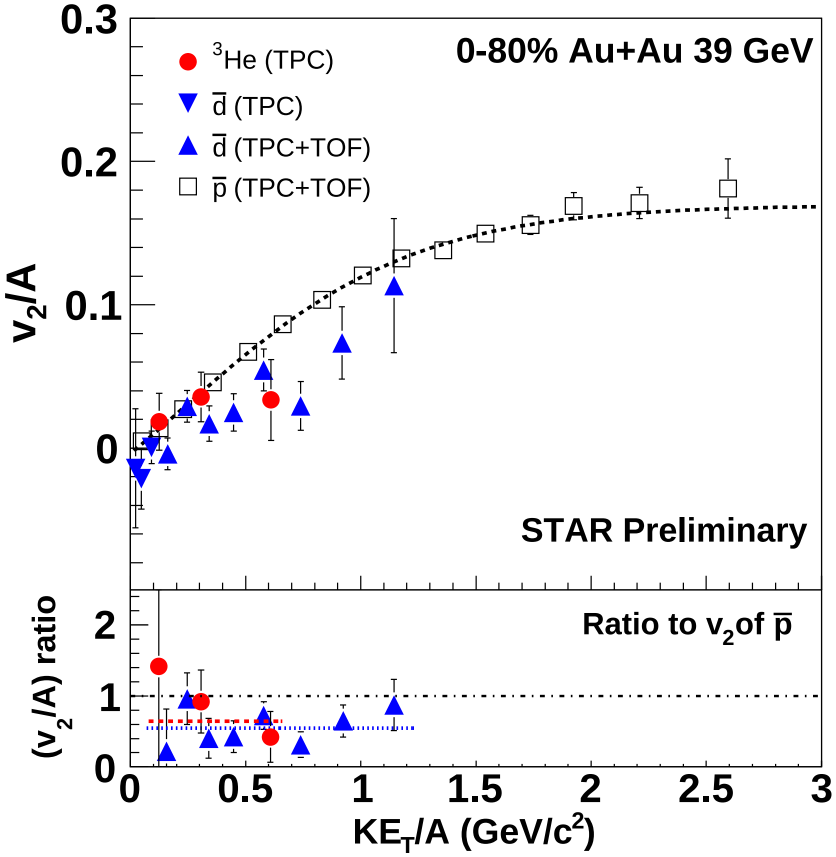

Figure 4.22: $\overline{d}$ and ^3He v_2 as a function of KE_T, both v_2 and KE_T have been scaled by A. $\overline{p}$ (open square) v_2 are shown in the plot as a comparison. The dotted line is a fit to the v_2 of $\overline{p}$. The ratio of $\overline{d}$ to $\overline{p}$ and ^3He to $\overline{p}$ is shown in the lower panel of the plot.

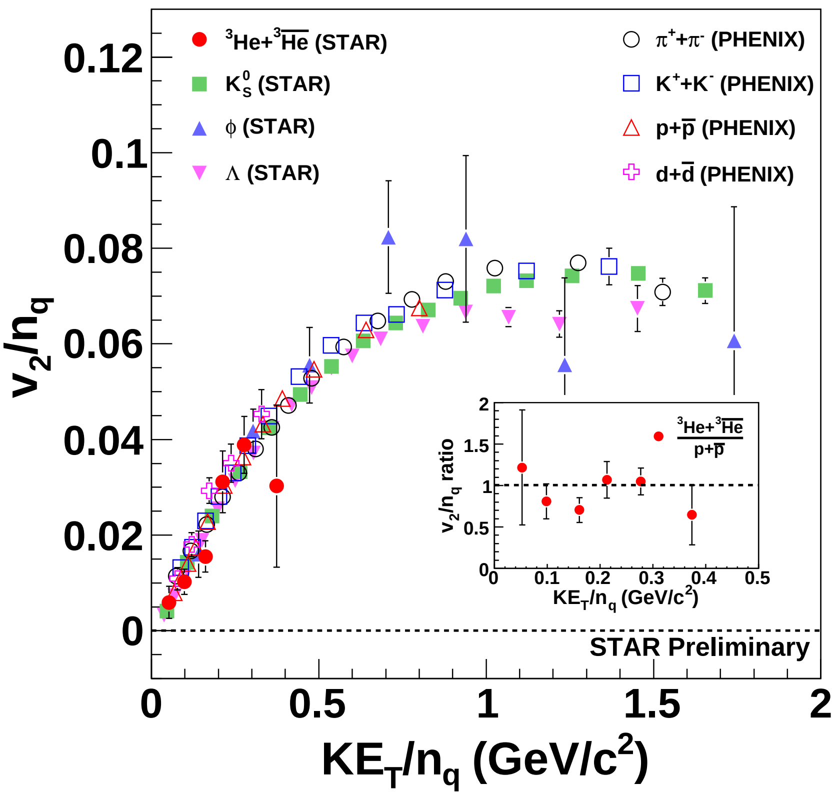

Figure 4.23: v_2/n_q as a function of KE_T/n_q for different particles in minimum bias Au+Au collisions at $\sqrt{s_{NN}}$ = 200 GeV. The inset is the ratio of ^3He+$\overline{^3He}$ to $p+\overline{p}$.

baryons and mesons [21]. This is also consistent with the picture that partonic collectivity dominates the transverse expansion dynamics of the nucleus-nucleus collisions at RHIC.

4.3.3 Centrality Dependence

The v_2 of ^3He integrated over the measured p_T range (i.e. $p_T > 1.4$ GeV/c) has been measured for three different centrality classes, $0-10\%$, $10-40\%$ and $40-80\%$ in Au+Au collisions at $\sqrt{s_{NN}}$ = 200 GeV. The number of participants (N_{part}), number of binary collisions (N_{bin}) and participant eccentricity (ε_{part}) obtained from Glauber calculation [22] for these three centrality bins are listed in Table 4.6. Figure 4.25 shows the integrated v_2 of ^3He as a function of centrality. The integrated v_2 of ^3He is higher in peripheral collisions compared to the central collisions. Figure 4.26 shows the

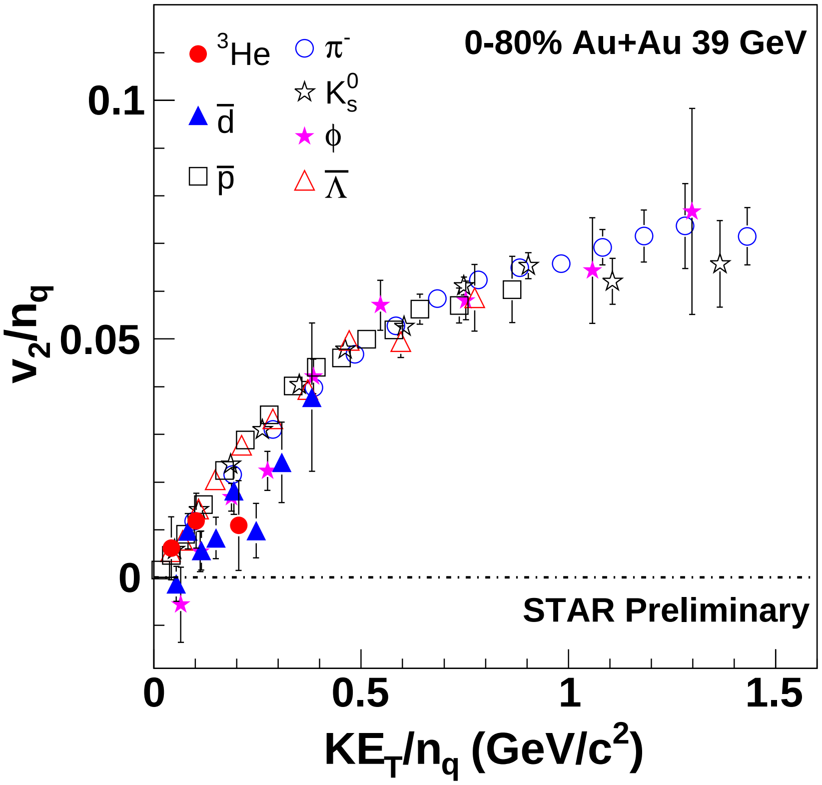

Figure 4.24: v_2/n_q as a function of KE_T/n_q for different particles in minimum bias Au+Au collisions at $\sqrt{s_{NN}}$ = 39 GeV.

Table 4.6: Initial geometric quantities for various collision centrality in Au+Au collisions at $\sqrt{s_{NN}}$ = 200 GeV [22].

% cross section	N_{part}	N_{coll}	ε_{part}
0-10	326 ± 6	939 ± 72	0.1054 ± 0.0001
10-40	173 ± 10	393 ± 47	0.2829 ± 0.0001
40-80	42 ± 7	57 ± 14	0.5343 ± 0.0002

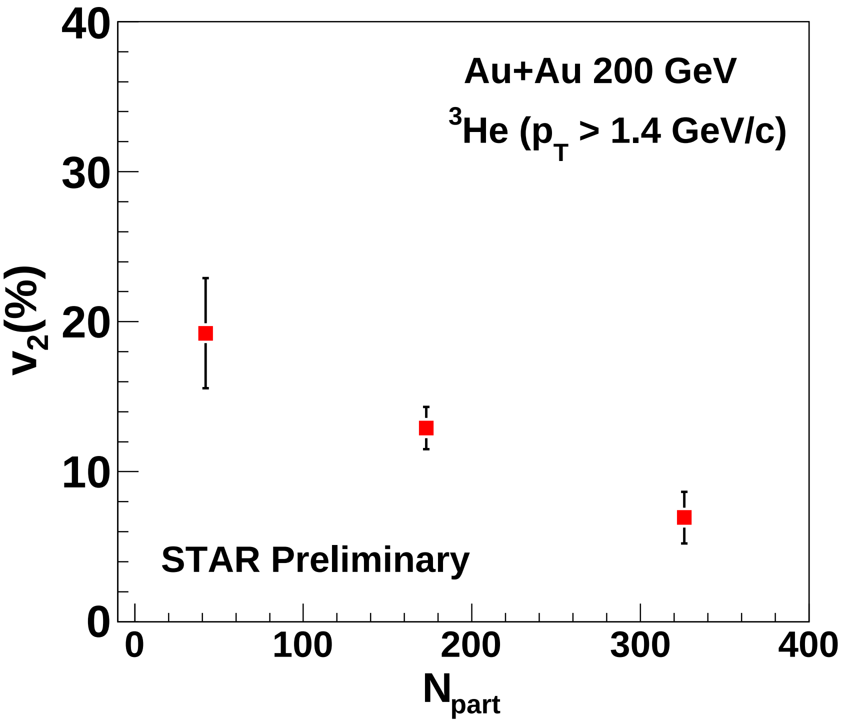

Figure 4.25: v_2 as a function of centrality for ^{3}He in Au+Au collisions at $\sqrt{s_{NN}}$ = 200 GeV. The shown errors are statistical only.

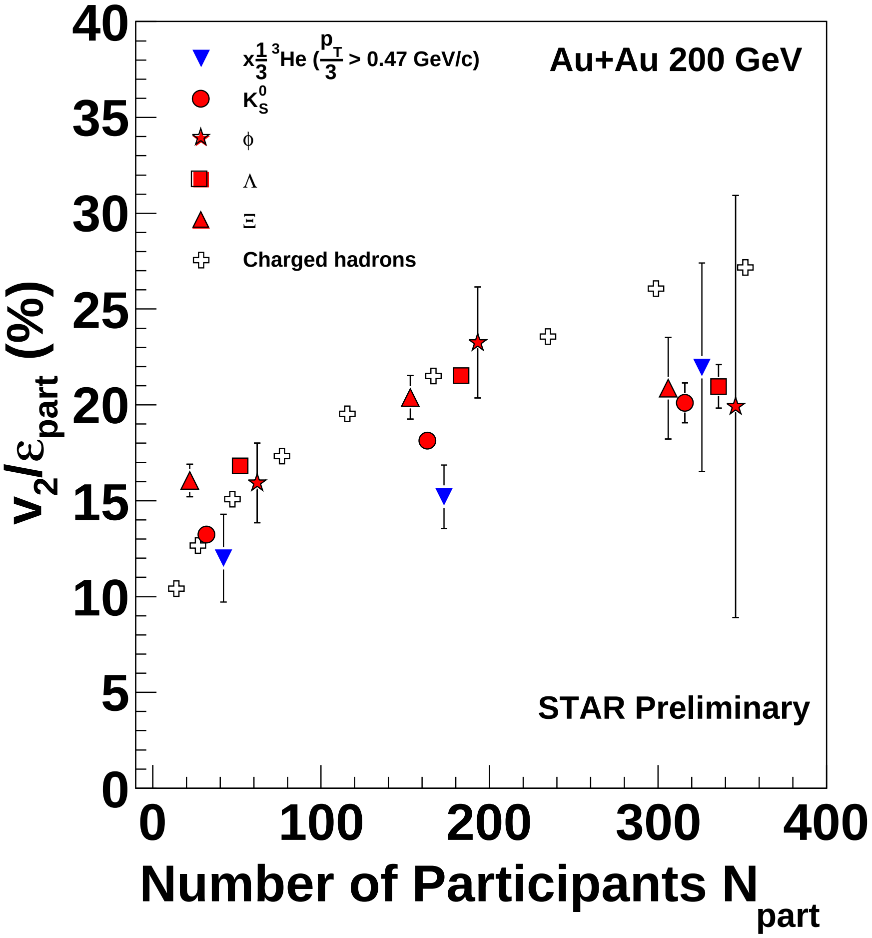

Figure 4.26: v_2/ε as a function of centrality for different particles in Au+Au collisions at $\sqrt{s_{NN}}$ = 200 GeV [22], the ^3He value is scaled down by a factor of 3. The errors shown here are statistical only.

centrality dependence of the ratio of the integrated v_2 over the eccentricity (v_2/ε_{part}) for charged hadrons, K_s^0, ϕ, Λ, Ξ and ^3He in Au+Au collisions at $\sqrt{s_{NN}}$ = 200 GeV. The v_2 of ^3He is integrated over the measured p_T range (i.e. $p_T > 1.4$ GeV/c) and scaled down by a factor of 3. To calculate integrated v_2 of identified particles (K_s^0, ϕ, Λ, and Ξ) including charged hadrons, the $v_2(p_T)$ were integrated over p_T weighted with the yield distribution from functions fitted to their respective spectra [22]. This ratio (v_2/ε_{part}), to some extent, reflects the strength of the collective expansion. For more central collision, the larger value of this ratio for ^3He, along with other hadrons, indicates a stronger collective expansion.

4.3.4 Blast-Wave Model and Mass Dependence

The Boltzmann-Gibbs Blast Wave (BGBW) model is a hydrodynamically motivated model with a compact set of parameters of temperature (T), flow velocity (β), and flow profile (ρ), which can describe the transverse momentum (p_T) distributions of particles with different masses [6, 11]. This model calculates particle production properties by assuming the particles are emitted thermally on top of a expanding fireball after the collision. This BGBW model gives quantitative predictions for different observables such as transverse momentum spectra, elliptic flow, and Hanburry-Brown-Twiss (HBT) radii [7]. However, such BGBW descriptions have limitations [8]. So, the Tsallis statistics [10] has been implemented in the Blast-Wave model (TBW) and applied successfully to describe the identified particle spectra and v_2 at mid-rapidity at RHIC [8, 9]. In TBW model, the sources of particle emission is changed from a Boltzmann distribution to a Tsallis distribution in the Blast-Wave model. We have used the same TBW model as in Ref. [9] for our study:

$$\frac{dN}{m_T dm_T d\phi} \propto m_T \int_0^{2\pi} d\phi_s \int_{-Y}^{+Y} dy \cosh(y) \times \int_0^R r dr (1 + \frac{q-1}{T} E_T)^{-1/(q-1)},$$

where the transverse energy $E_T = m_T \cosh(y)\cosh(\rho) - p_T \sinh(\rho)\cos(\phi_b - \phi)$, the flow profile in transverse rapidity

$\rho = \sqrt{(r\cos(\phi_s)/R_X)^2 + (r\sin(\phi_s)/R_Y)^2}(\rho_0 + \rho_2 \cos(2\phi_b))$,

and $\tan(\phi_b) = (R_X/R_Y)^2 \tan(\phi_s)$ relates the azimuthal angle of the coordinate space (ϕ_s) to the angle of the flow direction (ϕ_b) of the emitting source. The parameter q characterizes the degree of non-equilibrium. Figure 4.27 and Figure 4.28 show the TBW fit to the p_T spectra and v_2 of identified particles (π, K, and p) in minimum bias Au+Au collisions at $\sqrt{s_{NN}} = 200$ GeV, respectively. The p_T spectra and v_2 experimental data used for fitting are obtained from Refs. [11, 29, 19, 22]. The BW fitting parameters for the minimum bias data are listed in Table 4.7. The BW parameters obtained from the fits are used to predict the d, $\overline{d}$, ^3He and $\overline{^3He}$ spectra and v_2. The BW predictions and the experimental data for light nuclei agree with each other within the acceptable deviations.

The $< p_T >$ for identified particles π, p and ϕ are calculated using the Levy function fits to their corresponding p_T spectra, where as in case of ^3He the exponetial function is used. The integrated elliptic flow ($< v_2 >$) is calculated by convoluting

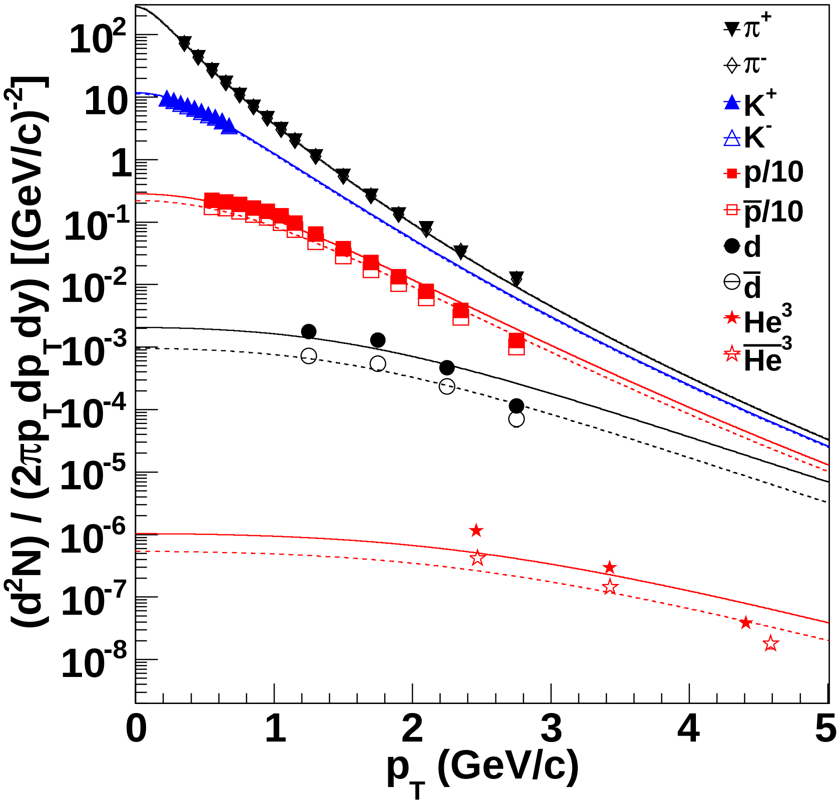

Figure 4.27: The transverse momentum spectra for identified particles including light nuclei ($d(\bar{d})$ and $^3He(\overline{^3He})$) in minimum bias ($0-80\%$ centrality) Au+Au collisions at $\sqrt{s_{NN}} = 200$ GeV. The symbols represent experiment data points. The curves represent the TBW fit for the hadrons. The curves for the light nuclei are the TBW prediction using parameters from the fit to other hadrons.

Table 4.7: Values of parameters and best χ^2 from TBW fit to identified particle p_T spectra and v_2 in minimum bias Au+Au collisions at $\sqrt{s_{NN}} = 200$ GeV.

T (MeV)	q	ρ_0	ρ_2	$\frac{R_X}{R_Y}$	χ^2/ndf
88.3 ± 1.2	1.049 ± 0.003	0.86 ± 0.013	0.054 ± 0.001	0.89 ± 0.002	512.6 /137

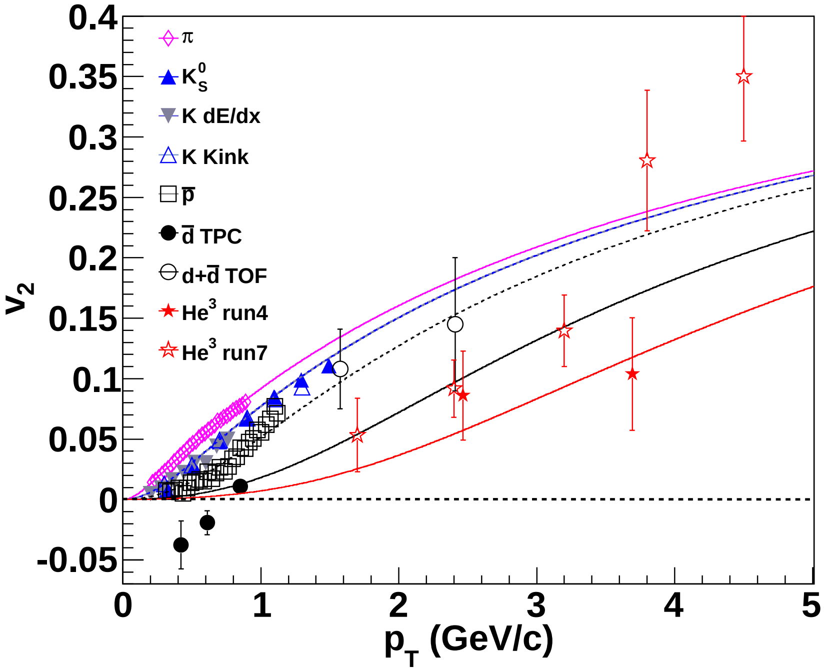

Figure 4.28: v_2 as a function of p_T for identified particles including light nuclei ($d(\overline{d})$ and $^3He(\overline{^3He})$) in minimum bias ($0-80\%$ centrality) Au+Au collisions at $\sqrt{s_{NN}}$ = 200 GeV. The symbols represent experiment data points. The curves represent the TBW fit for the hadrons. The curves for the light nuclei are the TBW prediction using parameters from the fit to other hadrons.

the differential $v_2(p_T)$ with the transverse momentum spectra as:

$$< v_2 >= \frac{\int v_2(p_T) dN/dp_T dp_T}{\int dN/dp_T dp_T}. \tag{4.13}$$

To calculate the $< v_2 >$ for ^3He and other identified particles each $v_2(p_T)$ distribution is fitted with the function as mentioned in Eq. 4.12, which was inspired by parameterizations of quark number scaling [20]. Since the p_T spectra and $v_2(p_T)$ measurements are restricted to a limited p_T range due to the available statistics, extrapolations down to $p_T = 0$ GeV/c and up to higher p_T are made. The statistical errors in $< p_T >$ and $< v_2 >$ are calculated by taking lower and upper limit of errors on the fitting parameters. An error band of 5% is assumed for BW predicted $< p_T >$ and $< v_2 >$ for ^3He and other identified particles. The mass dependence of mean v_2 and mean transverse momenta ($< p_T >$) for identified particles (π, K, p, ϕ, d and ^3He) in minimum bias Au+Au collisions at $\sqrt{s_{NN}}$ = 200 GeV and the predictions from the Blast-Wave (BW) model are shown in Fig. 4.29. The v_2 of ^3He integrated over the measured p_T range (i.e. $p_T > 1.4$ GeV/c) from FTPC event plane is shown for the comparison. Both v_2 and $< p_T >$ trends are consistent with expectations from Blast-Wave model fit. The v_2 values up to ^3He mass has reasonable agreement within the BW formalisim, but differences seen in $< p_T >$ beyond ϕ meson mass.

4.3.5 Collision Energy Dependence

The collision energy dependence of $v_2(p_T)$ for the light nuclei ($d(\overline{d})$ and $^3He(\overline{^3He})$) is studied by comparing the results from minimum bias Au+Au collisions at $\sqrt{s_{NN}}$ = 200 GeV and 39 GeV as shown in Fig. 4.30. As a comparison, the $\overline{p}$ v_2 from minimum bias Au+Au collisions at $\sqrt{s_{NN}}$ = 200 GeV and 39 GeV are superimposed on the plot [18, 19]. Due to the limited statistics in the Au+Au 200 GeV and 39 GeV data set, the statistical errors on v_2 of light nuclei are large. Within the large statistical uncertainties, the v_2 of light nuclei seems to be consistent in these two different collision energies.

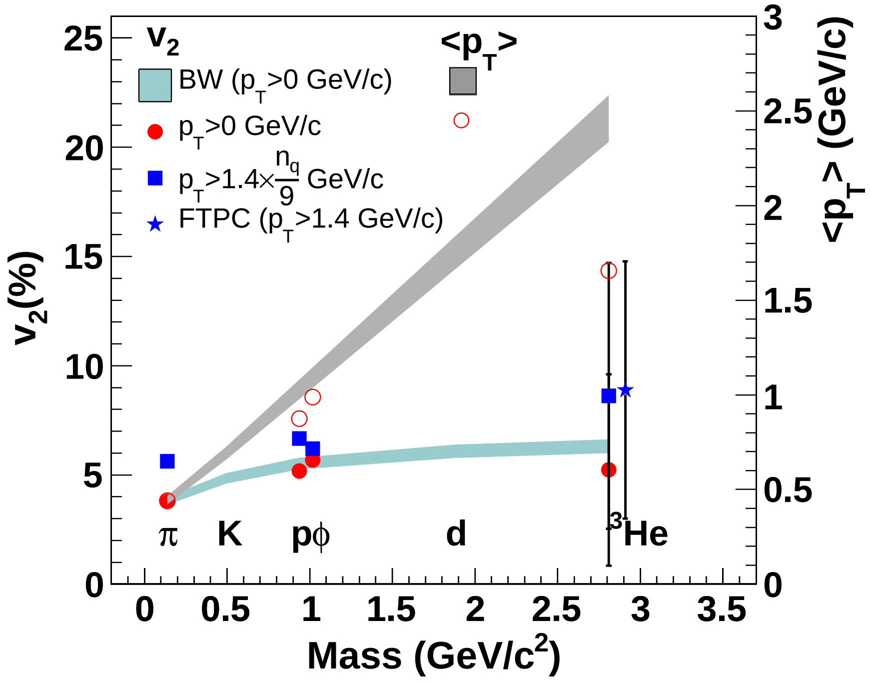

Figure 4.29: Mean v_2 and mean transverse momenta for identified particles $(\pi, K, p, \phi, d$ and $^3He)$ as a function of particle mass in minimum bias Au+Au collisions at $\sqrt{s_{NN}} = 200$ GeV. Blast-Wave model calculations are also shown as shaded bands.

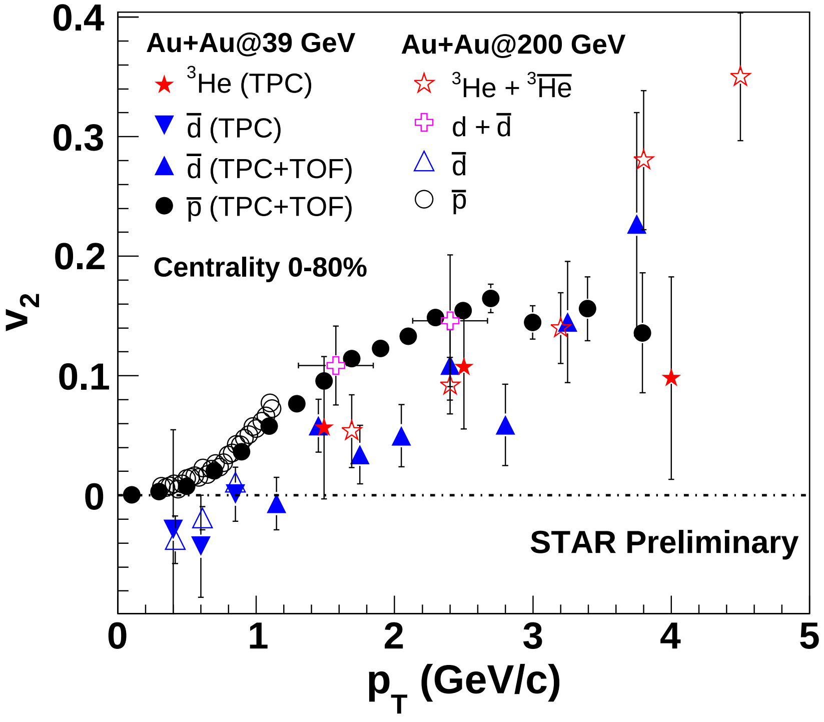

Figure 4.30: v_2 as a function of p_T for $d(\overline{d})$ and $^3He(\overline{^3He})$ from 0-80% of the collision centrality in Au+Au collisions at $\sqrt{s_{NN}}$ = 200 GeV and 39 GeV. v_2 of $\overline{p}$ at the two energies are shown for the comparison [18, 19].

4.3.6 Dynamical Coalescence Model

The light nuclei and antinuclei are formed through coalescence of nucleons and antinucleons in the relativistic heavy ion collisions [2, 3, 4]. A popular model for describing the production of light clusters in heavy ion collisions is the dynamical coalescence model, which has been used extensively at both intermediate [30, 31] and high energies [32, 33]. In this model, the probability for producing a cluster is determined by the overlap of its Wigner phase-space density and the nucleon phase-space distribution at freeze-out. The multiplicity of a M-nucleon cluster in a heavy ion collision is given by

$$N_M = G \int d\mathbf{r}_{i_1} d\mathbf{q}_{i_1} ... d\mathbf{r}_{i_{M-1}} d\mathbf{q}_{i_{M-1}} \times \langle \sum_{i_1 > i_2 > ... > i_M} \rho_i^W (\mathbf{r}_{i_1} \mathbf{q}_{i_1} ... \mathbf{r}_{i_{M-1}} \mathbf{q}_{i_{M-1}}) \rangle \tag{4.14}$$

where $\mathbf{r}_{i_1} ... \mathbf{r}_{i_{M-1}}$ and $\mathbf{q}_{i_1} ... \mathbf{q}_{i_{M-1}}$ are, respectively, the M-1 relative coordinates and momenta in the M-nucleon rest frame, ρ_i^W is the Wigner phase-space density of the M-nucleon cluster, and $\langle ... \rangle$ denotes the event averaging. The spin-isospin statistical factor G is 3/8 for d and 1/3 for t and ^3He [31].

For light nuclei, the Wigner phase-space densities are obtained from their internal wave functions, which are taken to be those of a spherical harmonic oscillator [34, 35],

$$\psi = (3\pi^2 b^4)^{-3/4} exp(-\frac{\rho^2 + \lambda^2}{2b^2}) \tag{4.15}$$

The Wigner phase-space densities are then given by

$$\rho^W = 8^2 exp(-\frac{\rho^2 + \lambda^2}{b^2}) exp(-(\mathbf{k}_\rho^2 + \mathbf{k}_\lambda^2) b^2) \tag{4.16}$$

where (ρ, λ) and $(\mathbf{k}_\rho, \mathbf{k}_\lambda)$ are the relative coordinates and momenta, respectively. The parameter b is determined to be 1.96 fm for d, 1.61 fm for t and 1.74 fm for ^3He from their measured root-mean-square radii [36, 37].

The coordinate and momentum space distributions of nucleons at freeze-out are taken from a multiphase transport (AMPT) model within the string melting scenario [38]. The parton scattering cross section of 10 mb has been used in the model. The AMPT model is a hybrid model that uses minijet partons from hard processes and strings from soft processes in the Heavy Ion Jet Interaction Generator (HIJING) model [39] as the initial conditions for modeling heavy ion collisions at ultrarelativistic energies. Scatterings among partons are modeled by Zhang's parton cascade

(ZPC) [40] model, which at present includes only two-body scatterings with cross sections obtained from the pQCD with screening masses. In the default AMPT model, partons are recombined with their parent strings when they stop interacting, and the resulting strings are converted to hadrons using the Lund string fragmentation model as implemented in the PYTHIA program [41]. The final state hadronic scatterings are modeled by a relativistic transport (ART) model [42]. Since the initial energy density in heavy ion collisions at RHIC is much larger than the critical energy density at which the hadronic matter to QGP transition would occur [43, 44], the AMPT model has been extended by converting initial excited strings into partons [45]. In this string-melting scenario, hadrons that would have been produced from string fragmentation are converted instead to their valence quarks and/or antiquarks. Interactions among these quarks are again described by the ZPC parton cascade model. Since inelastic scatterings are at present not included, the resulting partonic matter consists of only quarks and antiquarks from melted strings. To take into account the effect of stronger scattering among gluons if they were present, the scattering cross sections between quarks and antiquarks are taken to be the same as those for gluons. These quarks and antiquarks are converted to hadrons when they stop scattering with other partons. The transition from partonic matter to hadronic matter is achieved using a simple coalescence model, which combines the two nearest quark and antiquark into mesons and three nearest quarks or antiquarks into baryons or antibaryons that are close to the invariant mass of these partons. Details of the AMPT model can be found in Ref. [38]. Figure 4.31 shows v_2 as a function of p_T for $\overline{p}$, $d(\overline{d})$ and $^3He + \overline{^3He}$ in minimum bias Au+Au collisions at $\sqrt{s_{NN}} = 200$ GeV. The v_2 of $\overline{p}$, $d(\overline{d})$, and $^3He(\overline{^3He})$ are well described by the dynamical coalescence model [33], which indicates that the light nuclei and antinuclei are formed through coalescence of nucleons and antinucleons.

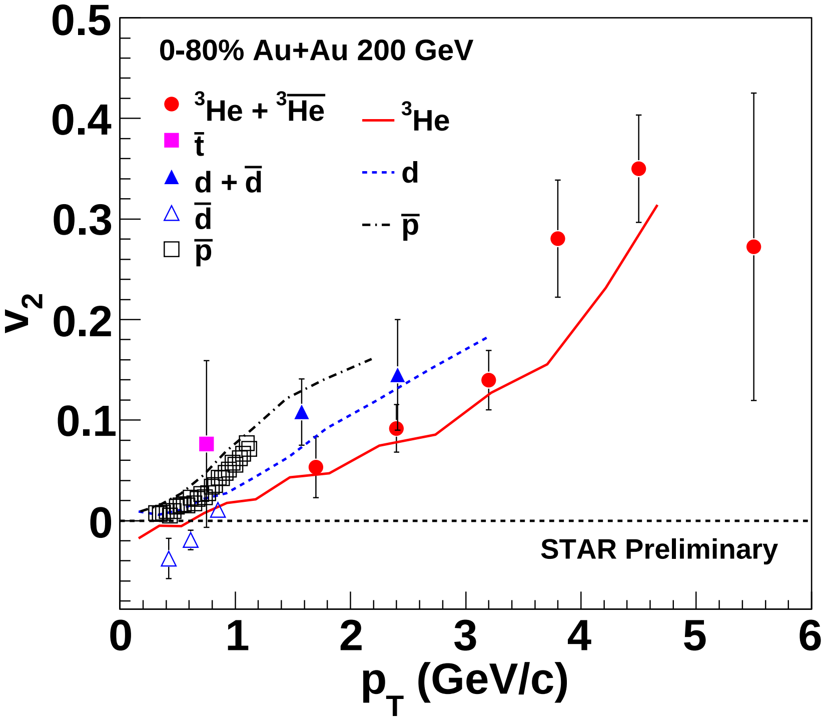

Figure 4.31: v_2 as a function of p_T for $d(\overline{d})$, $\bar{t}$, and ^3He+$\overline{^3He}$ from 0-80% of the collision centrality. v_2 of $\overline{p}$ is shown in the plot as a comparison [19]. The lines are calculations using a dynamical coalescence model [33]. See text for details.

Bibliography

[1] R. Fries *et al.*, Ann. Rev. Nucl. Part. Sci. **58**, 177 (2008).

[2] H. H. Gutbrod *et al.*, Phys. Rev. Lett. **37**, 667 (1976).

[3] R. Scheibl and U. Heinz, Phys. Rev. C **59**, 1585 (1999); W. J. Llope *et al.*, Phys. Rev. C **52**, 2004 (1995).

[4] H. Sato and K. Yazaki, Phys. Lett. B **98**, 153 (1981).

[5] S. T. Butler and C. A. Pearson, Phys. Rev. **129**, 836 (1963).

[6] F. S. Bieser *et al.*, Nucl. Instr. Meth. A **499**, 766 (2003).

[7] W. J. Llope *et al.*, Nucl. Instr. Meth. A **522**, 252 (2004).

[8] K. H. Ackermann *et.al.* (STAR Collaboration), Nucl. Instr. Meth. A **499**, 624 (2003).

[9] W. J. Llope *et.al.*, Nucl. Instr. Meth. B **241**, 306 (2005).

[10] M. Shao *et al.*, Nucl. Instr. Meth. A **558**, 419 (2006).

[11] H. Bichsel, Nucl. Instr. Meth. A **562** 154 (2006).

[12] Run 7 Au+Au 200 GeV centrality selection.
http://www.star.bnl.gov/protected/lfspectra/atimmins/AuAu200GeV/Centrality/page.html

[13] A. M. Poskanzer and S. A. Voloshin, Phys. Rev. C **58**, 1671 (1998).

[14] N. Borghini, P. M. Dinh and J. Y. Ollitrault, Phys. Rev. C **62**, 034902 (2000).

[15] J. Barrette *et al.* (E877 Collaboration), Phys. Rev. C **56**, 3254 (1997).

[16] B. I. Abelev *et al.* (STAR Collaboration), arXiv:nucl-ex/0909.0566.

[17] P. Huovinen *et al.*, Phys. Lett. B **503**, 58 (2001).

[18] A. Schmah (for the STAR Collaboration), J. Phys. G **38**, 124049 (2011).

[19] J. Adams *et al.* (STAR Collaboration), Phys. Rev. C **72**, 014904 (2005).

[20] X. Dong, S. Esumi, P. Sorensen, N. Xu, and Z. Xu, Phys. Lett. B **597**, 328 (2004).

[21] B. I. Abelev *et al.* (STAR Collaboration), Phys. Rev. Lett. **99**, 112301 (2007); A. Adare *et al.* (PHENIX Collaboration), Phys. Rev. Lett. **98**, 162301 (2007).

[22] B. I. Abelev *et al.* (STAR Collaboration), Phys. Rev. C **77**, 054901 (2008).

[23] E. Schnedermann, J. Sollfrank, and U. W. Heinz, Phys. Rev. C **48**, 2462 (1993).

[24] F. Retiere and M. A. Lisa, Phys. Rev. C **70**, 044907 (2004).

[25] Z. Tang *et al.*, Phys. Rev. C **79**, 051901 (R) (2009); M. Shao *et. al.*, J. Phys. G **37**, 085104 (2010).

[26] Z. Tang *et al.*, arXiv:nucl-ex/1101.1912.

[27] C. Tsallis, J. Stat. Phys. **52**, 479 (1988).

[28] J. Adams *et al.* (STAR Collaboration), Phys. Rev. Lett. **92**, 112301 (2004).

[29] B. I. Abelev *et al.* (STAR Collaboration), Phys. Rev. Lett. **97**, 152301 (2006).

[30] M. Gyulassy, K. Frankel, E. A. Relmer, Nucl. Phys. A **402**, 596 (1983); J. Aichelin *et al.*, Phys. Rev. Lett. **58**, 1926 (1987); V. Koch *et al.*, Phys. Lett. B **241**, 174 (1990).

[31] L. W. Chen, C.M. Ko, B. A. Li, Phys. Rev. C **68** 017601 (2003); Nucl. Phys. A **729**, 809 (2003).

[32] J. L. Nagle *et al.*, Phys. Rev. C **53**, 367 (1996); R. Mattiello *et al.*, Phys. Rev. C **55**, 1443 (1997); L. W. Chen, C. M. Ko, Phys. Rev. C **73**, 044903 (2006).

[33] Y. S. Oh and C. M. Ko, Phys. Rev. C **76**, 054910 (2007); S. Zhang *et al.*, Phys. Lett. B **684**, 224 (2010).

[34] R. Scheibl, U. Heinz, Phys. Rev. C **59**, 1585 (1999).

[35] A. T. M. Aerts, C. B. Dover, Phys. Rev. D **28**, 450 (1983).

[36] T. Ericsson, W. Weise, Pions and Nuclei, Clarendon, Oxford, 1988.

[37] C. R. Chen, G. L. Payne, J. L. Friar, B. F. Gibson, Phys. Rev. C **33**, 1740 (1986).

[38] Z. W. Lin, C. M. Ko, B. A. Li, B. Zhang, and S. Pal, Phys. Rev. C **72**, 064901 (2005).

[39] X. N. Wang and M. Gyulassy, Phys. Rev. D **44**, 3501 (1991).

[40] B. Zhang, Comput. Phys. Commun. **109**, 193 (1998).

[41] T. Sjostrand, Comput. Phys. Commun. **82**, 74 (1994).

[42] B. A. Li and C. M. Ko, Phys. Rev. C **52**, 2037 (1995); B. A. Li, A. T. Sustich, B. Zhang, and C. M. Ko, Int. J. Phys. E **10**, 267 (2001).

[43] B. Zhang, C. M. Ko, B. A. Li, Z. Lin, and B. H. Sa, Phys. Rev. C **62**, 054905 (2000); L. W. Chen and C. M. Ko, Phys. Lett. B **634**, 205 (2006).

[44] D. Kharzeev and M. Nardi, Phys. Lett. B **507**, 121 (2001).

[45] Z. W. Lin and C. M. Ko, Phys. Rev. C **65**, 034904 (2002).

Chapter 5

Search for Anti-Alpha

5.1 Introduction

Ultrarelativistic heavy ion collisions can produce high temperature and high energy density matter, similar to the big bang at the beginning of the universe. In both cases, matter and antimatter are formed with comparable abundance. However, it is still a mystery how this matter-antimatter symmetry got lost in the evolution of the universe with no significant amount of antimatter apparently being present. Nuclei are abundant in the universe today, but antinuclei heavier than antiproton have been observed only as rare products of interactions at particle accelerators [1, 2]. The antimatter helium-4 nucleus ($^4\overline{He}$), also known as the anti-α, consists of two antiprotons and two antineutrons. It has not been observed previously, although the α particle was identified a century ago by Rutherford. The relatively short-lived expansion in nuclear collisions allows antimatter to decouple quickly from matter, and avoid annihilation. Thus, the high energy accelerator of heavy nuclei provides a favorable environment for producing and studying antimatter.

5.2 Methods for Searching Anti-Alpha

In year 2007 (run 7) Au+Au 200 GeV, STAR's main TPC [3] was used for tracking and identification of charged particles. Measurements of the ionization energy loss (dE/dx) of charged tracks in the TPC gas are used to identify the light nuclei such as

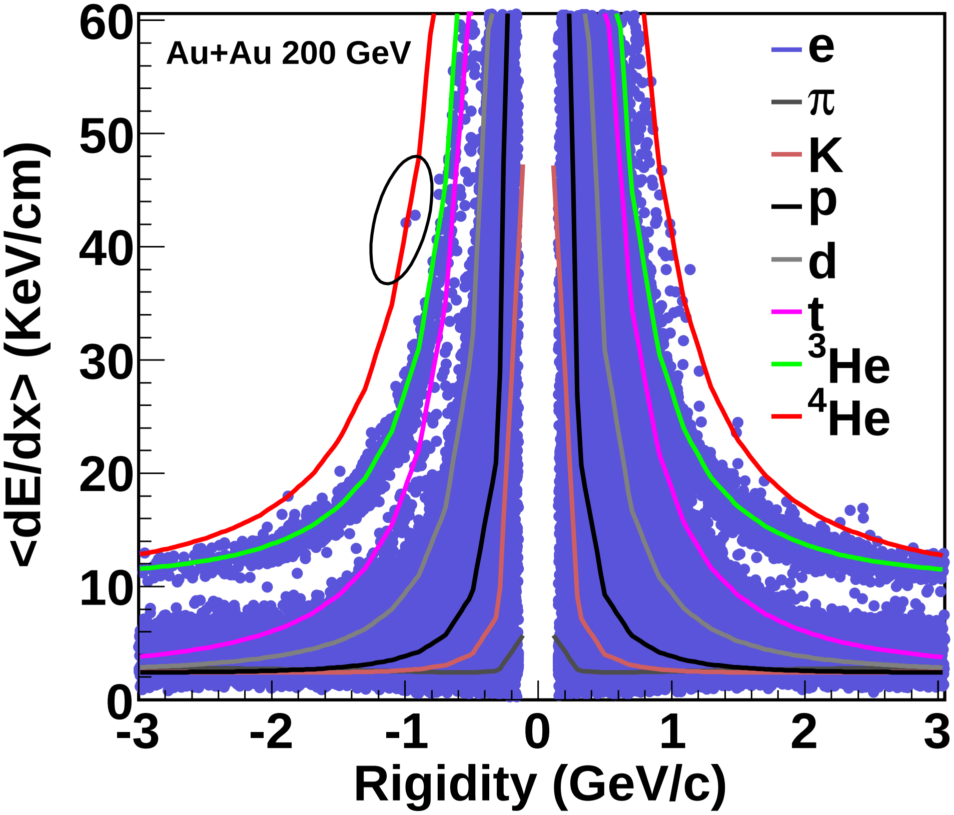

Figure 5.1: TPC dE/dx as a function of rigidity. Different color lines are expected dE/dx values for different charged tracks predicted by the Bichsel function [4]. The two $^4\overline{He}$ candidates are encircled by an ellipse.

Table 5.1: Track selection criteria for identification of light nuclei.

Cut Description	**Value**
$\lvert\eta\rvert$	< 1.0
dca	< 1.0 cm
$nHitsFit$	≥ 25
$nHitsFit/nHitsPoss$	> 0.52 and < 1.05
p_T	> 0.15 GeV/c

d, t, ^3He, ^4He, and their antiparticles. The TPC tracks used in the present analysis are primary tracks. To select good tracks, various quality cuts are required to be applied to each track measured in the TPC. The track quality cuts are presented in Table 5.1. In order to have uniform detector performance, a pseudorapidity cut of $|\eta| < 1.0$ is applied in the data. To avoid admixture of tracks from secondary vertices, a constraint is imposed on the distance of closest approach (dca) between each track and the event vertex. The multiple counting of split tracks is avoided by requiring all tracks to have a minimum number of 25 fit points used in the reconstruction of the track. The effect of track splitting is minimized by further requiring that the number of fit points is more than half the number of total possible hit points for a track. Tracks can have a maximum of 45 hits in the TPC. The low momentum tracks ($p_T \leq 0.15$ GeV/c) can not traverse the entire TPC due to their large track curvature inside the solenoidal magnetic field. So, those tracks are avoided by requiring all tracks to have $p_T > 0.15$ GeV/c.

Figure 5.1 shows the ionization energy loss (dE/dx) of charged tracks as a function of rigidity ($rigidity = momentum/charge$) measured by the TPC. It can be seen that the light nuclei (d, t, ^3He, and ^4He) and their antiparticles can be identified very well using TPC. A distinct band of positive particles centered around the expected value for ^4He (red line) is shown in Fig. 5.1. This indicates that the detector is well-calibrated. For rigidity around -1 GeV/c, two negative particles are particularly well separated from the $^3\overline{He}$ band and are located very close to the expected dE/dx line for $^4\overline{He}$. These two tracks are considered as the anti-α ($^4\overline{He}$) candidates, which are encircled by an ellipse in the Fig. 5.1. At high momentum, the dE/dx values

Table 5.2: Track information of the two $^4\overline{He}$ candidates in year 2007 minimum bias Au+Au collisions data at $\sqrt{s_{NN}}$ = 200 GeV.

Variables	**Track A**	**Track B**
Run Id	8112087	8127001
Event Id	22394	31049
RefMult	271	410
Vertex (cm)	(0.466, -0.142, 5.331)	(0.484, -0.181, -3.399)
Track Id	425	1250
Pseudorapidity (η)	0.530	-0.114
ϕ (radian)	-1.926	-0.432
dca (cm)	0.244	0.626
nHitsFit	33	27
nHitsdEdx	22	18
|rigidity| (GeV/c)	0.945	0.969
dE/dx (GeV/cm)	4.299×10^{-5}	4.203×10^{-5}

of $^3\overline{He}$ and $^4\overline{He}$ merge. So, the Time-of-Flight (TOF) system is needed to separate these two species, which was not fully installed at STAR in the year 2007.

5.3 Anti-Alpha Candidates

The detailed track information about these two anti-α candidates, denoted as Track A and Track B, produced in run 7 minimum bias Au+Au collisions at $\sqrt{s_{NN}}$ = 200 GeV, are listed in Table 5.2. The validity of all the track information of these two anti-α candidates have been checked. The two anti-α tracks, Track A and Track B, are displayed in the STAR event display as shown in the Fig. 5.2 and Fig. 5.3, respectively. The STAR event display is an interface to draw a three-dimensional picture of an event in the STAR detector geometry. The two anti-α candidates are clearly visible in the STAR event display.

Along with these two $^4\overline{He}$ candidates, there are another 16 $^4\overline{He}$ candidates have been observed in run 10 Au+Au collisions at $\sqrt{s_{NN}}$ = 200 GeV and 62 GeV [5]. In run 10 Au+Au collisions, full coverage of TOF was installed at STAR. Hence, both TPC and TOF were used for the identification of $^4\overline{He}$. The top two panels of Fig. 5.4 shows the dE/dx (in units of multiples of $\sigma_{dE/dx}$, $n_{\sigma_{dE/dx}}$) as a function of calculated

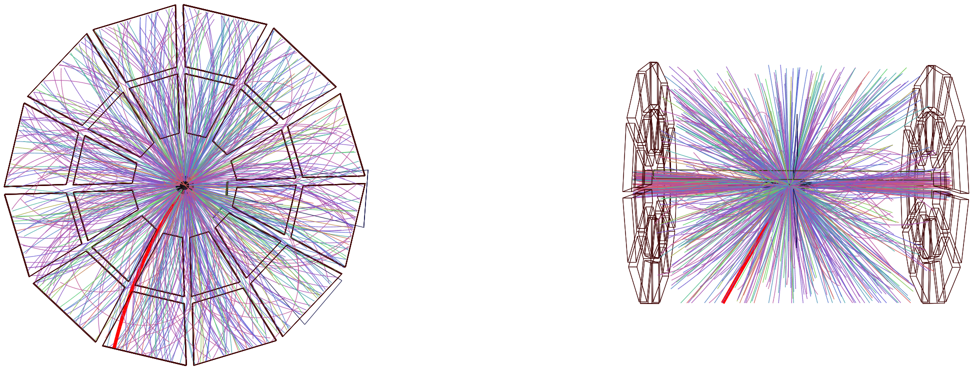

Figure 5.2: Tracks in TPC from an event which contains first $^4\overline{He}$ candidate (Track A) are shown in STAR event display with the beam axis normal to the page (left) and with the beam axis horizontal (right). The $^4\overline{He}$ candidate is highlighted in bold red line.

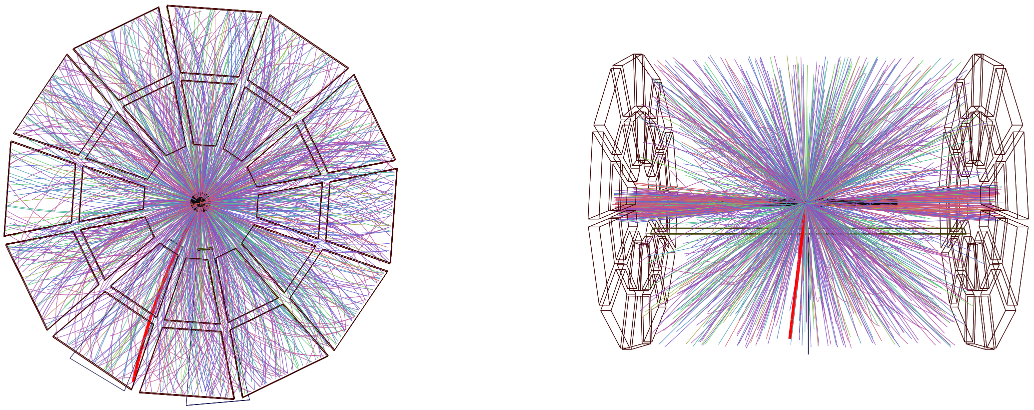

Figure 5.3: Tracks in TPC from an event which contains second ${}^{4}\overline{He}$ candidate (Track B) are shown in STAR event display with the beam axis normal to the page (left) and with the beam axis horizontal (right). The ${}^{4}\overline{He}$ candidate is highlighted in bold red line.

mass for negatively (first panel) and positively (second panel) charged particles. Here, $\sigma_{dE/dx}$ is the r.m.s. width of the dE/dx distribution for ^4He or $^4\overline{He}$. The mass of the particle is calculated as

$$m = (p/c)\sqrt{(t^2c^2/L^2 - 1)}, \tag{5.1}$$

where t is the time of flight, L is the path length, and c is the speed of light. In the second panel, ^4He particles cluster around $n_{\sigma_{dE/dx}} = 0$ and mass = 3.73 GeV/c^2, the appropriate mass for ^4He. A similar but smaller cluster of particles can be found in the first panel for $^4\overline{He}$. The bottom panel shows the projection onto the mass axis of the top two panels for particles with $n_{\sigma_{dE/dx}}$ of -2 to 3. There is clear separation between $^3\overline{He}$ and $^4\overline{He}$ mass peaks. There are 16 counts for $^4\overline{He}$ observed in run 10 Au+Au collisions at $\sqrt{s_{NN}}$ = 200 GeV and 62 GeV. The combined measurements of energy loss and the time of flight allow a clean identification of $^4\overline{He}$.

5.4 Blast-Wave Model Prediction and Invariant Yield

As described in section 4.3.4 of chapter 4, the Tsallis statistics in a Blast-Wave model (TBW) has been implemented to describe the identified particle spectra and v_2 at mid-rapidity at RHIC [8, 9]. We have used the same TBW model as described in Ref. [8], to predict the transverse momentum spectra of light nuclei. In this TBW model, the sources of particle emission is changed from a Boltzmann distribution to a Tsallis distribution in the Blast-Wave model:

$$\begin{aligned}\frac{dN}{m_T dm_T} &\propto m_T \int_{-Y}^{+Y} \cosh(y)dy \int_{-\pi}^{+\pi} d\phi \\ &\times \int_0^R rdr(1 + \frac{q-1}{T}(m_T\cosh(y)\cosh(\rho) - p_T\sinh(\rho)\cos(\phi)))^{-1/(q-1)},\end{aligned} \tag{5.2}$$

where $\rho = \tanh^{-1}(\beta_s(\frac{r}{R})^n)$ is the flow profile growing as n-th power from zero at the center of the collisions to β_s at the hard-spherical edge (R) along the transverse radial direction (r), and $\beta = \beta_s/(1 + 1/(n+1))$ is the average flow velocity and β_s is the maximum flow velocity. We have used $n = 1$ for this study. The parameter q characterizes the degree of non-equilibrium and T is the temperature.

The TBW fit has been done for the spectra of identified particles that include $\pi^{\pm}$, $K^{\pm}$, p, $\bar{p}$, ϕ, Λ, $\bar{\Lambda}$, Ξ, and $\bar{\Xi}$ [8]. The fit parameters and χ^2/ndf are listed in Table 5.3.

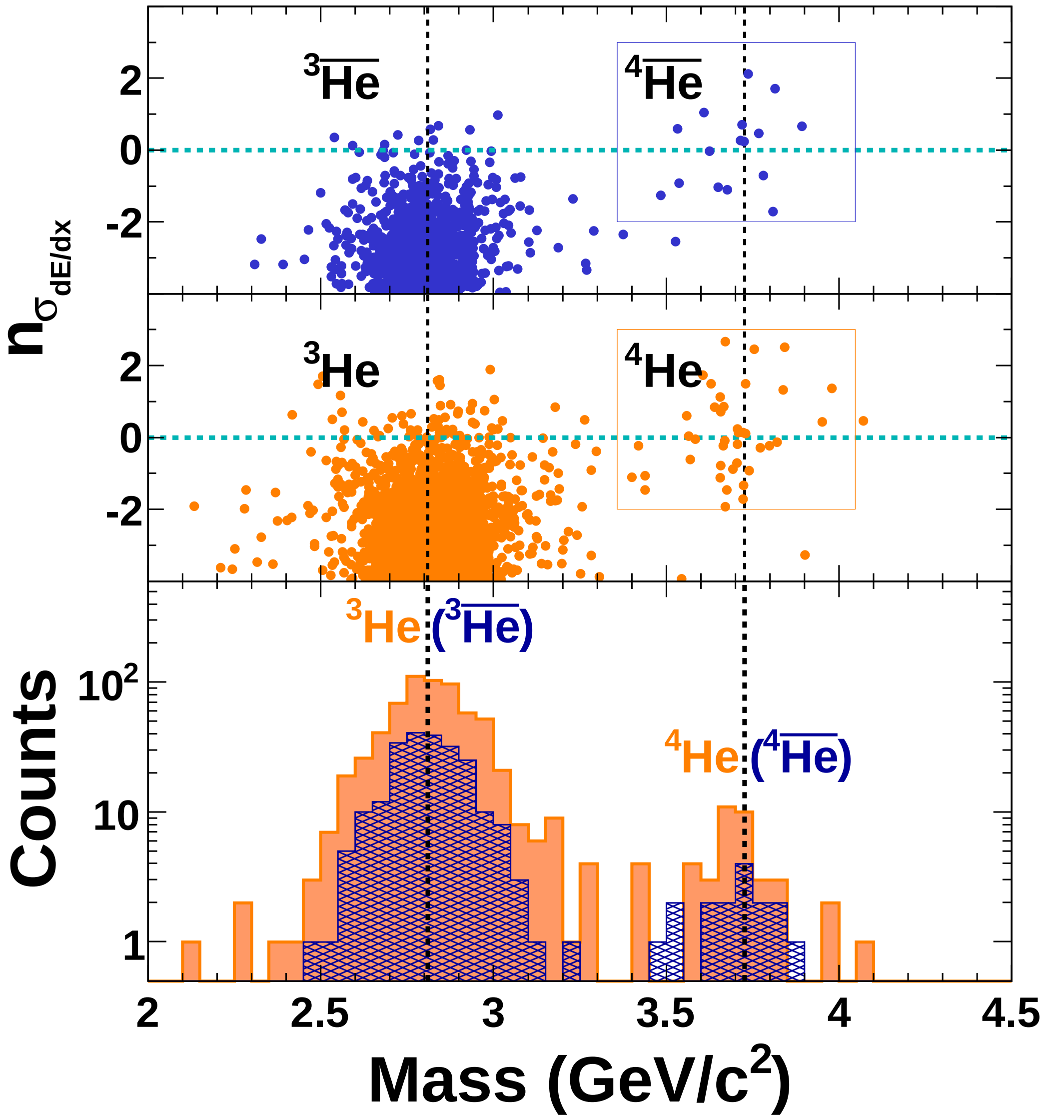

Figure 5.4: The top two panels show the dE/dx in units of multiples of $\sigma_{dE/dx}$, $n_{\sigma_{dE/dx}}$, of negatively charged particles (first panel) and positively charged particles (second panel) as a function of mass measured by the TOF system. The masses of ^{3}He ($^{3}\overline{He}$) and ^{4}He ($^{4}\overline{He}$) are indicated by the vertical lines at 2.81 GeV/c^2 and 3.73 GeV/c^2, respectively. The horizontal line marks the position of zero deviation from the expected value of dE/dx ($n_{\sigma_{dE/dx}} = 0$) for ^{4}He ($^{4}\overline{He}$). The rectangular boxes highlight areas for ^{4}He ($^{4}\overline{He}$) selections : $-2 < n_{\sigma_{dE/dx}} < 3$ and $3.35\,\mathrm{GeV/c^2} <$ mass $< 4.04\,\mathrm{GeV/c^2}$ (corresponding to a $\pm 3\sigma$ window in mass). The bottom panel shows a projection of entries in the upper two panels onto the mass axis for particles in the window of $-2 < \sigma_{dE/dx} < 3$.

Table 5.3: Values of parameters from TBW fit to identified particle transverse spectra for different centralities in Au+Au collisions at $\sqrt{s_{NN}} = 200$ GeV. Quoted errors are quadratical sum of statistical and uncorrelated systematic errors.

centrality	β	T (GeV)	$q-1$	χ^2/ndf
0-10%	0.470±0.009	0.122±0.002	0.018±0.005	130/125
10-20%	0.475±0.008	0.122±0.002	0.015±0.005	119/127
20-40%	0.441±0.009	0.124±0.002	0.024±0.004	159/127
40-60%	0.282±0.017	0.119±0.002	0.066±0.003	165/135
60-80%	$0^{+0.05}_{-0}$	0.114±0.003	0.086±0.002	138/123

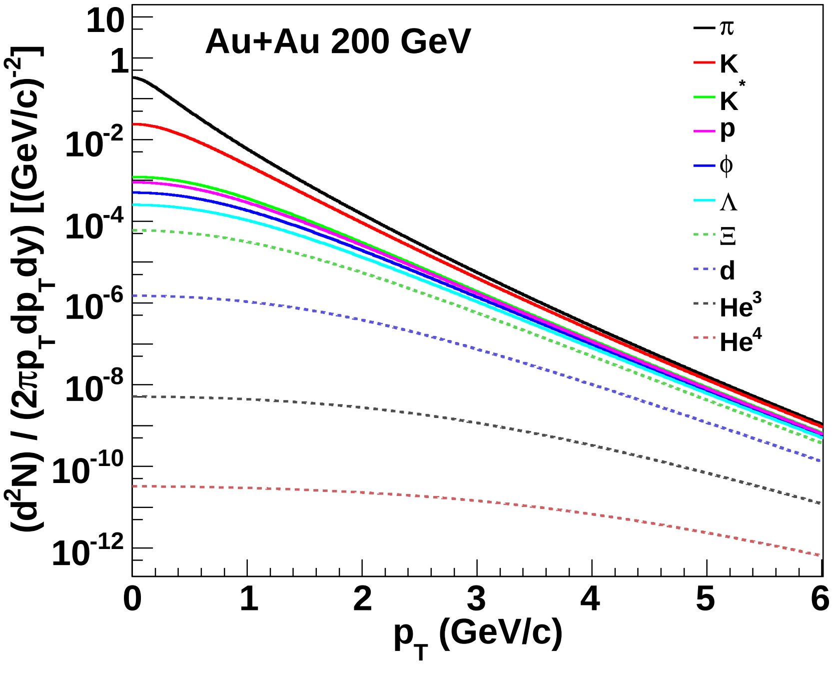

Figure 5.5: The transverse momentum spectra for identified particles including light nuclei ($d(\overline{d})$, ${}^3He({}^3\overline{He})$, and ${}^4He({}^4\overline{He})$) in 0-10% Au+Au collisions at $\sqrt{s_{NN}} = 200$ GeV. The spectra for light nuclei are predicted by TBW model using parameters from the fit to other hadrons.

Table 5.4: Values of yield ratios from TBW model in 0-10% Au+Au collisions at $\sqrt{s_{NN}} = 200$ GeV.

Centrality	$\frac{^4He(3-4\text{ GeV/c})}{^4He(0-8\text{ GeV/c})}$	$\frac{^3He(2.25-3\text{ GeV/c})}{^3He(0-8\text{ GeV/c})}$	$\frac{^4He/^3He(p_T/\lvert B\rvert=0.875\text{ GeV/c})}{^4He/^3He(0-8\text{ GeV/c})}$
0-10%	0.215	0.212	1.014

These parameters from TBW fits are used to predict the d, ^3He and ^4He spectra. Figure 5.5 shows the p_T spectra from TBW model for identified particles including light nuclei ($d(\bar{d})$, $^3He(^3\overline{He})$, and $^4He(^4\overline{He})$) in 0-10% Au+Au collisions at $\sqrt{s_{NN}}$ = 200 GeV. Similarly, the p_T spectra in other centralities have been obtained for light nuclei. The minimum bias spectra are obtained from the number of participant (N_{part}) weighted sum of the corresponding spectra in each centrality bin. The yield ratio of ^4He and ^3He are obtained in a p_T per baryon number window centered at $p_T/|B| = 0.875$ GeV/c with a width of 0.25 GeV/c and for the whole range of $p_T/|B|$, which differ by only 1%. Ratios calculated by TBW model in 0-10% Au+Au collisions at $\sqrt{s_{NN}} = 200$ GeV are listed in Table 5.4.

The observed counts are used to calculate the antimatter yield with appropriate normalization (the differential invariant yield) in order to compare with the theoretical expectation. The calculated ratios are $^4He/^3He = (3.0 \pm 1.3(\text{stat})^{+0.5}_{-0.3}(\text{sys})) \times 10^{-3}$ and $^4\overline{He}/^3\overline{He} = (3.2 \pm 2.3(\text{stat})^{+0.7}_{-0.2}(\text{sys})) \times 10^{-3}$ for central Au+Au collisions at $\sqrt{s_{NN}}$ = 200 GeV. The differential yields ($d^2N/(2\pi p_T dp_T dy)$) for $^4He(^4\overline{He})$ are obtained by multiplying the ratio of $^4He/^3He$ ($^4\overline{He}/^3\overline{He}$) with the ^3He ($^3\overline{He}$) yields [12]. Figure 5.6 shows the exponential [13] invariant yields versus baryon number in 200 GeV central Au+Au collisions. Empirically, the production rate reduces by a factor of $1.6^{+1.0}_{-0.6} \times 10^3$ ($1.1^{+0.3}_{-0.2} \times 10^3$) for each additional antinucleon (nucleon) added to the antinucleus (nucleus). This general trend is expected from coalescent nucleosynthesis models [14], originally developed to describe production of antideuterons [15], as well as from thermodynamic models [16].

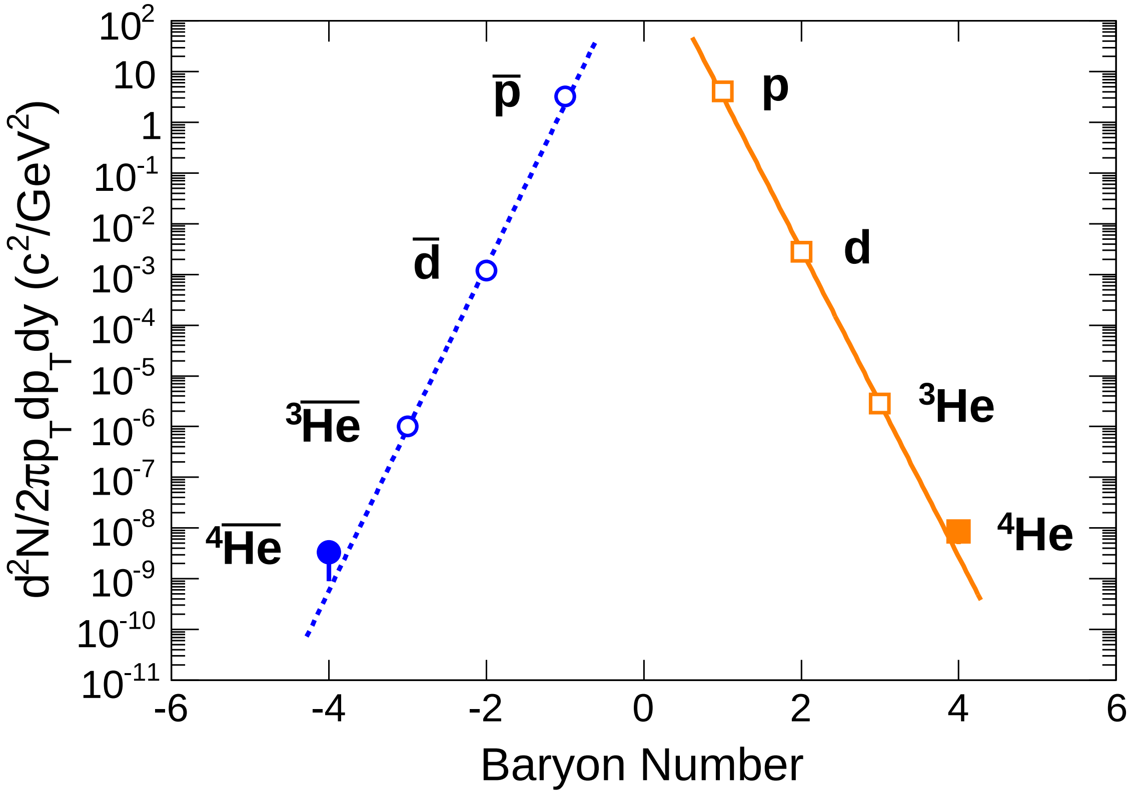

Figure 5.6: Differential invariant yields as a function of baryon number B, evaluated at $p_T/|B| = 0.875$ GeV/c, in central 200 GeV Au+Au collisions. The lines represent fits with the exponential formula $\propto e^{-r|B|}$ for positive and negative particles separately, where r is the production reduction factor. Errors are statistical only. Systematic errors are smaller than the symbol size, and are not plotted.

5.5 Summary

We have shown that $^4\overline{He}$ exists, and have measured its rate of production in nuclear interactions. This provides a benchmark for possible future observations of $^4\overline{He}$ in cosmic radiation. Barring a new breakthrough in accelerator technology, or the discovery of a completely new production mechanism, it is likely that the $^4\overline{He}$ will remain the heaviest stable antimatter nucleus observed in the foreseeable future.

Bibliography

[1] J. Alcaraz *et al.*, Phys. Lett. B **461**, 387 (1999).

[2] H. Fuke *et al.*, Phys. Rev. Lett. **95**, 081101 (2005).

[3] K. H. Ackermann *et.al.* (STAR Collaboration), Nucl. Instr. Meth. A **499**, 624 (2003).

[4] H. Bichsel, Nucl. Instr. Meth. A **562** 154 (2006).

[5] H. Agakishiev *et al.* (STAR Collaboration), Nature **473**, 353, 2011.

[6] E. Schnedermann, J. Sollfrank, and U. W. Heinz, Phys. Rev. C **48**, 2462 (1993).

[7] F. Retiere and M. A. Lisa, Phys. Rev. C **70**, 044907 (2004).

[8] Z. Tang *et al.*, Phys. Rev. C **79**, 051901 (R) (2009); M. Shao *et. al.*, J. Phys. G **37**, 085104 (2010).

[9] Z. Tang *et al.*, arXiv:nucl-ex/1101.1912.

[10] C. Tsallis, J. Stat. Phys. **52**, 479 (1988).

[11] J. Adams *et al.* (STAR Collaboration), Phys. Rev. Lett. **92**, 112301 (2004).

[12] B. I. Abelev *et al.* (STAR Collaboration), arXiv:0909.0566 [nucl-ex].

[13] T. A. Armstrong *et al.* (E864 Collaboration), Phys. Rev. Lett. **83**, 5431 (1999).

[14] H. Sato and K. Yazaki, Phys. Lett. B **98**, 153 (1981).

[15] S. T. Butler and C. A. Pearson, Phys. Rev. Lett. **7**, 69 (1961).

[16] P. Braun-Munzinger and J. Stachel, Nature **448**, 302 (2007).

Chapter 6

Conclusion

The present thesis shows some interesting data on particle production, particularly involving π and ϕ meson in d+Au collisions and light nuclei (d, t, ^3He and ^4He) in Au+Au collisions at RHIC. The first set of results correspond to production of ϕ mesons and pions in d+Au collisions at $\sqrt{s_{NN}}$ = 200 GeV. The data set used for this study was taken in the year 2008 with significantly reduced material (∼1/10) and high statistics (∼3) compared to previous runs at RHIC. The ϕ mesons were reconstructed via their hadronic decay channel $\phi \rightarrow K^+K^-$. Both decay daughters of ϕ meson (K^+ and K^-) and pions are identified using the Time Projection Chamber (TPC). The transverse momentum spectrum for ϕ meson in 0-20% d+Au collisions is found to be well described by a Levy function. This is mainly due to the power-law tail at intermediate and high p_T.

We have studied the nuclear modification factor (R_{dAu}) of the ϕ meson and compared it to those of π, K and p in central d+Au collisions. This has been done in order to understand the particle species dependence of Cronin effect. This is also expected to shed some light on the initial conditions reached in the d+Au collisions at RHIC. For ϕ meson, R_{dAu} is found to increase with p_T going above unity and is seen to be higher than R_{AuAu} at intermediate p_T. This enhancement of R_{dAu} of ϕ meson at the intermediate p_T is associated with the Cronin effect which can result from either momentum broadening due to multiple soft (or semi-hard) scattering in initial state, or final state interactions as suggested in the recombination models. These mechanisms also lead to different particle species (baryon/meson) and/or mass dependence in the nuclear modification factors. In the intermediate p_T ($2.5 < p_T < 4$ GeV/c), R_{dAu} of ϕ meson has been found to follow closely the same for other mesons. However, we need a further high precision measurement of R_{dAu} to differentiate very well between different particles and particle production scenarios.

The rapidity asymmetry (Y_{Asym}) of ϕ meson has also been studied in the most central d+Au collisions. This has been done to understand the particle production mechanism in forward (d going side) and backward rapidities (Au going side). The Y_{Asym} for ϕ meson is found to be greater than unity in the measured p_T region for both $|y| < 0.5$ and $0.5 < |y| < 1$. Similar to other hadrons, the Y_{Asym} for ϕ meson in the d+Au collisions is found to be larger for $0.5 < |y| < 1$ than for $|y| < 0.5$. This indicates the presence of some rapidity dependent nuclear effects. However, there is no strong particle type dependence observed for Y_{Asym} in the measured p_T region.

In addition, we have presented some results on pion production at mid-rapidity from d+Au collisions at $\sqrt{s_{NN}} = 200$ GeV. The transverse momentum spectra for π^- and π^+ at mid-rapidity ($|y| < 0.1$) have been obtained in 0-20% d+Au collisions at $\sqrt{s_{NN}} = 200$ GeV. The spectra for π^- and π^+ are well described by the Bose-Einstein function. The average transverse momenta $< p_T >$ of π^- and π^+ have been extracted from the spectra and are found to be 0.371 ± 0.003 and 0.371 ± 0.002, respectively. Similarly, the integrated particle multiplicity densities dN/dy of π^- and π^+ have been extracted from the spectra and are found to be 8.72 ± 0.36 and 8.74 ± 0.33, respectively. Within the statistical and systematic uncertainties, these data are consistent with the same obtained from previous measurements at the STAR experiment. The $< p_T >$ of pions in central d+Au collisions is found to be larger than that in peripheral Au+Au collisions. This can be due to jets, k_T broadening, and multiple scattering, because these effects can be stronger in d+Au collisions than in peripheral Au+Au collisions. However, the larger value of $< p_T >$ as obtained in central Au+Au collisions in comparison with the same for central d+Au collisions, can be due to other effects that include transverse radial flow, thermodynamic pressure, and some contributions from (semi-)hard scattering.

The next set of results correspond to the production of light nuclei such as d, t and ^3He. The v_2 of light nuclei has been measured in Au+Au collisions at $\sqrt{s_{NN}}$ = 200 GeV and 39 GeV, using the standard event plane method. The measured

v_2 for $d(\overline{d})$ and $^3He(\overline{^3He})$ as a function of transverse momentum p_T is found to follow an approximate atomic mass number (A) scaling. The v_2 values for light nuclei are further found to scale with the number of constituent quarks (NCQ) of their constituent nucleons and are consistent with NCQ scaled v_2 for baryons and mesons. This indicates that partonic collectivity dominates the expansion dynamics of the nucleus-nucleus collisions at RHIC. A negative v_2 is observed for $\overline{d}$ in the low transverse momentum region. This negative v_2 at low p_T is consistent with a large radial flow. Such a radial flow is expected to push low p_T particles to high p_T region resulting in a depletion in the number of low p_T particles, predominantly in the event plane.

The centrality dependence of v_2 for light nuclei has been studied and compared those with that for other hadrons in Au+Au collisions at $\sqrt{s_{NN}} = 200$ GeV. An increase of p_T integrated v_2 scaled by the participant eccentricity as a function of collision centrality has been observed for $^3He + \overline{^3He}$ similar to other hadrons. This behavior indicates a stronger collective expansion for more central collision. We have studied the mass dependence of average transverse momentum ($< p_T >$) and the average v_2 and compared those with Tsallis Blast-Wave (TBW) model predictions. Both v_2 and $< p_T >$ trends are consistent with expectations from a TBW model fit. A dynamical coalescence model calculation has been carried out for the v_2 of light nuclei in Au+Au collisions at $\sqrt{s_{NN}} = 200$ GeV. In this model, the probability for producing a cluster is determined by the overlap of its Wigner phase-space density and the nucleon phase-space distribution at freeze-out. The coordinate and momentum space distributions of nucleons at freeze-out are taken from a multiphase transport (AMPT) model within the string melting scenario. The measured v_2 of light nuclei in Au+Au collisions at $\sqrt{s_{NN}} = 200$ GeV are in good agreement with the dynamical coalescence model calculation.

In search for heavier antimatter nuclei, we have presented some interesting data on the observation of the antimatter helium-4 nucleus, also known as the anti-α ($\overline{\alpha}$) in the STAR experiment at RHIC. The anti-α consisting of two antiprotons and two antineutrons, is the heaviest observed antinucleus to date. In total 18 $^4\overline{He}$ counts were detected at the STAR experiment in 10^9 recorded Au+Au collisions at $\sqrt{s_{NN}} =$ 200 GeV and 62 GeV. Two $^4\overline{He}$ counts out of those 18 counts, are observed in the year

2007 Au+Au collisions at $\sqrt{s_{NN}} = 200$ GeV and forms a part of this thesis. These two candidates are identified by measuring the mean energy loss per unit track length ($\langle dE/dx \rangle$) in the TPC gas. The Tsallis Blast-Wave (TBW) model calculation has been done to predict the transverse momentum spectra for anti-α in Au+Au collisions at $\sqrt{s_{NN}} = 200$ GeV. The observed $^4\overline{He}$ yield is consistent with expectations from thermodynamic and coalescent nucleosynthesis models. This provides an indication of the production rate of even heavier antimatter nuclei and a point of reference for possible future observations in cosmic radiation.